UNIVERSITY OF MINING AND GEOLOGY
"ST. IVAN RILSKI"

JOURNAL

OF

MINING AND GEOLOGICAL

SCIENCES

Volume 62

Number 1

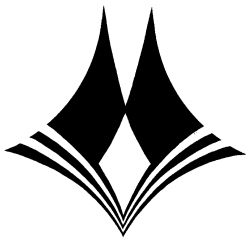

Sofia 2019

University of Mining and Geology “St. Ivan Rilski”
1, Prof. Boyan Kamenov Str., 1700 Sofia, Bulgaria
http://www.mgu.bg

ISSN 2682-9525 (print)
ISSN 2683-0027 (online)

www.mgu.bg/new/journal

CONTENTS

VOLCANIC RING MORPHOSTRUCTURES IN THE WESTERN SREDNOGORIE, BULGARIA

Ivan Marinov, Kamen Popov, Nenko Temelakiev

University of Mining and Geology "St. Ivan Rilski", 1700 Sofia; imarrinov@gmail.com; kpopov@mgu.bg; nenkotemelakiev@outlook.com

ABSTRACT. The focus of this study is the interpretation of images obtained by the ASTER optical instrument on the TERRA satellite. Its data is processed and presented in stereoscopic 3D images. Anaglyphic glasses with red and cyan colour filters are used to obtain the realistic effect of the images. The structural analysis of the data shows two ring morphostructures with distinct pattern of radial and concentric lineaments forming a clear circular morphology with a diameter of up to 9 km, located around the town of Breznik and the Kliosura village in the Western Srednogorie, Bulgaria. The radial structures show clearer sharpness with respect to the drainage system and the relief, compared to the concentric structures and the radial pattern, is predominant. The ring morphostructures are formed among the volcanic rocks of the Breznik and Klisoura paleo-volcanoes, represented by lava flow, epiclastic and pyroclastic products. A characteristic feature is the distribution of the proximal faces, represented by lava flows, volcanic bomb, and lapilli tuff in the central parts of the morphological structure, which locate the Breznik paleo-volcano approximately around the centre of the ring morphostructure. It is assumed that the radial and concentric lineaments are probably relatively well preserved remains of a volcanic cone. The tectonic events, which occurred during and after the final stage of the most intense volcanic activity, led to the formation of radial and concentric faults. They probably serve as channels for the movement of the ore hydrothermal fluid and ore hosting structures for gold-silver Milin Kamak deposit and Klisoura ore occurrence.

Keywords: ring morphostructures, lineaments, volcanic cone, Western Srednogorie

ВУЛКАНСКИ КРЪГОВИ МОРФОСТРУКТУРИ В ЗАПАДНОТО СРЕДНОГОРИЕ, БЪЛГАРИЯ

Иван Маринов, Камен Попов, Ненко Темелакиев

Минно-геоложки университет "Св. Иван Рилски", 1700 София

РЕЗЮМЕ. В настоящето изследване е извършен анализ на изображения, получени от оптичния инструмент ASTER на сателита TERRA. Данните от него са обработени и представени като стереоскопични 3D изображения. За получаване на реалистичен ефект от изображенията са използвани анаглифни очила, с червен и циан цветни филтри. Структурният анализ на данните показват две кръгови морфоструктури с отчетлив рисунък от радиални и концентрични линеаментни структури, оформящи ясно обособени кръгови морфоструктури с диаметър до 9 km, ситуирани около град Брезник и село Клисура в Западното Средногорие, България. Радиалните разломи показват по-ясно изразена отчетливост по отношение на дренажната система и релефа, в сравнение с концентричните структури, като радиалният рисунък е преобладаващ. Кръговите морфоструктури са оформени сред вулканските продукти на Брезнишкия и Клисурския палеовулкани, представени от лавови потоци, епикластични и пирокластични продукти. Характерна особеност е разпределението на проксималните окологърлови фациеси, представени от лавови потоци, бомбени и лапилови туфи в централните участъци на морфоструктурата, които ситуират Брезнишкия палеовулкан приблизително около центъра на морфоструктурата. Приема се, че радиалните и концентричните линеаменти вероятно представляват относително добре запазени останки от вулкански конус. Тектонските събития, възникнали по време и след заключителния стадий на най-интензивната вулканска дейност са довели до образуването на радиални и концентрични разломи, които вероятно са послужили като канали за придвижване на рудоносните хидротермални разтвори и рудовместващи структури за златно-сребърното находище "Милин камък" и рудопроявление Клисура.

Ключови думи: кръгови морфоструктури, линеаменти, вулкански конус, Западно Средногорие

Introduction

The ring morphostructures, subject of this study, are situated in Western Bulgaria near the town of Breznik. The structures have a diameter of up to 9 km and shape the positive part of Zavala and Viskyar Mountains, which are part of Sredna Gora Mountain Range. The ring morphostructures in the Srednogorie Tectonic Zone have been a subject of study in a number of publications (Baltakov, 1975; Popov, Spiridonov, 1990; Spiridonov, 1999; Jelev et al., 2003). Many of the structures are considered as a reflection of the Late Cretaceous volcano-plutonic activity in the Apuseni-Banat-Timok-Srednogorie Magmatic and Metallogenic Belt (ABTS) (Popov et al., 2002). According to the definition of Spiridonov (1999), the ring morphostructures are structures, grouped in an arched or circular shape that may incorporate geological formations of the same and different ages. The typical ring magmatic structures in ABTS played a crucial role as ore-controlling structures and many of the ore deposits were associated with them (Spiridonov, 1999). According to Baltakov (1975), part of the morphostructures, situated in Panagurishte Ore Region are likely to represent concealed plutonic body or offshoots. They can be observed and traced on the surface through their structural configuration. A great part of the volcanic complexes in ABTS shows a distinct radial-concentric shape and Spiridonov (1999) considers them as composite local volcanic morphostructures, which built up the bigger morphostructures from the third order.

The main objectives of this study are: 1) interpretation of stereo image data, obtained from the ASTER optical instrument; 2) recognition of the lineament structures; 3) determining the morphological character of the ring structures; 4) interpretation of the genesis on the morphostructure.

Geological setting

In tectonic position, the area belongs to the Apuseni-Banat-Timok-Srednogorie Magmatic and Metallogenic Belt. The zone is characterised by extensional geodynamical regime and development of Late Cretaceous magmatic activity with numerous submarine volcanoes (Popov et al., 2002). Volcanic activity began in Coniacian and ended during Campanian ages (Bairactarov, 1989). The formations of Breznik, Klisoura and Vidrica paleo-volcanoes are established around the ring morphostructures. They are associated with high potassium calc-alkaline, calc-alkaline and shoshonitic series (Dabovski, 2009; Velev, 2012). The Upper Cretaceous rocks around the town of Breznik contain a succession of various potassium trachybasalts, shoshonites, ash, psephitic, lapilli and bomb tuffs as pyroclastic and epiclastic products are predominance (Fig. 1) (Velev, 2012). They belong mainly to the Breznik paleo-volcano and they form up to 1400 m thick volcanic formations (Marinov, Bairactarov, 1980). Further to the North-West they are covered by the rocks of Vidrica paleo-volcano (Dabovski, 2009). In a regional tectonic situation, the rocks are part of the Srednogorie Tectonic Zone that is divided into two main units – Sofia and Lyubash (Marinova, 2010). The most characteristic feature of the Lyubash Unit is the distinct absence of volcanic products and respectively – the ore deposits, associated with Upper Cretaceous magmatic activity. The Lyubash Unit is considered as a Late Alpine monoclinal structure (Zagorchev, 1995). The magmatic presence is regarded as an important feature for distinguishing between both tectonic units and respectively the Sofia Unit is composed of various volcanic and sedimentary rocks. The boundary between them is the Pernik fault zone (Marinova, 2010).

The rocks that form the basement belong to various Paleozoic, Mesozoic and Lower Cretaceous sedimentary successions developed mainly in the southern part of the study area (Fig. 2).

The Paleozoic rocks are built mainly of Silurian argillites, Devonian flysch and Permian conglomerates, breccia and sandstones. The distribution of these rocks is immediately south of Breznik in the Lyubash Unit. The Mesozoic rocks consist of various terrigenous-carbonate sediments that build up the Lyubash Unit and part of Sofia Unit as tectonic confined blocks.

The rock that form the cover belong to Paleogene and Neogene sediments, considered as sedimentary fill in graben systems and partially cover the southern and southwestern edge of the studied area. The Pernik graben is situated to the South of the area and consists of Oligocene and Miocene continental clastic molasse association. To the south-west, the Neogene succession fills the Graovo graben partly covering the south edge of Sofia Unit.

Fig. 1. Outcrops around the town of Breznik and Klisoura village
a, volcanic bombs up to 1.5 m, south of Babica village; *b*, unsorted volcanic bombs, south of Babica village; *c*, unsorted bomb tuffs, close view; *d*, poorly sorted lapilli tuff, near of the Klisoura monastery

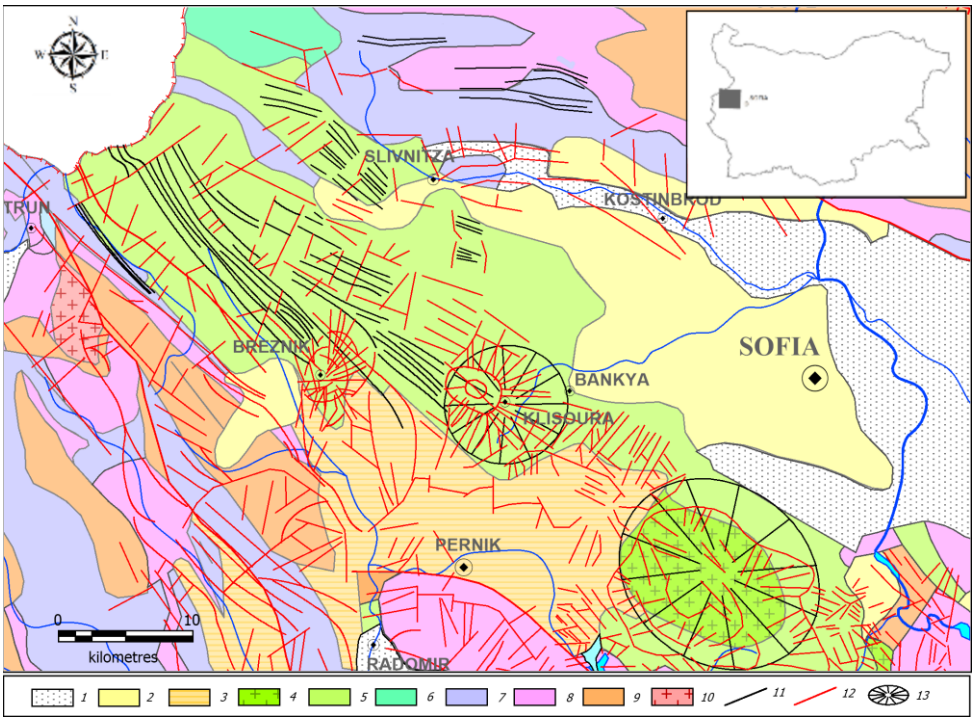

Fig. 2. Simplified geological map of the Western Srednogorie (based on Milev et al., 2007, with modifications)
1, Quaternary sediments; *2*, Neogene sediments; *3*, Paleogene sediments; *4*, intrusive complex in the Western Srednogorie; *5*, volcanogenic-sedimentary formations in the Western Srednogorie; *6*, Lower Cretaceous sediments; *7*, Jurassic sediments; *8*, Triassic sediments; *9*, Paleozoic sediments; *10*, Stara Planina granodiorite and granite (Devonian–Lower Carboniferous); *11*, lineaments interpreted as supposed sedimentary strata; *12*, lineaments interpreted as supposed faults; *13*, volcanic cones by Milev et al. (2007)

Data used

In this study, the remote sensing method has been applied for lineament mapping, visualisation and interpretation. Images obtained by ASTER (Advanced Spaceborne Thermal Emission and Reflection Radiometer) optical instrument on the board of TERRA satellite (Abrams, Hook, 2000) has been used to help lineament extraction. For the purpose of this study, mainly optical stereo-images acquired by near infrared bands 3n and 3b of ASTER optical instrument were processed by the methodology described by Popov (2011).

When the satellite is in orbit over the Earth surface, it captures images from two separate positions to obtain a couples of stereo images. The first image is orthogonal with respect to the ground, or so called “nadir looking” and the second one is inclined – “backward looking”. The nadir and backward looking sensors have a spectral range for 3th band (0.76–0.86 μm). Therefore, to prepare epipolar image couples, both images have been paired through up to 55 control points that allow precise overlapping. A total of seven georeferenced ASTER scenes, provided by the U.S. Geological Survey, and covering the Wester Srednogorie area were interpreted in this study. In order to produce on screen a stereo effect 3n/3b/3b was used as RGB band combination (Fig. 3). The processed images were rotated 90 degrees anti-clockwise to achieve a stereo effect visible with 3D anaglyph red/cyan glasses. The cloud-free epipolar images were interpreted in GIS software for lineament extraction and drawing. In parallel with the interpretation of remote sensing data, geological mapping and detailed fieldwork were carried out by the authors around the ring morphostructure near the town of Breznik in order to identify the lineaments and rock succession and respectively, part of the lineament structures were traced on the ground.

Results and discussion

The results obtained from the remote sensing methods represent two distinctly visible ring morphostructures with roughly equal sizes (Figs. 2–4). Both structures are located inside the volcanic formations of the Sofia Unit. They match exactly with the probable volcanic centres in the Western Srednogorie Magmatic Zone.

The eastern ring morphostructure is situated at the foot of Lyulin Mountain, western from the town of Bankya, around the villages of Klisoura, Mala Rakovica and Radui. It corresponds with the Klisoura paleo-volcano that is described as part of a lower volcanogenic-sedimentary unit (Dabovski, 2009). Alongside this unit, further paleo-volcano centres of Dragotino, Radulovo, Galabovo, Zlatusha and numerous subvolcanic bodies and necks have been formed. They clearly shape a linearly elongated zone, probably caused by magmatic active NW-SE Burel fault zone (Gochev et al., 1970). These paleo-volcanoes do not show clearly visible ring morphostructures on the epipolar scenes. Further to the East, multiple intrusion rocks of the dome-shaped Vitosha pluton show structures with a visible circular shape. In the Map of Alpine magmatism in Bulgaria (Dabovski et al., 1989) and the Metallogenic map of gold deposits in Bulgaria (Milev et al., 2007), the position of the ring morphostructure around Klisoura roughly coincides with the volcanic cone that has been described west, near the town of Bankya.

The western ring morphostructure is situated around the town of Breznik and the villages of Viskyar, Babica, Goz, Arzan

and Dolni Romantsi. On the epipolar 3D images, the structure has a distinct circular shape with a diameter up to 9 km. The ring morphostructure has been outlined by clearly visible concentric and radial faults, which shape the local drainage system. Unlike the Klisoura, which has highlighting concentric lineaments, the Breznik ring morphostructure have more distinct radial faulting (Fig. 4). It directly coincides with the position of Breznik paleo-volcano and, as opposed to Klisoura paleo-volcano, it belongs to the upper volcanogenic-sedimentary unit. Apparently, this ring morphostructure is a result of active volcanic activity during the Campanian stage. The lineament structures occurred during the most intensive deformations of the volcano-tectonic stage after eruptions and explosions. On the other hand, the specific configuration of lineaments obviously shows remains of a well-preserved volcanic apparatus. During the most extensive eruptions and subsequent deformation events, the newly formed structures may serve as feeder channel and/or hosting structures for hydrothermal fluid or lava products. Near Breznik, the gold-silver Milin Kamak deposit is situated, which is assigned as an intermediate sulphidation epithermal deposit (Sabeva et al., 2017). There are eight parallel ore zones with EW direction and dipping to the South. The structural analysis and ore models made in Leapfrog show three main fault systems (Marinov, 2018). They spatially coincide with the position of the concentric and radial lineaments. The products of Breznik paleo-volcano are highly altered with intensive acid leaching and are associated with argillic, advanced argillic, quartz-sericite and propylite rocks. In a plan view, the dykes and ore zones have a particular arched form which presumably associated with concentric lineaments observed on epipolar images. The volcanic fault and neck structures served as an up-flowed pathway for the dykes and later ore-bearing fluids. The local stress field created by the most intense volcanic activity can be regarded as probable explanation for the direction peculiarity of ore hosted structures with East-West direction that stands obliquely from the regional structures with direction 140–160°. Obviously, the position of the intensively altered rocks and the intermediate sulphidation epithermal deposit show an approximately close relationship with the central part of the ring morphostructure and can be regarded as an indication for the close distance of the gold-silver ore deposit Milin Kamak to the volcanic centre. On the other hand, the highly altered rocks in Klisoura ore occurrence also show a distinctly close relationship with the ring morphostructure western of Bankya. One of the specific features of the proximal volcanic facies is their position in the central part of ring morphostructure. The thick-bedded lava flow, volcanic bomb and lapilli tuff are closely related to the volcanic neck and slope and mark the position of the Breznik and Klisoura paleo-volcanoes approximately to the central part of the ring morphostructure (Fig. 1).

The area in Western Srednogorie was an arena of thrust-nappe deformation events during the Laramian phase of Alpine orogeny, which led to the formation of South-West vergent Krasava syncline (Marinova, 2010). The second tectonic event arosed during the Illyrian phase and have resulted in N-S strike-slip and normal faults, which cut the earlier nappe structures. However, our observations show that both deformation events did not rework completely the lineaments form of the ring structures and they are still clearly visible in present day topographic relief and are marked by the drainage systems. During the Neogene, sedimentary fill graben systems partially covered up and concealed the south-eastern part of the ring lineaments.

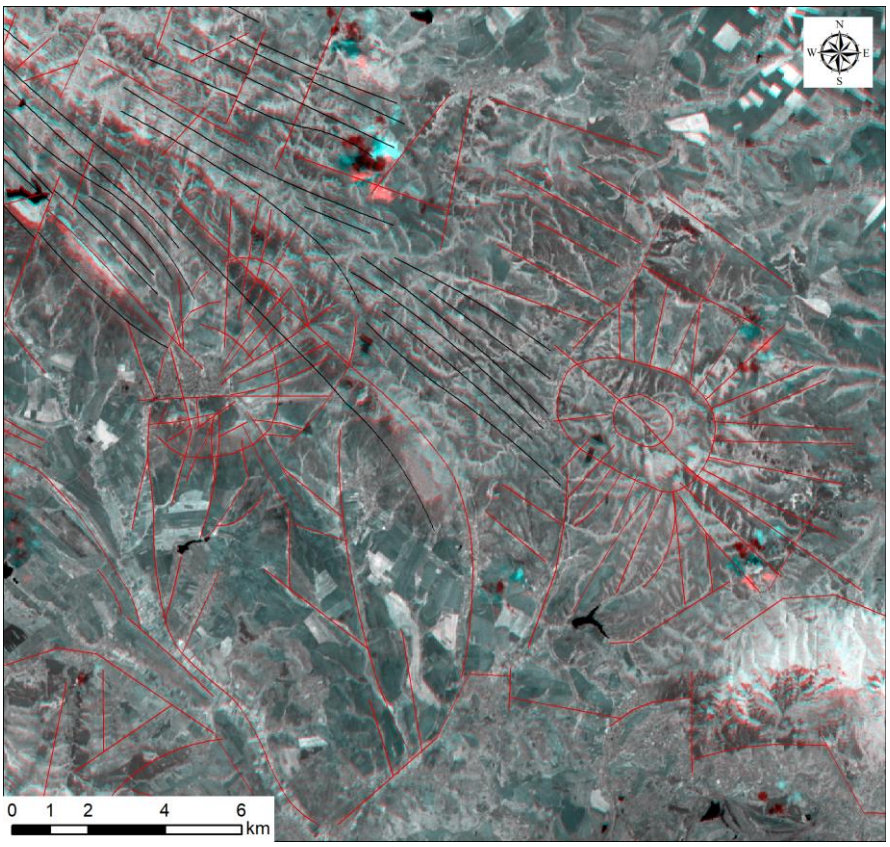

Fig. 3. ASTER stereo image over the town of Breznik area with outlined lineaments and ring morphostructures

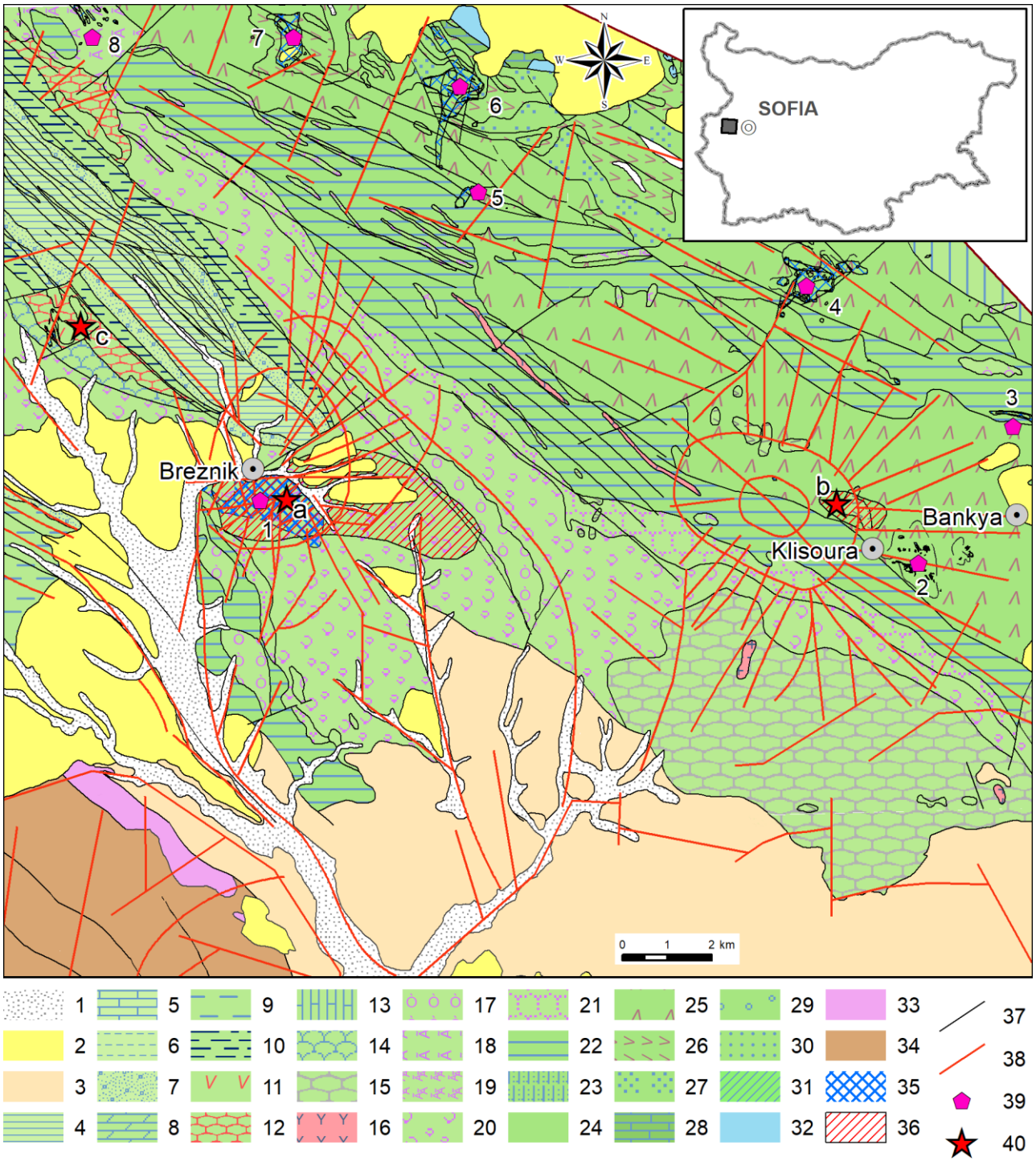

Fig. 4. Geological map of Breznik area (based on Marinova et al., 2010 with modifications)
1, Quaternary sediments; *2*, Neogene sediments; *3*, Paleogene sediments; *4*, sandstone-marly formation; *5*, reef limestone; *6*, bituminous shale; *7*, sandstone formation; *8*, conglomerate-sandstone-marly formation; *9*, sandstone-argillite formation; *10*, flysch formation; *11*, amphibole, amphibole-pyroxene andesite; *12*, pyroclastic-tuffite formation; *13*, formation of detrital-organogenic limestones; *14*, marly-tuffite formation; *15*, Lyulin volcanic complex – agglomerate tuff, ash tuff, tuffite; *16*, monzodiorite; *17*, coarse porphyritic latite and trachyte; *18*, trachybasalt and shoshonite lava and lava breccia; *19*, trachybasalt and shoshonite dyke; *20*, pyroclastic formation; *21*, package of psammo-aleuritic tuffs; *22*, tuffite-marly formation; *23*, marly-clayey-sandy formation; *24*, marly-limestone formation; *25*, Andesite and pyroclastic; *26*, biotite-amphibole andesite; *27*, limestone-sandstone formation; *28*, limestone-marly formation; *29*, conglomerate-sandstone formation; *30*, limestone formation; *31*, marly-limestone formation (Lower Cretaceous); *32*, Jurassic sediments; *33*, Triassic sediments; *34*, Paleozoic sediments; *35*, hydrothermally altered rocks; *36*, proximal volcanic facies – lava flow, bomb tuff, lapilli; *37*, lineaments interpreted as supposed sedimentary strata; *38*, lineaments interpreted as supposed faults; *39*, ore deposits and occurrences (*1*, Milin Kamak Au-Ag deposit, *2*, Klisoura ore occurrence, *3*, Pozharevo ore occurrence, *4*, Zlatusha ore occurrence, *5*, Gurgulyat ore occurrence, *6*, Bratushkovo ore occurrence, *7*, Radulovtsi ore occurrence, *8*, Pishtene ore occurrence); *40*, supposed paleo-volcanic centres (*a*, Breznik paleo-volcano, *b*, Klisoura paleo-volcano, *c*, Vidrica paleo-volcano)

Conclusions

The recognition of lineament structures by stereo images, obtained by the ASTER instrument on TERRA satellite and the fieldwork on the ground allowed to distinguish two clearly visible ring morphostructures situated around the town of Breznik and the Klisoura village. The possibility to acquire optical stereo-images nowadays is considered as an extremely useful tool for structural investigation. The ring morphostructures are regarded as a reflection of the Late Cretaceous Breznik and Klisoura paleo-volcanoes and probably represent preserved fragments of volcanic cones. They have an obvious radial and concentric pattern with a slightly elliptical shape. Lineaments show apparent direction that is different from regional structures with direction 140-160°. On the ground, the radial structures are more distinguishing and easy to trace than concentric ones and control the local drainage systems. The spatial position of lava flows, volcanic bombs and lapilli tuffs is an indicator for proximal facies and mark the paleo-volcanoes proximity to the central part of ring morphostructures. A characteristic feature regarding stress field during most intense deformation and evolution of volcano is the formation of numerous radial and concentric structures that contribute to the development of intensive hydrothermal activity and may serve as channels and hosting faults for ore-bearing fluids and dykes. Our observation shows that ore hosted faults in Milin Kamak Au-Ag deposit are probably created from this local stress field shortly after the most intensive activity. The position of lineaments close to the hinge line of the synclinal presumably explains the low erosion level, conserved Upper Cretaceous proximal facies and make the structure to stand out in present day relief. The close relationship between the altered rocks and ring morphostructures could contribute to ore and exploration geology and could be used as an indication and basis for future mineral prospecting and investigation of other ore controlling ring morphostructures in Apuseni-Banat-Timok-Srednogorie Magmatic and Metallogenic Belt.

Acknowledgements. The authors are grateful to Seequent Limited for providing academic license of Leapfrog Geo and ESRI Bulgaria for ArcGIS license.

References

Abrams, M., S. Hook. 2000. *ASTER User Hand Book. Version 2.0*. Jet Propulsion Laboratory, California Institute of Technology, 135 p.

Bairactarov, I. 1989. *Upper Cretaceous Metallogeny of Western Srednogorie and Plana Mountain*. PhD Thesis, Research Institute for Mineral Resources, Sofia, 197 p. (in Bulgarian)

Baltakov, G. 1975. Endodynamic determination of the contemporary morphogenetic processes in the Ihtimansko Srednogorie. – *Ann. Univ. Sofia*, *69*, 2, 33–39 (in Bulgarian with English abstract).

Dabovski, C., A. Harkovska, B. Kamenov, B. Mavroudchiev, G. Stanisheva-Vasileva, Y. Yanev. 1989. *Map of Alpine Magmatism in Bulgaria (Geodynamic Approach), 1:1000000*. CIPP in Map-making, Sofia.

Dabovski, H., B. Kamenov, D. Sinnyovsky, E. Vasilev, E. Dimitrova, I. Bairactarov. 2009. Upper Cretaceous geology. – In: Zagorchev, I., H. Dabovski, T. Nikolov (Eds.). *Geology of Bulgaria. Part II. Mesozoic Geology*. Marin Drinov Acad. Publ. House, Sofia, 305–638.

Gočev, P., V. Kostadinov, M. Matova, I. Velinov. 1970. The structure of a part of the southern strip of the Western Srednogorie. – *Rev. Bulg. Geol. Soc.*, *31*, 3, 289–301 (in Bulgarian).

Jelev, V., L. Nikova, J. Crummy, F. Mitreva. 2003. Characteristic of Bardo ring morphostructure (Bulgaria). – *Ann. Univ. Min. and Geol.*, *46,* Part I, 53–58.

Marinov, T., I. Bairaktarov. 1980. Alkaline basalts in the Western Srednogorie. – *C. R. Acad. Bulg. Sci.*, *33*, 4, 529–532.

Marinov, I., N. Temelakiev, P. Doychev, K. Popov. 2018. Ore controlling factors at the gold-silver deposit Milin Kamak, Western Srednogorie, Bulgaria. – *Rev. Bulg. Geol. Soc.*, *79*, 3, 125–126. (in Bulgarian with English abstract).

Marinova, P., V. Grozdev, D. Ivanova, D. Sinnyovsky, I. Petrov, P. Milovanov, A. Popov. 2010. *Explanatory Note to the Geological Map of the Republic of Bulgaria. Scale 1:50000. Map Sheet K-34-46-G (Breznik)*. Ministry of Environment and Water, Bulgarian Geological Survey, Sofia, 63 p.

Milev, V., V. Georgiev, N. Obretenov. 2007. Metallogenic map of gold deposits in Bulgaria. – In: *Milev, V. (Ed.). Gold Deposits of Bulgaria*. Zemya'93, Sofia, 208 p. (in Bulgarian)

Popov, K. 2011. Recognition of the Panagyurishte ring morphostructure by satellite stereo-images. – *Ann. Univ. Min. Geol., 54*, Part I, 81–88.

Popov, P., H. Spiridonov. 1990. On the Morphostructure of the Ore Districts in the Sredna Gora Region. – *Ann. Higher Inst. Mining and Geol.*, *36*, Part I, 31–39 (in Bulgarian).

Popov, P., T. Berza, A. Grubich, I. Dimitru. 2002. Late Cretaceous Apuseni-Banat-Timok-Srednogorie (ABTS) Magmatic and Metallogenic Belt in the Carpathian-Balkan orogen. – *Geologica Balc., 32, 2-4*, 145–163.

Sabeva, R., V. Mladenova, A. Mogessie. 2017. Ore petrology, hydrothermal alteration, fluid Inclusion, and sulphur stable isotopes of Milin Kamak intermediate sulphidation epithermal Au-Ag deposit in Western Srednogorie, Bulgaria. – *Ore Geol. Rev*., *88*, 400–415.

Spiridonov, H. 1999. *Ring Morphostructures in the Sredna Gora*. "Prof. Marin Drinov" Acad. Publ. House, Sofia, 270 p. (in Bulgarian)

Velev, S., R. Nedialkov, I. Peycheva, A. von Quadt. 2012. Geological and petrological characteristics of the volcanic centres from the upper volcanogenic–sedimentary unit from the Western Srednogorie. – *Geologica Macedonica*, *3,* 7–12.

Zagorchev, I., V. Kostadinov, D. Chounev, R. Dimitrova. I. Sapunov, P. Chumachenko, S. Yanev. 1995. *Explanatory Note to the Geological Map of Bulgaria on Scale 1:100000, Vlasotince and Breznik Map Sheets*. Committee of Geology and Mineral Resources, Geology and Geophysics, Sofia, 60 p. (in Bulgarian with English abstract)

MINERALISATION IN ORE ZONE 1, MILIN KAMAK DEPOSIT, WESTERN SREDNOGORIE, BULGARIA

Daniela Nikolova, Sergey Dobrev, Kalin Ruskov

University of Mining and Geology "St. Ivan Rilski", 1700 Sofia; danny.nikolova@abv.bg

ABSTRACT. The Milin Kamak deposit is located in the Western Srednogorie zone. This zone is part of the Late Cretaceous Apuseni-Banat-Timok-Srednogorie magmatic and metallogenic belt. The mineralisation is gold-silver, epithermal, intermediate sulfidation type. The deposit represents a product of the Breznik paleovolcano. Ore mineralisation is formed in three stages: quartz-pyrite, quartz-polymetallic and carbonate-gold. In this study mineral composition of Ore Zone 1 is discussed, represented by pyrite, marcasite, arsenopyrite, chalcopyrite, galena, sphalerite, tennantite-tetrahedrite, enargite, bornite, covellite, hematite, pyrrhotite, seligmanite-bournonite, jordanite (?), robinsonite (?) and native gold. The gangue minerals are represented by quartz, carbonates and barite.

Keywords: Late Cretaceous, Western Srednogorie, Milin Kamak, ore zone 1, ore minerals

МИНЕРАЛИЗАЦИЯ НА РУДНА ЗОНА 1, НАХОДИЩЕ "МИЛИН КАМЪК", ЗАПАДНО СРЕНОГОРИЕ, БЪЛГАРИЯ

Даниела Николова, Сергей Добрев, Калин Русков

Минно-геоложки университет "Св. Иван Рилски", 1700 София

РЕЗЮМЕ. Находище "Милин камък" се намира в Западното Средногорие. Тази зона е част от къснокредния Апусени-Банат-Тимок-Средногорски магматичен и металогенен пояс. Минерализацията е златно-сребърна, епитермална, от умереносулфиден тип. Находището е продукт на Брезнишкия палеовулкан. Рудната минерализация е отложена в три стадия: кварц-пиритов, кварц-полиметален и карбонатно-златен. Разгледан е минералният състав на рудна зона 1, представен от пирит, марказит, арсенопирит, халкопирит, галенит, сфалерит, тенантит-тетраедрит, енаргит, борнит, ковелин, хематит, пиротин, селигманит-бурнонит, йорданит (?), робинсонит (?) и самородно злато. От нерудните минерали присъстват кварц, карбонати и барит.

Ключови думи: Късна Креда, Западно Средногорие, Милин Камък, рудна зона 1, рудни минерали

Geological settings of the Milin Kamak deposit

The Milin Kamak deposit is situated in the Sofia tectonic unit in the western part of the Srednogorie Zone of Apuseni-Banat-Timok-Srednogorie magmatic and metallogenic belt (Popov et al., 2002). It is located in propylitic, sericitic and argillic altered Late Cretaceous trachybasalt to andesitic volcanic and volcanoclastic rocks (Dabovski et al., 2009) – products of Breznic paleo-vulcano (Fig. 1). A part of the sequence is overlain by Paleogene and Neogene sediments. To the south-west, Permian to Jurassic sequence of continental to marine sediments, represented by sandstones, clay and limestone, is observed.

The gold-silver epitermal deposit Milin Kamak is situated south-west from the Krasava syncline. The major faults and shear zones are with N-W orientation, parallel to the paleo-subduction line (oceanic crust beneath the Eurasian continental margin – Dabovski et al., 2009). Later formed faults with NE direction are cross-cutting former ones. E-W striking secondary faults host the ore mineralisation.

The Ore Zone 1 is a vein with numerous apophyses. The ore body is with E-W orientation, dipping steeply to the south. It is located within intensively brecciated rocks and is considered to be the most promising part of the deposit.

Material and methods

For the purpose of this study 30 representative samples from drill holes and adits have been taken. All the samples are with visible ore mineralisation and high gold content. Position of samples (polished sections respectively) at level 760 m is given in Figure 2. Polished sections were investigated at the University of Mining and Geology "St. Ivan Rilski" (UMG) under reflected plane polarised light with microscope Meiji MT-9430. Microphotographs were taken with a digital camera Meiji Infinity-1 and a reflex digital photo camera Nikon D3200, mounted on a trinocular. Electron microprobe analyses of ore minerals have been done using X-ray spectral micro analyser JEOL JSM-6010 PLUS LA, with EDS spectrometer at the UMG "St. Ivan Rilski". The mode of operation is determined by the following analytical conditions: 20 kV accelerating voltage, 30 Pa pressure and High vacuum. The standards used are pure metal Cu and Al.

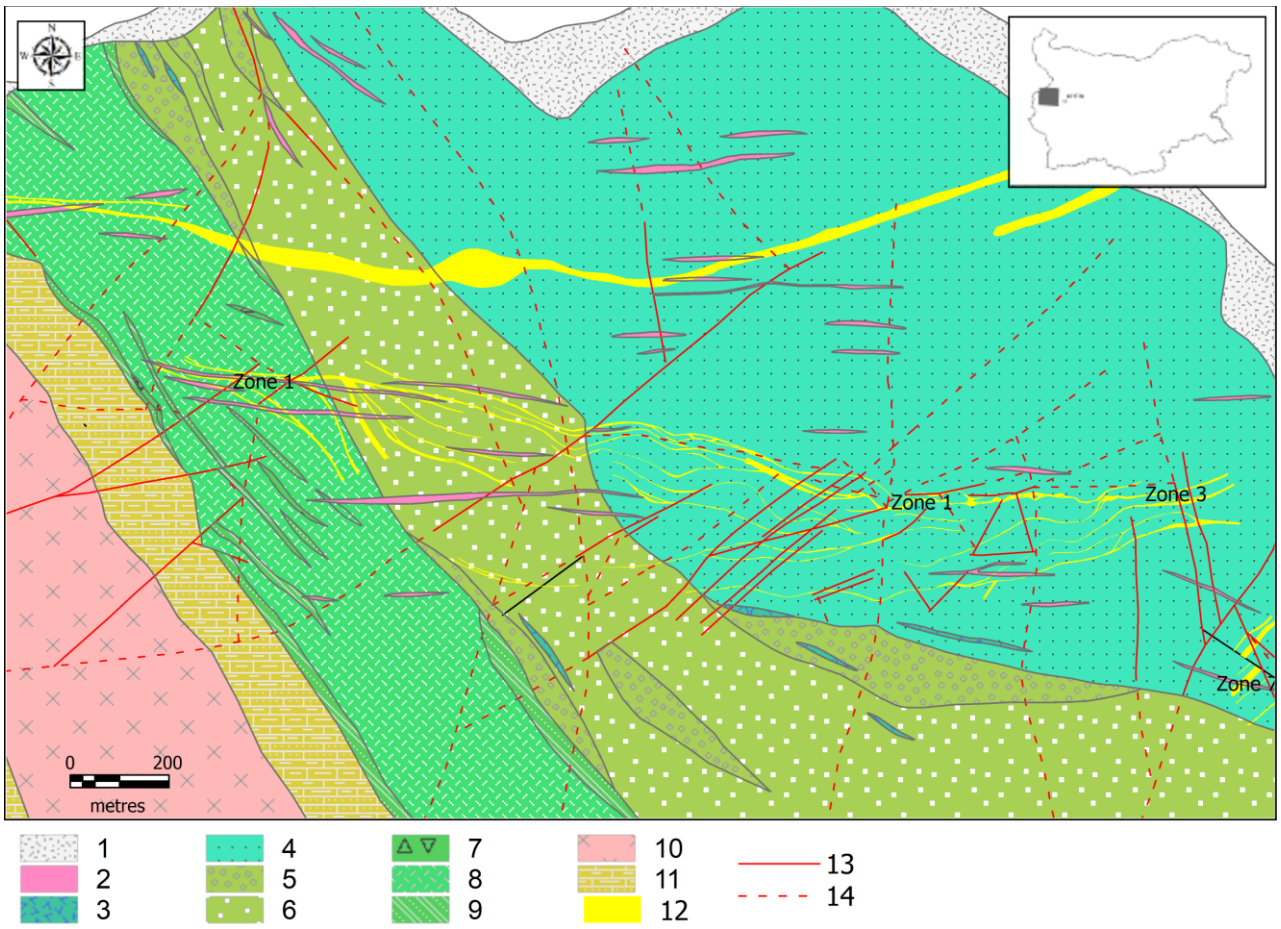

Fig. 1. Geological map of the Milin Kamak deposit and Ore Zones (data from "Thrace Resources" Ltd)
1, alluvial sediments; *2*, andesitobasalt dyke; *3*, basalt and andesitobasalt lavas; *4*, agglomerate tuffs; *5*, bomb–block tuffs; *6*, lapilli–psephitic tuffs; *7*, trachybasalt lavas; *8*, lapilli tuffs; *9*, beds of psephytic and pellitic tuffs; *10*, trachyandesites (plagioclase); *11*, sediment alternation; *12*, ore zone; *13*, certain fault; *14*, supposed fault

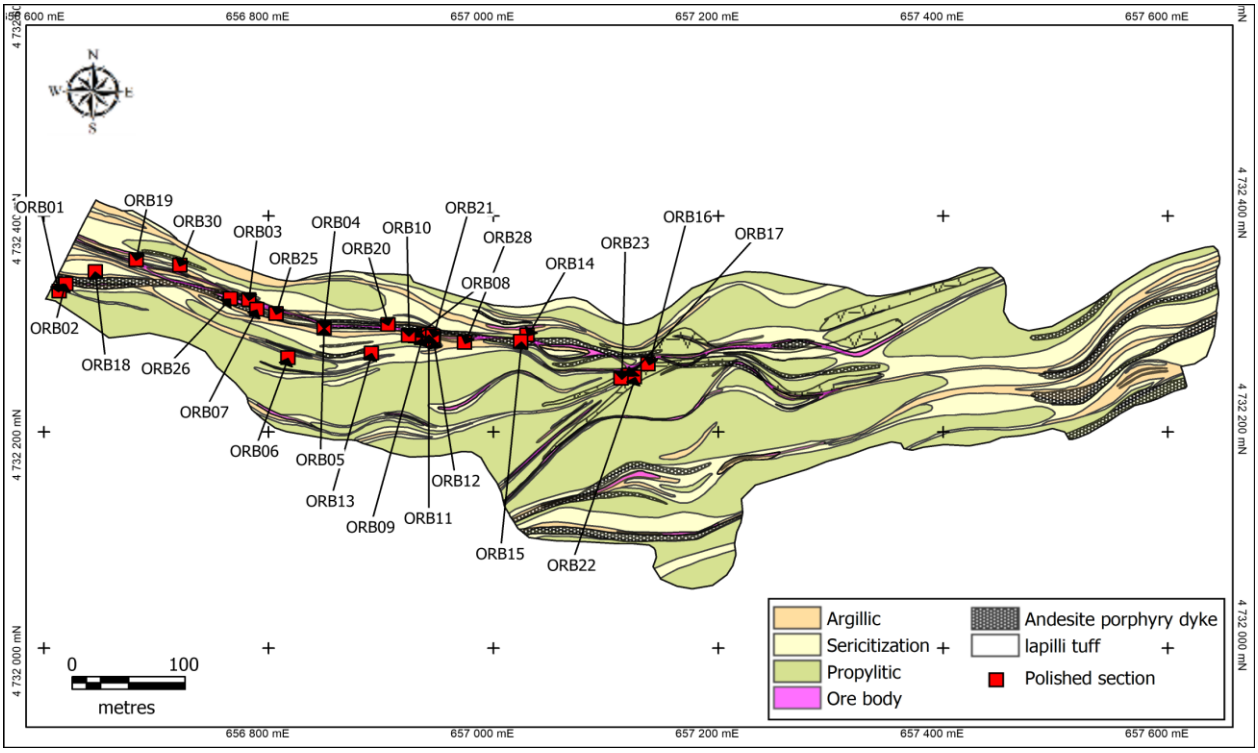

Fig. 2. Plan of level 760 with different types of alteration and position of samples (polished sections) in Ore Zone 1, Milin Kamak deposit (data from "Thrace Resources" Ltd.)

Mineralogy

Ore minerals

Pyrite is the main ore mineral. It appears as aggregates with xenomorphic to semi-euhedral shape (Fig. 3.F, 3.J) and size less than 100 μm (Fig. 3.B), in some cases with colloform structure ("melnikovite-pyrite"). It is often observed as large irregular grains with bay-like contours (Fig. 3.G), rarely as euhedral (Fig. 3.B) and subhedral grains, often with zonal structure. In larger grains inclusions from galena, chalcopyrite, sphalerite, pyrrhotite and tennantite-tetrahedrite (Fig. 3.H) are present. Pyrite appears as aggregates with irregular shape and sometimes with skeleton contours intensively corroded by carbonates. In some cases it associates with marcasite (Fig. 3.A). Single electron microprobe analysis determines content of As 1.69 wt% comparatively lower than reported by Stoykov et al. (2007). The calculated formula is $(Fe_{1.02}As_{0.03})_{1.05}S_{1.95}$ (Table 1).

Marcasite is the second by distribution ore mineral. It usually forms fine veinlets, platy and elongated prismatic to needle-like grains often in characteristic star-like aggregates (Fig. 3.J). Marcasite crystals with platy to prismatic habit often are rimming large pyrite aggregates (Fig. 3.A). Marcasite forms aggregates with mosaic structure together with pyrite in association with chalcopyrite, sphalerite and galena. Usually it forms fine-grained aggregates with a woody or colloform structure. Marcasite is observed as fine-grained strips among Mn-calcite with banded structure. In some cases it associates with chalcopyrite and sphalerite rimming large tennantite-tetrahedrite grains (Fig. 3.C). It demonstrates distinct bireflectance and strong anisotropy with colour effects from blue-green to dark brown. No impurities were determined with calculated formulas $Fe_{1.03}S_{1.98}$ and $Fe_{1.04}S_{1.95}$ (Table 1).

Arsenopyrite is rarely observed in rhombic shaped crystals and "larkspur" intergrowths (Fig. 3.B) or star-like aggregates. Arsenopyrite is characterised by high reflectance, white colour and strong anisotropy with colour effects (bluish to yellow-brown). The formulas based on microprobe analyses are $Fe_{1.04}As_{0.86}S_{1.09}$, $Fe_{1.04}As_{0.85}S_{1.11}$, $Fe_{1.05}As_{0.83}S_{1.12}$ (Table 1).

Chalcopyrite is established as emulsion within sphalerite grains and inclusions with size less than 20 μm in quartz, pyrite, marcasite (Fig. 3.C, 3.H), galena and sphalerite (Fig. 3.K). Together with marcasite, it forms a rim around sphalerite or pyrite grains and cross-cutting the latter ones in fine veinlets (Fig. 3.E). It is also observed as small grains within Mn-calcite. Chalcopyrite often forms joint aggregates with minerals from tennantite-tetrahedrite series (Fig. 3.E).

Galena also appears as individual grains with size up to 150 μm in peripheral parts of quartz veinlets. It is observed as euhedral crystals in sphalerite or corrodes pyrite grains as anhedral aggregates (Fig. 3.F). Galena is usually corroded by carbonates and barite. It often is observed together with bournonite-seligmannite and is overgrown by the latter one (Fig. 3.K). Microprobe analyses of two galena grains determine formulas $(Pb_{1.03}Sb_{0.04}Ag_{0.01})_{1.08}S_{0.92}$ and $Pb_{1.08}S_{0.92}$ (Table 1).

Sphalerite appears as coarse grains (from 3–4 mm to до 5–6 mm) with irregular shape (Fig. 3.C), often with rim from chalcopyrite and marcasite (Fig. 3.E). It appears as small inclusions in pyrite and forms aggregates with pyrite and marcasite, or with chalcopyrite, galena and mineral from tennantite-tetrahedrite series. Inclusions from pyrite are often observed, but chalcopyrite emulsion is not typical. Sphalerite is confirmed by single microprobe analysis – absence of iron (Table 1) and formula $Zn_{0.98}S_{1.02}$. It could be determined as cleiophane – manifests very intensive yellowish-brown internal reflections, often with well expressed zonal structure (Fig. 3.D).

Tennantite-tetrahedrite. A mineral from this series is found comparatively rare. It forms individual grains with large inclusions from chalcopyrite and smaller from galena and sphalerite. Such grains are often rimmed by fine-grained marcasite aggregates (Fig. 3.C). The mineral from tennantite-tetrahedrite series often associates with sulfides (chalcopyrite, sphalerite, galena and marcasite) and some sulfosalts (bournonite), filling interstitial spaces between large cracked pyrite grains in some cases accompanied by native gold (Fig. 3.J). Mainly As varieties have been determined, but also pure Sb members are present (Table 2). The latter ones are brighter in backscattered electrons. Microprobe analyses taken on different in brightness image from tennantite-tetrahedrite grain determines two end members of the series (Table 2) – mainly As (Zn-tennantite) $(Cu_{10.45}Zn_{1.69})_{12.14}(As_{2.63}Sb_{1.41})_{4.04}S_{12.82}$, and Sb – Ag-bearing Zn-tetrahedrite – $(Cu_{8.11}Ag_{2.40}Zn_{1.77})_{12.28}Sb_{4.07}S_{12.65}$. The composition of tennantite-tetrahedrite is similar to the theoretical, with a negligible S deficiency (Table 4).

Enargite. Among massive galena, a single grain from a grey mineral with distinct anisotropy was observed (Fig. 3.F). Microprobe analysis proves enargite (Table 3) with calculated formula $Cu_{3.04}As_{0.96}S_{4.00}$.

Bornite was found as single rounded inclusions within a pyrite grain. It did not manifest anisotropy and is characterised by a pink colour with brown shade. Presence of a chalcopyrite grain at the same photo suggests that bornite is an ore mineral with a primary origin.

Covellite is observed as inclusion together with minerals from tennantite-tetrahedrite series only in one pyrite grain (Fig. 3.G). The latter one is with indigo blue colour, shows strong bireflectance and pleochroism (to pale blue) and very strong anisotropy with colour effects (purple-red). No doubt it is an alteration product over chalcopyrite in the zone of secondary copper enrichment of the deposit.

Hematite was found as elongated prismatic inclusions with size up to 25 μm in just one pyrite grain associating with marcasite and sphalerite. Hematite grains manifest distinct anisotropy and in the largest one red internal reflection could be observed.

Pyrrhotite is observed as rounded drop-like inclusions with size up to 10 μm in some pyrite grains and is characterised by creamy colour and distinct anisotropy (Fig. 3.H).

Seligmannite-bournonite series mineral is often found as prismatic grains among gangue, observed at the periphery of galena grains or as separate individuals in close vicinity to galena grains, sphalerite, chalcopyrite and marcasite. They manifest distinct anisotropy and usually are with well expressed lamellar structure (Fig. 3.I). Colour in reflected light is light grey with reflection lower than that of galena. Minerals from seligmannite-bournonite series associates closely with other sulfosalt and late gangue minerals like barite and dolomite, often accompanied by native gold. Microprobe analyses determine mostly As varieties (seligmannite) but also pure bournonite presents (Table 3). The calculated formulas are with non-stoichiometric composition.

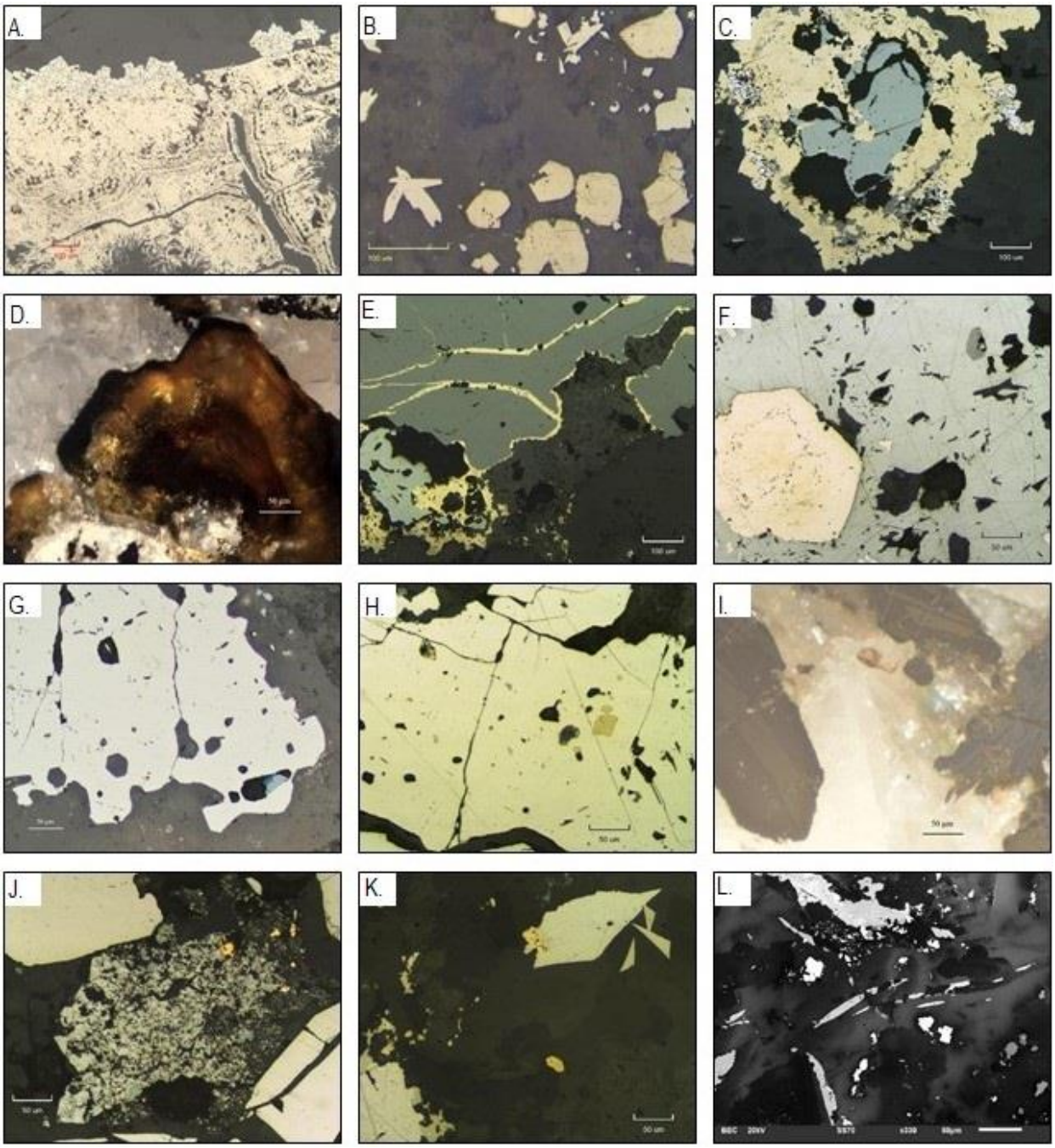

Fig. 3. Microphotographs in reflected plane polarised light, parallel Nickols (*N //*). Same conditions for all photos if not specified
A. Pyrite with colloform structure. At the upper boundary of pyrite aggregate rim of marcasite is developed (white, bluish shade, with strong anisotropy); *B*. Euhedral and semi-euhedral pyrite grains (yellowish-white) situated at the right. At the top spear-like to prismatic arsenopyrite grains (white) are observed. At the left – typical for arsenopyrite "larkspur" intergrowth; *C*. Aggregate from chalcopyrite (yellow), sphalerite (grey) and marcasite (white with bluish shade) formed around tennantite-tetrahedrite grain (light grey, in the centre); *D*. Sphalerite grain (yellowish-brown internal reflections) with zonal structure within carbonate vein. (*N+)*; *E*. Sphalerite (grey) rimmed and cross-cut by chalcopyrite (yellow). At the bottom left an aggregate from tennantite-tetrahedrite (light grey) and chalcopyrite is observed; *F*. Euhedral pyrite grain (yellow-white, at the bottom, left) located within galena (white) from the vein. At the top right single enargite grain (grey) is situated; *G*. Pyrite (white) from the veinlet contains single inclusion from tennantite-tetrahedrite (light grey) and covellite (indigo-blue with bright purple-red colors of anisotropy) – most probably formed after chalcopyrite; *H*. Pyrite aggregate (yellowish-white) contains inclusions of chalcopyrite (yellow), sphalerite (grey) and pyrrhotite (creamy, showing strong anisotropy); *I*. Prismatic bournonite-seligmanite grains with well expressed lamellar structure. Isometric galena grain was also analysed (dark to black in the centre). (*N+*); *J*. Aggregate from marcasite (greyish-white) and tennantite (grey) with five small Au grains (bright yellow) located within the interstitial space among pyrite grains; *K*. Robinsonite (?) – light grey with greenish tint – rhombic shape and 3 smaller grains with triangle contours associate with chalcopyrite (yellow). At the bottom left galena grain (white) with bournonite (light grey) at the periphery; *L*. Two jordanite grains (bright white) among dolomite (dark grey) and barite (light grey, bright). To the right from them galena crystal (white with square shape) is observed.
SEM, Backscattered electron image, COMPO regime

Table 1. *Microprobe analyses of sulfides and native gold from Milin Kamak deposit*

Mineral	Pyrite	Marcasite		Arsenopyrite			Galena		Sphalerite	Gold					
Elements (wt. %)	MK1	MK2	MK3	MK4	MK5	MK6	MK7	MK8	MK9	MK10	MK11	MK12	MK13	MK14	MK15
Fe	47.02	47.61	48.28	37.18	37.11	37.48	–	–	–	1.77	–	–	–	–	–
As	1.69	–	–	40.73	40.24	39.70	–	–	–	–	–	–	–	–	–
Pb	–	–	–	–	–	–	88.33	88.86	–	–	–	–	–	–	–
Sb	–	–	–	–	–	–	–	2.09	–	–	–	–	–	–	–
Ag	–	–	–	–	–	–	–	0.31	–	4.30	2.27	2.22	3.30	1.83	2.77
Au	–	–	–	–	–	–	–	–	–	93.93	97.73	97.78	96.7	98.17	97.23
Zn	–	–	–	–	–	–	–	–	66.32	–	–	–	–	–	–
S	52.39	52.39	51.72	22.10	22.65	22.82	11.67	11.74	33.68	–	–	–	–	–	–
Σ	101.1	100	100	100.01	100	100	100	103	100	100	100	100	100	100	100

Table 2. *Microprobe analyses of minerals from tennantite-tetrahedrite series from Milin Kamak deposit*

Mineral	Tennantite-tetrahedrite					Tennantite					Tetrahedrite			
Elements (wt. %)	MK16	MK17	MK18	MK19	MK20	MK21	MK22	MK23	MK24	MK25	MK26	MK27	MK28	MK29
Cu	41.35	40.68	42.4	41.15	42.06	45.09	37.38	37.18	42.73	46.78	38.46	37.46	38.07	28.76
Fe	0.70	1.94	–	–	–	5.62	6.68	7.09	0.45	5.70	–	2.31	1.82	–
Zn	7.58	7.50	7.06	6.73	7.10	2.28	6.45	6.54	6.73	–	6.60	6.41	5.74	6.47
Ag	–	–	–	–	–	–	–	–	–	–	1.22	1.07	0.83	14.47
As	9.87	11.62	12.59	10.22	12.05	19.36	15.05	12.81	12.64	19.57	2.75	2.98	3.22	–
Sb	14.69	11.99	11.00	15.25	11.65	–	4.31	6.73	10.96	–	26.58	25.53	26.34	27.66
S	25.81	26.28	26.95	26.65	27.15	27.66	30.13	29.65	26.46	27.95	24.38	24.24	23.90	22.64
Σ	100	100.01	100	100	100.01	100.01	100	100	99.97	100	99.99	100	99.92	100

Table 3. *Microprobe analyses of bournonite-seligmannite, jordanite, enargite, robinsonite (?) from Milin Kamak deposit*

Mineral	Bournonite-seligmannite			Bournonite			Seligmannite			Jordanite			Enargite	Robinsonite (?)	
Elements (wt. %)	MK30	MK31	MK32	MK33	MK34	MK35	MK36	MK37	MK38	MK39	MK40	MK41	MK42	MK43	MK44
Pb	48.20	48.25	46.91	48.16	47.82	46.48	50.0	48.81	50.26	68.62	69.37	69.57	–	44.46	44.29
Cu	12.38	11.84	11.86	12.39	11.97	12.17	12.75	13.04	12.99	–	–	–	49.14	–	–
As	10.30	7.72	9.25	–	–	–	15.91	15.55	14.32	7.36	7.86	7.53	18.25	4.75	5.18
Sb	12.09	15.36	14.80	23.18	23.72	24.38	3.27	4.96	5.18	9.49	8.16	8.57	–	32.99	32.84
S	17.03	16.84	17.18	16.27	16.49	19.97	18.08	17.64	17.25	14.53	14.61	14.33	32.61	17.80	17.70
Σ	100	100	100	100	100	100	100.01	100	100	100	100	100	100	100	100.01

Table 4. *Crystallochemical formulas of minerals in Tables 1–3 (only those not given in the text) calculated mainly after Chvileva et al., 1988*)

Gold (MK10)	$(Au_{0.87}Ag_{0.07}Fe_{0.06})_{1.00}$
Gold (MK11)	$(Au_{0.96}Ag_{0.04})_{1.00}$
Gold (MK12)	$(Au_{0.96}Ag_{0.04})_{1.00}$
Gold (MK13)	$(Au_{0.94}Ag_{0.06})_{1.00}$
Gold (MK14)	$(Au_{0.97}Ag_{0.03})_{1.00}$
Gold (MK15)	$(Au_{0.95}Ag_{0.05})_{1.00}$
Tennantite-tetrahedrite (MK16)	$(Cu_{10.45}Fe_{0.45}Zn_{1.60})_{12.50}(As_{2.60}Sb_{0.40})_{4.00}S_{12.82}$
Tennantite-tetrahedrite (MK17)	$(Cu_{8.60}Fe_{1.88}Zn_{1.47})_{11.95}(As_{2.52}Sb_{0.81})_{3.33}S_{13.60}$
Tennantite-tetrahedrite (MK18)	$(Cu_{10.45}Zn_{1.69})_{12.14}(As_{2.63}Sb_{1.41})_{4.04}S_{12.82}$
Tennantite-tetrahedrite (MK19)	$(Cu_{10.19}Zn_{1.62})_{11.81}(As_{2.15}Sb_{1.97})_{4.12}S_{13.08}$
Tennantite-tetrahedrite (MK20)	$(Cu_{10.24}Zn_{1.68})_{11.92}(As_{2.49}Sb_{1.48})_{3.97}S_{13.11}$
Tennantite (MK21)	$(Cu_{10.47}Fe_{1.48}Zn_{0.51})_{12.46}As_{3.80}S_{12.70}$
Tennantite (MK22)	$(Cu_{8.65}Fe_{0.27}Zn_{1.79})_{12.45}(As_{3.30}Sb_{0.51})_{3.81}S_{12.83}$
Tennantite (MK23)	$(Cu_{8.60}Fe_{1.88}Zn_{1.47})_{11.95}(As_{2.52}Sb_{0.81})_{3.33}S_{13.60}$
Tennantite (MK24)	$(Cu_{10.27}Fe_{0.20}Zn_{1.83})_{12.30}(As_{2.08}Sb_{1.91})_{3.99}S_{12.71}$
Tennantite (MK25)	$(Cu_{10.93}Fe_{1.50})_{12.33}As_{3.84}S_{12.83}$
Tetrahedrite (MK26)	$(Cu_{10.13}Zn_{1.69}\ Ag_{0.19})_{12.01}(As_{0.61}Sb_{3.65})_{4.26}S_{12.73}$
Tetrahedrite (MK27	$(Cu_{9.80}Zn_{1.63}Fe_{0.69}Ag_{0.16})_{12.28}(As_{0.65}Sb_{3.49})_{4.14}S_{12.57}$
Tetrahedrite (MK28)	$(Cu_{10.13}Zn_{1.69}Ag_{0.19})_{12.01}(As_{0.61}Sb_{3.65})_{4.26}S_{12.73}$
Ag-bearing Zn-tetrahedrite (MK29)	$(Cu_{8.11}Ag_{2.40}Zn_{1.77})_{12.28}Sb_{4.07}S_{12.65}$
Bournonite-seligmannite (MK30)	$Pb_{1.17}Cu_{0.98}(As_{0.69}Sb_{0.50})_{1.29}S_{2.67}$
Bournonite-seligmannite (MK31)	$Pb_{1.19}Cu_{0.95}(As_{0.53}Sb_{0.64})_{1.17}S_{2.69}$
Bournonite-seligmannite (MK32)	$Pb_{1.24}Cu_{1.04}Sb_{1.02}S_{2.71}$
Bournonite (MK33)	$Pb_{1.24}Cu_{1.04}Sb_{1.02}S_{2.71}$
Bournonite (MK34)	$Pb_{1.23}Cu_{1.00}Sb_{1.04}S_{2.75}$
Bournonite (MK35)	$Pb_{1.17}Cu_{1.01}Sb_{1.05}S_{2.77}$
Seligmannite (MK36)	$Pb_{1.17}Cu_{0.98}(As_{1.03}Sb_{0.05})_{1.08}S_{2.75}$
Seligmannite (MK37)	$Pb_{1.14}Cu_{1.00}(As_{1.01}Sb_{0.19})_{1.20}S_{2.70}$
Seligmannite (MK38)	$Pb_{1.19}Cu_{1.01}(As_{0.94}Sb_{0.21})_{1.15}S_{2.65}$
Jordanite (MK39)	$Pb_{14.84}(As_{4.39}Sb_{3.50})_{7.89}S_{20.31}$
Jordanite (MK40)	$Pb_{14.93}(As_{4.71}Sb_{3.00})_{7.71}S_{20.45}$
Jordanite (MK41)	$Pb_{15.16}(As_{4.51}Sb_{3.16})_{7.67}S_{20.17}$
Enargite (MK42)	$Cu_{3.04}As_{0.96}S_{4.00}$
Robinsonite (?) (MK43)	$Pb_{4.48}(Sb_{5.65}As_{1.31})_{6.96}S_{11.56}$
Robinsonite (?) (MK44)	$Pb_{4.45}(Sb_{5.62}As_{1.44})_{7.06}S_{11.50}$

Jordanite (or geocronite?) mineral phase by its composition was established in one of the polished sections. It appears as small single grains in barite-dolmite veinlet (Fig. 3.L) and as inclusions in bournonite-seligmannite. In reflected light it is a little bit brighter than the latter one with weak anisotropy. Microprobe analyses determine content of Pb close to the theoretical but also vast excess of As and Sb as well as significant deficit of S (Table 3). It is closely associated with gold, connected to late barite and carbonates.

Robinsonite (?) was observed as a single grain with rhombic shape in just one polished section, accompanied by three triangular grains close to it (Fig. 3.K). It manifests strong anisotropy with colour effects. Initially the mineral was determined by its optical characteristics as comparatively often found jamesonite $Pb_4FeSb_6S_{14}$, but lack of Fe excluded this possibility. Determined by microprobe analyses content of Pb, Sb with As admixture and S (Table 3) in such ratio defines this mineral phase as the only possible one – robinsonite $Pb_4Sb_6S_{13}$. But calculated formulas are with extremely non-stoichiometric composition – some excess of Pb, vast excess of Sb and As and a significant deficit of S.

Native gold with size of grains 5–15 μm is observed in late quartz-pyrite or carbonate-barite veinlets and in the interstitial spaces between pyrite grains in association with marcasite and sulfosalts (Fig. 3.J). Coarse gold grains (up to 140 μm) appear in groups within dolomite-barite veinlet with bournonite-seligmannite minerals in close spatial vicinity to pyrite aggregates. Gold is high probe – the content of Ag varies from 1.83 to 4.30 wt% (Table 1).

Gangue minerals

Gangue minerals are quartz, calcite, Mn-calcite, dolomite and barite. All microprobe analyses of carbonate minerals should be acccepted as qualitative, due to the carbon coating of polished sections. Qualitative microprobe analysis of dolomite (Fig. 3.L) estimates ratio of Ca:Mg:Fe approximately 5:4:1.

Barite was determined by quantitative microprobe analyses and is well distinguishable in backscattered electrons as mineral phase brighter than pyrite (Fig. 3.L). Calculated formulas are: $(Ba_{0.98}Sr_{0.06})_{1.04}S_{0.99}O_4$, $(Ba_{0.99}Sr_{0.05})_{1.04}S_{0.99}O_4$, $Ba_{1.01}S_{0.99}O_4$ and $(Ba_{0.84}Sr_{0.12})_{0.96}S_{1.02}O_4$.

Conclusions

New described minerals from Ore Zone 1 in Milin Kamak deposits are enargite, bornite, covellite, jordanite (?) and robinsonite (?). They are not mentioned in previous studies by Crummy et al. (2001), Stoykov et al. (2007), Sabeva and Mladenova (2012), and Sabeva et al. (2017).

Samples from Ore Zone 1 could be separated into two big groups. The first one comprises samples from altered, intensively pyritised volcanic rocks and in some cases with macroscopically observed quartz-pyrite veinlets. The second group represents samples from infilling ore veins with quartz-carbonate-sulfide matrix or quartz-carbonate veinlets, often containing barite and numerous sulfide ore minerals.

The first group of samples could be characterised by the following mineral composition: pyrite, marcasite, sphalerite, chalcopyrite and in less amount galena, minerals from tennantite-tetrahedrite group and arsenopyrite.

Mineral association (mainly pyrite and marcasite) of the first group of samples corresponds to the quartz-pyrite stage of mineralisation (Sabeva, Mladenova, 2012; Sabeva et al., 2017), but there is a question what is the place of found in almost all of the samples sphalerite, chalcopyrite and galena. On the other side, if this mineral association corresponds to the second quartz-polymetallic stage (Sabeva, Mladenova, 2012; Sabeva et al., 2017), presence of sphalerite, chalcopyrite and galena is similar, but there is a total lack of sulfosalts and gold is a high probe, not electrum. The second group of samples could be subdivided to two sub-groups.

The first subgroup includes samples with comparatively limited presence of sphalerite, galena and chalcopyrite. No sulfosalt minerals have been determined in these samples.

The next sub-group is characterised by the presence of sphalerite, galena, minerals from tennantite-tetrahedrite and seligmannite-bournonite series. Rare minerals are enargite, jordanite (?) and robinsonite (?). Gold grains have been determined in association with carbonate minerals and barite exactly in the samples from this sub-group. Gold grains are quite unevenly distributed with size from 8–10 μm to 140–150 μm. This mineral association could correspond to the so-called third carbonate-gold stage of mineralisation, but the main difference here is the presence of sulfosalt minerals.

Microscopically visible gold was determined in only 3 polished sections. This could be explained by its quite irregular and uneven distribution. The other factor could be the extremely small size of the grains, invisible under an optical microscope. Of course, presence of gold micro inclusions in sulfide minerals could not be excluded.

Acknowledgements. The authors should like to thank Thrace Recourses Ltd. and personaly Eng. Plamen Doychev for the support during the implementation of this study. Part of the studies is done under a project financied by Thrace Resources Ltd.

References

Chvileva, T., M. Bessmertnaia, M. Spiridonov. 1988. *Handbook for Determination of Ore Minerals in Reflected Light*. Nauka, Moscow, 508 p. (in Russian)

Crummy, J., I. Mutafchiev, I. Velinov, R. Petrunov. 2001. The Breznik epithermal Au occurrence, Western Srednegorie – Bulgaria: an ‘‘atypical”(?) low-sulphidation hydrothermal system. – In: Piestrzynski, A. et al. (Eds). *Mineral Deposits at the Beginning of the 21st Century. Balkema, Lisse*; *Proceedings 6th Biennial SGA Meeting, Cracow, Poland,* 723–726.

Dabovski, C., B. Kamenov, D. Sinnyovsky, E. Vasilev, E. Dimitrova, I. Bairaktarov. 2009. Upper Cretaceous geology. – In: Zagorchev, I., C. Dabovski, T. Nikolov (Eds). *Geology of Bulgaria. Part II. Mesozoic Geology.* Marin Drinov Academic Publishing House, Sofia, 305–611 (in Bulgarian with English abstract).

Popov, P., T. Berza, A. Grubic, I. Dimitru. 2002. Late Cretaceous Apuseni-Banat-Timok-Srednogorie (ABTS) Magmatic and Metallogenic Belt in the Carpathian-Balkan Orogen. – *Geologica Balc.*, *32*, 145–163.

Sabeva, R., V. Mladenova. 2012. Mineral composition of epithermal gold-silver deposit Milin Kamak, Western Srednogorie. – *Ann. Univ. de Sofia, Fac. gèol. et gèogr., 104*, 1-Gèol., 65–88 (in Bulgarian with English abstract).

Sabeva, R., V. Mladenova, A. Mogessie. 2017. Ore petrology, hydrothermal alteration, fluid inclusions, and sulfur stable isotopes of the Milin Kamak intermediate sulfidation epithermal Au-Ag deposit in Western Srednogorie, Bulgaria. – *Ore Geology Reviews*, *88*, 400–415.

Stoykov, S., S. Strashimirov, R. Moritz, D. Dimitrov, J. Todorov. 2007. Mineral composition of the Breznik-Bardoto Au epithermal ore occurrence (Preliminary data). – *Ann. Univ. Mining and Geol., 50*, Part I, 117–122.

INDICATIONS FOR THE ACTIVITY OF THE TUNDZHA FAULT IN THE MARBLE EXPOSURES AT THE KONEVETS GORGE OF RIVER TUNDZHA, SOUTHEASTERN BULGARIA

Dian Strahilov, Ivan Dimitrov

University of Mining and Geology "St. Ivan Rilski", 1700 Sofia; idim68@abv.bg

ABSTRACT. It is believed that the Tundzha fault (or fault swarm) is a significant in depth and lateral distribution structure, buried under the Quaternary alluvial sediments of the Tundzha valley, between the towns of Yambol and Elhovo. So far, this fault has been mentioned in a significant number of publications but no field geological data for its existence have been offered. The Tundzha valley is divided in two parts, the Yambol part and the Elhovo part, by the Konevets sill (gorge). In this area the river valley changes its direction from northwest to northeast, and is tens of meters wide. There are numerous kinematic arguments, that in this area, composed of metamorphosed Triassic carbonates, the evidence of fault shear, along the Tundzha fault, must be well visible. Indeed, the thin bedded marbles carry the traces of intense deformations. In this work, results of structural analyses are shown, including superimposed folding and kinematic analysis of faults and conjugate joints. They suggest for a significant fault tectonics and superposition of various stress fields, indicative not only for the Tundza fault, which is striking north-south, but also for the west-east striking structural trend along the Northern border of the Sakar-Strandzha dome, known as the Boznia zone. Thus, the Tundzha fault remains elusive but the evolution of the Konevets sill is clarified as a rock strip, protruding along the west-east strike-slip zone.

Keywords: Tundzha valley, joints, faults, folds, directions of principal stresses

ИНИДИКАЦИИ ЗА АКТИВНОСТТА НА ТУНДЖАНСКИЯ РАЗЛОМ В МРАМОРНИТЕ РАЗКРИТИЯ ОТ ДЕФИЛЕТО НА РЕКА ТУНДЖА ПРИ СЕЛО КОНЕВЕЦ, ЮГОИЗТОЧНА БЪЛГАРИЯ

Диян Страхилов, Иван Димитров

Минно-геоложки университет "Св. Иван Рилски", 1700 София

РЕЗЮМЕ. Предполага се, че Тунджанският разлом или разломен сноп, е значителна по дълбочина и латерално разпространение структура, погребана под кватернерните седименти на долината на р. Тунджа, между градовете Ямбол и Елхово. Досега за този разлом се споменава в голям брой публикации, но към момента не са представени теренни геоложки данни за неговото съществуване. Долината на р. Тунджа е разделена на две части: Ямболска и Елховска, като между тях се разполага Коневецкият праг (дефиле). В този участък долината сменя посоката си от северозападна на североизточна и е широка едва няколко десетки метра. Поради редица кинематични съображения, в този участък, изграден от триаски мраморизирани карбонати, е най-целесъобразно да се търсят следи от приразломно сръзване, свързано с Тунджанския разлом. В действителност тънкопластовите доломитни мрамори от Коневецкия праг са много интензивно деформирани. В тази работа се представят резултатите от структурни изследвания, включващи анализ на многофазна нагънатост и кинематичен анализ на пукнатини и разломи. Данните действително указват за проява на значима разломна тектоника и налагане на различни стресови полета, не само характерни за Тунджанския разлом, който е с посока север-юг, но също и за запад-източните деформации, характерни за северната граница на Сакар-Странджанската зона, известна като Босненска дислокация. Така че към момента кинематиката на Тунджанския разлом остава неясна, но за сметка на това се изяснява еволюцията на Коневецкия праг, като скална пластина, претърпяла отседни движения в запад-източна посока.

Ключови думи: долина на Тунджа, пукнатини, разломи, гънки, посоки на главни напрежения

Introduction

The Konevets gorge, known in the Bulgarian geomorphologic literature as the Konevets sill, separates the middle Tundzha valley into two hydrologically separate parts, known as the Yambol trough and the Elhovo trough. When and how it appeared is not clear yet, but it has obviously existed at least since the late Neogene, because it splits into two separate depositional environments the Elhovo Neogene (Pontian-Dacian) coal basin (Fig. 1). Savov (1983) named it Yambol and Elhovo syncline. The Yambol syncline contains discontinues and thin coal layers, but the Elhovo syncline has 3 well defined and several meters thick coal layers. To the north of the gorge the Yambol syncline, or more appropriately the Yambol structural depression, is 12 km long and 8 km wide, while to the south of the gorge the Elhovo depression is 18 km long and approximately 12 km wide (Savov, 1983).

The gorge itself is carved into Triassic low-grade metamorphic calcitic and dolomitic marbles, which pinch the valley into tens of meters narrow space. The marbles form a well-defined strip, which is running in the east-west direction for tens of kilometres along the northern border of the Strandzha Zone of Southeast Bulgaria (Čatalov, 1990). The marble exposures are located on both sides of the river, but better exposed rocks are found only on the west side (Fig. 2).

The Tundza fault was first proposed by Čatalov (1965) without serious field or theoretical evidence. The first geophysical data were provided by Sockerova et al. (1966) using seismic data from the earthquake that happened on 15 of March 1964, with a shallow epicentre (h=5 +/-3km), located

to the west of Yambol, below the village of Skobelevo. Reading this paper the reader will be left with mixed feelings. It is because the writhers do not specifically attribute this earthquake and many other tremors from the Yambol seismic zone, to the N-S trending fault along the valley of Tundzha, namely the Tundzha fault, but to other NW-SE trending faults. The only possible argument in favour of the Tundza fault in this paper is the slight elongation of the macro-seismic effects, shown on the isoseist map of the earthquake, to the south along the Tundza River valley. Nevertheless, drawn on the map in this paper by P. Gochev as a N-S trending reverse or normal fault (Fig. 11 in Sokerova et al., 1966) this structure began its life in the Bulgarian literature.

Bonchev et al. (1969) used the fault to develop their model of blocky macro-fabric of the Stranzha Zone.

The most exhaustive attempt to define this fault was made by Savov and Petkov (1972). They attempted to interpret regional magnetic and gravimetric data as well as any usable information that was available at the time. As a result, they offered not a single structure but an array of three faults namely the Yambol fault, the Konevets fault and the Lesovo fault (Fig. 1).

The exposures studied in this paper (Fig. 2) are located in the area between the tips of the Konevets fault and the Lesovo fault. However, the locations, scope of the deformation zones, and the kinematic nature of these faults are not specified in detail. The main argument used by the authors was the existence of gravity and magnetic maximums and steep gravity transitions, which may be aligned to indicate elongated faulted blocks. However, the map of gravity and magnetic signature provided by the authors emphasised the ambiguity of such speculations.

In the later works, the Tundza fault was assumed as existing and was usually shown as a single line (e.g. Vrablianski, 1975) following loosely the Tundza River valley. It is worth mentioning that on the geological map of Bulgaria in scale 1:100000, Elhovo map sheet (Dabovski et al., 1993; 1994) the existence of such fault is not indicated by any means.

Review of the tectonic activity in the Tundzha structural depression was provided by Aleksiev and Georgiev (1996). They published new data about significant earthquakes in the Yambol seismic zone and a map of the vertical crustal movements. Direct evidence about the existence of the Tundza fault or fault zone are not offered but the Yambol seismic zone, elongated in west-east direction, is better characterised. The grouping of the epicentres suggests a fault control by the west-east striking structures.

Preliminary data from structural analysis of surface exposure in the Konevets sill are provided in this paper. The purpose is not to prove or refute the existence of the Tundzha fault, but to bring into consideration additional data and to provide much needed geological consideration into this discussion, which so far relied only on indirect arguments.

The main usefulness of the study area comes from the fact that the studied exposures are the only rocks exposures in the Tundza River valley between Yambol and Elhovo, and the river valley changes direction exactly at the studied point (Fig. 1). So if shearing along the valley occurred, it would be expressed in some way in the marbles of the Konevets gorge.

The preliminary character of the study stems from the finding that there is evidence of superimposed stress fields, so additional efforts are needed to discern these stress fields, which may happen in another publication specifically focused on fault striation analysis not only for these exposures but for the entire region.

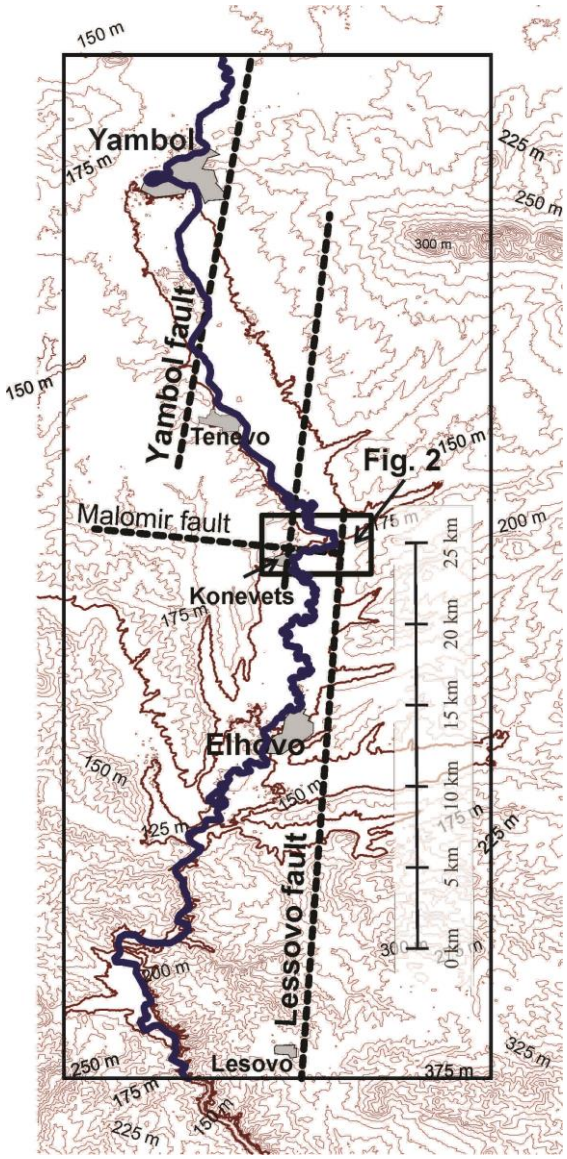

Fig. 1. Location of the Konevets sill in the middle of the Tundzha valley: three interpreted faults, believed to represent the Tundzha north-south striking fault swarm (Savov, Petkov, 1972), are shown in their approximate position with dashed lines; the position of another inferred fault, running in west-east direction and named as the Malomir fault (Savov, Petkov, 1972) is also indicated

Study area

The study area (Fig. 2) is naturally unexposed but numerous small pits have been made by local miners, extracting marble for quicklime production in the past. In these pits bedding can be measured as well as hinges of numerous small folds, joints and small faults. Evidence for existence of a single large fault is not available but the small scale folding and faulting are very prominent.

The overall strike of the beds in these exposures is NW-SE, which is emphasised by a large fold with a hinge in the

same direction. All the observed small scale structures are either reworked in parallelism with this trend or superimposed on it.

The marble beds are exposed in two packages: a thin-bedded one, originally comprising clay rich limestone with some marls, and a thick-betted package, which was thoroughly dolomitised and at present is mined in a larger quarry, known as the Konevets quarry. The younging is to the north, so the thick-bedded or massive dolomites consistently overlay the thin-bedded marbles along a strike in normal superposition.

Fold superposition

In the course of this study 134 bedding planes have been measured throughout the area to the west of the river. Plotted on a stereographic net, they demonstrate the girdle of the predominant NW-SE trending fold, shown with beta (β) axes f1 in Figure 3.

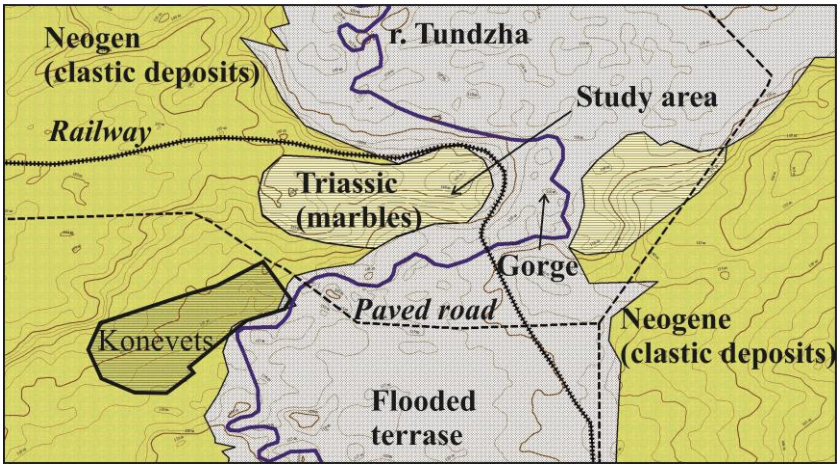

Fig. 2. Sketch map of the Konevets sill, showing the area where the structural geological measurements were made; the studded exposures are in the marble to the west of the Tundzha River; topographic contours are superimposed on the sketch to emphasise the geomorphology of the gorge

In addition, three other fold girdles can be recognized shown with circles around the β axes and numbered f2, f3 and f4 in Figure 3. From these, f2 and f3 are relatively easy to discern but f4 is indicated by only several measurements. This picture corresponds to a complex interference pattern. The girdles can be seen also on the β intersection plot shown in Figure 4.

The first, and easy, conclusion from this geometry is that the main fold (f1) has a curved hinge plunging between 20° and 50° to NW. The curvature of the hinge is emphasised by the size of the circle of Figure 3. This curvature is common for a "whale back" or a "turtle back" shaped folds that are usually formed by two stages of deformation.

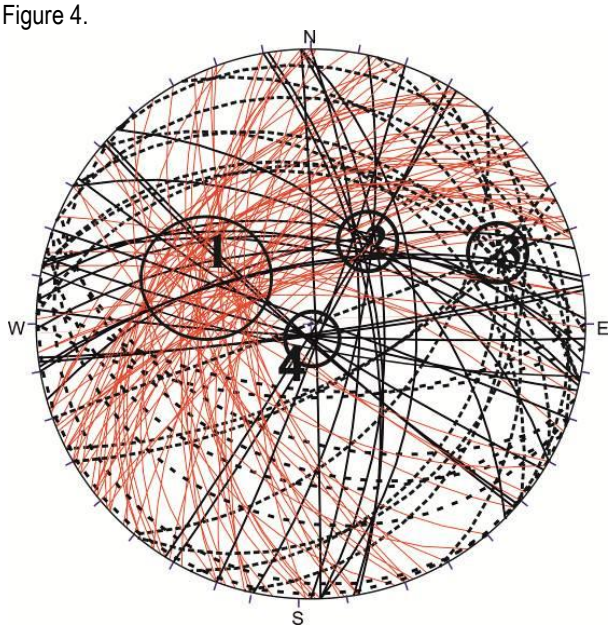

Fig. 3. Great circles of 134 bedding planes from exposures shown in Fig. 2: the beds show one well defined gird represented by an area of bed intersections numbered f1, but also 3 other not so well defined girdles, represented by intersection f2, f3 and f4

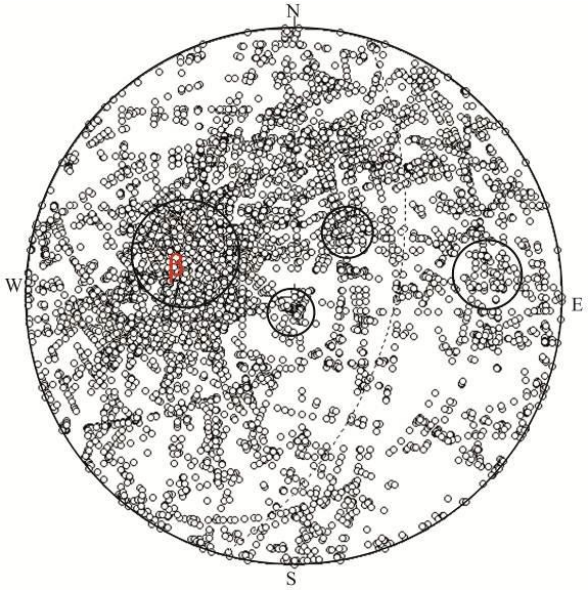

Fig. 4. The same data as in Fig. 3, processed to show the beta (β) intersections of the beds: the intersection are found using the software package Geoorient made by Rod Halcomber

The origin of girdle 4 is relatively clear. These folds were found to be kinks (Fig. 5) on a very steep to vertical beds. The kinks reflect bedding – parallel strike-slip shear, which resulted in nearly vertical plunges of the kink folds. Small faults, striking in the same direction, have also been found. Because this shear happened in a plane close to the axial surface of f1, it is likely to be cinematically related to the main folding.

Fig. 5. Small folds formed by bedding parallel shear. The folded beds and the hinge lines are emphasised by dark lines. The scale is a GPS receiver shown on the left.

Not all small folds have been formed this way. There is a variety of small fold geometry (Figs 6, 7), which reflect different mechanisms and possible different timing of these deformations. F2 and f3 are ambiguous and at this stage of the study they cannot be properly explained.

Fig. 6. Fault related fold with axial surface tangential to the tectonic mirror of the fault visible at the left side of the picture: for a scale the tree visible in the upper right corner can be used

The complexity of the deformation is reflected in the texture of the rocks. More than in any other location in the region, extensional vain textures are visible here (Fig. 8). In some exposures the two dimensional areal expansion measured by the area of the veins on bed surfaces reaches 20%. The nature of this volume enlargement is not clear. It is possible that fault related brecciating on a wider scale is also present but it is not observed, because of the limited exposure.

There is a possibility that a major fault zone still exists but it is covered by the alluvial sediments of Tundzha River, so only its vicinity is recorded in these exposures. The so-called Lesovo fault of Savov and Petkov (1972) was shown on their map to tip in the area of the Konevets gorge, however it is rather interpretation and speculation than a proven fact.

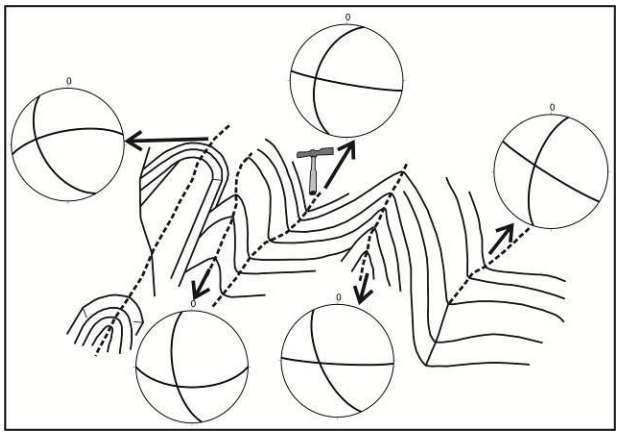

Fig. 7. Small folds redrawn from a photograph: the orientation of the beds is shown on the stereograms (scale is a silhouette of a geological hammer)

Fig. 8. Typical texture of a bed surface, exposing "chocolate tablet" extensional vein pattern: all the veins on the picture are calcitic with fibres grown perpendicular to the vain walls; to the right of the coin two hydraulic extensional gaps are visible, which were also filled with calcite

Analysis of the small folds

The abundance of small folds is the most conspicuous feature of these exposures. The orientation of small fold hinges was measured directly or was assembled by stereographic intersection of fold limbs. Most of the measured hinges plunge westward but some are horizontal or plunge shallowly to NE. In order to clarify their origin some geometric analyses were made.

When tested for a conical best fit (Fig. 9) it appears that the fold hinges arrange in a cone, the axis of which corresponds to the hinge of the prominent regional fold numbered f1 in this paper.

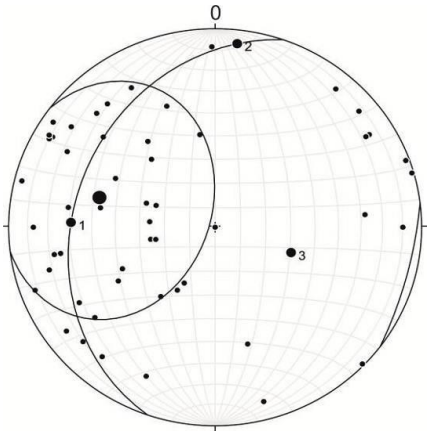

Fig. 9. Cylindrical and conical best fit, found by Bingham approximation of 52 fold's small axes, from exposures shown on Fig. 2: for the Bingham analysis the package Stereonet was used, which is made by Rick Allmendinger and distributed for free; the results of the analysis are as follows:

Axis	*Eigenvalue*	*Trend*	*Plunge*	*±min*	*±max*
1	0.5655	272.0	30.8	14.3	20.9
2	0.2595	006.6	07.7		
3	0.1749	109.1	58.1	14.2	45.8

Best fit great circle (strike, dip RHR) = 199.1, 31.9, Conical best, Data set name: Konevets small folds, axis trend & plunge = 285.0, 41.6; half apical angle = 46.1

The cylindrical best fit arranges them around a plane that might represent the prominent direction of bedding, unfolded around the hinge of f1. These observations suggest the possibility that the majority of the small folds are contained in the limbs of the f1 fold and thus can even predate the f1 formation. However, not all small folds comply with this geometry.

It is reasonable to find where the fold axes fall, when the plot is rotated around the hinge of f1. For this purpose, the geometry is simplified to only the hinges and two limbs for each fold found in this exposures (Fig. 10).

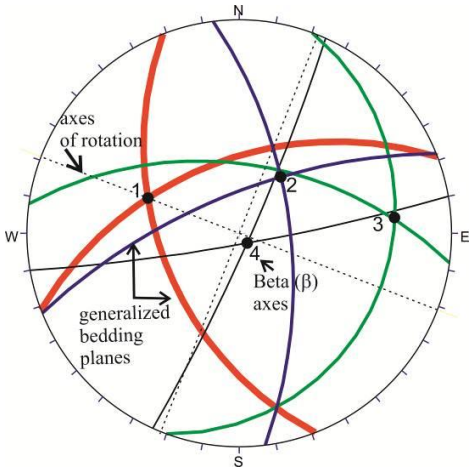

Fig. 10. Simplified representation of the bed intersections shown on the previous figures. The axes of rotation used to unfold the data about the hinge of the main fold f1 are shown with dotted lines

If the hinge of f1 is rotated to horizontal (Fig. 11) it is obvious that f2 and f4 hinges are relatively far from the limbs of f1, so they are obviously not contained in the general stratification folded by f1, hence, further rotations will prove no connection between them.

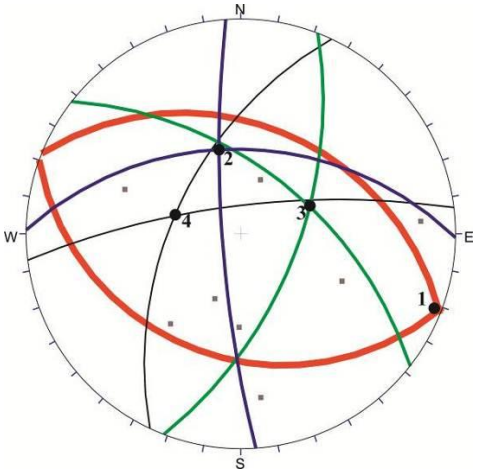

Fig. 11. All beds rotated, so that the hinge of the main fold (1) is horizontal

The hinges of f4 are far from the limbs of f1, so most likely they are fault related folds. F3 also appear not to be related to the f1 geometry. This analysis shows that the fold pattern needs further field work and possibly on a larger region.

Analysis of the joints

In most regions of the world the joints group statistically in three or four statistical maximums as two of them represent a conjugate shear couple and one of them represent the extensional joints (Hancock, 1985). This, however, is indicative of a simple stress field, which did not rotate with the time and do not carry the signature of the simultaneous or superimposed action of different stress fields.

In the studied domain, the joint pattern is complex. The joints disperse on a larger area of the stereographic net, forming more than four maximums. It was possible, by isolating conjugate shear joints from the nearby exposures, to construct the stereogram in Figure 12. On this figure, three couples of shear joints are shown. All couples were measured directly on a rock surface, where the polished walls of the joints are visible and the line of intersection can be observed.

As it is seen, the joints (Fig. 12) intersect at very different places on the net. If the line of intersection is interpreted as the direction of the intermediate principle stress, than it can be seen that each couple of shear joints represents a different stress field.

Analysis of small faults

In order to derive the orientation of the instantaneous stress axes, fault slip analysis (e.g. Allmendinger et al., 1989) was made using fault striations on fault planes. Only faults with simultaneous exposure of striation and steep steps perpendicular to it were used, so the direction and the sign of the movement could be found unambiguously on these surfaces. Principal stress directions from 6 faults from exposures in the most eastern part on the west board of the valley are shown in Figure 13. This plot indicate for a NW

plunging principal stress, which is compliant with a normal fault striking in the NW or NE quadrant as suggested by Savov and Petkov (1972).

However, the above shown analysis is not conclusive. It is because the joints indicate for a more complex stress field and the small folds from f4 indicate for a consistent W-E directed bedding-parallel shear. Because of the uneven exposure it is likely that not all significant small faults were measured or they were not split into groups representing contemporaneous stress fields.

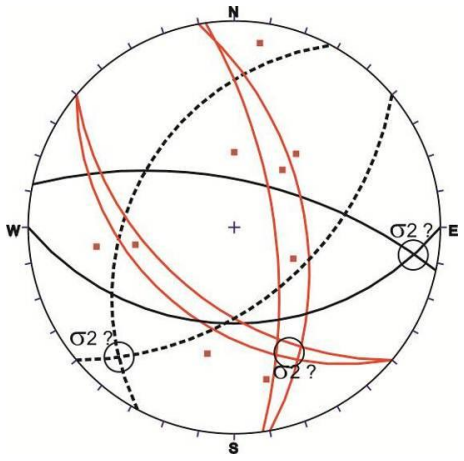

Fig. 12. Three sets of conjugate joints, measured in exposures on the western slope of the gorge (Fig. 2): the position of the intermediate stress (σ2) at the intersection of the joints is indicated

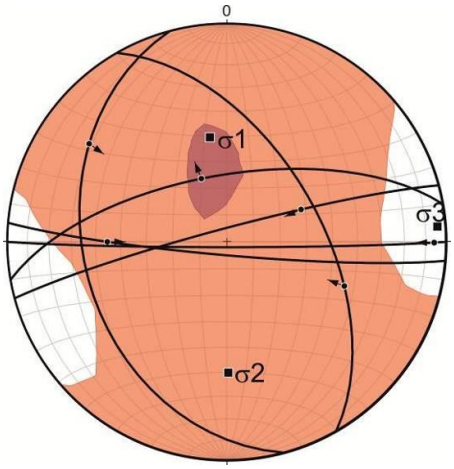

Fig. 13. Orientation of principal stresses found by 6 faults with striation, using the FaultKin software, made by Richard W. Allmendinger: the great circles of the faults, the directions of striations and the direction of the principal axes of stress are shown on the plot

Conclusions

The structural analysis of the Konevets gorge shows that the small, decimetre to metre scale structures, were formed by different deformation mechanisms at different geological times. Most of the small folds are contained in the stratification that was folded by the main NW trending alpine folds of the region, roughly coeval with the late Cretaceous magmatic activity. So, these small folds may predate the pick of folding and some of them may be even sin-sedimentary slump folds or formed by early tectonic folding in Jurassic or Early Cretaceous time, which is very difficult to be discerned at present.

The small folds, which are not contained in the stratification and are with steeply plunging hinges (f4) correspond to a bedding parallel strike-slip shear. These can be contemporaneous to the main folding or connected to a later strike-slip shear like the one related to the Malomir Fault of Savov and Petkov (1972).

The joints suggest multiple brittle deformations and obviously different stress fields. The fault slip analyses confirmed the conclusions about a north-south striking normal fault but the data are insufficient to draw concrete conclusions.

Acknowledgements. This study was supported by the Research project N224/11.03.2019 (Science Fund of the University of Mining and Geology "St. Ivan Rilski", Sofia).

References

Aleksiev, G., Ts. Georgiev. 1996. Geodinamic problems of the Tundzha structural decline. – *J. Bulg. Acad. Sci.*, *1*, 27–33 (in Bulgarian with English abstract).

Allmendinger, R. W., J. W. R. Gephart, A. Marrett. 1989. *Notes on Fault Slip Analysis. Prepared for the Geological Society of America Short Course on "Quantitative Interpretation of Joints and Faults", November 4–5, 1989*. Department of Geological Sciences, Cornell University, Ithaca, New York, 1–59.

Bončev, E., S. Savov, G. Čhatalov. 1969. Über die Schollengliederung des Strandža-Antiklinoriums. – *Bull. Geol. Inst., Ser. Geotectonics*, *18*, 143–157 (in Bulgarian with German abstract).

Čatalov, G. 1965. New tectonic structures in the area between Sakar Mountain and Strandzha Mountain. – *Proc. Bulg. Acad. Sci.*, *18*, 9, 861–864 ((in Russian).

Čatalov, G. 1990. *Geology of Strandzha Zone in Bulgaria*. BAS, Sofia, 271 p. (in Bulgarian with English abstract)

Dabovski, C., S. Savov, G. Chatalov, G. Shiliafov. 1993. *Explanatory Note to the Geological Map of Bulgaria in Scale 1:100000. Elhovo Map sheet*. Committee of Geology and Mineral Resources, Geology and Geophysics, Bolid, Sofia, 75 p. (in Bulgarian with English abstract)

Dabovski, C., S. Savov, G. Chatalov, G. Shiliafov. 1994. *Geological Map of Bulgaria in Scale 1:100000. Elhovo Map sheet*. Committee of Geology and and Mineral Resources, Geology and Geophysics, Sofia.

Hancock, P. L. 1985. Brittle microtectonics: Principles and practice. – *J. Struct. Geol.*, *7*, 437–457.

Savov, S. 1983. Structure of Elhovo structural depression. – *Rev. Bulg. Geol. Soc.*, *44*, 3, 326–331 (in Bulgarian with English abstract).

Savov, S., I. Petkov. 1972. About the deep structure of the Tundza fault swarm. – *Bull. Geol. Inst., Ser. Applied Geophys.*, *21*, 123–133 (in Bulgarian with Russian abstract).

Sokerova, D., E. Grigorova., P. Gochev. 1966. Study of the elements of the seismotectonic characteristics of the earthquake of 15 March 1964 in the Yambol district. – *Bull. Geophys. Inst., Bulg. Acad. Sci.*, *9*, 101–118 (in Bulgarian).

Vrablianski, B. 1975. On the neotectonic activity of the fault structures in Bulgaria. – *Geotecton., Tectonophys., Geodynam.*, *2*, 15–27 (in Bulgarian with English abstract).

PRELIMINARY RESULTS FROM THE TASLADJA BAIR'S DYKE'S STUDY, AN INDICATOR FOR THE STRUCTURAL EVOLUTION OF THE PROHOROVO COPPER PORPHYRY SYSTEM IN SOUTHEASTERN BULGARIA

Dian Strahilov, Banush Banushev, Ivan Dimitrov

University of Mining and Geology "St. Ivan Rilski", 1700 Sofia; idim68@abv.bg

ABSTRACT. The Prohorovo pluton is intruded in a complex geological environment in the south-eastern part of the Sveti Ilija ridge, municipality of Nova Zagora, Sliven district. This magmatic body is of interest, because it is related to a copper–molybdenum, vein-porphyry mineralisation. The pluton occupies a hypabyssal intrusion level, as the intrusion of the main magmatic body, as well as the smaller sub-intrusions are controlled by two fault systems striking to northeast and northwest. During the eighties and nineties of the last century, there were efforts to study the faults in the vicinity of the pluton and an agreement was reached, that they determine the geometry of the hydrothermal system. However, there are still unsolved issues regarding the degree to which the faults control the intrusion of the igneous bodies, screen the hydrothermal fluids or create fractured environment favourable for mineral deposition. So far, it is not clear if the ore hosting fractures are product of the faults or of the sub-intrusive process itself, which can also lead to fracturing of the host rocks. Several NE striking dykes have been recently exposed in a dolomitic quarry, in the locality of Tasladja bair, which is adjacent to the Prohorovo pluton. The dykes were hydrothermally altered and hydraulically brecciated. A fault slip analysis reveals that the faults, the pluton and the dykes were created by the same stress field. It confirms the assumption that the dykes are synchronous to the metal bearing hydrothermal mineralisation and offer an opportunity to model the intrusion of the pluton in a straightforward manner using the geometry of the faults, which controlled it.

Keywords: dyke swarm, copper porphyry hydrothermal system, faults, fractures, fault-slip analysis, principal stresses

ПРЕДВАРИТЕЛНИ РЕЗУЛТАТИ ОТ АНАЛИЗА НА ДАЙКИТЕ ОТ ТАСЛАДЖА БАИР, ИНДИКАТОР ЗА СТРУКТУРНАТА ЕВОЛЮЦИЯ НА ПРОХОРОВСКАТА МЕДНО-ПОРФИРНА ХИДРОТЕРМАЛНА СИСТЕМА В ЮГОИЗТОЧНА БЪЛГАРИЯ)

Диян Страхилов, Бануш Банушев, Иван Димитров,

Минно-геоложки университет "Св. Иван Рилски", 1700 София

РЕЗЮМЕ. Прохоровският плутон е внедрен в сложна геоложка обстановка в югоизточната част на Светиилийските височини, община Нова Загора, област Сливен. Магматичното тяло представлява интерес, защото с него е свързана медно-молибденова минерализация от прожилково порфирен тип. Плутонът е внедрен на хипоабисално ниво, като както внедряването на плутона, така и многобройните по-малки субинтрузивни тела са контролирани от две разломни системи с посока североизток и югоизток. През осемдесетте и деветдесетте години на миналия век са положени усилия за изучаване на разломите в околностите на плутона, като е постигнато съгласие, че те определят геометрията на хидротермалната система. Съществуват обаче недоизяснени въпроси за това, до каква степен тези разломи контролират внедряването на интрузиите, екранират флуидните системи или създават подходяща за рудовместване среда. Не е изяснен въпросът до каква степен напукването, което вмества рудната система, е продукт на тези разломи, и до каква степен играе роля спецификата на субинтрузивния процес, който също води до напукване и създаване на благоприятна за рудоотлагане среда. Няколко дайки с посока североизток са разкрити неотдавна в доломитната кариера, разположена в местността Тасладжа баир, в съседство с рудоносния Прохоровски плутон. Дайките са хидротермално променени и хидравлично брекчирани. Анализ на напреженията чрез разломни стриации разкрива, че разломите, плутонът и дайките са формирани при действието на едно и също поле на напреженията. Това потвърждава идеята, че дайките са синхронни на рудната минерализация и дава възможност да се моделира еднозначно внедряването на плутона, като се използва геометрията на разломите, които са го контролирали.

Ключови думи: дайков сноп, медно порфирна хидротермална система, разломи, пукнатини, анализ на разломни придвижвания, главни напражения

Introduction

The copper-molybdenum porphyry deposit Prohorovo is located in the middle part of the Saint Ilija heights in Southeast Bulgaria. It was prospected in several stages, starting from 1931 and continuing to present day, each one of them bringing new details and emphasising the significance of the structural control on this mineralisation.

The deposit is located at the roof of a small quartz-diorite pluton with the shape of the letter "L" as one arm of the intrusion is striking to northwest and the other is striking to northeast (Fig. 1). Both directions coincide with the dominant fault structures of the region. The regional structure, on which the faults were superimposed, is the Sveti Ilija monoclyne, which was originally mapped by Nedialkov (1964) as the ages of the rock formations were scrutinised by Čatalov (1963; 1965; 1985; 1990) and the overall structural environment by Varhotov et al. (1983) and Tsankov (1983).

The works of Bogdanov (Bogdanov, Bogdanova, 1984; Bogdanov, 1987) provide the understanding of the hydrothermal alteration processes around the Prohorovo pluton, which Ignatovski (1989) summarised into a simple zonation model comprising: 1 – K-feldspar alteration in the internal part, mainly in the intrusion itself; 2 – quarts-white micas-pyrite-lepidolite alteration in the endo-contact and the immediate contact area; 3 – quartz-kaolinite-chlorite alteration

in the immediate vicinity, and in the exo-contact; 4 – propylitic alteration at large, around the intrusion, being the most external zone of hydrothermal affects. The structure of the deposit itself and its vicinity was studied by Ignatovski who published several works, of which most detailed is Ignatovski (1986).

It is important to note that this pluton was not injected into very reactive host rocks. Although some skarns exist, formed in the Triassic carbonates, the dominant lithology of the host rocks of the intrusion is that of a silica rich Paleozoic volcanic lava and pyroclastic flows and Paleozoic clastic deposits, mainly conglomerates with minor sand and breccia, which are also very silica rich and non-reactive in geochemical sense.

In spite of this, significant amount of metals was accumulated, which according to Ignatovski (1980) and Chobanova (1981) was controlled by the intense fracturing of the host rocks and the intrusion. They studied the small scale fractures that formed the ore bearing veinlets and revealed their systematic nature (Ignatovski, 1980) and at the same time their indirect relationship to the main faults.

This prompted Ignatovski (1986) to emphasise on the hydraulic faulting as a very important process in this deposit, however he did not manage to clarify the mechanical nature of this process, partly because the hydraulic faulting and brecciation were not well understood in Bulgaria at that time.

This paper contains preliminary results of a study of a dyke swarm in the vicinity of the Prohorovo pluton, which was recently exposed in a dolomitic quarry. This swarm can be judged to pass through the pluton, or at least through its vicinity, and obviously expose structural features that can be spread over the roof of the intrusion. In this sense, the study will contribute with data about the evolution of the deposit itself.

The preliminary nature of the study follows from the fact that not all field data are processed to this point and they are not assembled in a unified model, so it is mainly reporting interesting features that will be examined in depth at future.

Geological setting

The middle part of the Sveti Ilija heights, where the Prohorovo pluton was intruded, comprises Upper Cretaceous, Jurassic, Triassic and upper Paleozoic volcanic and sedimentary rocks (Fig. 1). All rocks older than the Triassic were metamorphosed in lower greenschist facies. Abundant veins of milky quartz called “quartz segregation veins” by Čatalov (1990) injected the rocks during this metamorphic event.

According to Kamenov et al. (2000) the Prohorovo pluton was intruded about 90 Ma BP.

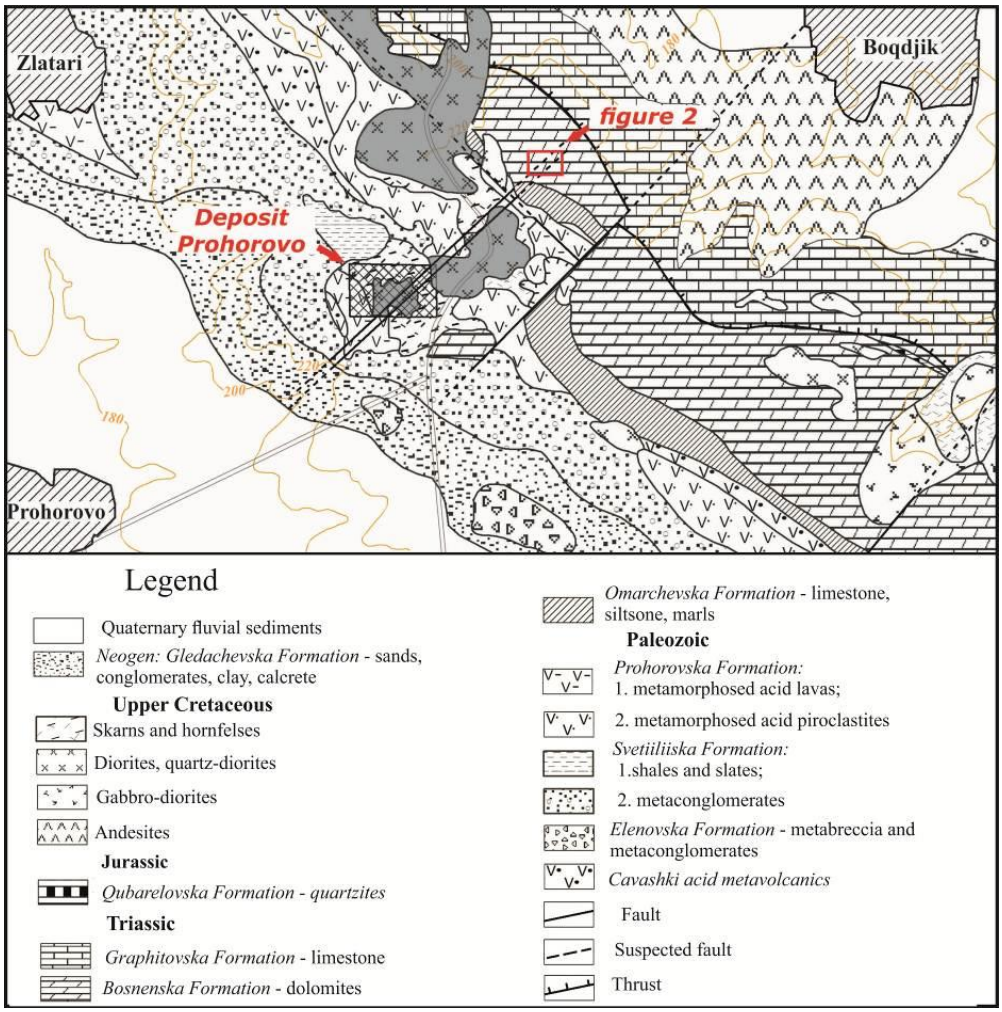

Fig. 1. Geological map of the Prohorovo area of the Sveti Ilija heights (modified after Čatalov, 1985)

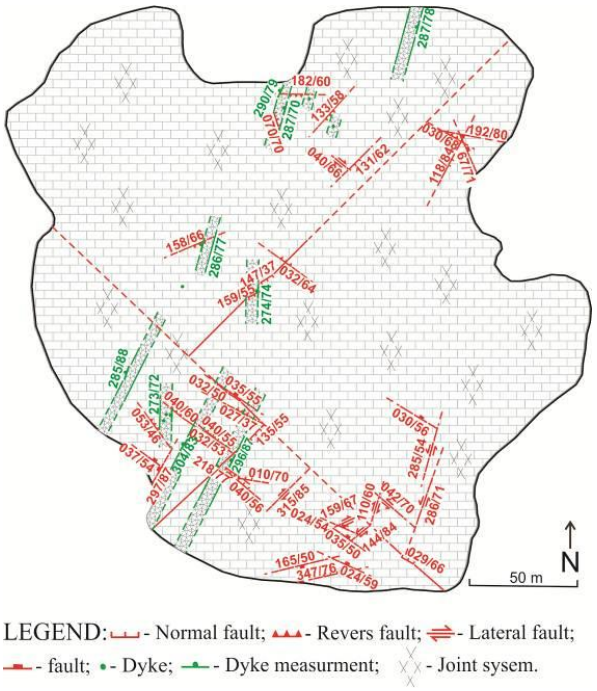

Fig. 2. Exposed area of the Tasladja Bair's quarry with indicated position of dyke segments and larger faults

The main structure of the heights is a monoclinal antiform (a step-like fold) younging to NE, with hinge striking NW-SE. Parallel to the hinge is the Saint Ilija fault, striking to NW and parallel to the bedding, which was partly utilised by the Prohorovo diorite intrusion. Another set of faults, striking to NE, crosscuts the monocline. Some of the faults proven beforehand that cut the intrusion are shown in Figure 1. Not far from the intersection of the two fault sets, a quarry was developed in the dolomitic marbles (Fig. 2). The quarry provided the field material for this paper.

Petrological features of the dykes

The dykes from the Tasladja Bair were sampled and studied in laboratory conditions by examination in thin sections and by chemical assay. For the thin section examination a polarising microscope NIKON Eclipse LV100ND was used and the assay was made in the geochemical laboratory of UMG Sofia using s spectrometer ICP-OES-720 of Agilent Technologies.

The rocks that contain the dykes are layered, fine-grained dolomites (Fig. 3a) with minor alteration. They were stained with iron hydroxides along fractures and were reworked into breccia. In the brecciated zones calcite veins and voids filled with spar crystals are quite common. The carbonates are pure with only a minor amount of fine quartz up to 0.15 mm in size. Fine veinlets of calcite about 0.04 to 0.2 mm thick are the only inhomogeneity visible under microscope.

The dykes of diorite- porphyry injected into the dolomites are 1.5–3 m thick. They are displaced by faults, so only short segments from each one can be observed (Fig. 2). All of the observed dykes have been brecciated and the brecciation is more intense near the contacts. The diorite-porphyry is green, light green or yellow, thin-grained with rare phenocrysts of plagioclase and altered mafic minerals. The texture is massive and the magmatic structure is porphyritic. They comprise primary magmatic plagioclases, amphiboles, biotite, apatite, magnetite and secondary chlorite, carbonate, epidote, zoisite, albite and quartz. The phenocrysts (porphyries) are of plagioclase and amphiboles. The plagioclases are prismatic or plate-like and are replaced by thin-grained carbonate and small amount of chlorite as the peripheral parts of the crystals are relatively fresh (Fig. 3b). Some of them were replaced by thin flakes of white mica and chlorite. They might contain inclusions of apatite and reach a size of up to 0.9 x 1.7 mm, but it is usually around 0.5 x 1 mm.

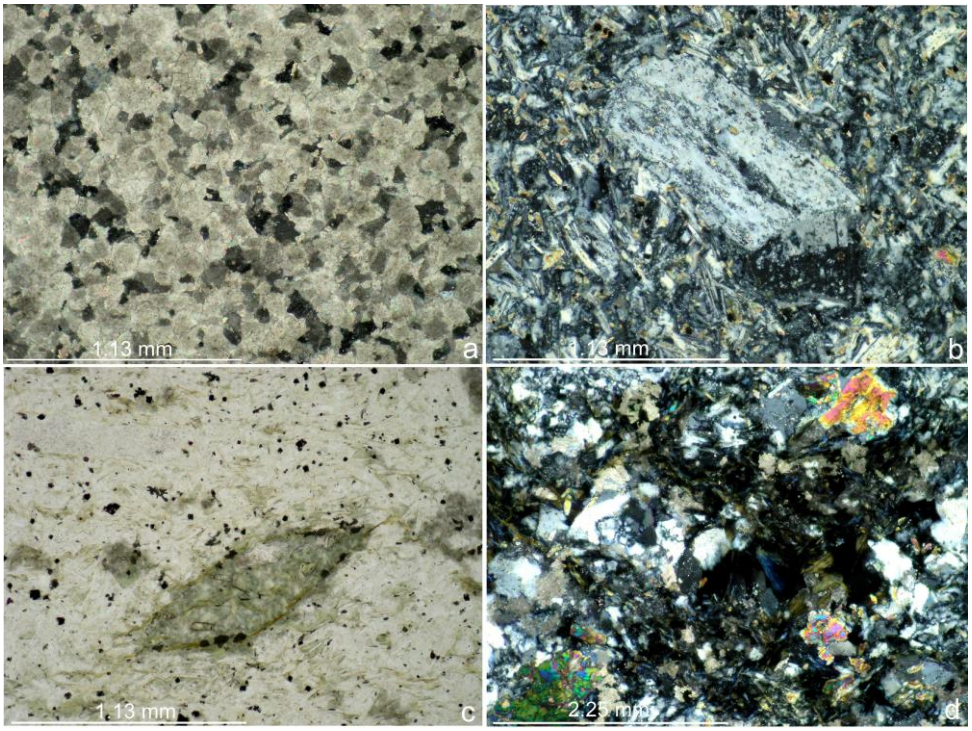

Fig. 3. Micro-photographs of rock varieties from dykes observes in the Tasladja Bair's quarry
a, thin-grained, equigranular dolomite, crossed polarisers; *b*, porphyritic plagioclase, partially replaced by chlorite, crossed polarisers; *c*, fully altered mafic mineral, parallel polarisers; *d*, aggregate of epidote, chlorite and quartz, crossed polarisers

The mafic minerals were prismatic, but the nearly complete alteration by chlorite and epidote made their shape unrecognizable. The crystal shapes indicate that the mafic minerals were amphiboles (Fig. 3c). In the more altered parts of the dykes the mafic minerals were completely altered, so they are not recognizable. The main accessory minerals are prismatic to needle-like apatite and magnetite. The matrix of the rock comprises also micro-prismatic minerals. These are mainly plagioclases but also biotite, chlorite, carbonates, albit, xenomorphic quartz, magnetite and apatite.

The fresh plagioclase crystallites are with average size of 0.03x0.15 mm, and show a well discernible parallel flow pattern.

The biotite is presented by small, overgrown by chlorite, flakes. At some places lens-like aggregates of secondary minerals – zoisite, epidote, chlorite and quartz in various amounts mark the position of replaced primary crystals. The secondary minerals are not distributed evenly as in the domains they predominate. Thin veins of quartz up to 0.2 mm thick are also present.

Hydrothermal alterations. The dykes were affected by secondary hydrothermal changes expressed in deposition of chlorite, epidote, carbonate, and albite characteristic for a propylitic type alteration (Table 1). The primary rock forming minerals have been partially or completely replaced as the change of the mafic minerals is more pronounced. The alteration is more intensive in the peripheral brecciated zones of the dykes, where the easy access of hydrothermal fluids resulted in thorough conversion to clay minerals.

Table 1. *Description of the hydrothermal alteration of the dykes from the Tasladja Bair*

Sample №	Rock type	Primary minerals	Hydrothermal mineral alteration
Smpl. 4-2	Diorite porp-yry	Plagioclases, mafic minerals (amphibo-les), biotite, apatite, magnetite	Chlorite, carbonate, epidote, zoisite, albite, quartz

Petrochemical peculiarities. On the alkaline – silica classification diagram the dykes appear in the field of the granodiorites (Fig. 4). The rocks are oversaturated with silica and with predominance of Na_2O over K_2O, as the ratio K_2O/Na_2O is 0.62. The al' coefficient is 2.66 and the per-alkaline index is 0.56 (Table 2). On the Peccerillo and Taylor (1976) diagram, in coordinates K_2O-SiO_2, the dyke appears in the field of the *calcium – alkaline series* (Fig. 5). It is likely that the SiO_2 was enriched by secondary processes, such as introduction of quartz in the rock mass.

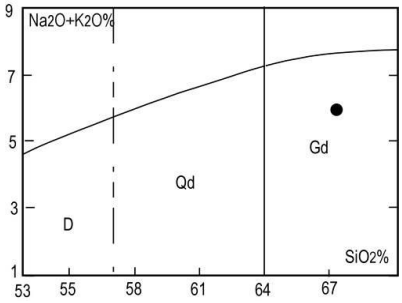

Fig. 4. Graph in coordinates ($K_2O + Na_2O$) - SiO_2 (Bogatikov et al., 1981) for petrochemical separation of volcanic rocks. The position of the dyke from Tasladja Bair is indicated with a dot

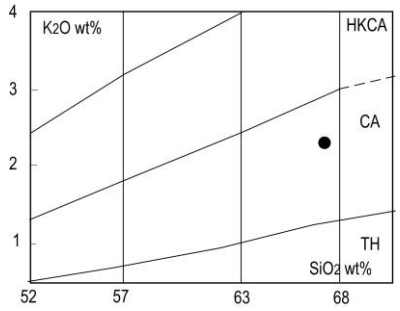

Fig. 5. Graph in coordinates K_2O – SiO_2 (Peccerillo, Taylor, 1976): *TH*, tholeiitic series; *CA*, calcium alkaline series; *HKCA*, high potassium–calcium alkaline

Based on the thin section study, and the petrochemical analysis, it can be concluded that the dykes, that intruded the Triassic dolomites, have modified chemistry, so their protholite was most likely that of diorite porphyry, the same as the main variety of the Prohorovo pluton.

Table 2. *Chemical composition (wt%) of a dyke (Smpl. 4-2) from the Tasladja Bair; K/Na = K_2O/Na_2O; al≒ $Al_2O_3/(Fe_2O_3 + FeO + MgO)$; Pl=$Na_2O + K_2O/Al_2O_3$ (mol). UMG, Sofia, analyst D. Dragoeva*

Parameter	value	Parameter	value
SiO_2	67.55	K_2O	2.29
TiO_2	0.44	P_2O_5	0.09
Al_2O_3	15.22	SO_3	0.05
Fe_2O_3t	3.44	LOI	3.43
MnO	0.05	Total	99.92
MgO	2.27	K/Na	0.62
CaO	1.41	al¢	2.66
Na_2O	3.68	Pl	0.56

The name diorite porphyry is adopted following the principles of the International Union of Geological Sciences (IUGS), according to which the fully crystalline igneous rocks are classified based on their modal composition (Le Maitre, 1989).

Structural setting

In the quarry the strike of the beds is varying between 120° and 130° to SE and the dip is 40–60° to NE, so the quarry exposes the geometry of the Saint Ilija monocline.

The dolomites are moderately jointed as the joints were developed in two sets: a NW striking set and a NE striking set (Fig. 6).

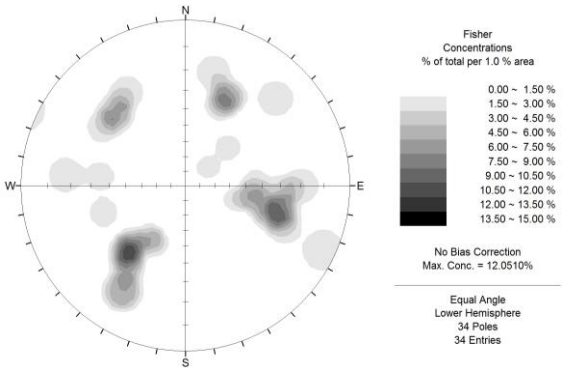

Fig.6. Statistical diagram of 42 joints from the Tasladja Bair's quarry. The statistic is made with the package Geoorient, distributed by Rod Halcomber

In the quarry, faults of two sets are observed: one striking to the NW quadrant and the other striking to the NW quadrant.

The range of the faults cannot be judged straightforward but it appears that some of the NW striking ones are splays of the main Saint Ilija fault, which is of strike-slip kinematics, and most likely control the NW arm of the Prohorovo pluton (Fig. 1). The NE set of faults is also very common in the heights and was also utilised by the intrusion, so even though the measured faults are not the most important structures in the region; they are still representative of the regional kinematics and informative about the evolution of the Prohorovo pluton.

Effects of the hydraulic brecciating

At first glance the rocks of the observed dyke segments appear faulted. One of the possible interpretations is that they were injected along faults, which later were reactivated and the material inside was sheared. This idea can be rejected based on three premises. The first one is that the dikes are usually extensional features with their walls perpendicular to the minimal (σ3) tectonic stress, so shearing is usually not involved but rather pure extension at the time of their formation. The second is the observation of a very serrated dyke walls, that exclude shearing along them, and the third is the texture of the brecciated rock fragments (Fig. 7) inside the dykes, which imply fragment separation without much rotation (rotation is equivalent to shearing) of the fragments relative to one another.

Fig. 7. Hydraulically brecciated dyke, (under the hammer) and serrated dolomitic contact of the dyke on the right side of the pictures

The action of a hot fluid is implied as the culprit for the brecciation. This has the implication that being hot also means that the fluids were pressurised. And it coincides with the observation of hydrothermal alteration of the dykes, which was described earlier. As it was observed on the field all dyke segment shown in Figure 2 were brecciated in various degrees.

Fault slip data analysis

Slicken-lines on a fault plane represent the direction of some relative displacement between the two blocks separated by the fault. Fault data include both the fault plane and slicken-line orientations (Fig. 8), the latter including the relative sense of movement along the line.

The goal is to use these measurements to calculate the so-called paleostress tensor (Almendinger at al., 1989; Marrett, Allmendinger, 1990). Paleostress tensors provide a dynamic interpretation (in terms of stress orientation) to the kinematic (movement) analysis of brittle features. The calculation does not yield a true paleostress tensor since it is a statistic calculation on fractures that integrate a geologically significant amount of time.

The systematic relationship that exists between brittle structures and principal stress directions provides a basis for interpreting paleostress directions. In particular, it is important to separate, in the field, the different compression directions that may correspond to separate paleostress tensors responsible for a successive deformation event.

The principal stresses' directions are distinguished by fault slip analyses, i.e. the eigenvectors of the stress tensor, represented by the three unit vectors, and by the principal stress magnitudes, i.e. the corresponding eigenvalues, taken positive in compression. σ1≥σ2≥σ3.

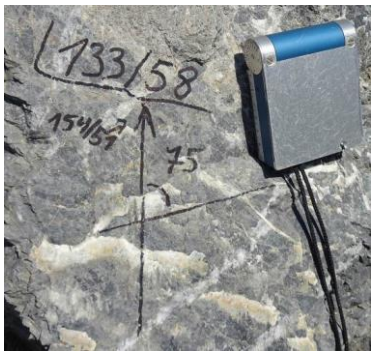

Fig. 8 Example of marking the fault kinematic axes on a fault surface from Tasladja Bair quarry, using the Aki-Richards format, described in the manual of the FaultKin software (Marrett, Allmendinger, 1990) for rakes of striae on planes

In the course of the present study, fault slip data were collected for 22 faults, which were processed separately based on their directions and all together (Figs 9–11). The results are very straightforward and geologically meaningful. In spite of their orientation, the faults indicate for a maximum compressive stress oriented NE-SW. It is the same even for the NW striking faults. The calculations are made using Linked Bingham approximation with software FultKin distributed free for academic purposes by R. Almendinger as the theory is described by Marrett and Allmendinger (1990).

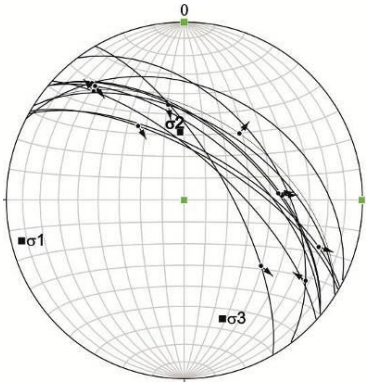

Fig. 9. Principal stress orientations from 10 faults measured in the Tasladja Bair's quarry. The faults are striking in the NW quadrant. The axis of the maximum principal stress is plunging to W-SW. The calculations are made with FaultKin

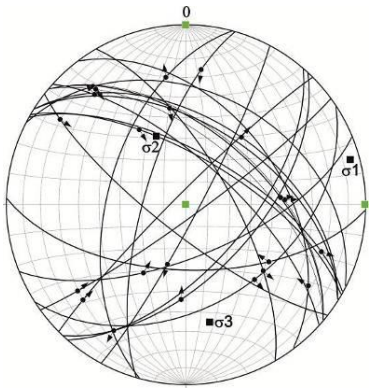

Fig. 10. Principal stress orientations of all 22 faults measured in the Tasladja Bair's quarry. The axis of the maximum principal stress is plunging to E-NE. The calculations are made with FaultKin

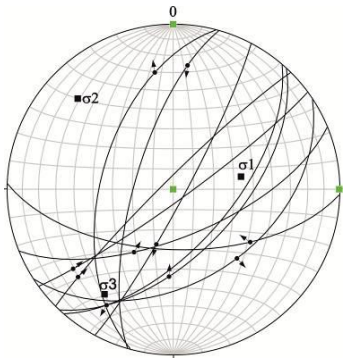

Fig. 11. Principal stress orientations from 10 faults measured in the Tasladja Bair's quarry. The faults are striking in the NE quadrant. The axis of the maximum principal stress is plunging to NE. The calculations are made with FaultKin

Discussion and conclusions

The dykes were of primary dioritic composition but were enriched with silica during the hydrothermal alteration. They are intensely brecciated by a hydraulic process. Inferred from the faults slip data, the principal stress axis acting around the Prohorovo pluton was oriented in SW-NE direction, which is also the direction needed for extensional formation of the dykes (they must be close to parallel with the σ1). So the dykes and the faults are linked. It also suggests that the studied fault orientations have been active from the Late Cretaceous till present. The inferred stress orientation is the only possible one that can create opening of the both arms (the NW and the NE) of the intrusive body, so this stress field is obviously responsible for the creation of the pluton itself.

References

Allmendinger, R. W., J. W. R. Gephart, A. Marrett. 1989. *Notes on Fault Slip Analysis. Prepared for the Geological Society of America Short Course on "Quantitative Interpretation of Joints and Faults", November 4 & 5, 1989*. Department of Geological Sciences, Cornell University, Ithaca, New York, 59 p.

Bogatikov, O. A., N. P. Mihailov, V. I. Goniushkova (Eds). 1981. *Clasiffication and Nomenclature of the Magmatic Rocks.* Nedra, Moscow, 160 p. (in Russian)

Bogdanov, B., P. Bogdanova. 1984. Mineral paragenetic associations and genetic peculiarities of the copper porphyry deposit Prohorovo, Iambol district. – *Bull. Nat. Inst. of Raw Materials, Sofia*, *1*, 175–174.

Bogdanov, B. 1987. *The Copper Deposits of Bulgaria*. Tehnica, Sofia, 388 p. (in Bulgarian).

Čatalov, G. 1962. Triassic and Jurassic low crystalline schists in the eastern part of Sveti Ilija hills. – *Contrib. Geol. Bulg., Ser. Stratigr. and Tecton.*, *4*, 41–50 (in Bulgarian).

Čatalov, G. 1963. Lithostratigraphy of the rocks in the western part of the Sveti Ilija Heights (SW Bulgaria). – *C. R. Acad. Bulg. Sci.*, *36*, 10, 1319–1322.

Čatalov, G. 1965. Young Paleozoic in the Saint Ilija ridge. – *Bull. Geol. Inst.*, *14*, 107–134 (in Bulgarian with Russian abstract).

Čatalov, G. 1985. Contribution to the stratigraphy and lithology of the Paleozoic and Triassic rocks of Saint Ilija hills. – *Rev. Bulg. Geol. Soc.*, *46*, 1, 53–70 (in Bulgarian with English abstract).

Čatalov, G. 1990. *Strandzha Zone in Bulgaria*. Tehnica, Sofia, 263 p. (in Bulgarian with English abstract)

Chobanova, A. 1981. Statistic structure of the copper mineralization in the deposit Prohorovo. – *Ore Forming Processes and Mineral Deposits*, *16*, 49–61 (in Bulgarian with English abstract).

Le Maitre, R. W. (Ed.). 1989. *A Classification of Igneous Rocks and Glossary of Terms. Recommendations of the IUGS Subcommission on the Systematics of Igneous Rocks.* Blackwell, Oxford, 193 p.

Ignatovski, P. 1980. Relationship between the fracturing and ore deposition in the copper-phorphyry deposits Asarel, Tcar Asen, Vlaikov vrah, Prohorovo and Studenets. – *Ore Forming Processes and Mineral Deposits*, *12*, 60–80 (in Bulgarian with English abstract).

Ignatovski, P. 1986. Ore-bearing significance of the local tectonic structures in the Prohorovo porphyry copper ore deposit. – *Ore Forming Processes and Mineral Deposits*, *23*, 26–34 (in Bulgarian with English abstract).

Ignatovski, P. 1989. Metalogenic specifics of the copper porphyry ore formation from the Saint Ilija Heights. – In: *Mineral Raw Material Base of Bulgaria – Achievements and New Tasks*. Tehnica, Sofia, 87–89 (in Bulgarian).

Kamenov, B., E. Tarassova, R. Nedialkov, B. Amov, P. Monchev, B. Mavroudchiev. 2000. New radiometric data from Late Cretaceous plutons in Eastern Srednogorie area, Bulgaria. – *Geochem., Miner., Petrol.*, *37*, 13–24.

Marrett, R. A., R. W. Allmendinger. 1990. Kinematic analysis of fault-slip data – *J. Struct. Geol.*, *12*, 973–986.

Nedialkov, N. 1964. Study of the Triassic magmatism in the region of Sain Ilija ridge. – In: Cankov, V. (Ed.). *Volume in Honor of Academician Y. Yovchev*. Sofia, 743–768 (in Bulgarian).

Peccerillo, A., S. R. Taylor. 1976. Geochemistry of Eocene calc-alkaline volcanic rocks from the Kastamonu area, Northern Turkey. – *Contrib. Mineral. Petrol., 58*, 63–81.

Tsankov, Ts. 1983. Alpine deformations in Sveti Ilija hills. – *Geotecton., Tectonophys., Geodynam.*, *16*, 19–42 (in Bulgarian with English abstract).

Varhotov, V., I. Bojkov, D. Donev, K. Haralampieva. 1983. New data on the volcanism and fault tectonics of the Saint Ilija hills. – *Rev. Bulg. Geol. Soc.*, *44*, 2, 188–193 (in Bulgarian with English abstract).

GEOLOGICAL SETTING AND ORE MINERALIZATION CHARACTERISTICS OF BABYAK DEPOSIT, WESTERN RHODOPE, BULGARIA

Nenko Temelakiev, Strashimir Strashimirov, Stefka Pristavova

University of Mining and Geology "St. Ivan Rilski", Sofia 1700; nenkotemelakiev@outlook.com

ABSTRACT. Some new data for ore mineralogy, rock alterations and structure analyses at Babyak Ag-Mo-Au deposit, Western Rhodope, Bulgaria are presented. The result of research suggests distinguishing the tectonic, magmatic and hydrothermal events associated with ore-forming processes. Two main ore mineralization stages related to the chain of structural events are distinguished. The early Mo-Bi-W-Ag mineralization is related to greissen-like type alteration and it is controlled by semi-brittle moderately dipping normal faults, most likely linked to regional detachment faults. The later Au-Pb-Zn-Cu mineralization accompanying by quartz-sericite alteration is controlled by steep dextral strike-slip and normal faults, probably related to the activity of the regional Ribnovo fault zone and Babyak-Grashevo shear zone. Based on the new data obtained by this study could supposed the granite-related ore mineralization of the Babyak deposit.

Keywords: Babyak deposit, ore mineralization, rock alteration, structural control, Western Rhodopes

ГЕОЛОЖКИ СТРОЕЖ И ХАРАКТЕРИСТИКА НА РУДНАТА МИНЕРАЛИЗАЦИЯ НА НАХОДИЩЕ БАБЯК, ЗАПАДНИ РОДОПИ, БЪЛГАРИЯ

Ненко Темелакиев, Страшимир Страшимиров, Стефка Приставова

Минно-геоложки университет "Св. Иван Рилски", 1700 София

Резюме. Представени са нови данни за рудната минералогия, околорудните изменения и структурите на Ag-Mo-Au находище Бабяк, Западни Родопи. Резултатите от изследването позволяват да се отделят тектонски, магматични и хидротермални събития асоцииращи с рудообразователните процеси. Два основни рудообразувателни стадия свързани със структурни събития са разграничени. Ранната Mo-Bi-W-Ag минерализация се свързва с грайзеноподобен тип метасоматична промяна, която се контролира от недълбоки разломи с крехко-пластични деформации вероятно свързани с регионални разломи на отлепване. По-късната Au-Pb-Zn-Cu минерализация е в асоциация с кварц-серицитов тип промяна контролираща се от стръмни разломи най-вероятно свързани с регионалната Рибновска и Бабяк-Грашевска зони. Въз основа на получените резултати от изследването се предполага за рудната минерализацията на Бабяк, че е гранит-свързан тип.

Ключови думи: находище Бабяк, рудна минерализация, околорудно изменени скали, структурен контрол, Западни Родопи

Introduction

The Babyak deposit is located in the municipalities of Belitsa and Yakoruda, Blagoevgrad region, South-Western Rhodopes (Fig. 1).

As a part of the Rhodope massif, two major stages of the Alpine development (compression and extension) form the modern structure of the region (Ivanov, 1988; Ricou et al., 1998; Ivanov, 2000;). The compression stage is associated with the emergence of a system of superposition located thrust plates with south vergence, which caused a significant thickening of the earth's crust. The metamorphic basement in the region of the studied deposit is considered to be a synmetamorphic thrusted complex composed of the plates of the Ograzhden, Maliovishka and Sarnishka lithotectonic units. The thickening of the earth is followed by the processes of the Late Alpine regional extension and the formation of extension structures such as the "metamorphic core complexes" (Ivanov, 1998; Ivanov et al., 2000) and the main first order positive structure in the region was formed – Rila-West Rhodope complex Dome intruded by abundant granitoids of the early extensive stage. The internal structure of the region is complicated by Mesta graben, Ribnovo fault and Babyashko-Grashevo dislocation. The last is tracked from west to east in the immediate vicinity of the southern boundary of Babayk area.

In the 70's of the 20th century a surface and underground study was carried out in the area of the Babiak locality and the presence of Mo, Bi, Ag, Au, Ph, Zn and Cu mineralization was found (Delchev, Dimitrov, 1964; Mileva, 1964). The Babyak ore field is interpreted in the different away during the years – as a quartz-molybdenite mineral formation closely related to the aplitic granitoids and greisen type alteration by Maneva et al. (1994) or as Mo-hydrothermal mineralization with zonal structure genetically related to the late phases of the West Rhodope batholith (Kolkovski, Georgiev, 2006). The Babyak - Mo (Ag- and Au-bearing) deposit is considered as a part of the Babyak orefield related to the Maastrichtian–Lutetian Rila-Rhodope Metallogenic Zone by Popov et al. (2019).

The present article is a result of the ore mineralization and rock's alteration study in the region and structure analyses for the clarification of the structural control of the ore formation processes in the Babyak deposit (Temelakiev et al., 2017).

Geological setting

The investigated ore zones from the Babyk deposit are located in the close proximity to the contact between Rila-

Western Rhodope batholith (granitoides and related pegmatites and aplites) and the metamorphic frame represented by high-grade metamorphic rocks of the Sarnitsa lithotectonic unit (aplitic and biotite gneisses – Fig. 2).

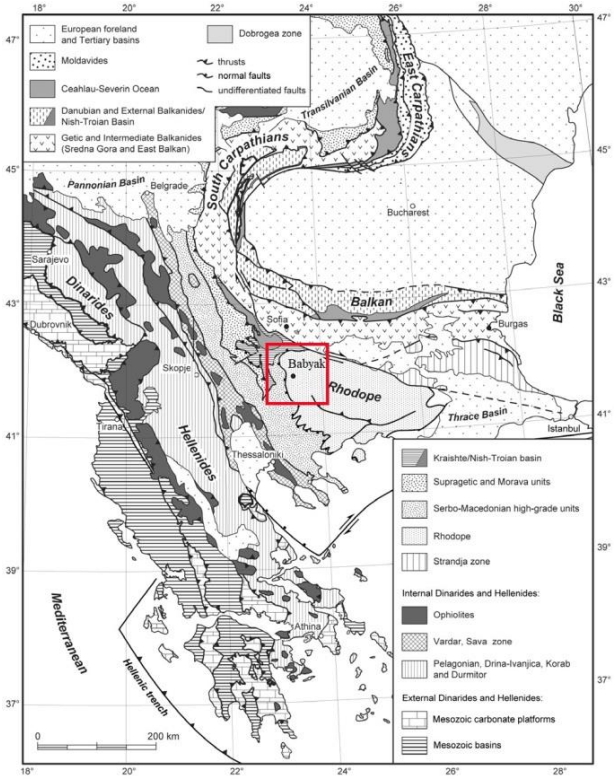

Fig. 1. Tectonic map of the south-western Balkan Peninsula (after Bernoulli, 2001; Schmid et al., 2008)

Sarnitsa lithotectonic unit. It croups out in the frame of the Rila-Western Rhodope batholith in the valley of the Mesta River, from Dagonovo to Yakoruda villages to the North. The rock association of this unit is presented by biotite and amphibole-biotite gneisses, marbles and lens-like bodies of metagabbro and ultrabasites. The leptitic gneisses are the most distributed in this unit. The rocks are folded and intersected by pegmatites and quartz veins oftenly parallel to the gneiss's foliation.

Rila-Western Rhodope batholith. Three types of granitoids are distinguished in the frame of batholith: 1) coarse, irregularly-grained and sometimes porphyry, amphibole-biotite and biotite granodiorites; 2) medium grained biotite and less often two-micas granites; 3) fine-grained biotite-muscovite aplitic granites, such as lenses, veins and stock bodies. The batholith is made up of two plutons differing in age and tectonic position according to Kamenov et al. (1999). The granodiorites of the first type are part of an older (~80 Ma) synmetamorphic pluton with calcium-alkaline composition and mantle magma contaminated by earth material. The granites of the second and the third types, aged 35–40 Ma, are genetically interconnected phases of a post-metamorphic pluton with high alkaline-calcium character.

Dykes. They include lamprophyres, dioritic, granodiorites and quartz-diorite porphyrites, granite porphyry, gabbro-diabases, meta-dolerites and micro-gabbros among the rocks of the Rila-West Rhodope batholith and more rarely in the metamorphites are established. They have different thickness and direction – from centimetres to several meters, and from 300–340° to N and NE (10–70°) direction with sharp intrusive contacts without visible hydrothermal alteration.

Paleogene. It comprises Priabonian breccias, conglomerates and breccia-conglomerates along to the two boards of the grab are involved. The Oligocene rocks are grouped into two facies: volcanogenic (rhyolites and trachy-andesites) and sediment-tuffogeneous (molasse-like and tuffogeneous horizont).

Neogene. Includes clayey-sandy, sandy and conglomerate facies formed in the northern part of the Mesta Depression. The Neogene in the area is perceived as one unit - upper sandstone-conglomerate formation (Sarov et al., 2011).

Quaternary. It has a relatively limited distribution in the area of study. Fluvio-glacial, delluvial and alluvial sediments are presented.

Ore setting

The magmatic-hydrothermal stage of the Rila-Western Rhodope batholith is characterized by the development of a large number of aplites, pegmatites and quartz veins (with and without ores). The latters are oriented mainly to the NE or NW following the main geological structures in the region. The veins without ores are with irregular thickness and the contacts with the hosted rocks are weakly hydrothermally altered. This type of veins contains milky whitish quartz with rare pyrite crystals. The ore-containing veins are with regular thickness, massive structure and consisted of grey-whitish quartz. The established ore minerals into them are pyrite, molybdenite, galena, sphalerite, chalcopyrite, specularite and wolframite. The contacts with the hosted rocks are sharp ones accompanying with thick (up to 10 m and more) zone of hydrothermal alteration. Two zones (zones 5 and 6) enriched of ores exist in the central part of the studied deposit.

Zone 5 is the best developed ore zone in the deposit according to thickness and intensity of the ore mineralization. It is composed by quartz-iron oxide-sulphide vein with a variable thickness from 0.3 to 20.0 m with a slope of 45–60° at the surface and up to 25–35° in depth. The vein is sunk to the W-SW conforming to the metamorphic foliation of the hosted rocks. Close to its lower contact with the hosted gneisses shear zone is developed followed by reactivation accompanied with brittle deformations.

Zone 6 includes two parallel quartz-pegmatite veins with apophysis developed west of the zone 5. The thickness of the veins is from 0.5 to 10.0 m. The slope is to W-SW and varies from 40–45° on the surface to 30–35° in the depth. Both zones are developed close to the contact between Rila-Western Rhodope batholith and hosted metamorphic rocks.

Materials and methods

The study was made on 120 representative drill rock and ore samples. The petrographic and ore thin-sections were used to obtain information for textures and minerals composition of the primary and altered rocks and ores. The microscopic investigation was made using microscope Meiji7390 for transmitted and reflected light and digital camera Olympus 5050 for microphotos.

The phase composition of the hydrothermally altered was determined by powder X-ray diffraction (XRD), at the University of Mining and Geology "St. Ivan Rilski". The powder XRD

patterns were recorded on a Bruker D2 Phaser diffractometer using Ni-filtered Cu Kα radiation in the 2Θ range 4–80º, step size 0.02º. The textures and chemical composition of the ore mineralization were characterized by Scanning electron microscopy fitted with energy dispersive spectrometer JEOL JSM-6010 PLUS/LA in the University of Mining and Geology "St. Ivan Rilski" using nature etalons.

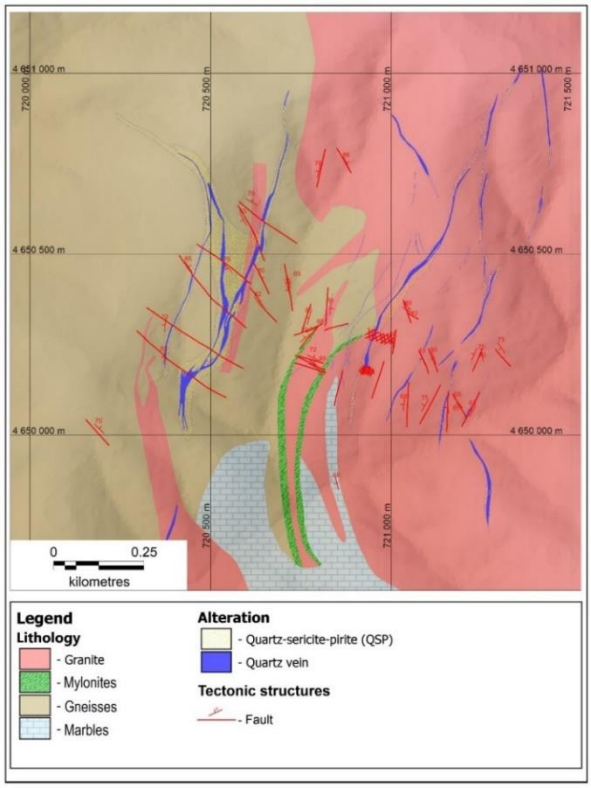

Fig. 2. Detailed geological map of the Babyak ore deposit

Results

Rock composition

The investigated ore zones from the Babyk deposit are located in the close proximity to the contact between Rila-Western Rhodope batholith (granitoids and related pegmatites and aplites) and the metamorphic frame represented by high-grade metamorphic rocks of the Surnitsa lithotectonic unit (aplitic and biotite gneisses).

Gneisses are light grey to milky white in colour aplitic and biotite gneisses, fine-grained with a fine layered structure, lepido-granoblastic texture and mineral composition of quartz, feldspars (microcline and acid oligoclase), muscovite and biotite and accessories of zircon, apatite and garnet.

Granites are also light grey in colour, hetero-grained with massive fabric intersected by nets of open fractures. Their textures are granitic and poikilitic in places. The granites are with mineral composition of quartz, plagioclase, K-feldspar, biotite and accessories – zircon, apatite, titanite and ore mineral (magnetite?).

Pegmatites are with mineral composition of quartz, K-feldspar, acid oligoclase and muscovite. All investigated pegmatites are brittle (mainly) to plastic deformed – cracked, brecciated to cataclazed and mylonitized.

Rock alterations

Greisen-like type alteration (GTA). It has a local development with formation of coarse flaked white mica (individual flakes or aggregates), clay minerals, K-feldspar, albite and tourmaline. Quartz, sericite-muscovite and fluorite fill the open cracks, also. This type of alteration in the studied ore field is mentioned by Delchev and Dimitrov (1964) and Maneva et al. (1994), also.

Quartz-sericite-pyrite type (QSP). Wide developed alteration with uneven intensity among gneisses, granites and pegmatites. The alteration is associated with intensive brittle deformations and formation of breccia and cataclastic textures in the rocks. The relics of the primary minerals (if they are preserved) are cracked to defragmented and replaced by hydrothermal sericite and quartz, mainly. The hydrothermal mineral association is the most intensive developed in the inter-clast interstices and in the plane of the metamorphic foliation in the gneisses, also. In the vicinity to the zones with the intensive formation of hydrothermal quartz and ore mineralization QSP alteration totally erased the primary features of the primary rocks.

Ore mineralization

On the base of the study the followed characteristics of the distribution and features of the ore mineralization could be pointed: 1) the presence of pyrite, galena, sphalerite, chalcopyrite, molybdenite, gold, electrum, lead-bismuth minerals, bursaite(?), covelline, chalcosine, arsenopyrite, tennatite – tetrahedite and malachite; 2) the ore minerals are presented as finely disseminated crystals with sizes 1.0–2.0 mm; thick layers (veins), irregularly in shape aggregates (from 2.0–3.0 up to 30–40 mm) and massive ore-bunch of pyrite and molybdenite (mainly) ± chalcopyrite; 3) the wide distributed ore assemblages in the deposit are: (I) pyrite-molybdenite associated with Pb-Bi sulphosalts related to the greisen-like type alteration and (II) pyrite-galena-sphalerite-gold mainly related to the QSP alteration; 4) the ore textures supposed that during formation of the second ore assemblage there are remobilization of the minerals like molybdenite (mainly) and Pb-Bi sulphosalts (limited?).

Relation ore-mineralization/rock alteration

The formation of the Mo-Bi-Ag mineralization with pyrite I, molybdenite I, Pb-Bi sulphosalts and wolframite could be related with the appearance of the GTA. The ore texture of this assemblage shows clear post-deformation genesis – short veins, fine layered aggregates developed around quartz and rock fragments, fills up the fragment interstices or the open fractures.

The main part of the studied ore mineralization is situated among QSP type altered rocks developed among intensively tectonized gneisses, granites and pegmatites. This type of hydrothermal alteration associated with the Au-Pb-Zn-Cu and the ore assemblage is presented by pyrite 2, chalcopyrite, galena, sphalerite, gold, electrum, remobilized molybdenite II. They are fine disseminated among quartz-sericite mass or are concentrated in the fragment's interstices as spotty aggregates, cracked to defragmented crystals, long prismatic to flaked aggregates (for molybdenite) plastically deformed or segregated in the sphere aggregates.

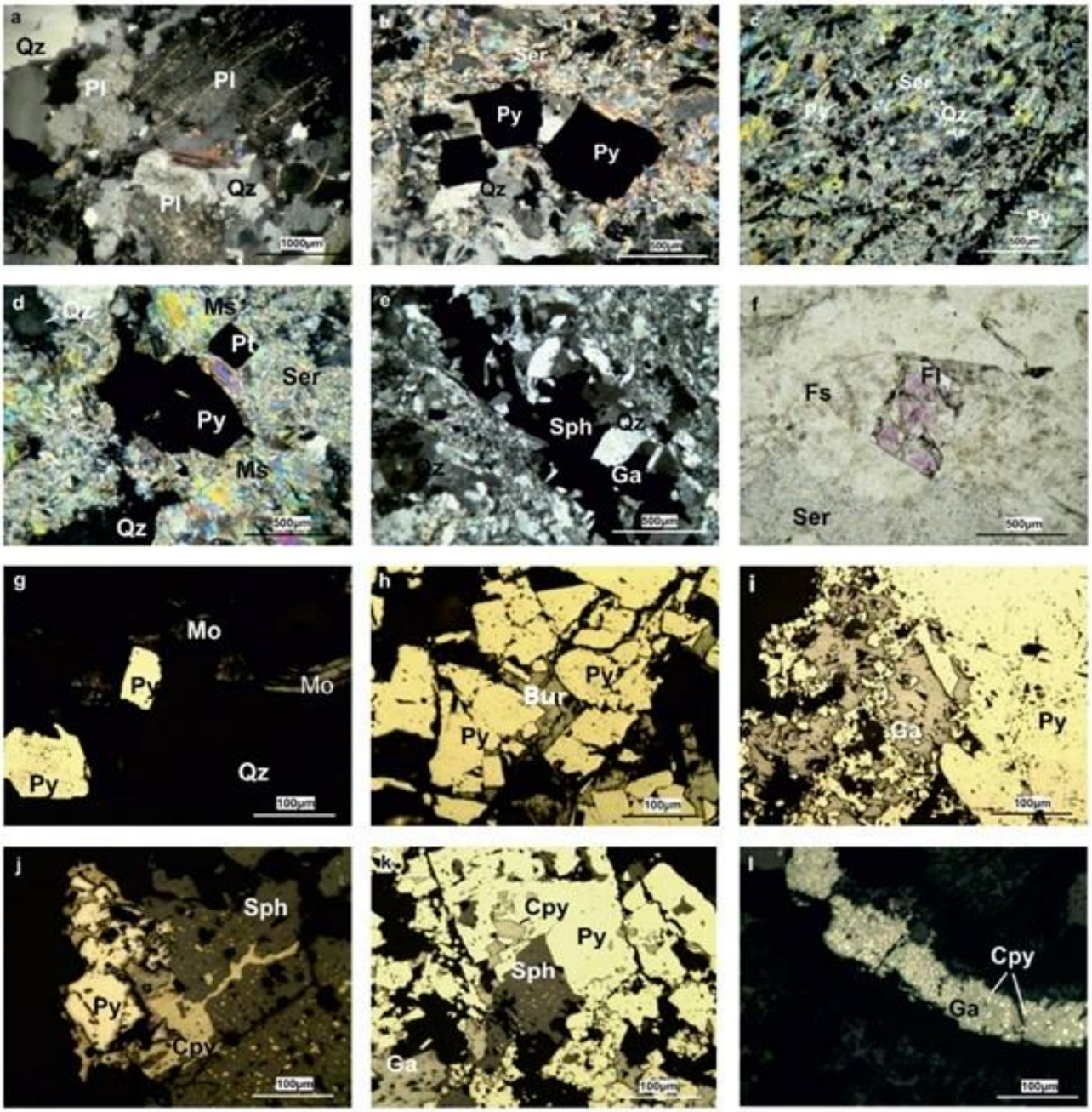

Fig. 3. Microphotos of rocks and ore mineralization: *a*, well preserved biotite granite, transmitted light; *b–c*, QSP type metasomatites, transmitted light; *d–f*, GTA, transmitted light; *g–h*, first stage ore mineralization, reflected light; *i–l*, second starde of ore mineralization, reflected light. Abbreviations: *Qz*, quartz; *Pl*, plagioclase; *Ser*, sericite; *Ms*, muscovite; *Fs*, feldspar; *Fl*, fluorite; *Py*, pyrite; *Sph*, sphalerite; *Ga*, galenite, *Mo*, molybdenite; *Cpy*, chalcopyrite; *Bur*, bursaite (?)

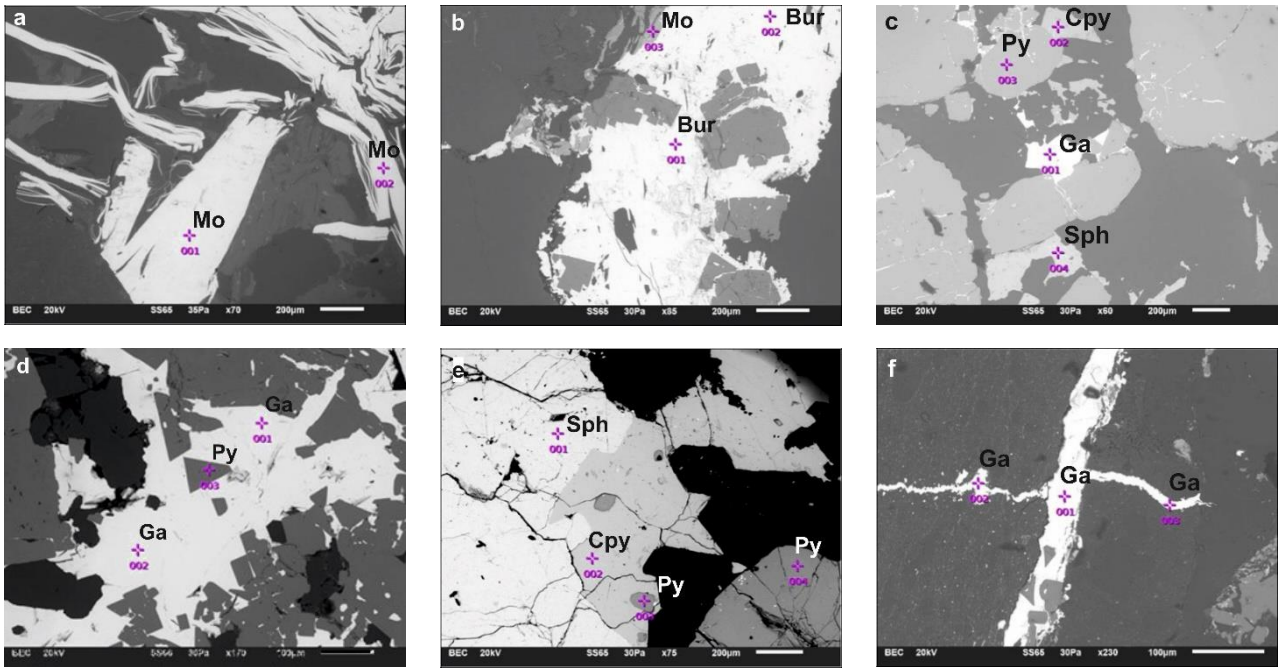

Fig. 4. SEM- EDX images of the studied ore mineralization

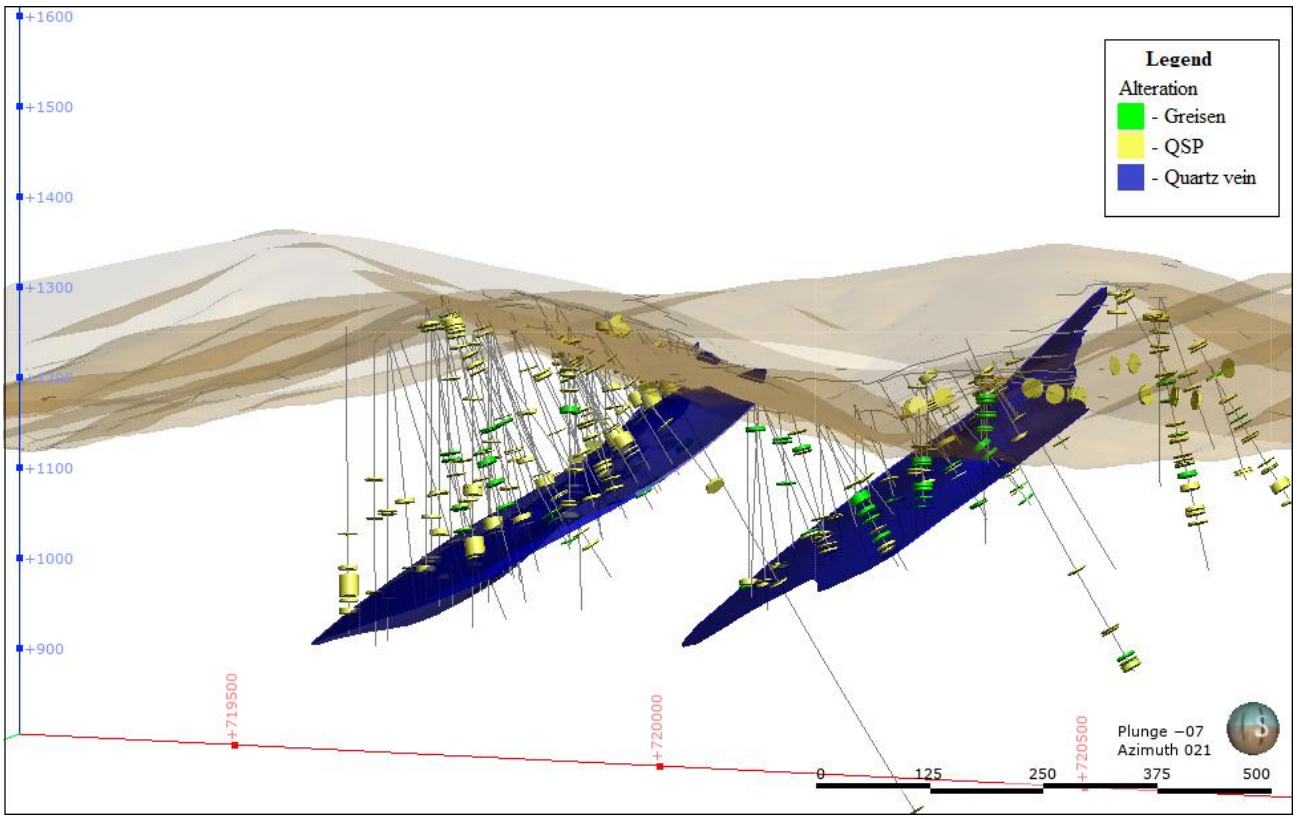

Fig. 5. 3D geological model presenting the alteration and ore zones

Tectonic, magmatic and hydrothermal events associated with ore-forming processes at Babyak Ag-Mo-Au deposit

In order to establish the structural control of the Babyak deposit an attempt to distinguish the time and nature of the main structural, tectono-magmatic and mineralization events observed in the area of the deposit was made. The following events (from the earliest to the latest) are distinguished:

D1. Formation of a regionally expressed foliation S1 that has entirely affected the rocks of the Surnitsa lithotectonic unit. Its formation is related to the Early Alpine structure (Sarov et al., 2011);

D2. Locally developed slanted plastic shear zones with formation of imposed mylonitic foliation S2. These shear zones

kinematically are oriented to the W and SW and are with extension character. Their formation probably predetermined the elevation of the region, the intrusion (emplacement) of the Rila-Western Rhodopes batholith and the formation of the Western Rhodope Dome (Ivanov, 1998);

D3. The intrusion of the Rila-Western Rhodope batholith. It is considered to be a post-tectonic event due to the fact that the contacts of the batholith with the metamorphic hosted rocks are clearly intrusive and the granites cross up the plastic structures described above;

D4. Late magma activity, characterized by the emplacement of a large number of aplites and pegmatites, passing through quartz hydrothermal veins in the contact zone of the batholith. During this event brittle to brittle-plastic shear zones parallel to the regional foliation and the earlier extensional plastic shear zones and inclined to the west shear zones of brittle deformation type are developed. This deformation event can also be interpreted as genetically related to the regional extension and elevation of the pluton and the associated with this process detachment faults. They are associated with local development of hydrothermal high-temperature alteration (GTA) in the granites (mainly) and quartz - pegmatite contacts and formation of Mo-Wo-Bi-Ag mineralization.

D5. It is presented by late steep to sub-vertical fault destructions with NW-SE direction, intersecting the earlier structures. These faults are with brittle character, dip to WSW or ENE direction and they affected and brecciated all rocks - metamorphites, granites, aplites, pegmatites and quartz veins. With this event could be related the wide developed quartz-sericity-pyrite (QSP) hydrothermal alteration in the ore field and formation of Au-Pb-Zn-Cu mineralization.

Conclusions

The obtained data of this study for the Babyak deposit assumes at least two stages of formation on the ore-forming structures in the locality. The first stage includes Mo-Wo-Bi-Ag mineralization, which is probably genetically linked to the formation of pegmatites and quartz veins. It is concentrated in the inclined to the west shear zones of brittle deformation type D4 affects mainly the quartz-pegmatite periphery areas followed the crystallization. The steep dextral strike-slip faults of type D5 which are related to the activity of the regional Ribnovo fault zone and Babyak-Grashevo shear zone,mainly, control the deposition of the second stage Au-Pb-Zn-Cu mineralization. It should be note that this mineralization is observed along the structures type D4, also, in the southern part of the deposit which is result, probably, of the late re-activation during formation of structures type D5 (Temelakiev et al., 2017).

Based on the new data obtained by this study could supposed the granite-related ore mineralization of the Babyak deposit.

References

Delchev, A., S. Dimitrov. 1964. Geology and geochemical features of the Babyak deposit, Blagoevgrad region. – *Ann. Dir. Geology*, *15*, 5–37 (in Bulgarian).

Ivanov, Ž. 1988. Apercu general sur l'evolution gèologique et structurale du massif des Rhodopes dans le cadre des Balkanides. – *Bull. Soc. Geol. France*, *8*, IV, 2, 227–240.

Ivanov, Ž. 1998. *Tectonics of Bulgaria*. Sofia University "St. Kliment Ohridski", Sofia, 579 p. (in Bulgarian)

Ivanov Ž., 2000. Tectonic position, structure and tectonic evolution of Rhodope massif. – In: *Guide ABCD-GEODE. Borovets, Bulgaria*, 1–4.

Kamenov, B., I. Peicheva, L. Klain, K. Arsova, Y. Kostitsin, E. Salnikova. 1999. Rila-West Rhodope batholith: petrological and geochemical constrains for its compositional character. – *Geochem., Mineral. Petrol.*, *36*, 3–27.

Kolkovski, B., V. Georgiev. 2006. Late Alpine metallogeny of Western and Central Rhodopes. – In: *National Scientific Conference* "*Geosciences 2006*". Bulg. Geol. Soc., Sofia, 235–237.

Maneva, B., L. Naftali, D. Manev. 1994. Metallogeny and potential mineral resources in Central and West Rhodope. – *Rev. Bulg. Geol. Soc.*, *55*, 2, 37–49 (in Bulgarian with English abstract).

Mileva, G. 1964. Particularities and micro-parageneses of the main ore minerals from the complex deposit "Babyak", Blagoevgrad area. – *Ann. NIPRORUDA, 3*, 227–233 (in Bulgarian).

Popov, K., P. Popov. 2019. The Alpine late collisional Rila-Rhodope Metallogenic Zone of the Balkan Orogenic System. – *Rev. Bulg. Geol. Soc.*, *80*, 1, 55–79.

Ricou, L. E., J.-P. Burg, I. Godfriaux, Ž. Ivanov. 1998. Rhodope and Vardar: the metamorphic and the olistostromic paired belts related to the Cretaceous subduction under Europe. – *Geodinam. Acta*, *11*, 6, 285–309.

Sarov, S., S. Moskovski, T. Zhelezarski, N. Georgiev, E. Voynova, D. Nikolov, I. Georgiev, V. Valev, N. Markov. 2011. *Explanatory Note to the Geological Map of the Republic of Bulgaria. Scale 1:50000. Belitsa Map Sheet*. Ministry of Environment and Water, Bulgarian Geological Survey, Sofia, 68 p. (in Bulgarian with English abstract)

Schmid, M. S., D. Bernoulli, B. Fügenschuh, L. Matenco, S. Shefer, R. Schuster, M. Tischler, K. Ustaszewski. 2008. The Alpine-Carpathian-Dinaridic orogenic system: correlation and evolution of tectonic units. – *Swiss J. Geosciences*, *101*, 1, 139–183.

Temelakiev N., K. Ruskov, N. Petrov. 2017. Structural control on the ore-forming processes at Ag-Mo-Au deposit Babyak, Western Rhodope. – In: *National Scientific Conference* "*Geosciences 2017*". Bulg. Geol. Soc., Sofia, 127-128 (in Bulgarian with English abstract).

BURIAL AND THERMAL HISTORY RECONSTRUCTION OF SOUTH SAKAR DEPRESSION, BULGARIA

Gergana Meracheva

University of Mining and Geology "St. Ivan Rilski", 1700 Sofia; g.meracheva@gmail.com

ABSTRACT: In tectonic aspect, the studied area is located in the South Sakar depression, which in the south-southeast turns into the large hydrocarbon Thrace basin in Turkey. The purpose of this study is buried history modelling and thermal history modelling of the studied region. This enables a reconstruction and characterisation of the sediment filling processes of this part of the basin and assessment of the hydrocarbon generation and migration from tertiary sediments. In the process of buried history reconstruction, periods of sedimentation followed by hiatus and erosion periods are observed. These periods, along with the heat flow changes for the region, have an impact on the maturity of the sediments. In the present study, a 1D thermal maturity model of three litho-stratigraphic units, which are part of shale-marl and terrigenous-limestone-marl formations and are evaluated as potential source rocks in the tertiary section of the depression, is created. The thermal maturity model shows that sedimentary sequences from Eocene to Pliocene Ages can generate liquid and/or gaseous hydrocarbons.

Keywords: petroleum system modelling, thermal history reconstruction

РЕКОНСТРУКЦИЯ НА ИСТОРИЯТА НА ПОТЪВАНЕ И ГЕОТЕРМИЧНАТА ЕВОЛЮЦИЯ НА ЮЖНОСАКАРСКОТО ПОНИЖЕНИЕ, БЪЛГАРИЯ

Гергана Мерачева

Минно-геоложки университет "Св. Иван Рилски", 1700 София

РЕЗЮМЕ: В тектонско отношение, изследваният район е разположен в Южносакарското понижение, което на юг-югоизток преминава към големия нефтогазоносен Тракийски басейн в Турция. Целта на настоящата разработка е моделиране на историята на потъване и геотермичната история на изследвания район. Това позволява реконструкция и характеризиране на процесите на образуване на седиментния пълнеж на тази част от басейна и оценка на въглеводородната генерация и миграция от терциерните седименти. В процеса на реконструкцията на историята на потъване се наблюдават периоди на седиментация, последвани от периоди на прекъсване или ерозия. Тези периоди, заедно с измененията на топлинния поток за района, оказват своето влияние върху степента на зрялост на седиментите. В настоящата разработка се прави 1D модел на термичната зрялост на три литолого-стратиграфски единици, влизащи в състава на глинесто-мергелната и теригенно-варовиково-мергелната задруга, които са оценени като потенциални генериращи скали в терциерния разрез на понижението. Моделът на термичната зрялост на Южносакарското понижение показва, че седиментните последователности с възраст от еоценската до плиоценската епохи могат да генерират различни по фазово състояние въглеводородни продукти.

Ключови думи: петролно-системно моделиране, реконструкция на геотермичната история

Introduction

The South Sakar depression, located in South-eastern Bulgaria, is continuation of the large structural unit that goes beyond the borders of our country and is called the Thrace basin. After purposeful geological-geophysical and drilling activities it has been evaluated as a petroleum system with a significant potential (Karahanoglu et al., 1995; Gurgey, 2009; Şen, 2011). The area of research is characterised with a poor exploration for hydrocarbons. The limited data does not allow a complete characterisation of the hydrocarbon potential of the Tertiary sediments. The several studies in this regard give grounds for preliminary assessment of the source rock potential of the Tertiary sediment complex as fair to good (Palakarcheva, Stefanova, 2013; Meracheva et al., 2017a, b). This gives a basis for further studies in order both to reconstruct and characterise the sediment filling processes of this part of the basin, and to model and assess subsequently the hydrocarbon generation and migration from Tertiary sediments.

Geological setting

In earlier publications (Zaneva-Dobranova, Meracheva, 2014; Meracheva, Zaneva-Dobranova, 2018) the issue of the different concepts about the tectonic belonging of the studied area was examined in details. For the purpose of the present study, a tectonic position is assumed (Fig. 1), which is determined according to tectonic zonation of Southern Bulgaria (Zagorchev et al., 2009), the characteristics of the structure, development of the main structure units and the relation between them.

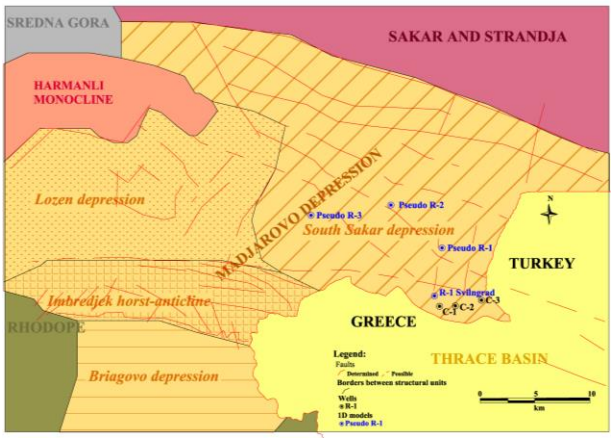

Fig. 1. Tectonic scheme of the studied area (after Zagorchev et al., 2009; with modifications) and location of the 1D models

The tertiary section in the region of research consists of sedimentary rocks of Paleogene and Neogene age (Fig. 2). It overlies discordantly above different level pre-Paleogene fundament and is partly or fully covered by eluvial, proluvial and alluvial sediments of the Quaternary (Kozhoukharov et al., 1995). At the base of the Tertiary section, according to data from the seismic surveys, north of R-1 Svilengrad Well, a zone with unclear configuration and characteristic sand-conglomerate and turbiditic facies is observed.

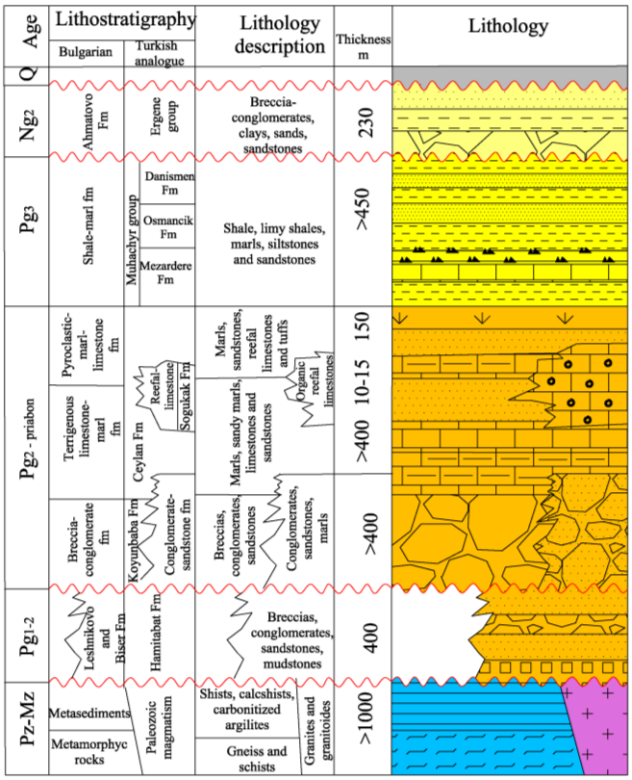

Fig. 2. Lithostratigraphic scheme of the Tertiary section of studied area

These rocks are with similar lithological features and could be assigned to the surface exposed to the west of studied area Biser and Leshnikovo Formations of Palaeocene–Eocene (?) age. In the area of South Sakar Depression, they are considered (Palakarcheva, Stefanova, 2013; Meracheva, Zaneva-Dobranova, 2018) as analogues of the Hamitabat Formation in the Turkish part. Above them or directly on the fundament overlay with transgression the clastic-carbonate rocks of the formations of Priabonian age, assigned to breccia-conglomerate, conglomerate-sandstone, terrigenous-limestone-marl and pyroclastic-marl formations. These sediments are in complex spatial relationships. In some places a smooth lithofacies replacement of the rocks from one formation to the neighbouring is observed. To southeast, their probable correlates are the sediments of the Koyunbaba and Ceylan Formations (Meracheva, Zaneva-Dobranova, 2018). The rocks in the section are followed by the Oligocene deposits of the shale-marl formation, represented by marls, marly limestones, shales, sandstones and siltstones. This formation could be correlated with the lithostratigraphic units of the Muhacir Group on Turkish territory – Mezardere, Osmancik, Danismen Fms. To the west of the South Sakar Depression the section is represented by tuffs, tuffites and reefal limestones. The Paleogene deposits are discontinuously covered by Neogene sedimentary rocks included within the scope of the Ahmatovo Formation.

Methodology and methods of modelling

In this study a petroleum system modelling is carried out in order to reconstruct the burial and thermal history of the studied area. The result of this is used for further petroleum system simulation of hydrocarbon generation and expulsion processes in the studied area, both from the evaluated potential source rocks of shale-marl (analogue of the Mezardere Formation in the Turkish part) and terrigenous-limestone-marl (analogue of Ceylan Formation in the Turkish part) formations, and from deposits, analogues of proven in the central part of the basin the Hamitabat Formation (Hosgörmez, Yalçın, 2005; Gürgey, 2009). For the 1D petroleum-system modelling geological and geochemical data from the deep R-1 Svilengrad Well are used. These data are interpolated in several sections to the north and west of R-1 Svilengrad Well, using for the purpose selected interpreted seismic sections and subsequently calculated thicknesses of the litho-stratigraphic units in the 3D structural model (Meracheva, Zaneva-Dobranova, 2018). Three new 1D models of reconstruction on conditional (pseudo) wells – Pseudo R-1, Pseudo R-2, Pseudo R-3, were created on this basis (Fig. 1).

For reconstruction of burial and thermal history in the software are imported as follows:

- Data of the geological research related to periods of deposition, erosion and hiatus, with their respective ages, lithology and thickness;
- Data obtained from geochemical research of the rocks of shale-marl formation – quantity of Total organic carbon (TOC), Hydrogen index (HI), thermal maturity data (T_{max});
- Thermal maturity calibration data from R-1 Svilengrad well – uncorrected formation temperature, measured in the well (Bottom hole temperature – BHT); maximal temperature, obtained at pyrolysis (T_{max});
- Heat flow data – thermal conductivity of the formation and calculated geothermal gradient for the region.

For the purpose of petroleum system modelling, the geochemical parameters of the source rock, in the range of the shale-marl formation, are averaged. For TOC mean values are assumed to be 1.42 wt%, and for HI mean value is 135 mg HC/g TOC. Initially, burial history curves for the sediment section are reconstructed, considering thicknesses of the sediment formations, their ages and the periods of deposition and erosion.

For the reconstruction of thermal history, one of the modern approaches used in the recent years by the researchers in the petroleum sciences has been applied (Botoucharov, 2005; Hosgörmez, Yalçın, 2005; Huvaz et al., 2007; Hakimi et al., 2018). For this purpose, the necessary calculations from the available data for the area are carried out.

For the calibration and reconstruction of the heat flow and the geothermal history in modelling the temperature-sensitive parameters are used – temperature at pyrolysis (T_{max}) and formation temperature (BHT) (Pepper, Corvi, 1995; Makeen et al., 2016; Hakimi et al., 2018).

When creating the 1D heat flow model, Fourier low equation is used, thus the heat flux values are calculated after measuring the temperature and the thermal conductivity. For these calculations the data of formation temperature measured during the geophysical logging of wells (BHT) are used. Considering that the temperature values measured in this way are lower than the actual temperature of the respective formation, due to the cooling effect of the drilling fluid circulating at the bottom of boreholes, corrections can be made in the cases of sufficient information (Deming, 1994). Therefore, the average values of the thermal conductivity of the rocks in the research area is considered to be analogous to the one determined in the Turkish part of the Thrace basin on a significant number of wells (Engin, 1999). The data obtained from the studies in the Thrace basin in Turkey were taken into account in the simulation of the heat flow and in the creation of a conceptual model of reconstruction of the geothermal history of the research area. These data, as well as the values used in the model for the geothermal gradient, calculated from the measured temperature in R-1 Svilengrad well, are compared with existing studies for the geothermal gradient of this part of Bulgaria (Velinov, Boiadjieva, 1981).

Results of the petroleum system modelling

Petroleum system modelling of burial and subsidence history of the Tertiary sediments

At reconstruction of the burial history of the studied part of the basin, periods of sedimentation, followed by periods of hiatus and erosion are observed (Fig. 3). The large unconformity, with an average thick erosion of 450 m has been recognized during the middle-late Eocene, which is probably related to the Illyrian tectonic phase. Another unconformity is typical for the period of Miocene age, which shows an uplift process. However, these erosion periods together with the heat flow of the area affect thermal maturity range of the sediments.

The burial history curves show typical for this type of basins tectono-stratigraphic phases – syn-rift and post-rift. Both syn-rift phases are characterised by approximately the same rate of sedimentation when relatively thick sediment complexes are deposited. During the post-rift phase, the rate of sedimentation significantly decreases. The transgression that occurred at the end of the Palaeocene – the beginning of the Eocene(?), resulting in a rapid subsidence of the basin, led to deposition of about 1000 m thick sediment complex in most of the studied area (Fig. 3, pseudo-wells P-1, P-2, P-3). This period is characterised by relatively high rate of sedimentation of an average about ~65 m per million years. Afterwards, a short period occurs for the entire basin, characterised by the absence of sedimentation (Fig. 3, R-1 Svilengrad Well), and in some places with an erosion (Fig. 3, pseudo-wells). During the Priabonian Age again a period of intensive sedimentation and subsidence of the sediment basin occurred, which continued until the end of early Miocene. Then, in the researched area, the rate of sedimentation is ~78 m per Ma and a sediment complex is formed with a present-day thickness to about 1300 m. This rapid subsidence, the deposition of a thick sediment sequence for a relatively short time, and the presence of volcanic activity near to the area are an indication of extensional tectonic activity in the formation of the basin, which is also confirmed by the model of burial history curves.

On the burial history curves, a short period during the middle Miocene is observed, when the sediments uplifted to the surface and some of the deposited rocks once again eroded. This period is associated with the wide-spread tectonic phase, during which a large part of the faults, mainly normal faults, formed in the previous tectonic phase, are reactivated and form numerous folds, anticlines and structures. On the burial history curves, it is evident that after the end of the late Miocene, the deposition of medium rate of sedimentation of the overburden rocks started with ~40 m per Ma, which in places in the studied area reached a thickness of over 250 m. For comparison, the rate of sedimentation in the central parts of the basin (Huvaz et al., 2007) is higher, and respectively, the thickness of the sediments deposited during these tectonic phases is greater, which affects the degree of maturity of the organic matter into the sediments. In addition, the deposition of the upper Neogene sediments in the last 7 million years to some extent also influences the maturation of the potential source rock complex with Paleogene age, burying them to a depth where further HC generation processes could potentially take place.

Heat flow modelling and reconstruction of thermal history

The Thrace basin can be classified as a moderate-high heated basin, with geothermal gradient (measured in wells) above the world average. It ranges from 26°C/km to 43°C/km (Huvas, 2007). It should be noted that the central part of the basin is with a much lower geothermal gradient compared to its margins where the research area is located.

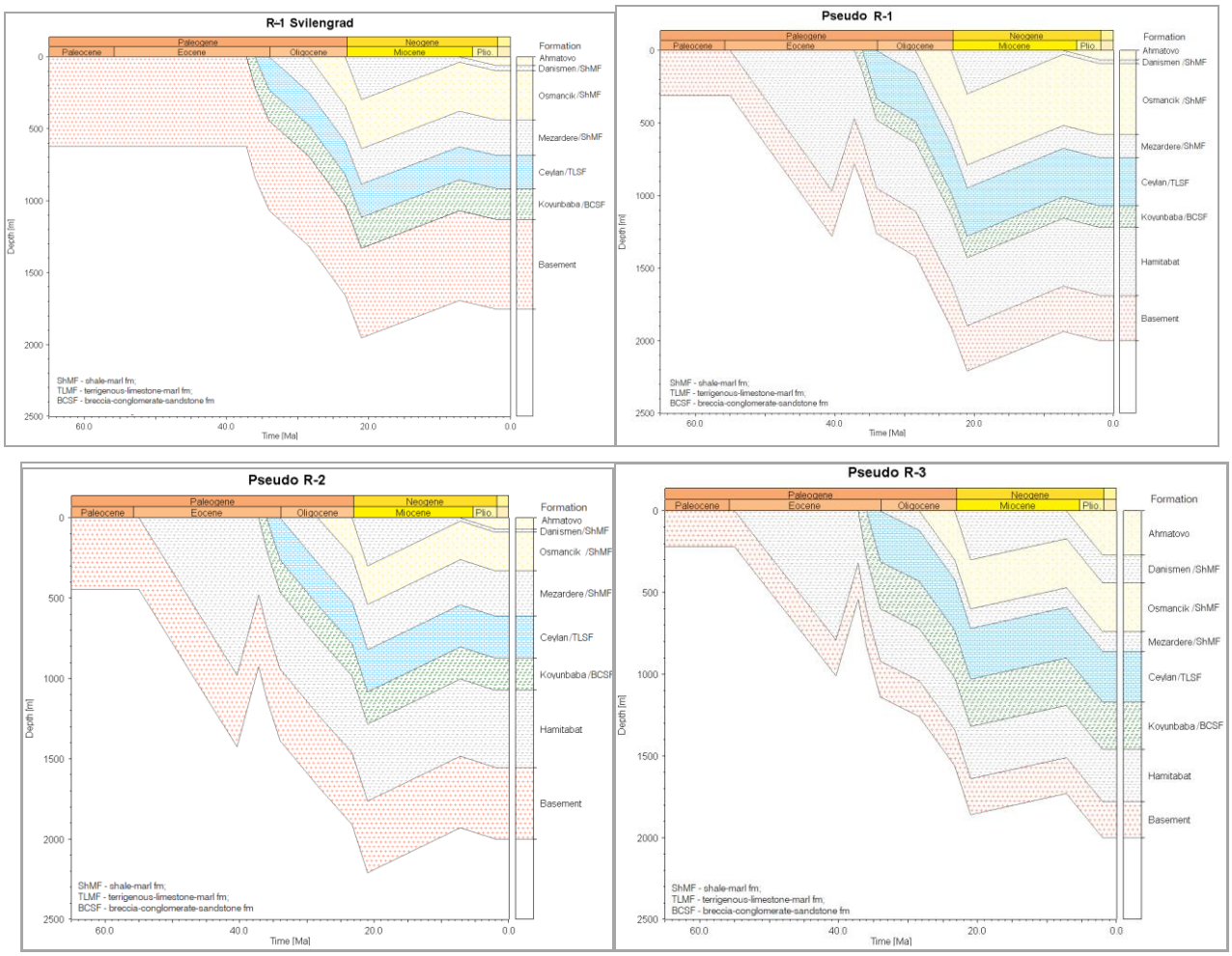

Fig. 3. Burial history reconstruction: 1D models of R-1 Svilengrad Well and pseudo wells R-1, R-2 and R-3

This trend is associated with several factors:

1) At the edges of the fundament and/or the graben margins a high heat flux is usually observed. The heat is concentrated in the high-conductivity rocks of the fundament, not in the relatively low-conductive adjacent sediments. For the conditions of the Thrace basin, it has been found that this factor has a great influence on the thermal gradient changes in the horizontal direction, especially in its northern edges, where the thickness of the sediments decreases significantly;
2) According to the concept of the heat flux distribution in the fundament, the inner parts of a sediment basin, where deposition of sediments is in larger quantities and the earth's crust is thinner (as a result of isostasy), are expected to be cooler compared to areas with a thicker upper crust. This explains the increased values of the geothermal gradient near the highs on the Thrace basin (Sakar-Strandzha Anticlinorium, Central-Thrace High);
3) Lateral thermal conductivity variation is explained with different thermal conductivity of the mineral composition of the rocks;
4) Younger sediments are usually cooler than older ones, resulting in lower geothermal gradient values in areas where sedimentation is higher. This explains the fact that the sediments deposited in the central part of the Thrace basin are cooler and thicker compared to the thinner layers in the margins of the basin.

The created paleo-heat flow model was based on the calibrated thermal maturity data from pyrolysis temperature (T_{max}), which is matched to those obtained in the software (Tmax_Pepper & Corvi, 1995, TIII_TIISA). In order to achieve an acceptable range for the reconstruction of the thermal history of the studied area, multiple scenarios of the paleo-heat flow models have been performed. After the analysis of the sensitivity of the paleo-heat flow model against the influence parameters, a final conceptual model of the heat flow in the region of P-1 Svilengrad Well was obtained. This model shows (Fig. 4), that the values range from 60 to 120 mW/m^2 and are higher than that of the present-day. Until the beginning of the Eocene the values kept constant (60 mW/m^2), then considerably increased from 97 to 107 mW/m^2.

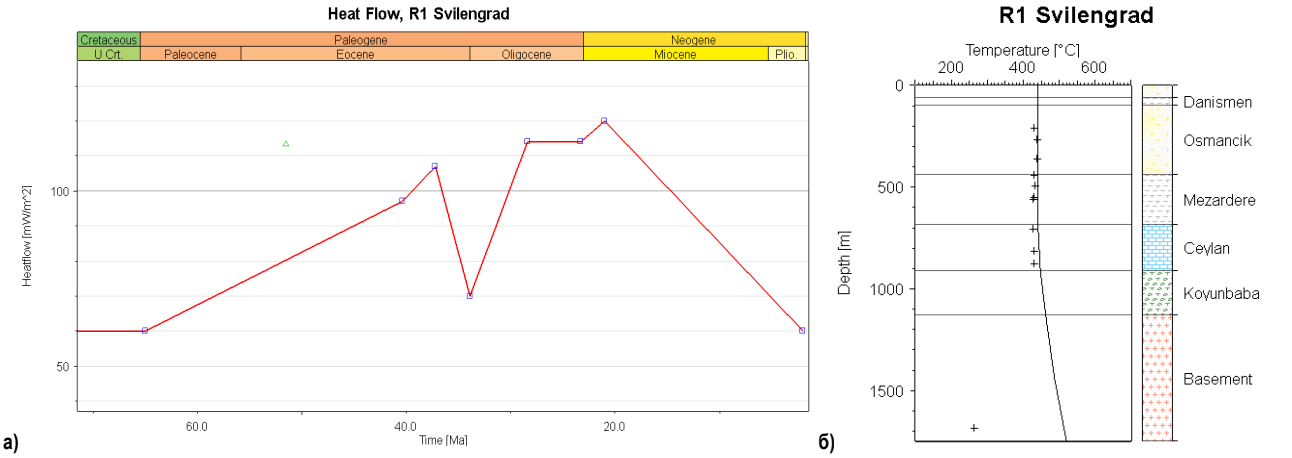

Fig. 4. Paleo-heat flow model for R-1 Svilengrad Well (a), calibrated values optimised modelled by the software with those measured at pyrolysis (b)

Increased values and occurrence of peak values are probably related to tectonic processes of basin opening. These processes influence thermal maturity of organic matter and generation potential of the potential source rock Hamitabat Formation and its analogue sediments on the Bulgarian territory. At the end of the Priabonian, a period of low heat flow values is observed (70 mW/m^2), followed by a new increase in the heat flow values with a trend of constant during the Oligocene (114 mW/m^2). At the end of the Miocene and the beginning of Pliocene, the highest peak in the value of heat flux (120 mW/m^2) was reached, which mark the beginning of new rift phase.

In order to create the temperature model, the present-day heat flow value of 58.5 mW/m^2 is assumed, which corresponds to the optimal present-day temperature modelled in the software with measured bottom-hole temperature in the well (Fig. 5). The model indicates that the paleo-temperature reached peak values during the Miocene, which coincides with the highest paleo-heat flow values at the same time.

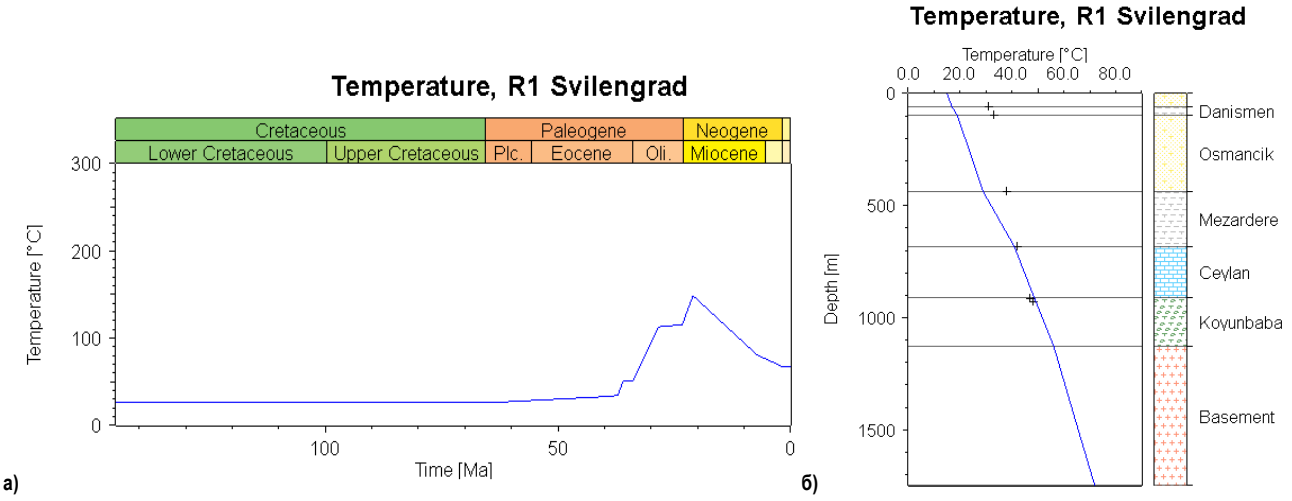

Fig. 5. Paleo-temperature model of R-1 Svilengrad Well (a), calibrated optimal present-day temperature values modelled by the software with measured bottom-hole temperature in the well (b)

This increase in paleo-heat flow and paleo-temperature values during the Miocene probably play an important role for thermal maturity of the organic matter and petroleum generation history of both estimated potential source rock of shale-marl and terrigenous-limestone-marl formations (Meracheva et al., 2017), as well as in the proved source rock Hamitabat Formation in the Turkish part of the basin (Gürgey, 2009).

Thermal maturity history modelling of potential source rock formation

Based on the fact that the sediments of shale-marl formation (analogue of Mezardere Fm.) were evaluated as potential gas generating and the Turkish researchers' suggestion (Hosgörmez, Yalçın, 2005), that Ceylan and Hamitabat Formations are the other two potential HC source rock for most of the oil and gas fields in the Thrace basin, a 1D maturity history modelling of these three lithostratigraphic units is made in this paper. 1D petroleum system thermal modelling was performed on four wells – R-1 Svilengrad – real and Pseudo P-1, Pseudo P-2, Pseudo P-3 – conditional wells. For the Hamitabat Formation, the lowest TOC and HI measured values in the Turkish part of the basin were obtained from the nearest Habiller-2 well. In this well the TOC values are 0.98 wt% and HI values – 164 mg HC/g respectively (Gürgey, 2009). For input parameters of the Ceylan Formation the

average values used by the researchers for the analysis and thermal maturity reconstruction models in the basin (Hosgörmez et al., 2005; Hosgörmez, Yalçın, 2005; Palakarcheva, Stefanova, 2013) were taken in this paper – for TOC – 1.08 wt% and for HI – 256 mg HC/g respectively.

The thermal maturity model shows the HC generation zones for all sediment sequences during the different periods (Fig. 6). This hydrocarbon generation zone is simulated on the basis of the method used in the software, with three stages being distinguished: immature; oil window – early oil generation, main oil generation, late oil generation; gas window – wet gas, dry gas. The maturity models for all four simulated wells are similar and show that the potential source rock formations are at different stages of thermal maturity of organic matter.

Main conclusions

Evaluated as potential source rocks of the shale-marl formation, an analogue of the Mezardere Formation, they are in immature stage of maturity of organic matter in the studied area and could only generate biogenic gas. The models of the four wells show that evaluated as potential source rocks of the terrigenous-limestone-marl formation, analogue to Ceylan Formation, entered the oil window at the beginning of the Miocene and are at this stage to date. Thermal maturity models of the sediments, analogous of the proven source rock Hamitabat Formation in Thrace Basin, show that it has reached the peak of oil generation and has entered the oil window area relatively earlier than other potential source rock formations. In the regions of the three pseudo-wells located in the graben, the maturity of the Hamitabat Formation began in the Eocene, which can also be inferred from the burial history modelling. As can be seen from the created maturity models, the lower levels of the formation are adjacent to the gas window, which suggests that in close proximity to the study area where the formation is at a greater depth, it has reached maturity in order to produce gas since the beginning of the Miocene age to the present day.

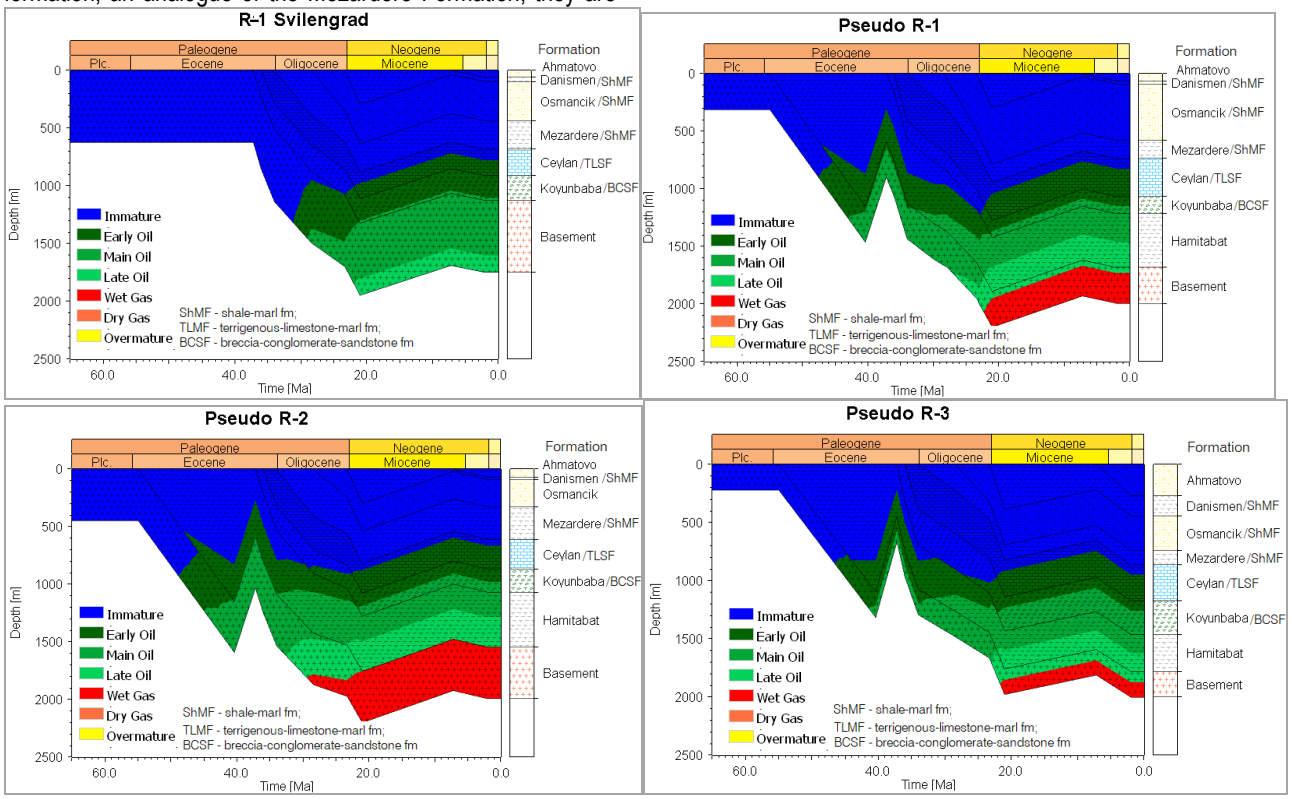

Fig. 6. Thermal maturity models of R-1 Svilengrad well and pseudo-wells – Pseudo R-1, Pseudo R-2, Pseudo R-3

References

Botoucharov, N. 2005. Tectonic subsidence and hydrocarbon potential of Mesozoic sediments in the central part of South Moesia peri-platform. – *Ann. Univ. Sofia, 98*, Liv. 1 – Gèol., 65–86 (in Bulgarian with English abstract).

Deming, D. 1994. Overburden rock, temperature and heat flow. – In: Magoon, L. B, W. G. Dow (Eds). *The Petroleum System – from Source to Trap: AAPG Memoir, 60*, 165–186.

Engin, M. E. 1999. Trakya Bölgesindeki bazı kuyulara ait değişik formasyonların ısı iletkenlik katsayıları. – *Research Group Thermal Study Documents*, 4 p.

Gürgey, K. 2009. Geochemical overview and undiscovered gas resources generated from Hamitabat petroleum system in the Thrace Basin, Turkey. – *Marine and Petrol. Geol.*, *26*, 1240–1254.

Hakimi, M., A. Al-Matary, O. Hersi. 2018. Burial and thermal history reconstruction of the Mukalla-Sayhut Basin in the Gulf of Aden, Yemen: Implications for hydrocarbon generation from Paleocene potential source rock. – *J. African Earth Sci.*, *144*, 59–75.

Hosgörmez, H., M. N. Yalçın. 2005. Gas-source rock correlation in Thrace basin, Turkey. – *Marine and Petrol. Geol.*, *22*, 901–916.

Hoşgörmez, H., M. N. Yalcin, B. Cramer, P. Gerling, U. Mann. 2005. Molecular and isotopic composition of gas occurrences in the Thrace basin (Turkey) origin of the gases and characteristics of possible source rocks. – *Chemical Geology*, *214*, 179–191.

Huvaz, O., N. Karahanoglu, V. Ediger. 2007. The thermal gradient history of the Thrace Basin, NW Turkey: Correlation with basin evolution processes. – *J. Petrol. Geol.*, *30*, 3–24.

Karahanoglu, N., A. Erler, H. I. Illieez. 1995. Mathematical approach to hydrocarbon generation history and source-rock potential in the Thrace basin. – *Marine and Petrol. Geol.*, *12*, 587–596.

Kozhoukharov, D., I. Boyanov, E. Kozhoukharova, A. Goranov, S. Savov, G. Shilyafov. 1995. *Explanatory Notes to the Geological Map of Bulgaria on Scale 1:100000. Svilengrad Map Sheet*. Committee of Geology and Mineral Resources, Avers, Sofia, 65 p. (in Bulgarian with English abstract)

Makeen, Y. M., W. H. Abdullah, M. J. Pearson, M. H. Hakimi, O. M. A. Elhassan, Y. T. Hadad. 2016. Thermal maturity history and petroleum generation modelling for the Lower Cretaceous Abu Gabra Formation in the Fula sub-basin, Muglad basin, Sudan. – *Marine and Petrol. Geol.*, *75,* 310–324.

Meracheva, G., E. Zaneva-Dobranova. 2018. 3D structural model of Thertiary sediments in NW part of Thrace basin. – *J. Mining and Geol. Sci.*, *61*, Part I, 11–16.

Meracheva, G., M. Stefanova, S. Marinov, E. Zaneva-Dobranova. 2017a. Geochemical appraisal of hydrocarbon generative potential of Bulgarian part from the Thrace basin: I. Linear biomarkers. – *Bulg. Chemical Comm.*, *49*, Sp. Edition B, 151–158.

Meracheva, G., M. Stefanova, S. Marinov, E. Zaneva-Dobranova. 2017b. Geochemical appraisal of hydrocarbon generative potential of Bulgarian part from the Thrace basin: II. Cyclic biomarkers. – *Bulg. Chemical Comm.*, *49*, Sp. Edition B, 159–166.

Palakarcheva, G., M. Stefanova. 2013. Source rock hydrocarbon potential of the Bulgarian part of Thrace basin. – *Ann. Univ. Mining and Geol.*, *56*, Part I, Geol. and Geophys., 86–92 (in Bulgarian with English abstract).

Pepper, A., P. Corvi. 1995. Simple kinetic models of petroleum formation. Part I: oil and gas generation from kerogen. – *Marine and Petrol. Geol.*, *12*, 3, 291–319.

Şen, Ş. 2011. Petroleum Source Rock Assessment of the Southwestern Thrace Basin, NW Turkey. – *Energy Sources 33*, Part A, 1005–1017.

Velinov, T., K. Boiadjieva. 1981. *Geotermichni izsledvania v Bulgaria*. Tehnika, Sofia, 154 p. (in Bulgarian).

Zagorchev, I., H. Dabovski, T. Nikolov (Eds). 2009. *Geology of Bulgaria. Vol. II. Mesozoic Geology*. Prof. Marin Drinov Acad. Publ. House, Sofia, 766 p.

Zaneva-Dobranova, E., G. Meracheva. 2014. Hydrocarbon reservoir systemof the east part of the South Sakar depression. – *Ann. Univ. Mining and Geol.*, *57*, Part I, 65–70 (in Bulgarian with English abstract).

RECOGNIZING DEBRIS FLOW HAZARD IN HEAVILY FORESTED WATERSHEDS: AN EXAMPLE FROM ETROPOLE AREA, CENTRAL BULGARIA

Zornitsa Dotseva[1], Ianko Gerdjikov[1], Nikolai Dobrev[2], Dian Vangelov[1]

[1] Sofia University "St. Kliment Ohridski", 1504 Sofia; zori.geo@gmail.com
[2] Geological Institute, Bulgarian Academy of Sciences, 1113 Sofia

ABSTRACT. The mountainous Etropole area is well known with frequent river floods that occur during the summer period. On 1st of August, 2014 extreme rainfall event initiated not only river floods, but also debris flows in steeper riches of the smaller valleys. One of the affected areas is situated at the margin of Etropole Basin, on the slope to the south of Etropolska Ribaritsa village. Related to debris flows and floods, erosional and depositional geomorphic forms were documented in two watersheds three months after the event. The debris flow deposits have comparatively small volume (tens of m^3) and consist exclusively of the Kostina Formation quartzites. Field studies also demonstrated that the occurrences of the Quaternary deposits are not only limited to the bottom of Etropole Basin, but they cover almost completely the slopes south of Etropolska Ribaritsa village. The matrix of these deposits often contains a lot of clay and they play an important role for supply of clasts material for debris flows. Field data, eyewitness reports as well as morphometric data indicate debris flows as a significant hazard for the local communities. These findings support the need for taking mitigation measures and also the necessity for more extensive hazard assessment of debris flows in the Etropole area.

Keywords: debris flow, floods, natural hazard, GIS analysis, Quaternary deposits

РАЗПОЗНАВАНЕ НА ОПАСНОСТТА ОТ ДЕБРИТНИ ПОТОЦИ В ЗАЛЕСЕНИ ВОДОСБОРИ: ПРИМЕР ОТ РАЙОНА НА ЕТРОПОЛЕ, ЦЕНТРАЛНА БЪЛГАРИЯ

Зорница Доцева[1], Янко Герджиков[1], Николай Добрев[2], Диан Вангелов[1]

[1] Софийски университет "Св. Климент Охридски", 1504 София
[2] Геологически институт, Българска академия на науките, 1113 София

РЕЗЮМЕ. Планинският район около гр. Етрополе е известен с честите речни приждания, които се случват през летният период. На 1 август 2014 г. екстремни валежи инициират не само речни приждания, но и кално-каменни потоци в по-стръмните части на по-малките долини. Един от засегнатите райони е разположен в края на Етрополският басейн, на склона южно от с. Етрополска Рибарица. Свързаните с кално-каменните потоци и наводненията ерозионни и акумулационни геоморфни форми са описани в два водосбора три месеца след събитието. Отложенията от кално-каменни потоци имат сравнително малък обем (десетки m^3) и се състоят изключително от кварцитите на Костинската свита. Теренните проучвания показват, че наличието на кватернерни отложения не е ограничено само до дъното на Етрополският басейн, но те покриват почти изцяло склоновете южно от с. Етрополска Рибарица. Матрикса на тези отложения често съдържа много глина и те играят важна роля за подхранването на кално-каменните потоци с кластичен материал. Теренните данни, докладите от очевидци, както и морфометричните данни показват, че кално-каменните потоци представляват значителна опасност за местните общности. Тези констатации потвърждават необходимостта от предприемане на мерки за превенция, както и необходимостта от по-разширено оценяване на риска от възникване на кално-каменни потоци в района на гр.Етрополе.

Ключови думи: кално-каменни потоци, наводнения, природна опасност, ГИС анализ, Кватернерни отложения

Introduction

Heavy or excessive rainfalls are common during the period May-July in Bulgaria and they often lead to flash floods. In mountainous terrains these rainfalls sometimes lead to the formation of mass movement processes known as debris flows. Debris flows are common events in mountainous areas causing losses of infrastructure and property damages. They are defined as very rapid to extremely rapid surging flow of saturated debris in steep channels (Hungr, 2005).

Debris flows events are not so prominent on the territory of Bulgaria, but they are starting to occur more often in last years and this is a result mainly of the climate. There is some data about the southern slopes of Stara Planina Mountain like Kazanlak area (Kenderova, Baltakova, 2013), near Tzurkvishte and Anton villages (Kamenov, Iliev, 1963; Iliev-Bruchev et al., 1994; Gerdjikov et al., 2012). Similar events have been described near Lozen village (Sofia region), Pirin Mountains (Baltakova et al., 2018), Rhodopes (Bruchev et al., 2001), Yamna village (Etropole area) (Dotseva et al., 2014), Asparuhovo (Varna town), and a lot similar events at the Kresna Gorge (Dobrev, Georgieva, 2010; Nikolova et al., 2018) and Struma valley (Glovnya, 1958; Kenderova, Vassilev, 1997, 2002; Kenderova et al., 2013a, b; 2014).

This paper presents a description of debris flows that affected two watersheds in the area of Etropolska Ribaritsa village as well as it provides new data about the geology and geomorphology of the area and gives hints for the existence of debris flow hazard in heavily forested and generally supply-limited watersheds in the mountainous areas in Bulgaria. It is important to note, that the area of Etropolska Ribaritsa is not the typical place where the occurrences of debris flows can be expected: the slopes above the village are forested and there

are no significant outcrops of geological units that can produce significant volume of debris.

Study area – geomorphological and geological setting

The village of Etropolska Ribaritsa is located 3 km east of the City of Etropole (Fig. 1). The area is situated on the northern slope of Stara Planina Mountain and the topography is characterised by comparatively steep hills, incised by dense network of gullies and valleys (slopes less than 43°). The village is situated in the easternmost extension of hills – enclosed flat piece of land, recently denoted as Etropole Quaternary Basin (Dotseva, 2018). In the local area, the plain is situated to the south of the prominent mountainous crest, here named Cherni Vrah Ridge. The Ridge is trending east-west and its elevation is gradually increasing eastwards from 1000 m (area of Cherni Vrah Peak) to 1350 m.

The climate in the region is moderate-continental with mean annual temperature of 10.7°C and mean annual precipitation values of 895 mm (Etropole station data). A dense forest and bushy cover are typical for the slopes, while flat areas are occupied by meadows.

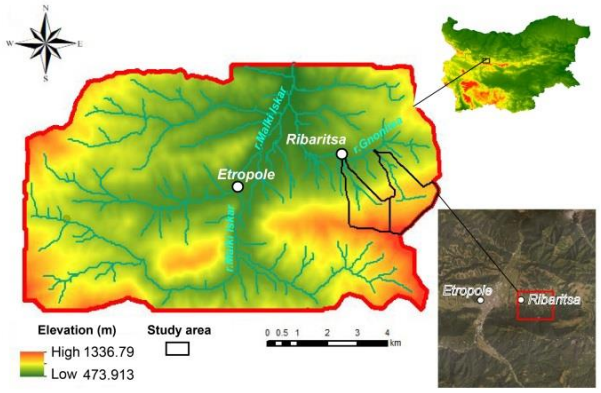

Fig. 1. Location of the studied area

The area is underlain only by Mesosoic sediments (Antonov et al., 2010), represented by Triassic limestones and dolostones, Lower Jurassic sandstones, conglomerates (Kostina Formation), Jurassic marls and sporadic limestones (Ozirovo Formation) (Fig. 2). It was recognized (Antonov, 1976) that the Triassic limestones built a prominent Alpine thrust (Etropole thrust), recently re-valuated by us (Vangelov et al., 2013). There are no data about the thickness and nature of the Quaternary slope and alluvial deposits. The crest and the upper parts of the northern slope of Cherni Vrah Ridge are built by resistant Triassic limestones and dolostones. To the north they are covered by 250 m wide in map view strip of the extremely well-lithified and strong coarse siliciclastic rocks of the Kostina Formation. The bedrock in the lower part of the northern slope is represented by dark shales, siltstones and rare claystones and limestones (Bachiishtenska Formation).

The research is focused on two watersheds situated to the south of the Etropolska Ribaritsa village. The watersheds drain into Gnoynitsa River – a right tributary of the Malki Iskar River.

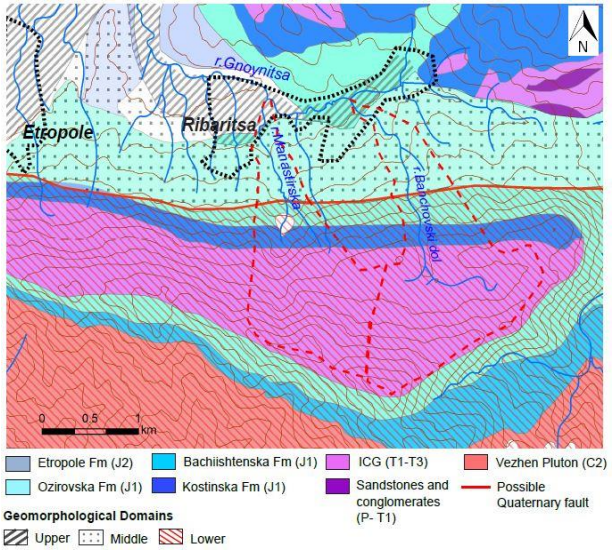

Fig. 2. Geological and geomorphological map of the studied area (after Antonov et al., 2010; modified)

The Monastery river watershed (2.64 km^2) is located to the south of Etropolska Ribaritsa village. Debris and vegetation carried by the flood formed a temporary dam at the bridge over the river channel – the result is a change in its course and formation of a new channel incised within alluvial deposits and soils. The Banchovski Dol watershed (3.46 km^2) is situated in the eastern part of the Etropolska Ribaritsa village. Debris flow deposits form elongated, parallel to the channel levee, reaching a height of up to 2 m.

Event description

The area of the town of Etropole and Etropolska Ribaritsa village was affected by heavy rainfall on the night of 31st July, 2014. The rainfall started on 31st July in the afternoon, continued for 16 hours and at 6:00 am on 1st August a state of emergency was declared in the Etropole Municipality after the report from Civil Defence.

The data from the meteorological stations located in the Elatsite Mine (5 km southwest from Etropolska Ribaritsa village) are used to assess the precipitation rate. The amount of precipitation for 1st August from 0:00 to 07:20 am was 91.7 mm. Heavy rainfalls on 28th July (67 mm) and 29th July (46.7 mm) should also be taken into consideration as the total rainfall in these three days was extremely high and led to floods and mobilisation of the material which could be involved in debris flows.

The rainfall and associated debris flows and flash-flood caused substantial infrastructure damage – main roads were closed, almost all the roads in Etropolska Ribaritsa were damaged, up to 20 homes were flooded, most of the agricultural production was destroyed and water-supplies were cut-off. Eyewitnesses talk about the presence of big boulders, rocks and mud driven by Gnoynitsa River downstream and for several cars and a truck carried away by the river.

Reconnaissance field work was carried out three months after the event. Our field data shows that the river channels produced a sediment load, estimated to tens of cubic meter volume. Much of the sediments transferred from the channels were deposited in the area before the river channels inflow into

the Gnoynitsa River, forming distinct cones and levees. The debris flow deposits consist of very poorly sorted clastic material with boulder size up to 1 m (Fig. 3).

Fig. 3. Monastery River (24.03532 E, 42.83062 N) debris flow poorly sorted deposits; looking upstream

Methodology

For the identification of the spatial distribution of debris flow hazards a number of methods are applied, such as GIS analysis and remote sensing, quantitative morphometric analysis and field studies.

Two watersheds affected by the event on 1st August, 2014 were selected for a more detailed study: Banchovksi Dol River and Monastery River (location shown on Fig. 1). For the extent and magnitude of 1st August, 2014 flash flood and the associated debris flows event data from eyewitnesses, reports, news publications and archives of Etropole Municipality were collected and analysed.

Field work included mapping of depositional and erosional features associated with debris flows as well as an attempt to delineate and characterise the origin of the Quaternary deposits that mantle the northern slope of Cherni Vrah Ridge.

A desktop study, based on a GIS, was realized, including analysis of a Digital Elevation Model (SRTM-ASTER), satellite and aerial imagery. SRTM-ASTER combined a digital elevation model with 25 m cell size and NDNR Hydrology tool in ArcGIS software were used for the extraction of the basin's boundary, flow direction, flow accumulation and drainage network and for the generation of thematic maps for Slope, Aspect and Hillshaded relief. GIS software was used also for processing and analysing the morphometric parameters of the watersheds. Some of the parameters were evaluated by mathematical equations.

Basin geometry was extracted in GIS environment. Parameters like Basin area (A) and Perimeter (P) are important factors for any watershed and influence on the hydrological conditions, run-off distance of the flows and sediment load. Basin Length (Lb) is measured by the longest path of the watershed, parallel to the mainstream (GIS derived) and was used for calculation of Form Factor and Relief Ratio. The Form Factor (Rf) (Horton, 1932) varies from 0 to the unity and represents the shape of the watershed – the higher the value of Form Factor, the more circular the shape is. The watershed shape influences the run-off distance, time and peak discharge.

Basin Relief (Melton, 1957) and Relief Ratio (Schumm, 1956; Strachler, 1958) were used for evaluation of the erosional properties and steepness of the basins. Low values of Relief Ratio indicate hard rocks and low degree of the slope, but Rh increases with the decreasing of the drainage area and the size of watersheds (Gottschalk, 1964). Elevation Relief Ratio is related with the morphometric erosional evolution of the watershed and indicates youth, mature or old stage. Melton Ruggedness Number (Melton, 1965) is a very appropriate slope index for debris flow recognition and represents the relief ruggedness within the watersheds (Melton, 1965). Drainage Intensity index reflects the erosion activity and the permeability of the soils in watersheds (Horton, 1932).

Lithology complements the overall picture, and may also be a factor for susceptibility of watersheds and debris flow forming. The bedrocks in the triggering zone were rated by their mechanical properties and their susceptibility to erosion and mobility.

Results

Analysis of DEM and its derivatives and remote sensing observations

The analysis of all available datasets (topographic maps in scale 1:5000, DEM and its derivatives as slope and various imagery data) indicates presence of three geological and geomorphological domains in the studied area (Fig. 2). They differ significantly in terms of slope dips, terrain ruggedness, small-water channels density and geometry and also in geological substrate.

The first domain (here referred as Upper domain) occupies the highest elevation in the area and is characterised by intermittent rock outcrops. Kostina quartzitic sandstones are the often forming cliffs with height up to several meters. More complicated is the landscape and the active processes at places where the Triassic carbonate rocks crop out: they can form devoid of vegetation ridges, can be completely covered by rubbles and soil and often are affected by karst processes (e.g. the area of Etropole monastery and to E-SE they are affected by large-scale karst phenomena). The lower boundary of the Upper domain is generally marked by a distinct, sharp break in slope (Fig. 2). This domain is strongly affected by erosional processes and is the main source of sediment supply for the Quaternary deposits.

The second domain (here referred to as Middle domain) occupies an intermediate position and here the slopes have dips less than 15°. Despite the general lower slope dips, the valleys and streams are comparatively deeply incised.

The third domain (here referred as Lower domain) is defined as the flat bottom of the Etropole Basin, delineated on the map on the basis of a calculated slope with dip less than 6°. Alluvial Quaternary sediments cover this flat area and river channels are unconfined (terminology of Bisson et al., 2005). Most of this area is strongly affected by anthropogenic modifications. The main active processes here are sporadic deposition along and next to the river channels (at times of extreme rainfalls) as well as fluvial reworking of older deposits.

Morphometric characteristics of the watersheds

The Monastery River and Banchovski Dol River watersheds were located at average altitude from 913 m to 961

m. Slopes between 20° and 45° are necessary to promote the initiation of debris-flows (Hungr, 2005). The mean slope in the studied watersheds is between 14.11 and 17.97 degrees.

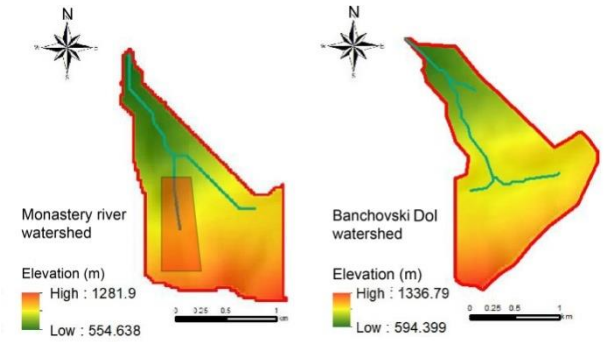

Fig. 4. Watersheds DEMs: Monastery watershed with inactive part of the stream shaded in red (left) and Banchovski Dol watershed (right)

While the Banchovski Dol Valley has a normal hydrological system, the Monastery River is strongly affected by karst processes. The upper part of the valley is completely dry and the active stream is initiated at the spring Ayazmoto, situated just next to the Monastery. Morphometric parameters of the studied watersheds were calculated and the results are presented in Table 1.

Table 1. *Morphometric parameters computed for the studied watersheds*

Basin geometry	Formula	Monastery River	Banchovski Dol
Area (A) (km^2)	GIS derived	2.64	3.46
Basin length (Lb) (km)	GIS derived	3.44	3.55
Form factor (Rf)	$Rf=A / Lb^2$ A - Watershed area; Lb - Basin length	0.22	0.27
Maximum altitude (Z) (m)	GIS derived	1281	1336
Minimum altitude (z) (m)	GIS derived	554	594
Mean altitude (Zmean) (m)	GIS derived	913	961
Maximum slope (Degrees)	GIS derived	33.12	28.96
Minimum slope (Degrees)	GIS derived	0.46	0.45
Mean slope (Degrees)	GIS derived	17.97	14.11
Basin relief (Bh) (km)	Bh=Z-z Z - max. altitude; z - min. altitude	0.72	0.74
Relief ratio (Rh) (km)	Rh=Bh / Lb Bh - Basin relief; Lb - Basin length	0.21	0.20
Elevation relief ratio (ERR)	ERR=Zmean-z /Z-z; Zmean - mean altitude; Z - max. altitude; z - min. altitude	0.49	0.49
Melton rugged-ness no (MRn)	$MRn=Bh-z/A^{0.5}$ Bh - Basin relief; z - min. altitude; A - Watershed area	0.44	0.39
Drainage intensity (DI) ($1/km^2$)	(DI = LD / A) LD - Total stream length; A - Watershed area	1.09	0.97

Basin geometry analysis shows that the Monastery River and the Banchovski Dol watersheds have small size, which is usual for debris flow occurrence – 2.64 km^2 and 3.46 km^2. The Form Factor for the two studied watersheds is 0.22 and 0.27, respectively, and shows that they have an elongated form. In terms of hydrological response, the elongated forms of the basins will provide not so fast discharge like those with circular form. According to the results for Basin Relief, Relief Ratio and Melton Ruggedness Number, the two watersheds show high susceptibility to debris flows and active erosional processes. This is also proved by the values of the Drainage Intensity index. The calculated ERR for the analysed watersheds is 0.49 which shows that they are subject to medium to high erosion processes and the relief can be classified as youthful to mature. The studied watersheds are underlain by Mesozoic quartzitic sandstones, limestones and dolostones, and Quaternary deposits, which have moderate to high susceptibility rates because of their unstable state under certain conditions (like heavy rainfall), high mobility rates and susceptibility to erosional processes.

Field studies

Field studies were conducted in the areas of the two selected watersheds. Most of the length of the lower reaches of the stream channels was investigated, as well as parts of the hill slopes. An important discovery is the presence of comparatively thick Quaternary cover, that not only occupies the bottom of the Etropole Basin, but also blankets the ridges and valley hill slopes. The bedrock is very locally represented, typically as two dimensional outcrops at the channels beds and rather sporadically on the slopes.

Four types of Quaternary deposits can be distinguished: alluvial, colluvial, mixed colluvial-alluvial and rock fall deposits. What is typical for all of these deposits is that they are built almost exclusively by clasts from the Kostina Formation. Limestone clasts are extremely rare. The lower domain is characterised by alluvial deposits where the active deposition is limited to the unconfined stream channels and occurs only in cases of heavy rainfalls. The ridges are covered by unconsolidated colluvium, with typical angular clasts reaching a size of up to 1 m. Colluvium is also typical for the upper reaches of the streams. The thickness is difficult to be estimated, most probably varies between 0 and 1–3 m. Mixed in origin colluvial-alluvial deposits are common in unconfined, first-order channels. They are represented by angular and variously rounded clasts that reach a size of up to 2–3 m. In some cases active channels or parallel to them rills cut 1–2 m deep into the sediments. The thickness is probably up to 5 m. Rock fall deposits are spatially limited to the foot of the travertine wall situated below the Etropole monastery.

The alluvial deposits, localised within the valleys in the middle domain are of special interest. All of them have typical features of debris flow deposits – presence of very large boulders, lobate surface morphology, position just next to the active river channel, formation of lateral levees. Older alluvial deposits (debris flow deposits 1 – DFD1) are everywhere incised by the active river channels. (Fig. 5).They are represented by weakly consolidated, most commonly matrix-supported breccia-conglomerates. The matrix is sandy with high clay content. Clasts are angular to sub-rounded and reach a meter in size. Morphologically DFD1 form decameter-scale

lateral levees, sometimes reaching several meters in height. The largest DFD1 is represented by an alluvial cone in the Monastery River Valley.

Younger alluvial deposits (debris flow deposits DFD2) are spatially restricted to the margins of the active river channels. Typically they are represented by lateral levees with length of about 3–10 m and height less than 1 m. It is important to note that the size of the largest boulders is gradually diminishing toward lower reaches of the valleys, thus toward the lower part of the middle domain the largest boulders are less than 1 m in diameter. Only in the valley of Monastery River our observations from 2014 event indicate presence of larger DFD2 (Fig. 6). The negative effects of the younger debris flows are marked by the road and bridge destruction – a feature observed during 2014 and 2019 field work.

Fig. 5. Banchovski Dol (24.04826 E, 42. 83359 N) with landscape representative for the Middle domain: comparatively steep valley slopes, active channel cutting bedrock as well as unconsolidated older DF deposits

Fig. 6. Debris flow deposits from the 2014 event, Monastery River (24.03532 E, 42.83062 N): conditions in July 2019 (left) and October 2014 (right)

Post-2014 debris flows/floods deposits can be distinguished on the basis of complete lack of vegetation. They have small volume (up to few cubic meters) and form meter-scale levees immediately next or even within the stream channels. Most commonly the debris are accumulated next to the channel curves, where the flooded river is attempting to make a cut-off chute (Fig. 7). Probably some of these deposits are related to the floods in the area of Etropole in 2018.

The small volume of the last years deposits as well as the presence of comparatively small clasts indicate low-magnitude events, due to the lack of stream transportation power in this low-gradient part of the valley. The presence of new depositions is indicative of the repeatability of phenomena under certain conditions and amounts of precipitation.

Within the middle domain the erosional features related to the debris flows activity are well-defined. Several forestry roads are cut by the active river channels and rather often they are incised 2–3 m deep into older alluvial deposits. The modified by debris flow erosion channels have a characteristic U-shape with flat bottom and vertical walls.

Fig. 7. Example of post-2014 deposits; meter-scale deposit situated next to the river curve, a place where during floods the river is attempting to make a cut-off chute (Eastern bank of Monastery River, 300 m above the confluence with Gnoynitsa River)

Discussion, conclusions and possible mitigation measures

Despite rather extreme climatic conditions, the 2014 event produced quite limited volume of the deposits reaching tens of cubic meters. Only in the Valley of Banchovski Dol River the flow had enough energy to bring large boulders very close to the bottom of the Etropole Basin. The magnitudes of the post-2014 events are even smaller: they are spatially limited to the stream channels or to their margins. The abundant unconsolidated older and modern alluvial deposits that mantle the valleys are the main source of debris for the modern debris flow events. It is clear that modern debris flow activity is mainly controlled by the occurrence of high-intensity rainfalls (probably exceeding 90 mm/24 h).

The area of Etropolska Ribaritsa can be regarded as a well-suited polygon for studying the processes that shaped the contemporary relief. Still, almost nothing is known about the precise age and sedimentology of the Quaternary deposits. Our study indicates that they are a very important factor with regard to providing supply for future debris flows.

An intriguing feature of the Quaternary sedimentary record is the presence of travertine rock falls. Their occurrence is spatially limited to the steep walls built by travertine and situated close to the main karst spring (Ayazmoto). The origin of these rock falls can be tentatively related to loosely dated XVIII century destructive Etropole earthquake. It can be speculated that the source of this earthquake is the well-defined lineament that follow the boundary between the defined here Upper and Middle geological-geomorphological domains. This supposition can be checked via geophysical and other studies.

In conclusion it is important to note that this contribution presents only initial report on occurrence of debris flows

unknown to this moment. Further studies on the distribution of debris flows phenomena and mapping of Quaternary sediments in the area of Etropole are needed to have a better picture about the spatial distribution of the areas threatened by the debris flow phenomena. A future analysis of the rainfall data can probably help to create a warning system, based on the amounts of precipitation. As an important mitigation measurement for the populated area of Etropolska Ribaritsa can be proposed the construction of check dams along the studied valleys.

Aknowledgments. This work has been carried out in the framework of the National Science Programme "Environmental Protection and Reduction of Risks of Adverse Events and Natural Disasters", approved by the Resolution of the Council of Ministers No 577/17.08.2018 and supported by the Ministry of Education and Science (MES) of Bulgaria (Agreement No D01-230/06.12.2018). The management of Elatzite-MED AD provided access to precipitation data from the company meteorological stations.

References

Antonov, M. 1976. Structure of the Etropole nappe. – *Rev. Bulg. Geol. Soc.*, *37*, 1, 37-47 (in Bulgarian with English abstract).

Antonov, M., S. Gerdjikov, L. Metodiev, V. Valev, Ch. Kiselinov, V. Sirakov. 2010. *Geological Map of the Republic of Bulgaria. Scale 1:50000. K-35-37-A (Glozhene) Map Sheet*. Ministry of Environment and Water, Bulgarian Geological Survey, Sofia.

Baltakova, A., V. Nikolova, R. Kenderova, N. Hristova. 2018. Analysis of debris flows by application of GIS and remote sensing: case study of western foothills of Pirin Mountain (Bulgaria). – In: *Debris Flows: Disasters, Risk, Forecast, Protection. Proc. 5th International Conference. Tbilisi, Georgia, 2018*. Publishing House "Universal", 22–32.

Bisson, P. A., D. Montgomery, J. Buffington. 2017. Valley segments, stream reaches, and channel units. – *Methods in Stream Ecology*, *1*, Academic Press, 21–47.

Bruchev, I., G. Frangov, R. Varbanov, P. Ivanov. 2001. Geological Hazards in the Western Periphery of the Rhodope Region. – *Int. Conf. "Geodynamic Hazards, Late Alpine Tectonics in the Rhodope Region",* Sofia, 17–27.

Dobrev, N., M. Georgieva. 2010. The debris flow in the northern part of Kresna Gorge: Characterisation of the source zone and material properties. – *Rev. Bulg. Geol. Soc.*, *71*, 1–3, 113–121 (in Bulgarian with English abstract).

Dotseva, Z., I. Gerdjikov, D. Vangelov. 2014. Case study of debris flows triggered by heavy rainfall – Etropole area, 2014. – In: *Proc. National Conference "Geosciences 2014"*, Bulg. Geol. Soc., Sofia, 85–86.

Dotseva, Z. 2018. *Mechanisms of formation, evolution, neotectonic and risk processes in part of extensional basins in Central Stara Planina Mountain*. PhD Thesys, Sofia University, Sofia, 273 p. (in Bulgarian)

Gerdjikov I., D. Vangelov, I. Glabadanidu. 2012. One underestimated geological hazard: the debris flows. – *Rev. Bulg. Geol. Soc.*, *73*, 1–3, 85–104 (in Bulgarian with English abstract).

Glovnya, M. 1958. Etude de geomorphologie dans la partie sud-ouest de la Rila planina – *Ann. Univ. de Sofia, Fac. biol., gèol. et gèogr.*, *60*, 3, 69–117 (in Bulgarian with French and Russian abstracts).

Gottschalk, L. C. 1964. Reservoir sedimentation. – In: Chow, V. T. (Ed.). *Handbook of Applied Hydrology*. Section 17-1, Part 1. McGraw Hill, New York, 1468 p.

Iliev-Broutchev, I. (Ed.). 1994. *Geological Hazards in Bulgaria – Map in Scale 1:500000 and explanatory text.* Bulg. Acad. Sci., Sofia, 143 p. (in Bulgarian with English abstract)

Horton, R. E. 1932. Drainage-basin characteristics. – *Trans. Am. Geophys. Union*, *13*, 350–361.

Hungr, O. 2005. Classification and terminology. – In: Jakob, M., O. Hungr (Eds). *Debris-flow Hazards and Related Phenomena.* Springer, Chichester, 739 p.

Kamenov, B., I. Iliev. 1963. Engineering geological subdivision of the Republic of Bulgaria. – *Works on the* Geology of Bulgaria, *Ser. Engineer. Geol. and Hydrogeol.*, 2, 5–123 (in Bulgarian with Russian and English abstracts).

Kenderova, R., I. Vassilev. 1997. Characteristic of the mud-flow on the 20-th September 1994 in the Zheleznitza gorge of The Struma River. – *Ann. Univ. de Sofia, 88*, Liv. 2, 29–50 (in Bulgarian with English and Russian abstracts).

Kenderova, R., G. Ratchev, A. Baltakova. 2013a. Forming and activity of debris flow in Middle Struma Valley (3–5 December 2010). – *Ann. Sofia University, 105*, *Book 2,* 15–32 (In Bulgarian with English and Russian abstracts).

Kenderova, R., A. Baltakova, G. Ratchev. 2013b. Debris flows in the Middle Struma Valley, Southwest Bulgaria. – In: Loczy, D. (Ed.). *Geomorphological Impact of Extreme Weather: Case Studies from Central and Eastern Europe*. Springer Geography, 281–297.

Kenderova, R., G. Rachev, A. Baltakova. 2014. Debris Flow in Middle Struma Valley. – *Ann. Sofia University*, *106*, *Book 2,* 13–40 (In Bulgarian with English abstract).

Melton, M. 1957. *An analysis of the relations among elements of climate, surface properties and geomorphology*. Technical Report, 11, Project NR. 389-042. Department of Geology, Columbia University, New York.

Melton, M. A. 1965. The Geomorphic and Palaeoclimatic Significance of Alluvial Deposits in Southern Arizona. – *Journal of Geology*, *73*, 1–38.

Nikolova, N., G. Rachev, R. Kenderova. 2018. Possible impact of climate and weather condition on debris flows occurrence (on the example of Kresna gorge, Bulgaria). – In: *Debris Flows: Disasters, Risk, Forecast, Protection. Proc. 5th Intern. Conf. Georgia,* Universal, Tbilisi, 166–175.

Pike, R. J., S. E. Wilson. 1971. Elevation-Relief Ratio, Hypsometric Integral and Geomorphic Area-Altitude Analysis. – *Geol. Soc. Am. Bull., 82*, 1079–1084.

Schumm, S. A. 1956. Evolution of drainage systems and slopes in badlands at Perth Amboy, New Jersey. – *Geol. Soc. Am. Bull.*, *67*, 5, 597–646.

Strahler, A. N. 1958. Quantitative Geomorphology of Drainage Basins and Channel Networks. – In: Chow, V. T. (Ed.). *Handbook of Applied Hydrology*. McGraw Hill, New York, 439–476.

Vangelov, D., Y. Gerdjikov, A. Kunov, V. Sirakov. 2013. Etropole "nappe" or back-thrust/pop-up structure, timing and mechanism of formation, C–W Bulgaria. – In: *Proc. National Conference "Geosciences 2013"*. Bulg. Geol. Soc., Sofia, 97–98.

FEATURES OF THE COMPOSITION AND THE STRUCTURE OF THE ELOV DEPOSIT NICKELIFEROUS WEATHERING CRUST (THE SEROV GROUP OF DEPOSITS, URALS)

Elena Nikolaeva[1], Irina Talovina[1], Asiia Duriagina[1], Gerhard Heide[2]

[1] Saint Petersburg Mining University, 199106 Saint Petersburg; legenda.92@mail.ru
[2] Technical University, Bergakademie Freiberg, 09599 Freiberg

ABSTRACT. The extremely complex geological structure of the Elov deposit's substrate, the large variety of source rocks that form it, the long period of development of various weathering processes occurring in different geological eras and in different climatic conditions led to the complicated structure of the weathering crust and the variety of decomposition products of source rocks, the vast majority of which have industrial concentrations of useful components. Before the discovering of the Serov group of deposits the nickel-bearing weathering crusts with similar structure were not previously known both in Russia and abroad. The purpose of this work is to investigate the mineral composition, as well as the geochemical features of the Elov deposit's rocks (Urals). The types of rocks of the Elov deposit were identified and studied, it may allow to find more search signs to the nickel and the minerals associated with it. The lateritic nickel ore deposits are widely distributed throughout the globe, so they are becoming increasingly important as a potential source of nickel.

Keywords: nickel-bearing weathering crust, Elov deposit, Urals

ОСОБЕНОСТИ НА СЪСТАВА И СТРУКТУРАТА НА СЪДЪРЖАЩАТА НИКЕЛ ИЗВЕТРЕНА КОРА НА ЕЛОВСКОТО НАХОДИЩЕ ОТ ГРУПАТА СЕРОВ (УРАЛ)

Елена Николаева[1], Ирина Таловина[1], Асия Дурягина[1], Герхард Хайде[2]

[1] Санктпетербургски минен университет, 199106 Санкт Петербург
[2] Технически университет, Бергакадемия Фрайберг, 09599 Фрайберг

РЕЗЮМЕ. Изключително сложната геоложка структура на субстрата на Еловското находище, голямото разнообразие на изходни скали, които го формират, дългият период на развитие на различни процеси на изветряне, протичащи в различни геоложки епохи и различни климатични условия, са довели до много сложна структура на изветрителната кора и огромно разнообразие от разграждащи се продукти от изходните скали, като по-голямата част от тях съдържат промишлени концентрации на полезни компоненти. Преди откриването на Серовската група от находища, изветрителна кора с подобна структура не е била известна досега както в Русия, така и в чужбина. Целта на тази работа е да се проучи минералният състав, както и геохимичните характеристики на скалите на Еловското находище (Урал). Идентифицирани и изследвани са типовете скали от Еловското находище, което позволява да бъдат открити признаци за наличието на никел и свързаните с него минерали. Латеритните находища на никелова руда са широко разпространени по целия свят, така че те стават все по-важни като потенциален източник на никел.

Ключови думи: никел-съдържаща изветрителна кора, Еловско находище, Урал

Introduction

During the last century, the nickel industry of the Urals was based on numerous supergene oxide–silicate ore deposits, which supplied raw materials to the Yuzhuralnikel and Ufaleinikel metallurgical plants, as well as Rezh and Buruktal mills. At present, new metallurgical plants are under active construction on the basis of the lateritic nickel ores of such type (>70% of the world's nickel reserves) in Australia, New Caledonia, Cuba, Indonesia, Samoa – New Guinea, Brazil, Columbia, Venezuela, and other countries. In terms of mineral composition, and, partially, geological position, the Uralian ores are similar to the Ni–bearing lateritic ores in the Earth's modern tropical belt, but they are not their complete analogues. The majority of the Uralian deposits mainly contain low–grade ores with Ni content of 0.7–1.0%. The wide compositional diversity of their ore and non – ore rock – forming minerals significantly affects the technology of nickel processing. The main Ni – carriers in the ores are Mg–silicates (serpentines, chlorites, and nontronites), with the minor contribution of iron and manganese hydroxides. The Ni content in these minerals is 1–3%, increasing in some chlorite and serpentine species to 7–12% or more. In this work, we have analysed the rock species from the Elov oxide–silicate nickel deposit.

Geology

The Serov group of nickel-cobalt ore deposits is located on the eastern slope of the Northern Urals. The main structural elements of the region are the Tagil megasynclinorium and the Verkhotursk-Verkhisetsk meganticlinorium of the Uralian orogen (Fig. 1). The megasynclinorium is represented by its eastern flank, which occupies the western part of the region, and the meganticlinorium is represented by the western flank, which covers the area which is situated to the east of the first one. The boundary between these structures passes through the Serov-Mauksk submeridional deep fault (Gottman, Pushkarev, 2009).

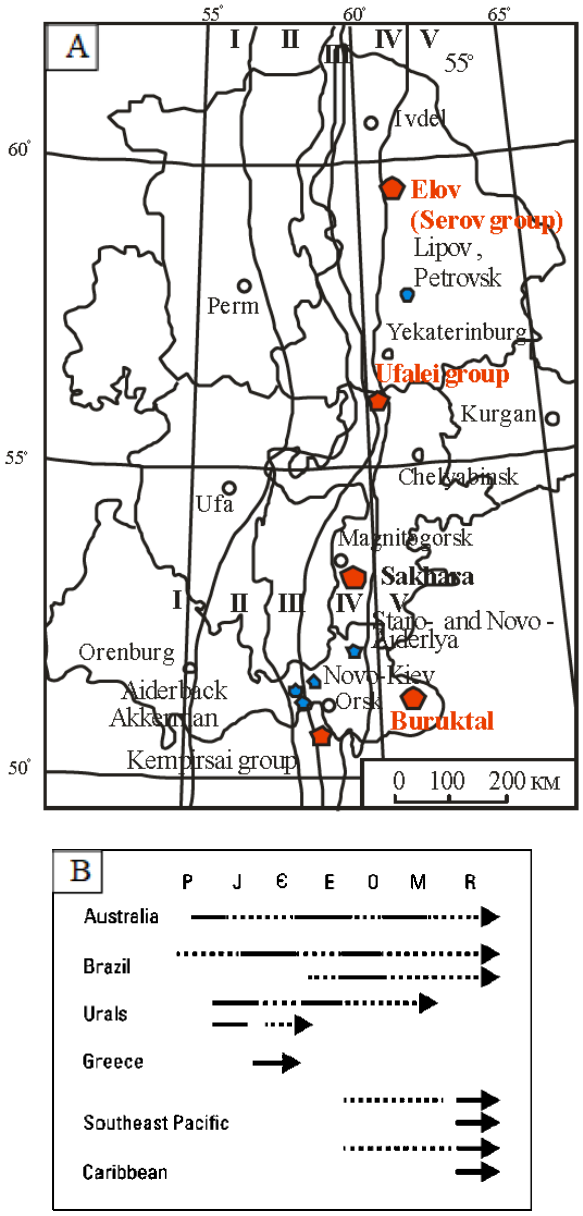

Fig. 1. (A) Main tectonic units of the central and northern Urals with the nickelhydrosilicate ore deposits (after Mikhailov, 2002) and (B) Periods of nickel laterite formation in various provinces (after Marsh et al., 2013)
Tectonic zones: *I*, the East-European platform; *II*, the Fore-Ural megazone; *III*, the Central-Ural megazone; *IV*, the Tagil-Magnitogorsk megazone; *V*, the East-Ural megazone. Main supergene nickel deposits: the Buruktal deposit, the Ufalei group (the Cheremshanka, the Sinara, the Rogozha deposits), the Serov group (the Elov deposit); *P*, Paleozoic; *J*, Jurassic; *Є*, Cretaceous; *E*, Eocene; *O*, Oligocene; *M*, Miocene; *R*, recent

The nickel ores in the Elov deposit were formed as a result of the weathering of the ultramafic rocks of the Kola massif which belongs to the Serov belt (Lazarenkov et al., 2006).

Lateritic weathering

Nickel-bearing ore mineralisation of the Elov deposit (Fig. 2) is confined to the weathering crust of ultramafic rocks of peridotite's formation which all nickel deposits of the Urals and the North Kazakhstan are related with (Bugelskiy et al., 1990; Vershinin, 1993).

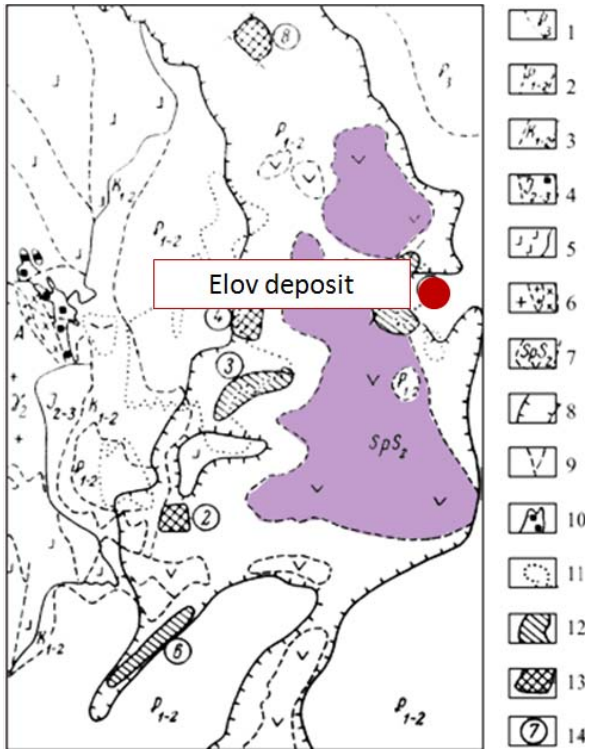

Fig. 2. Schematic geological and technological map of deposits of the Serov group (after Vershinin et al., 1988)
1–4, Meso-Cenozoic deposits of the weathering crust; *5–6*, Paleozoic formations; *7*, day stones of serpentinites; *8*, contours of serpentinites in accordance with magnetic survey and drilling; *9*, zones of tectonic dislocations; *10*, chalcopyrite-magnetite skarns; *11*, nodular-conglomerate sedimentary iron ores in the deposits of the Myssov suite; *12–14*, deposits of supergene nickel ores of various technological types: *12*, ores for alkaline hydrometallurgical process, *13*, ores for blast smelting process; *14*, numbers of deposits. The Serov group of deposits: 7, Elov; 6, Katasmin; 8, Ustey; 2–4, others

The Elov deposit (Fig. 3) contains a large number of minor intrusions in contrast with all other Urals' deposits and for the formation of the weathering crust with equivalent nickel content as in other deposits with similar composition it would be required twice the amount of nickel in the source serpentinites or double expansion of decayed and weathered serpentinites, from which fully leached nickel was redeposited in orebodies (Trescases, 1986).

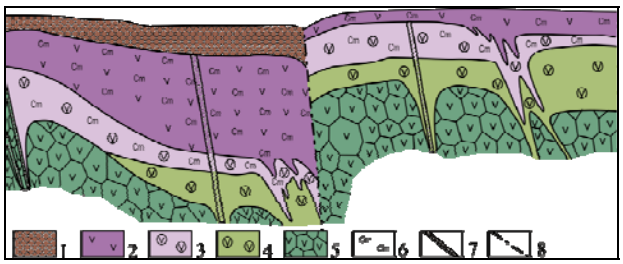

Fig. 3. Geological record of the weathering crust of the Elov deposit (after Berkhin et al., 1970)
1, nodular-conglomerate sedimentary iron ores (K_1); *2*, yellow earth; *3*, nontronited and ocherized serpentinites; *4*, leached serpentinites; *5*, disintegrated serpentinites; *6*, chamosites; *7*, chlorite vein-rock; *8*, fractures

According to calculations of the ratio of minor intrusions' height to the seam height of serpentinites in the central part of the Elov deposit, minor intrusions estimated for 40% of the total rocks thickness, sometimes in some small areas the volume of vein-shaped bodies exceeds the volume of the serpentinites (Mikhailov, 1999; 2002).

Processing

Currently, three different processes (Fig. 4) are used to extract the nickel and cobalt elements from the mined rocks. The Caron process and high-pressure-acid leaching (HPAL) are mainly used for the oxide ore subtypes. For the nickel clay deposits, the HPAL method is also used with priority, whereas for the serpentine subtypes, a pure melting method is preferred. Ongoing research is developing new extraction methods, such as the Dni-Hydrometallurgy process developed by DirectNickel, which can also process the entire laterite profile without prior separation. However, because of the complexity needed to handle and process the nickel-cobalt laterites, much research has focused on ore delineation and mineralogical identification for distinguishing rocks. Thus, it is important to characterise the mineralogy of the Elov deposit in more detail.

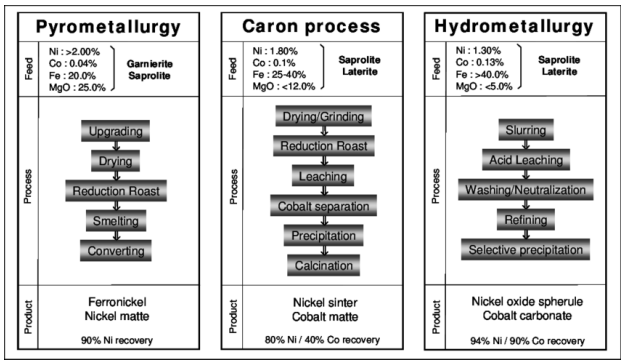

Fig. 4. Main processes for the extraction of nickel out of lateritic rocks

Materials and Methods

Samples

Nine samples were used for the investigation, which were collected during an excursion led by Prof. Dr. Irina Talovina (Saint Petersburg Mining University) and Prof. Dr. Gerhard Heide (TU Bergakademie Freiberg) in the active open pit Elov near the town of Serov in September 2014. The samples are crude ore as well as country rock that occur within the open pit area. The samples are listed in Table 1.

Analytical Methods

The mineralogical composition of the samples was determined by using x-ray diffraction phase analysis. All samples were prepared as powder preparations. The rocks were crushed with a hammer down to a grain size < 400 µm. The bulk samples were subsequently divided using quarter cross. Further crushing was done using the ball mill XRD-Mill McCrone with ZrO_2-grinding bodies. Technical ethanol (96%) was used for cooling and to guarantee careful grinding. After drying, the samples were homogenised by means of an Ardenne vibrator and finally sieved with a 200 µm sieve into an aluminum cuvette using the side-loading procedure. The measurements were executed with URD 6 (Mineralogical Laboratory, TU Bergakademie Freiberg) with Co-radiation.

Table 1. *The investigated samples with nickel content, %.*

Sample	Name	Ni
SV 02	Porphyritic serpentinite	0.117
SV 04	Chromite ore	0.056
SV 06	Talc-chlorite-schist	0.542
SV 07	Limonite ore	1.160
SV 08	Gangue rock	0.199
SV 09	Contact-zone of SV08	0.163
SV 10-1	Silicate nickel ore	0.101
SV 10-2	Silicate nickel ore	0.979
SV 11	Oxide nickel ore	1.030

To investigate the swelling capable minerals which show mainly wide reflexes in the 14 Å area, texture preparations were produced in the traditional way. The selected samples were first measured in an air-dried state, afterwards they were saturated in ethylene glycol vapour and then measured again. The ethylene glycol accumulates in the interlayers of the minerals and causes a widening of the structure, thereby increases the layer distance. After the second measurement, all texture preparations were annealed at 400°C and measured again. The last measurement was executed after an annealing process at 550°C.

Thermal analyses were carried out in the Mineralogical Laboratory of the TU Bergakademie Freiberg (Dipl.-Chem. Margitta Hengst). All measurements were realized by means of the STA 409 PC, and a heating rate of 10 Kelvin per minute, up to a maximum temperature of 1200°C. Purified air was used as a carrier gas for all analyses. The reference material for the DTA analyses was corundum (Földvari, 2011).

The observations on the scanning electron microscope (SEM) were mainly examined on polished thin sections of the solid rocks. Individual measurements were also carried out on strewn slides. For the investigations it was possible to use the CarryScope JCM-5700 from the "Terra Mineralia Freiberg" museum. This SEM is equipped with a Bruker EDX (133eV). The focus of this analytical method was the determination of the spinel group minerals. Further questions arose with regard to the distribution of the various valuable elements inside the rock units, primarily nickel. As far as possible, this method allowed the investigation of the local coupling of nickel to the various minerals.

Results

The chemical analyses show a significant accumulation of nickel in various rocks of the open pit. Most of the silicate dominated areas of the deposit contain higher nickel concentrations, however, they are not high enough to reach economic relevance. The rocks display nickel contents between 0.101% and 0.542%. An exception is the major amount of silicate nickel ore (SV 10-2), which at 0.979% shows significantly increased nickel contents of economic importance. It is note-worthy that only the unaltered areas of the silicate nickel ore have significantly elevated contents, while the

secondary silicified zone has only a very low nickel content of 0.101%. Since the biggest difference is found in the mineral composition, in this case the increased content of serpentine and especially smectite in the non-silicified areas, the nickel must be linked to exactly these minerals. It can be assumed that these are typical nickel-containing nontronites (Brindley et al., 1973; Brindley, 1984a, b).

The highest nickel contents were detected in the oxidic type nickel ore of SV 11 (1.03%) and in the limonite ore of SV 07 (1.16%). Thus, these areas are most enriched when considering the absolute contents. As far as the limonite ore is concerned, it can be assumed that the nickel is primarily coupled to nickel-rich goethite and very occasionally to nickel sulphides. The rock contains neither smectite nor talc, and the serpentine branch veins (apophysis) in which EDX analyses did not show any major nickel content, are the result of later secondary formation. According to the elevated position of the dehydroxilation peak, the thermal analyses of goethite indicate a significant foreign metal substitution, further substantiating the thesis of nickel-rich goethite (Talovina et al., 2008; 2010; 2011; 2012; Talovina, 2012a; 2012b). Although nickel sulphides have been detected in the limonite ore, their absolute contents are negligible compared to the substitutional placement in the goethite structure. This is corroborated by the missing peaks in the powder diffraction pattern as well as by the low sulphur content of the sample. It merely amounts to 0.10% sulphur content compared to the 1.16% nickel content. In the oxidic type nickel ore (SV 11), the nickel carrier cannot be reliably determined. However, enrichment in the silicate components seems to be plausible, especially in chlorite and smectite as well as in goethite, which also has increased *d* values. Also in this particular rock the serpentines showed no relevant nickel content throughout the EDX measurements.

Conclusion

The Serov group of deposits is one of the sedimentary-infiltration formations. The Orsk-Khalilovsk, Aydyrlinsk and other deposits, except the Elov deposit, belong to this kind of formations in the Urals. In this type a significant role belongs to the nickel-containing ore-forming ferruginous chlorite, i.e. shamosite $(Fe_5Al)(AlSi_3O_{10})(OH)_8$. The deposits of this type had experienced a rather complex history of formation, including the stage of epigenesis (destruction, transportation and deposition with the formation of ferrous sedimentary rocks) in addition to the lateritogenesis stage (cf. Yudovich et al., 2011).

The vertical zonal profile in the nickel weathering crust of the Elov deposit is observed (from the bottom up): serpentinised ultramafics (substrate)–serpentinite zone–nontronite zone–oxide-iron zone. Separately, it is worth noting the shamosite zone, which belongs to the converted part of the weathering crust of the Elov deposit, has a limited distribution and replaces serpentinite, nontronite and oxide-iron zones partially or completely.

The research displays a very diverse mineralogy in the rocks of the Elov deposit. It was shown that different types of rocks from variously weathered areas of the deposit have relevant nickel contents. Due to the different mineralogy of the nickel-bearing minerals between laterite and saprolite, both a selective mining and a selective processing of the individual types of ore should be considered.

References

Berkhin, S. I., K. G. Borodina, Y. Yu. Bugelsky, I. V. Vitovskaya, G. N. Kiselev, E. N. Kuzemkina, K. K. Nikitin, A. P. Sigov, L. S. Shakina, I. I. Edelstein, A. L. Yanitsky. 1970. *Nickel-bearing Weathering Crust of the Urals.* Nauka, Moscow, 286 p. (in Russian)

Brindley, G. W. 1984a. Chemical composition of berthierines – a review. – *Clays and Clay Minerals*, *30*, 2, 153–155.

Brindley, G. W. 1984b. *Crystal Structures of Clay Minerals and their X-ray Identification*. Mineralogical Society, London, 195 p.

Brindley, G. W., P. T. Hang. 1973. The nature of garnierites-1 structures, chemical composition and color characteristics. – *Clays and Clay Minerals*, *21*, 2, 27–40.

Bugelskiy, J. J., I. V. Vitovskaya, A. P. Nikitina. 1990. *Ekzogennye rudoobrazujushhie sistemy kor vyvetrivanija (Exogenic Ore-forming Systems of Weathering Crusts)*. Nauka, Moscow, 365 p. (in Russian)

Földvari, M. 2011. Handbook of thermogravimetric system of minerals and its use in geological practice. – *Occasional Papers of the Geological Institute of Hungary*, *2*, 1–180.

Gottman, I. A., E. V. Pushkarev. 2009. Geologicheskie dannye o magmaticheskoi prirode gornblenditov v gabbroul'tramafitovyh kompleksah Uralo-Alyaskinskogo tipa (Geological data on the magma nature of hornblendites in gabbroultramafic complexes of the Ural-Alaskan type). – *Litosfera*, *2*, 78–86 (in Russian).

Lazarenkov, V. G., I. V. Talovina, I. N. Beloglazov, V. I. Volodin. 2006. *Platinovye metally v gipergennyh nikelevyh mestorozhdenijah i perspektivy ih promyshlennogo izvlechenija (Platinum metals in supergene nickel deposits and prospects for their commercial extraction).* Nedra, St Petersburg, 188 p. (in Russian)

Marsh, E., E. Anderson, F. Gray. 2013. Nickel-cobalt laterites – a deposit model: Chapter H in *Mineral Deposit Models for Resource Assessment. – Scientific Investigations Report 2010–5070-H*. USGS, Reston, 38 p.

Mikhailov, B. M. 1999. Nickel ores in the Urals. – *Lithology and Mineral Resources*, *35*, 4, 351–364.

Mikhailov, B. M. 2002. Perspective of mineral base of nickel industry in Urals. – *Regionalnaya Geologiya i Metallogeniya*, *15*, 97–109 (in Russian).

Talovina, I. V. 2012a. *Geochemistry of Supergene Nickel Deposits of the Urals*. PhD Thesis, St. Petersburg, 270 p. (in Russian)

Talovina, I. V. 2012b. *Geohimija uralskih oksidno-silikatnyh nikelevyh mestorozhdenij (Geochemistry of the Ural Oxide-silicate Nickel Deposits)*. Natsionalnyi mineralno-syrevoi universitet “Gornyi”, St. Petersburg, 270 p. (in Russian)

Talovina, I. V., G. Heide. 2016. Serpentines of chrysotile-pecoraite series as genesis indicators of nickel deposits in the Urals weathering crusts. – *Journal of Mining Institute, 221,* 629–637.

Talovina, I. V., V. G. Lazarenkov, S. O. Ryzhkova, V. L. Ugolkov, N. I. Vorontsova. 2008. Garnierite in nickel deposits of the Urals. – *St. Petersburg State Mining Institute (Technical University), Lithology and Mineral Resources*, *43*, 6, 588–595.

Talovina, I. V., N. I. Vorontsova, S. O. Ryzhkova O. P. Mezentseva, A. G. Pilugin. 2012. Harakter raspredelenija redkozemel'nyh jelementov v rudah Elovskogo i Buruktalskogo gipergennyh nikelevyh mestorozhdenij

(Pattern of rare earth element distribution in ores of the Elov and Buruktal supergene nickel deposits). – *Zapiski Gornogo Instituta*, *196*, 31–35 (in Russian).

Talovina, I. V., V. G. Lazarenkov, N. I. Vorontsova, O. P. Mezentseva, S. O. Ryjkova, A. G. Pilugin. 2010. *Geochemistry of impurity elements in Buruktal supergene nickel deposit, South Urals.* – In: *Freiberg – St. Petersburger interdisziplinares Kolloquium junger Wissenschaftler.* Technische Universitat Bergakademie Freiberg, 40–43.

Talovina, I. V., V. G. Lazarenkov, U. Kempe, M. Tichomirowa, N. I. Vorontsova, A. G. Pilugin. 2011. Value in millerite and genesys of chamosite nickel ores in the Elov supergene deposit (Serov Group), North Urals. – In: *Scientific Reports on Resource Issues. Vol. 1. Latest Developments in Mineral Industry – Geology, Mining, Metallurgy and Management.* Technische Universitat Bergakademie Freiberg, 30–34.

Trescases, J. J. 1986. *Nickeliferous laterites: a review on the contributions of the last ten years. – Memoirs Geol. Surv. India, 120*, 52–62.

Vershinin, A. S. 1993. *Geology, Prospecting and Investigation of Supergene Nickel Deposits*. Nedra, Moscow, 302 p. (in Russian)

Vershinin, A. S., I. V. Vitovskaya, I. I. Edelstein, G. D. Varenya. 1988. *Technological Mineralogy of Nickel Supergene Ores*. Nauka, Leningrad (St. Petersburg), 274 p. (in Russian)

Yudovich, Y. E., M. P. Ketris. 2011. *Geochemical Indicators of Lithogenesis (Lithological Geochemistry)*. Geoprint, Syktyvkar, 742 p. (in Russian)

PETROLOGICAL STUDY OF METASOMATIC ALTERED GRANITOIDS FROM KANARATA DEPOSIT, SAKAR MOUNTAIN, SOUTHEASTERN BULGARIA

Stefka Pristavova[1], Nikoleta Tzankova[1], Nikolay Gospodinov, Petyo Filipov[2]

[1] University of Mining and Geology "St. Ivan Rilski", 1700 Sofia; stprist@mgu.bg
[2] Geological Institute, Bulgarian Academy of Sciences, 1113, Sofia; p_philipov@geology.bas.bg

ABSTRACT. The present article is a result of the study of the altered granitoid rocks cropping out in the north-eastern periphery of the Sakar batholith. The investigated rocks are enriched by amphibolite xenoliths and additionally, they are intensively metasomatically altered. The mineral composition of the studied rocks is presented by minerals of the amphibole group (Ca-Mg hornblende and barroisite), plagioclase (albite), quartz, K-feldspar (single grains), titanite, rutile, apatite, and zircon. The typical magmatic textures in the rocks are missing. The albite druses developed in the caverns represent intensively metasomatically re-worked amphibolite xenoliths, rutile, titanite, barroisite and apatite mineralisations that are genetically related to the process of Na-alteration. The dated U-Pb zircon population in the metasomatically altered granitoids shows igneous origin and the obtained data confirm the early Paleozoic age of the Sakar batholith.

Keywords: Sakar batholith, altered granitoid rocks, Na-metasomatites, albite druses

ПЕТРОЛОЖКО ИЗСЛЕДВАНЕ НА МЕТАСОМАТИЧНО ПРОМЕНЕНИ ГРАНИТОИДИ ОТ НАХОДИЩЕ КАНАРАТА, САКАР, ЮГОИЗТОЧНА БЪЛГАРИЯ

Стефка Приставова[1], Николета Цанкова[1], Николай Господинов, Петьо Филипов[2]

[1] Минно-геоложки университет "Св. Иван Рилски", 1700 София
[2] Геологически институт, Българска академия на науките, 1113 София

РЕЗЮМЕ. В тази статия са представени резултатите от изследването на променени гранитоиди, разкриващи се в североизточната периферия на Сакарския батолит. Изследваните скали са набогатени на амфиболитови ксенолити и допълнително са метасоматично променени с формиране на Na-метасоматити. Минералният състав на изследваните скали е представен от минерали от амфиболовата група (Ca-Mg амфибол и бароисит), плагиоклаз (албит), кварц, К-фелдшпат (единични зърна), титанит, рутил, апатит и циркон. Изследваните албитови друзи в каверните, съдържащи титанит, рутил, бароазит, апатит, представляват метасоматично променени амфиболитови ксенолити. Датираните цирконите са с магматичен генезис и получените данни потвърждават раннопалеозойската възраст на Сакарския батолит.

Ключови думи: Сакарски батолит, променени гранитоиди, Na-метасоматити, албитови друзи

Introduction

The Sakar granite batholith is well investigated during the years and a lot of information related to the mineralogy, petrology, structure features and geochemical specialisation has been published (Kamenov et al., 2010 and references therein). The accumulated data give us a relatively clear picture about the rocks in the batholith. The granites are emplaced into high-grade metamorphic frame represented by gneisses, gneiss-schists, amphibolites, meta-ultrabasites. These metamorphites are referred to the Prerhodopian Supergroup, Botourche Group – Zhalti Chal and Punovo Formations (according to Kozhoukharov et al., 1994) or to the late Paleozoic to early Mesozoic volcanic-sedimentary complex metamorphosed during Late Alpine together with the emplacement of the batholith (Ivanov et al., 2001; Gerdjikov, 2005). The following granite units are distinguished in the batholith: equigranular in the inner parts, porphyroid with large microcline megacrysts in the outer parts, and aplitoid-pegmatoides (Aleksandrovo type) in the north-eastern periphery. The presence of xenoliths from the hosted gneisses and amphibolites in the marginal parts of the batholith is a very common characteristic. The distinguished modal petrographic species are quartz-monzodiorite, quartz-monzonite, granodiorite and granite (Kamenov et al., 2010).

According to the geological setting the age of Sakar batholith is determined as early Palaeozoic – the pieces of granites are included in the Permian (?) and Early Triassic conglomerates (Savov, 1988; Chatalov, 1990) or Late Jurassic–Early Cretaceous (Ivanov et al., 2001). The ages of 320±18 Ma (Zagorchev et al., 1989), 499±70 Ma (Lilov, 1990), and 250±35 Ma (Skenderov et al., 1986) are published according to Rb/Sr radioisotope ratio. Dated zircons (U-Pb) show the early Palaeozoic age of magmatic crystallisation – 300 Ma (Peycheva et al., 2016) and 295–296 Ma (Bonev et al., 2017).

The present study is focused on the rock outcrops from the north and north-eastern periphery of the Sakar batholith in the Kanarata deposit, north of the village of Hlyabovo (Fig. 1). These granites are enriched by the amphibolite xenoliths from the hosted metamorphic frame and they are affected by an intensive process of Na-metasomatic alteration – albitization. The process of irregular albitization was mentioned in the previous studies as a local, not dated process (for example

south of the village of Orlov Dol) and it was supposed that its time is later than the crystallisation of the batholith, maybe post-Triassic (Kamenov et al., 2010).

The relevance of this study is due to insufficient published data about the mineralogy and geochemistry of these metasomatic altered granites and some minerals into them which represent valuable gemological samples. On the other hand, this natural raw material which is characterised by uniqueness, exhaustiveness and non-recoverability is extracted for feldspar material during the years which necessitate its timely study.

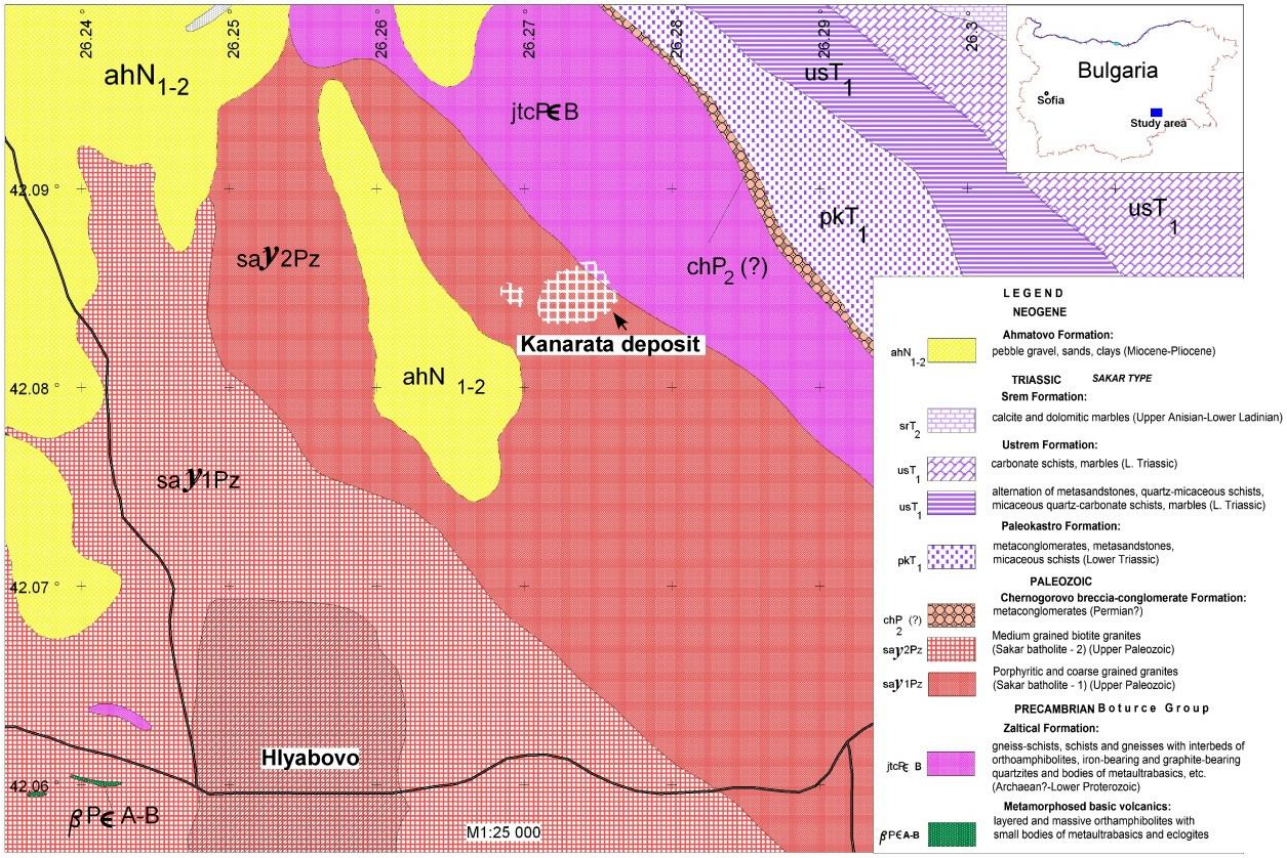

Fig. 1. Geological map of the studied area (after Kozhoukharov at al., 1994, with additional data)

Geological setting

The studied rocks are referred to the so-called Aleksandrovo type aplitod-pegmatoid granites. They outcrop close to the contact of the Sakar batholith with the metamorphic frame as elongated bodies and veins with east-western direction (Fig. 1). Minerals such as titanite, rutile, fibrous type amphibole, tourmaline, albite, epidote, molybdenite and etc. are established in these veins (Kozhoukharov et al., 1994).

In the frame of the Kanarata deposit intensively altered granitoids are revealed – leuco- to mesocratic medium grained with massive structure, fragile, strongly weathering. These rocks are enriched by lenses amphibolite xenoliths with sizes from 0.6 to 2.0 m. The boundaries with the hosted granites are intensively erased (Fig. 2a). Most of xenoliths are eroded and they are observed as caverns filled up by albite druses and minerals as rutile, titanite, apatite, minerals of amphibole group, chlorite, talc. (Fig. 2b).

Well-visible linear zones with variable thickness (from 5–20 cm up to 50–120 cm) are presented in the deposit. Along these zones, the rocks are altered and re-worked into whitish fine-to medium-grained varieties. The contacts are sharp ones with a segregated accumulation of whitish component along them (Fig. 2c).

The dykes and quartz veins are observed among granitoids, also. The dykes are with thickness of up to 45–50 cm, light to dark grey in colour, fine porphyry with massive structure. Along dyke's contacts chlorite-talc (?) aggregates are formed (Fig. 2d). Grey to whitish quartz veins (thickness up to 20–35 cm) are observed in the frame of the deposit and some of them contain big crystals of rutile and molybdenite (Fig. 2e).

Materials and methods

The study material was selected from several places in the Kanarata deposit – granitoids, assimilated amphibolite xenoliths into them, zones with albitization and dykes.

The samples were optically studied using Stereo-microscope OLYMPUS and Leitz polarised microscope with Camera OLYMPUS S52 (for thin sections).

The chemical composition of the mineral was determined by Scanning Electron Microscopy fitted with Energy Dispersive Spectrometer (SEM-EDS) and Electron Microprobe Analyses.

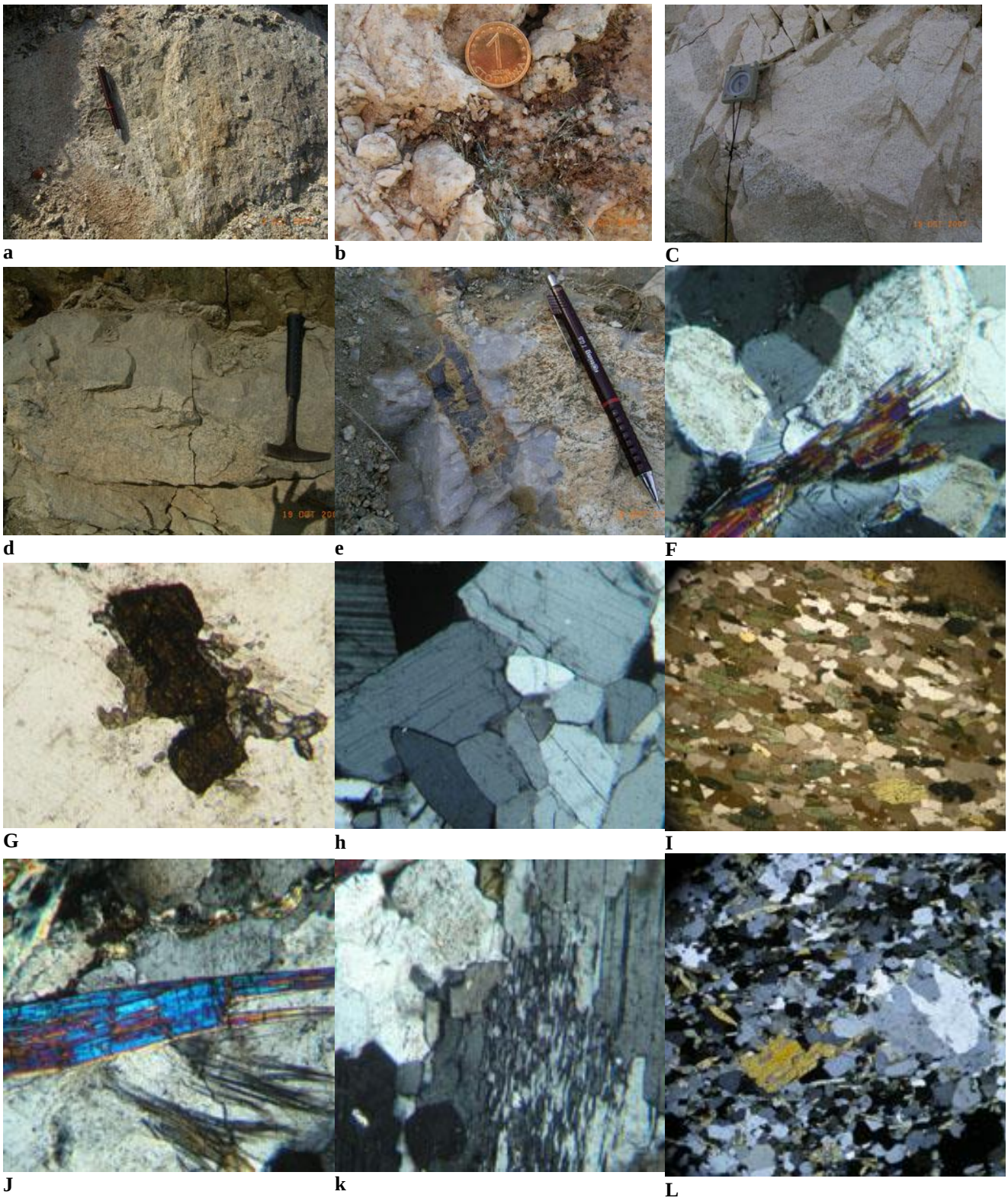

Fig. 2. Macro- and microphotos of studied rocks: *a*, amphibolite xenolith among granitoids; *b*, cavern filled up with albite and needles of amphibole mineral; *c*, linear zone of albitization; *d*, dyke among granitoids; *e*, quartz vein with molybdenite; *f*, amphibole crystal among plagioclase. CPL, Ob. F. W. = 1225 μm; *g*, rutile with "corona-like" of titanite, PPL, Ob. F. W. = 1225 μm; *h*, albite zone. CPL, Ob. F. W. = 1225 μm; *i*, general view of preserved amphibolite xenolith. CPL, Ob. F. W. = 1900 μm; *j*, barroisite crystals among albite. CPL, Ob. F. W. = 1225 μm; *k*, albite with with chest-board structure. CPL, Ob. F. W. = 1225 μm; *l*, general view of dike with porphyry crystals of amphibole and plagioclase. CPL, Ob. F. W. = 3900 μm

The analyses were performed on the representative samples using a JEOL at Eurotest-Control OOD. The chemical composition of the rocks was determined using AES ICP in the Laboratory of Geochemistry at the University of Mining and Geology "St. Ivan Rilski" and ICP-MS at the "AcmeLabs", Canada for the REE and trace elements.

A single sample of the albitized zone has been dated using U-Pb zircon geochronology. A total of 16 analyses were obtained on either autocrystic or antecrystic zircons and performed on New Wave UP193FX LA coupled to Perkin Elmer ELAN DRC-e quadrupole ICP-MS at the Geological Institute of the Bulgarian Academy of Sciences.

Results

Mineral and petrographic characteristics

The studied "granitoids" from the Kanarata deposit are represented by irregularly to regularly grained rocks with mineral composition of plagioclase, minerals of the amphibole group, quartz, sporadic grains of K-feldspar, titanite, rutile, apatite, zircon and imposed secondaries of sericite, epidote group minerals, chlorite.

Amphibole (up to 15–20%) – irregularly represented as long prismatic crystals with sizes of 1.8 mm along the long axis or small (up to 0.2–0.4 mm) grains segregated into aggregates. The crystals are light greenish with traces of re-crystallisation with the formation of long prismatic crystals along periphery contours (Fig. 2f). The chemical composition, according to Leake et al. (1997), is determined as Ca-Mg hornblende (Table 1).

Plagioclase (up to 70–75%) – short prismatic crystals in sizes from 0.5 to 2.0 mm. It is presented by two generations, at least: 1) crystals with zonal structure (turbid central part with fine flaked sericite and epidote aggregates and clear periphery); 2) clear crystals some of them with chess-board structure. The An-content in plagioclase vary from 2.6 to 0.79 (Table 2).

Quartz (up to 5%) is irregularly presented in shape grains in limited quantity.

Table 1. *Chemical composition of amphiboles*

	1	2	3	4	5	6	7	8
SiO_2	54.74	55.77	56.48	51.38	56.81	55.03	55.41	47.95
TiO_2	0.06	0.08	0.00	0.12	0.00	0.08	0.08	0.21
Al_2O_3	3.42	3.06	2.78	4.89	1.56	3.85	3.77	9.03
FeO	3.66	3.59	3.69	7.00	6.18	4.13	4.02	10.09
MnO	0.21	0.12	0.00	0.07	0.00	0.00	0.22	0.27
MgO	23.99	24.49	24.30	22.05	23.70	24.46	24.85	18.56
CaO	11.00	10.75	11.12	9.81	10.80	9.98	10.39	10.98
Na_2O	0.86	0.00	0.00	2.15	0.00	1.16	0.00	1.46
K_2O	0.00	0.00	0.00	0.00	0.04	0.04	0.00	0.22
∑	97.94	97.86	98.37	97.47	99.09	98.73	98.74	98.77
	Numbers of ions on the basis of 23 O							
Si	7.275	7.320	7.411	6.956	7.449	7.187	7.167	6.556
Al^{4+}	0.536	0.473	0.430	0.780	0.241	0.593	0.575	1.444
Al^{3+}	0.000	0.000	0.000	0.000	0.000	0.000	0.000	0.011
Fe^{3+}	0.407	0.394	0.405	0.792	0.678	0.451	0.435	1.154
Ti	0.006	0.008	0.000	0.012	0.000	0.008	0.008	0.022
Fe^{2+}	0.000	0.000	0.000	0.000	0.000	0.000	0.000	0.000
Mn	0.024	0.013	0.000	0.008	0.000	0.000	0.024	0.031
Mg	4.753	4.792	4.754	4.451	4.633	4.762	4.792	3.783
Ca	1.566	1.512	1.563	1.423	1.517	1.396	1.440	1.608
Na	0.222	0.000	0.000	0.564	0.000	0.294	0.000	0.387
K	0.000	0.000	0.000	0.000	0.007	0.007	0.000	0.038
∑	14.788	14.512	14.563	14.987	14.524	14.697	14.440	15.034
	Ca-Mg hornblende	Ca-Mg hornblende	Ca-Mg hornblende	Barroisite Na-Ca amph	Ca-Mg hornblende	Barroisite Na-Ca amph	Barroisite Na-Ca amph	Ca-Mg hornblende

1–3, altered granitoids; *4, 5*, amphibolite xenoliths; *6, 7*, albite druses; *8*, dyke

Table 2. *Chemical composition of plagioclases*

	1	2	3	4	5	6	7
SiO_2	66.89	66.11	66.55	66.9	66.31	63.28	62.48
Al_2O_3	19.44	19.85	20.11	19.86	20.39	22.22	23.25
FeO	0.00	0.00	0.00	0.00	0.11	0.06	0.09
CaO	0.19	0.50	0.62	0.12	0.05	3.05	3.26
Na_2O	13.12	12.85	12.90	12.98	11.73	9.73	9.90
K2O	0.00	0.00	0.00	0.00	0.00	0.09	0.04
∑	99.64	99.31	100.18	99.86	98.590	98.43	99.02
Numbers of ions on the basis of 32/O/							
Si	11.822	11.733	11.713	11.787	11.777	11.335	11.154
Al	4.049	4.152	4.171	4.124	4.268	4.691	4.892
Fe^{2+}	0.000	0.000	0.000	0.000	0.016	0.009	0.013
Ca	0.036	0.095	0.117	0.023	0.010	0.585	0.623
Na	4.495	4.421	4.402	4.434	4.039	3.379	3.426
K	0.000	0.000	0.000	0.000	0.000	0.021	0.009
∑	20.402	20.402	20.403	20.368	20.109	20.019	20.118
Mol. per cent of An, Ab and Or							
An	0.79	2.10	2.59	0.51	0.23	14.69	15.36
Ab	99.21	97.90	97.41	99.49	99.77	84.80	84.41
Or	0.00	0.00	0.00	0.00	0.00	0.52	0.22

1, 2, altered granitoids; *3*, amphibolite xenoliths; *4, 5*, albite druses; *6, 7*, dyke

Rutile – well rounded in shape crystals with sizes up to 0.1–0.2 mm grouped into aggregates. Around crystals, a thin "corona-like" structure of titanite is formed (Fig. 2g). The well-formed individual crystals of titanite are also presented. The rocks are enriched by the accessories apatite and zircon.

This mineral composition of the studied rocks is a result of the process of transformation of amphibolite xenoliths into "amphibole gneisses" during their granitisation and the imposed process of albitization. The typical magmatic textures are preserved only in limited places. The linear zones with processes of albitization have the same mineral composition where plagioclase (albite) build up more than 80% of the rock's volume forming hetero-hypidiomorphic texture (Fig. 2h).

The preserved amphibolite xenoliths are rarely observed. They are presented as fine crystalline rocks with well-expressed metamorphic foliation a clear boundary with the hosted granitoids (Fig. 2i) and mineral composition of minerals of amphibole group, plagioclase, quartz, sporadic grains of K-feldspar, titanite, rutile, apatite, zircon and imposed secondaries of sericite, epidote group minerals, chlorite and talc-serpentine(?) minerals. More frequently the xenoliths are totally affected by granitisation and imposed albitization and they are observed as caverns filled up by albite, amphibole group minerals, titanite, chlorite, and apatite. The amphibole mineral, here, is presented by dark greenish prismatic crystals (0.2–0.6 mm) with strong sub-parallel orientation and is regularly disseminated in the rock. It is presented by Ca-Mg hornblende and barroisite (Table 1). The last one is observed into albite caverns where it forms needle crystals with length of up to 10 mm (Fig. 2j) and chemical zoning expressed with decrease of Mg and increase of Na content from the centre to the periphery.

Plagioclase (up to 60%) is observed as isometric in shape albite grains with sizes of up to 0.2–0.4 mm. The grains are clear without of lamellar structure. In the caverns the plagioclase crystals are with sizes of up to 3.0 mm with chest-board structure (Fig. 2k) and An-member in the limit of 2.51–0.23 (Table 2). In the druses the albite crystals are up to 10.1–10.2 mm long with thickness of up to 6–7 mm. Their habit is represented by {001}, {010}, {110} and {201}. Some of the crystals are elongated parallel to the *a*-axis, with domination of {001} and {010}. The rest of the crystals are with platy shapes developed parallel to (010). There have been reports of crystal twins on albite law {010}. The albite crystals are white to colourless at the edges.

The caverns with albite are enriched by minerals as: apatite – long prismatic crystals (Dencheva, 2017), some intensively cracked or as clear fine needles; chlorite; rutile; titanite as clear and well-formed crystals.

Dykes are fine porphyry on plagioclase and amphibole rocks (Fig. 2l). The rock-forming minerals show weak sub-parallel orientation to the dyke's contacts. The amphibole is presented by Ca-Mg hornblende and the plagioclase by irregularly in shape spotted oligoclase crystals (Tables 1, 2). The specific feature of the dykes is the presence of rutile-titanite mineralisation reaching up to 5% of the rock's volume.

Petrochemical particularities

The published petrochemical data about the rocks of the Sakar batholith give us information about the calc-alkaline character and mixed plate margin orogenic and volcanic-arc with presence of mantle component in the magma source and crustal contamination (Kamenov et al., 2010; Bonev et al., 2017). The obtained chemical composition of the selected samples (Table 3) show the significant differences (see Kamenov et al., 2010) and they could be summarised in the following way: 1 – the studied rock samples are with lower contents of Fe_2O_3, CaO and K_2O and twice increased contents

of Na_2O and MgO; 2 – the lithophile elements as Rb, Ba, Cs and PEE are with lower contents; 3 – the contents of U and Th are higher (with the exception of sample 1). The processes of assimilation of amphibolite xenoliths and imposed Na-alteration (albitization) in the studied rocks are the main reasons for the mineral and chemical differences with the published data about granitoids from the Sakar batholith.

The significant differences of the chemical composition between rock affected by varying intensity of process of Na-alteration (whole rock and linear zone with intensive albitization) could also be found in the Kanarata deposit. For illustration of this process, the balance of components (after the oxide method of Barth) has been made of two samples (Table 4, 3–4). The variation of the main oxides is shown in Figure 3.

Table 3. *Chemical composition of the selected samples from studied rocks*

	1	2	3	4	5	6	7
SiO_2	62.85	65.38	65.39	67.28	57.24	68.17	56.19
TiO_2	0.64	0.9	0.85	0.08	1.97	1.09	1.05
Al_2O_3	18.43	17.23	18.56	19.81	15.01	15.33	16.86
Fe_2O_3	1.39	0.69	0.58	0.13	7.05	2.32	4.99
MnO	0.02	0.02	0.01	< 0.01	0.04	0.03	0.07
MgO	3.31	2.62	1.8	0.19	3.92	1.9	5.8
CaO	3.07	2.23	1.74	0.95	7.33	2.76	7.09
Na_2O	8.43	9.22	9.5	10.35	5.51	7.18	6.05
K_2O	0.39	0.33	0.29	0.31	0.37	0.34	0.38
Ba	31	8	14	8	13	22	26
Be	11	3	6	5	6	6	8
Cs	<0.1	<0.1	<0.1	<0.1	<0.1	<0.1	<0.1
Rb	3.5	0.1	0.8	0.5	1.2	1.3	1.5
Sr	436.3	109.9	219.6	202.6	383.2	200.6	621.5
Co	3.6	1.9	2.1	0.5	6.4	5.7	12.5
Hf	5	7	5.7	3.2	10.4	7.7	5.1
Nb	14	17.6	37.3	15.8	12.8	16.4	14.2
Ta	1.3	1.8	3.5	3.8	0.9	1.9	0.7
V	62	76	46	12	280	118	198
W	<0.5	1.3	1.4	<0.5	0.5	3.7	<0.5
Zr	157.6	232.5	190.3	45.7	390.6	232.6	168
Y	17	20.5	14.4	3	65.9	18.6	28.3
La	150.5	21.5	23.1	5.5	27.9	17.8	30.4
Mo	<0.1	<0.1	<0.1	<0.1	<0.1	<0.1	0.3
Cu	0.9	0.6	0.6	1	0.8	0.7	0.8
Pb	0.9	0.8	0.8	0.8	0.3	1.7	0.6
Zn	6	<1	3	<1	4	2	10
Ni	5.3	0.9	2.3	0.8	5.9	2.3	11.4
Cd	<0.1	<0.1	<0.1	<0.1	<0.1	<0.1	<0.1
Ag	<0.1	<0.1	<0.1	<0.1	<0.1	<0.1	<0.1
Au	1.7	1.9	<0.5	1.5	<0.5	0.9	1.6
Hg	<0.01	0.01	<0.01	<0.01	<0.01	<0.01	<0.01
Ga	17.2	13.8	15.9	16.9	22.9	19.1	22.2
Sn	3	4	3	<1	5	5	3
As	<0.5	<0.5	<0.5	<0.5	0.6	<0.5	<0.5
Sb	<0.1	<0.1	<0.1	<0.1	<0.1	<0.1	<0.1
Bi	<0.1	<0.1	<0.1	<0.1	0.3	<0.1	0.2
Tl	<0.1	<0.1	<0.1	<0.1	<0.1	<0.1	<0.1
Se	<0.5	<0.5	<0.5	<0.5	<0.5	<0.5	<0.5
Th	40.5	12.2	25.5	11.2	7.4	15.8	6.2
U	2.7	1.9	1.8	0.8	3.7	2	4.2
Ce	191	54.6	39.2	8.1	63.1	46.4	70.8
Pr	14.65	7.52	5.79	1.23	8.78	3.84	9.36
Nd	45.4	28.9	22.1	5.2	39.2	15.2	34
Sm	5.84	5.4	3.82	0.78	9.95	3.6	6.34
Eu	1.47	1.25	0.89	0.34	2.92	1.08	1.81
Gd	4.94	4.42	3.18	0.6	11.5	3.7	5.54
Tb	0.66	0.7	0.48	0.1	2	0.59	0.91
Dy	3.36	3.53	2.58	0.41	11.69	2.95	4.97
Ho	0.54	0.67	0.44	0.09	2.36	0.58	0.97
Er	1.71	1.91	1.41	0.31	6.97	1.7	2.9
Tm	0.24	0.27	0.2	0.05	0.99	0.26	0.4
Yb	1.62	1.95	1.41	0.32	6.34	1.88	2.8
Lu	0.24	0.3	0.22	0.07	0.93	0.3	0.44

1–3, altered granitoids; *4*, linear zone of albitization; *5, 6*, amphibolite xenoliths; *7*, dyke

Table 4. *Balance of components (a, absolute difference; b, as a percentage of the content in the whole rock)*

%	3	4	elements	A	b
SiO_2	62,85	67,28	Si	+ 2.65	+ 4.67%
TiO_2	0,64	0,08	Ti	- 0.38	- 88.00%
Al_2O_3	18,43	19,81	Al	+ 1.00	+ 5.10%
Fe_2O_3	1,39	0,13	Fe	- 0.86	- 89.00%
MnO	0,02	0,01	Mn		
MgO	3,31	0,19	Mg	- 4.17	- 94.00%
CaO	3,07	0,95	Ca	- 2.10	- 70.00%
Na_2O	8,43	10,35	Na	+2.97	+20.00%
K_2O	0,39	0,31	K	- 0.12	- 28.00%

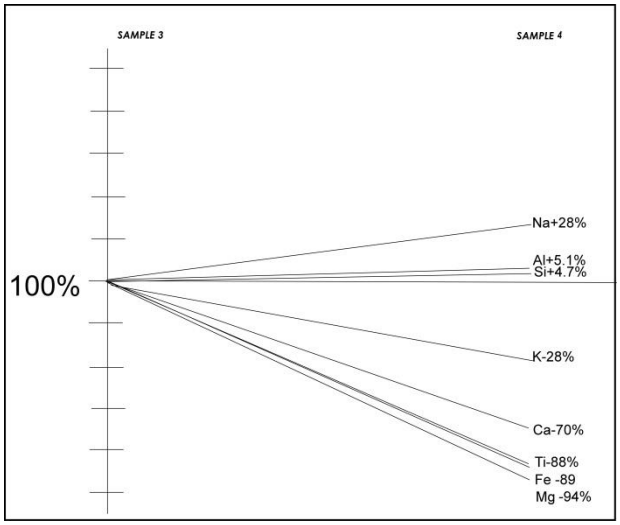

Fig. 3. Changes of the contents of the main elements
Sample 3 – altered granitoid; Sample 4 – zone of albitization

U-Pb zircon dating of the albitized granitoid

Zircon crystals were separated from the whole-rock (intensively albitized zone in the granitoids) using heavy liquids, then hand-picked and fixed in epoxy resin before polishing. Cathodoluminescence (CL) and back-scattered (BSE) images have been taken in order to study the internal structure and zonation of crystals. Laser crater of 35 μm, ablation frequency of 8 Hz and detection time within 0.002–0.003 s were used for all measurements that were calibrated with GEMOC-GJ1 zircon (Jackson et al., 2004) as external standard for fractionation correction. Fractionation correction and results were estimated using GLITTER 4.0 software (Macquarie University). Diagram plots and Concordia ages are delivered with only the concordant analyses using Isoplot 4.15 (Ludwig, 2011) application.

Zircons from albitized granitoid are with short to long prismatic and rarely pyramidal shapes (Fig. 4a, b). Resorption structures are relatively frequent and are mostly visible near cores. Crystals cored by unzoned re-crystallised interiors and rimmed by oscillatory terminations are very common (Fig. 4a, b). The Th/U ratio, varying within 0.37–1.77, is indicative of the magmatic origin for all the zircons. Inherited zircons and xenocrysts have not been identified over the course of this study, but the antecrystic zircons comprise considerable portion of all crystals analysed.

Half of analyses are interpreted to belong to antecrysts (329.79–311.23 Ma) incorporated in rocks derived from older magmatic pulses (Fig. 4d). Autocrystic zircon populations are aged, the youngest within 303.12–296.60 Ma, forming Concordia age at 298.4±1.6 Ma (Fig. 4c) and considered to reflect the timing of emplacement of Sakar granite. The obtained data confirm the Early Paleozoic age of magmatic crystallisation (Peycheva et al., 2016; Bonev et al., 2017).

Table. 5. *LA-ICP-MS isotopic ratios ($^{206}Pb/^{238}U$, $^{207}Pb/^{235}U$, $^{208}Pb/^{232}Th$) and $^{206}Pb/^{238}U$, and $^{207}Pb/^{235}U$ ages of zircons from the altered granitoids (● analysis of autocrystic zircon; ∗discordant value; ⁂ analysis of antecrystic zircon)*

N	Zr	Com-ment	Isotope ratios	Rho	Age, Ma	Ratio							
			$^{206}Pb/^{238}U$	2 SE	$^{207}Pb/^{235}U$	2 SE	$^{208}Pb/^{232}Th$	2 SE		$^{206}Pb/^{238}U$	2 SE	$^{207}Pb/^{235}U$	2 SE	Th/U
1	2r	●	0.0481	0.0007	0.3499	0.0189	0.0174	0.0017	0.61	303.12	8.61	304.61	28.12	0.47
2	5c	∗	0.0515	0.0006	0.3925	0.0133	0.0158	0.0015	0.64	324.00	7.60	336.19	19.23	0.44
3	5r	⁂	0.0486	0.0008	0.3362	0.0215	0.0158	0.0017	0.60	306.01	9.22	294.28	32.31	0.42
4	7	⁂	0.0525	0.0009	0.3833	0.0293	0.0162	0.0017	0.60	329.79	11.02	329.46	42.35	1.12
5	8	⁂	0.0501	0.0008	0.3639	0.0258	0.0159	0.0017	0.59	315.25	9.82	315.15	37.97	1.28
6	13c	∗	0.0455	0.0006	0.3671	0.0158	0.0093	0.0010	0.62	287.05	7.27	317.52	23.32	1.77
7	13r	●	0.0474	0.0006	0.3462	0.0159	0.0150	0.0012	0.61	298.51	7.75	301.89	23.75	0.49
8	12	⁂	0.0495	0.0007	0.3603	0.0160	0.0161	0.0013	0.61	311.23	7.98	312.40	23.67	0.50
9	25r	⁂	0.0509	0.0007	0.3749	0.0158	0.0161	0.0013	0.62	320.13	8.09	323.30	23.11	0.67
10	25c	●	0.0472	0.0008	0.3420	0.0259	0.0183	0.0018	0.59	297.53	10.09	298.67	38.66	0.37
11	28c	●	0.0474	0.0007	0.3452	0.0180	0.0130	0.0011	0.61	298.62	8.37	301.11	26.96	0.80
12	28r	⁂	0.0514	0.0007	0.3757	0.0194	0.0147	0.0013	0.61	322.96	8.83	323.90	28.36	0.49
13	35c	⁂	0.0501	0.0006	0.3619	0.0143	0.0151	0.0013	0.62	314.91	7.73	313.66	21.16	0.67
14	35r	●	0.0471	0.0006	0.3380	0.0156	0.0147	0.0014	0.61	296.60	7.75	295.67	23.43	0.53
15	41r	●	0.0471	0.0007	0.3379	0.0168	0.0142	0.0015	0.61	296.90	8.00	295.56	25.35	0.53
16	46	∗	0.0496	0.0007	0.3280	0.0173	0.0140	0.0015	0.61	312.27	8.47	288.04	26.18	0.57

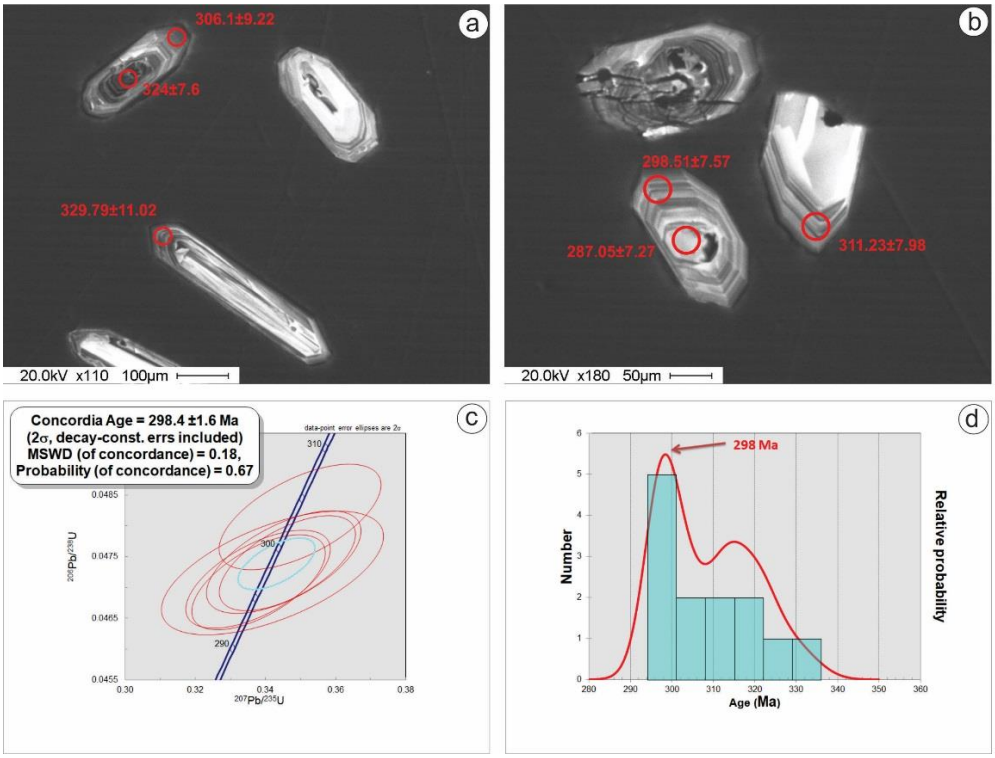

Fig. 4. Zircons from the studied albitized granitoids

Discussion and conclusion

The studied rocks from the Kanarata deposit are situated in the periphery area of the Sakar batholith. These rocks are characterised by completely different mineralogical and petrochemical characteristics as compared to the three distinguished granite units of the batholith. This is a result of the assimilation of the amphibolite xenoliths from the hosted high-grade metamorphic frame and superimposed intensive process of Na-alteration (albitization). The main characteristics of these rocks could be summarised as follows:

– The typical magmatic textures in the rocks are missing;

– The mineral composition is presented by minerals of the amphibole group (Ca-Mg hornblende and barroisite), plagioclase (albite), quartz, K-feldspar (single grains), titanite, rutile, apatite, zircon and imposed secondaries of sericite, epidote group minerals, chlorite;

– The superimposed process of albitization affects all rocks in the area of the deposit and it is most intensively developed along linear zones with east-west direction;

– The albite druses developed in the caverns represent intensively metasomatically re-worked amphibolite xenoliths and rutile, titanite, barroisite, and apatite mineralisations are genetically related to the process of Na-alteration;

– The increased content of MgO in the studied rocks and the presence of Mg-containing minerals could be a result of the assimilation of amphibolite xenoliths or a result of Mg-Na metasomatic process (?);

– The dated U-Pb zircon population in the metasomatically altered granitoids shows igneous origin and the obtained data confirm the Early-Paleozoic age of the Sakar batholith. The question about age of the process of albitization is still open.

The followed detailed study will clarify the mineralogy particularities of the Ti-containing minerals in the area and date the process of albitization.

Acknowledgement. This study has been supported by Project 127-2010 (Science Fund of the University of Mining and Geology "St. Ivan Rilski" in Sofia).

References

Bonev, N., P. Filipov, R. Moritz, R. Raicheva, M. Borisova. 2017. Ordovician and Carboniferous-Permian magmatism in the Sakar unit of the Sakar-Strandzha zone, Bulgaria. – In: *National Scientific Conference* "*Geosciences 2017*". Bulg. Geol. Soc., Sofia, 47–48.

Dencheva, S. 2017. Apatite from Sakar Mountain, Bulgaria – morphology and physical properties. – In: *National Scientific Conference* "*Geosciences 2017*". Bulg. Geol. Soc., Sofia, 21–22.

Gerdjikov, I. 2005. Structure of the metamorphic basement in the northern part of Sakar unit, SE Bulgaria. – *C. R. Acad. Bulg. Sci.*, *58*, 3, 289–296.

Ivanov, Z., I. Gerdzhikov, A. Kunov. 2001. New data about structure and tectonic evolution of the Sakar region. – *Ann. Univ. de Sofia, Fac. gèol et gèogr., 91*, Liv. 1 – gèol., 35–80.

Jackson, S. E., N. J. Pearson, W. L. Griffin, E. A. Belousova. 2004. The application of laser ablation-inductively coupled plasma-mass spectrometry to in situ U–Pb zircon geochronology. – *Chemical Geology*, *211*, 47–69.

Kamenov, B., V. Vergilov, H. Dabovski, I. Vergilov, L. Ivchinova. 2010. The Sakar batholith – petrology,

geochemistry and magmatic evolution. – *Geochem., Mineral. and Petrol.*, *48*, 1–37.

Kozhoukharov, D. 1988. Precambrian in the Rhodope massif. Lithostratigraphy. – In: Zoubek V. (Ed.*). Precambrian in Younger Fold Belts – European Variscides, the Carpathians and Balkans*. John Wiley & Sons, Chichester, 726–746.

Kozhoukharov, D., S. Savov, G. Chatalov, E. Kozhoukharova, I. Boyanov, E. Chelebiev. 1994. *Geological Map of Bulgaria on Scale 1:100000. Topolovgrad Map Sheet*. Committee of Geology and Mineral Resources, Geology & Geophysics, Sofia.

Leake, B., A. Wooly, C. Arps, W. Birch, M. Gilbert, J. Grice, F. Hawthorne, A. Kato, H. Kisch, V. Krivovichev, K. Linthout, J. Laird, J. Mandarina, W. Maresch, E. Nickel, N. Rock, J. Schumacher, D. Smith, N. Stephenson, L. Ungaretti, E. Whittaker, G. Youzhi. 1997. Nomenclature of amphiboles: report of the subcommittee on amphiboles of the international mineralogical association, commission on new minerals and mineral names. – *Canad. Mineral*., *35*, 219–246.

Lilov, P. 1990. Rb-Sr and K-Ar dating of the Sakar granitoid pluton. – *Geologica Balc.*, *20*, 6, 53–60 (in Russian with English abstract).

Ludwig, K. R. 2011. *User's Manual for Isoplot/Ex, Version 4.15. A Geochronological Toolkit for Microsoft Excel.* – Berkeley Geochronology Center Special Publication 4, Berkeley, CA, USA.

Peytcheva, I., S. Georgiev, A. von Quadt. 2016. U/Pb ID-TIMS dating of zircons from Sakar-Strandzha Zone: new data and old questions about the Variscan orogeny in SE Europe. – In: *National Scientific Conference* "*Geosciences 2016*". Bulg. Geol. Soc., Sofia, 71–72

Savov, S. 1988. Obzor stroenia Sakarskoi oblasti. – In: *Lineament kak Strukturi Sochlenenia Raznovuzrastnih Skladchatih Oblastei i Metalogenii.* Publ. House Bulgarian Academy of Sciences, Sofia, 98–114 (in Russian).

Savov, S., H. Dabovski. 1979. Metamorphic Triassic in the Topolovgrad syncline and its basement. – In: *Precambrian of the Rhodope Massive and the Embracing Phanerozoic Metamorphic Formation*. Publ. House Bulgarian Academy of Sciences, Sofia, 98–105 (in Russian with English abstract).

Skenderov, G., I. Palshin, Y. Mihailov, I. Bozhkov, L. Savova. 1986. About age of the Sakar granite pluton (South-East Srednogorie). – *Geochem., Mineral. and Petrol.*, *22*, 69–80 (in Russian with English abstract).

Zagorchev, I., P. Lilov, S. Murbat. 1989. Rb/Sr and K/Ar results of metamorphic and igneous rock from South Bulgaria. – *Geologica Balc.*, *19*, 3, 41–54 (in Russian with English abstract).

FOSSIL HUMUS MUD AND ITS NOVOCHERNOMORIAN BASE AT THE ATANASOVSKO LAKE, BURGAS LAKES COMPLEX, BULGARIA

Dimitar Sinnyovsky[1], Dimka Sinnyovska[1], Natalia Kalutskova[2], Nikolai Dronin[2], Andrei Medvedev[3], Natalia Telnova[3]

[1] University of Mining and Geology "St. Ivan Rilski", 1700 Sofia; sinsky@mgu.bg
[2] Moscow State University "M. V. Lomonosov", 119991 Moscow; nat_nnk@mail.ru
[3] Geographical Institute, Russian Academy of Sciences, 119017 Moscow; a.a.medvedeff@gmail.com

ABSTRACT. Fossil humus mud horizon covering Novochernomorian beach deposits crops out at the eastern shoreline of the Atanasovsko Lake 1 m above the modern lake surface. It is identified by the Nymphean accumulative terrace, formed during the Middle Ages about 1000 years ago, when the Black Sea surface was 2 m above the present sea level. The mud sediments are underlined by sandy-clayey-silty deposits that are considered to be bottom lake deposits which represent evidence of post Kalamitian sea-level decrease. In depressions such as the Burgas bay, part of which were the Burgas Lakes at that time, these deposits are commonly 2–4 m thick. Obviously, during the Late Kalamitian age the central part of the Burgas bay was a submerged shoreline with a sandy-clayey-silty sedimentation. Novochernomorian (Dzhemetinian) sediments are deposited in shelf environment when the Black Sea level was slightly higher compared to the present sea level. The boundary between the sands and the overlying humus mud is a clear erosion surface 1 m above the present lake level formed during the Fanagorian regression, when the sea level dropped. The humus is 1 m thick with shells of modern fauna, characteristic for the present humus mud in the Atanasovsko Lake.

Keywords: Atanasovsko Lake, Late Chernomorian deposits, fossil humus mud

ФОСИЛНА ХУМУСНА КАЛ И НЕЙНАТА НОВОЧЕРНОМОРСКА ПОДЛОЖКА В АТАНАСОВСКОТО ЕЗЕРО, БУРГАСКИ ЕЗЕРЕН КОМПЛЕКС, БЪЛГАРИЯ

Димитър Синьовски[1], Димка Синьовска[1], Наталия Калуцкова[2], Николай Дронин[2], Андрей Медведев[3], Наталия Телнова[3]

[1] Минно-геоложки университет "Св. Иван Рилски", 1700 София
[2] Московски държавен университет "М. В. Ломоносов", 119991 Москва
[3] Географски институт, Руска академия на науките, 119017 Москва

РЕЗЮМЕ. На източния бряг на Атанасовското езеро се разкрива фосилен хумусен хоризонт, покриващ Новочерноморските отложения на 1 m над съвременната повърхност на езерото. Той се идентифицира с акумулационната Нимфейска тераса, образувана през Средновековието преди около 1000 години, когато повърхността на Черно море е била с 2 m над съвременното морско ниво. Той се подстила от песъчливо-глинесто-алевритови отложения, които се считат за дънни езерни утайки, представляващи доказателство за следкаламитско понижение на морското ниво. В депресии като Бургаския залив, част от който по това време са и Бургаските езера, тези отложения обикновено са с дебелина 2–4 m. Очевидно, по време на Късноаламитската епоха централната част на Бургаския залив е била потопена брегова линия с песъчливо-глинесто-алевритова седиментация. Новочерноморските (Джеметински) седименти се отлагат в шелфова обстановка, когато нивото на Черно море е малко по-високо от сегашното. Границата между песъчливо-алевритовите утайки и покриващия ги хумусен слой на 1 m над сегашното ниво на езерото е рязка и вероятно е образувана по време на Фанагорийската регресия, когато морското ниво спада. Хумусът е с дебелина 1 m и съдържа черупки от съвременна фауна, характерни за днешната хумусна кал в Атанасовското езеро.

Ключови думи: Атанасовско езеро, късночерноморски отложения, фосилна хумусна кал

Introduction

Identification of Quaternary sea terraces along the sea coast and lake shores is part of the preliminary studies on the creation of Geopark "Burgas Lakes". The Atanasovsko Lake, which is part of the Burgas Lakes Complex, is the subject of investigation because of its interesting Holocene development as a firth basin. Due to their connection with the Black Sea basin, the Burgas Lakes have been sensitive to the sea-level changes during the last 7000 years when at least two transgressive-regressive stages occurred.

The present investigation is devoted to fossil humus deposits cropping out near the Atanasovsko Lake, located 2 m above the modern sea level and considered to be part of the Nymphean accumulative terrace.

Location

The outcrop is located on the eastern shoreline of the Atanasovsko Lake on the canal linking the lake with the Black Sea in the area called "Kyusheto" (Fig. 1). This outcrop was mentioned in our short communication published in the proceedings of last years' scientific conference "Geosciences" of the Bulgarian Geological Society (Sinnyovsky et al., 2018)

dedicated to the Nymphean terrace in the area of Burgas Lakes Complex.

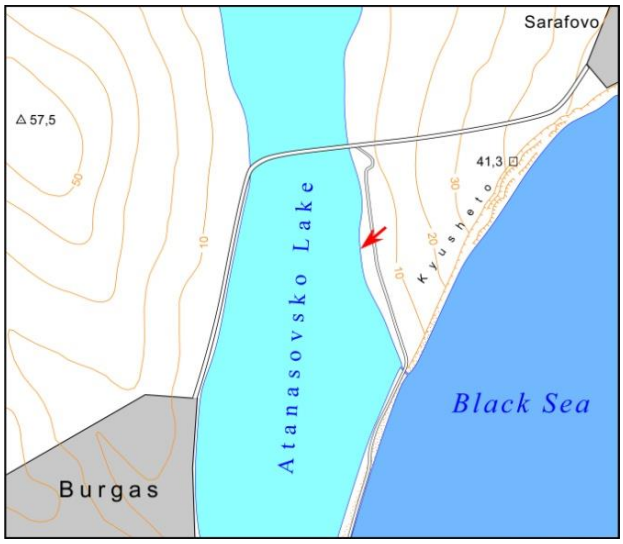

Fig. 1. Location of the investigated outcrop of the Nymphean terrace on the eastern shoreline of the Atanasovsko Lake in "Kyusheto" area between the lake and the Black Sea

The accumulation of fine-grained deposits during the Nymphean transgression is especially characteristic of the closed Burgas Lakes Complex. Its weak connection to the sea provided a calm environment for a clayey-silty sedimentation accompanied by humus deposits, characteristic of the modern deposits of the lakes. The outcrops of these factually modern deposits are very rare, because they are usually covered with soil and cane. For this reason, the artificial outcrop preserved on the canal slope provides good material for exploring the processes that took place during the high sea level during the Middle Ages.

Sea-level changes during the Late Chernomorian transgressive interval

The sea level rise during Novochernomorian transgression occurred at different speeds, with rapid rise periods alternating with periods of stagnation during which underwater terraces were formed (Larchenkov, Kadurin, 2011). According to these authors the Late Chernomorian transgressive interval is subdivided into two transgressive-regressive stages: Calamitian, between 7100 and 4100 years ago, and Dzhemetinian, between 4100 years ago and present days (Fig. 2).

The melting of the Wurm glaciers about 11000 years ago caused a massive influx of fresh waters to the Neweuxinian basin and marked the start of postglacial Novochernomorian Holocene transgression (Fedorov, 1976). The maximum sea level of the transgression in the Bronze Age (5600–4300 years ago) was 4–5 m higher than today. At that time the Novochernomorian terrace was formed, which is abrasive on the capes and accumulative in the bays (and firths such as the Atanasovsko Lake). Between 2500–1000 years ago during the so-called Phanagorian regression the sea level dropped to 3 m below the present sea level. The Nymphean transgression (Fedorov, 1960), which occurred some 1000 years ago, raised the sea level up to 1.5–2.0 m above the present sea level, immersing many archaeological monuments along the Black Sea coast.

The firth sedimentation in the Burgas Lakes Complex resulted in accumulation of sandy-clayey-silty deposits and humus mud containing recent bivalve shells. After the sea level dropped to the modern sea level these deposits remained in the form of a flat terrace named after the Nymphean transgression.

Transgessive interval		Transgessive-regressve stage	Time (ka)	Depth of sea (m)
Chernomorian	Late Chernomorian	Dzhemetinian	0-4.1	-2 to +2
		Kalamitian	4.1-7.1	-7.5
	Early Chernomorian	Vityazevian	7.1-8.9	10.5-12.5
		Bugazian	8.9-10.0	-25 to 22,5
Neueuxinian		Late Neueuxinian	10.0-18.0	-37 to -35
		Early Neueuxinian	18.0-30.0	-55 to -57

Fig. 2. Neoeuxinian and Chernomorian transgressive intervals and transgressive-regressive stages after Larchenkov and Kadurin (2011)

Table 1. *Results of the granulometric analyses of two samples (Sample 1 and Sample 2 of the section in Fig. 4)*

№ sample	Weight of sample	Dissol. Comp.	Undissol. Comp.	Fractions [mm]			Granulometry		
				1–0.1	0.1–0.01	<0.01	psammite	silt	clay
	g	%	%	%	%	%	%	%	%
1	20.00	17.40	82.60	21.35	33.35	27.70	21.35	33.55	27 70
2	20.00	23.25	76.75	6.60	36.60	33.55	6.60	36.60	33.55

Results

The section of the sediments investigated includes 1 m carbonate-sandy-clayey-silty deposits, 20 cm carbonate-clayey silt and 1 m humus mud (Figs 3, 4).

Fig. 3. Outcrop of the Nymphean sediments on the western slope of the channel near the Atanasovsko Lake

The granulometric analyses, represented in Table 1 revealed that the underlying sandy deposits (Sample 1 in Fig. 4) are sediments of mixed type, containing 17.40% carbonate and 82.60% insoluble residue, consisting of 21.35% psammite, 33.55% silt and 27.70% clay. According to this composition, the sample may be classified as carbonate-sandy-clayey hyposilt. The transitional interval (Sample 2 in Fig. 4) between the underlying sandy hyposilt and the overlying bituminous mud is composed of 20 cm yellow carbonate-clayey hyposilt composed of 23.25% carbonate, 33.55% clay, 36.60% silt and very low content of psammite component – only 6.60%.

The overlying black bituminous mud lies with an abrupt boundary over the carbonate-clayey silt. It contains shells of bivalves representing mainly the genus *Cardium*. These shells are not contemporaneous with the present shells of the genus because they are with dissolved inner and outer glance layer.

The data from the granulometric analyses testify to a regime of fine-grained terrigenous sedimentation, which shows that Atanassovsko Lake had no broad connection with the sea, regardless of the higher sea level during the Nymphean transgression. This is an evidence of sedimentation in a calm firth environment.

Right interpretation of the results is of important value for the future investigation of the Nymphean terrace, which depends on the access to reliable outcrops. The first impression during the field investigation of the lake shoreline was that sediments underlying the humus mud can be related to the Novochernomorian beach sands. However, the laboratory analyses revealed rather complicated composition of the granulometric fractions.

The soluble component is in the frame of the normal contents, taking into account biodetritic enrichment of the beach deposits. The psammite/silt amount is also within the normal range. With respect to all the variety of beach environments, the high content of clay fraction is not characteristic for the beach sands. Regardless of the proximity of the sea, it is more likely that these sediments are deposited at the bottom of the Atanasovsko Lake in conditions close to the modern environment.

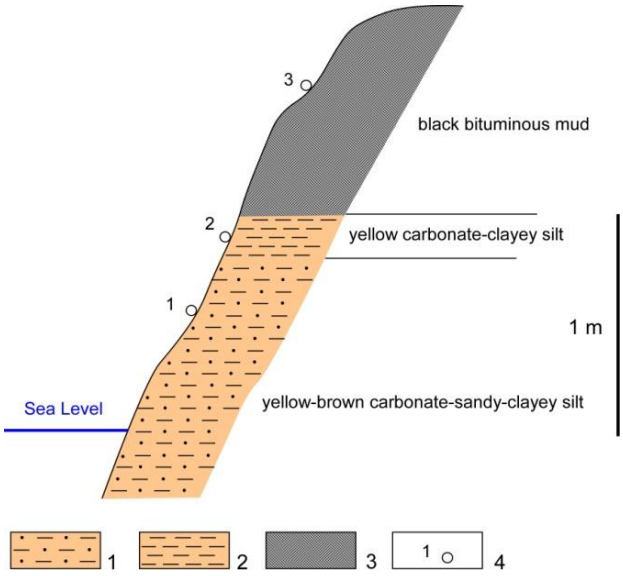

Fig. 4. Section of the Nymphean terrace at the Atanasovsko Lake *1*, yellow-brown carbonate-sandy-clayey silt; *2*, clayey silt; *3*, bituminous mud; *4*, sample

In general, the drastic decrease of the sandy component in the next sample reveals sea level rise, corresponding probably to the Nymphean transgression in the Middle Ages. The sea level rise should cause wider connection with the sea basin and better correspondence of the salinity between the lake and the sea.

Unfortunately, the total lack of outcrops does not allow successive investigation of this level, which can reveal more circumstances about the Nymphean paleoenvironment in the Burgas Lake Complex and can give answers to many questions about the existence of the Nymphean terrace. It is well outlined around the shoreline of the Burgas Lakes, forming a flat surface about 1.5–2 m above the lake water level covered by cane (Fig. 5).

Fig. 5. The Nymphean terrace is well expressed at the northern shoreline of the Atanasovsko Lake, forming a flat surface covered by cane about 2 m above the water

As Fedorov (1985) noted, the assessment of sea level fluctuations is based on studying the hypsometric level of ancient coastlines, with particular attention to neotectonic movements and mollusc fauna. However, the morphological expression of this terrace is not enough proof for its existence. Because it is about an accumulation terrace, the evidence of medieval sedimentation in the area is very important.

The artificial exhumation of such sediments is a very rare event since they are not developed in the urban area of Burgas where construction works are being developed. The Nymphean terrace is the result of a slight fluctuation at sea level, which is hardly noticeable along the coastline that falls within the hypsometric range of the modern wave zone (Sinnyovsky et al., 2018). Its identification is easier along the shorelines of Burgas lakes, which are protected by the wave activity of the sea. Here, in many places, there are well-marked reed overgrown lobes lying 1.5-2 m above the water surface. They can be identified, with a high degree of reliability, to be with a higher level of the water surface in the limans that are connected to the Burgas Bay and they follow the sea level fluctuations. In some places, the lowest terrace level is formed between the modern lake surface and a well-known old cliff of Upper Cretaceous volcanic fundament of agglomerate and bomb tufts forming the ancient coastline (Fig. 6).

Fig. 6. The lowest terraced level near the Burgas Lakes is formed between the modern lake surface and a well-known old cliff of Upper Cretaceous agglomerate tuffs and bomb tufts representing the ancient coastline

Finally, on the basis of archaeological data, the possible influence of sea level changes on late Holocene human societies of the Black Sea littoral areas was also documented. The aim of this investigation was to develop a basis for future investigations to link the geological events to the events engraved in human memory. There are many historical events confirming the higher sea level during the Middle Ages. Popov and Mishev (1974) cited historical facts from K. Škorpil, such as the position of the Asparuh Shaft in Northeast Bulgaria, which was built near the shoreline and now it is 600 m away from the modern coastline. There is also an evidence of swamping of the area between Varna and Asparuhovo quarter when the knights of Vladislav Varnenchik sunk with their horses in the swamps in the battle during the Varna Crusade in 1444.

This historical evidence corresponds to the data from numerous points of the Black Sea coastline about the higher sea level during the Middle Ages.

Conclusions

The available evidence of modern transgressive deposits at the Atanasovsko Lake strongly suggests a sea level rise during the Middle Ages period that caused accumulation terrace around the shoreline of the Burgas Lakes. This sea level rise is related to the so called Nymphean transgression. In the final Dzhemetinian transgressive-regressive stage of the Late Chernomorian transgressive interval the sea level rise caused carbonate-sandy-clayey hyposilt sedimentation which ended with humus deposits, elevated 1.5 m above the present sea level. The granulometric analyses show a fine-grained terrigenous sedimentation, which is an evidence that Atanasovsko Lake had no broad connection with the Black Sea, regardless of the higher sea level during the Nymphean transgression. This has contributed to sedimentation in a calm firth environment. The present study of the youngest Holocene deposits in the Burgas Lakes Complex provides a basis for scientific investigation of the last transgression in the geological history.

Acknowledgements. This research has been supported by the National Science Fund under contract DNTS/Russia 02/14, and contract 18-55-18013. The field investigations are performed with the support of the National Science Programme "Environmental Protection and Reduction of Risks of Adverse Events and Natural Disasters", approved by Resolution of the Council of Ministers No 577/17.08.2018 and supported by the Ministry of Education and Science (MES) of Bulgaria (Agreement № D01-230/06.12.2018).

References

Fedorov, P. V. 1960. Old Black Sea shorelines at Caucasus coast. – *Proc. Acad. Sci. USSR, Ser. Geol*., 2, 56–64.

Fedorov, P. V. 1976. Regularities of the sea-level changes in the Caspian, Black and Mediterranean seas during the Plejstocene. – In: *Quaternary Geology, Engineering Geology, Problems of the Arid Zone (XXV Session of IGC)*. Nauka, Moscow, 136–142.

Fedorov, P. V. 1985. On the problem of the Black Sea level changes during the Pleistocene. – In: Alekseev, M. N. (Ed.). *Geology and Geomorphology of the Shelf and Continental Slopes*. Nauka, Moscow, 131–136.

Larchenkov, E., S. Kadurin. 2011. Paleogeography of the Pontic Lowland and northwestern Black Sea shelf for the past 25 k.y. – In: Buynevich, I. V., V. Yanko-Hombach, A. S. Gilbert, R. E. Martin (Eds). *Geology and Geoarcheology of the Black Sea Region*. Geol. Soc. America, 71–84.

Popov, V., K. Mishev. 1974. *Geomorphology of the Bulgarian Black Sea Coast and Shelf*. Publ. House of the Bulgarian Academy of Sciences, Sofia, 267 p. (in Bulgarian)

Sinnyovsky, D., N. Kalutskova, N. Dronin, D. Sinnyovska. 2018. Nimphean terrace in the area of the Burgas Lakes. – *Rev. Bulg. Geol. Soc*., *79*, 3, 115–116.

FORAMINIFERAL ASSEMBLAGES FROM THE CRETACEOUS–TERTIARY TRANSITION IN THE EMINE FLYSCH FORMATION AT KOCHAN CAPE LOCALITY (EASTERN BALKAN): PRELIMINARY DATA

Boris Valchev

University of Mining and Geology "St. Ivan Rilski", 1700 Sofia; b_valchev@mgu.bg

ABSTRACT. A 24 m interval in the turbidites of the Emine Flysch Formation (upper Campanian–upper Paleocene), located at 300 m north of Kochan Cape in the Eastern Balkan, was studied in terms of the foraminiferal turnover across the Cretaceous–Tertiary transition. The samples, picked up from the lower 18 m contain planktonic foraminiferal assemblages typical for the uppermost Maastrichtian represented by *Pseudotextularia elegans* (Rhehak), *Laeviheterohelix glabrans* (Cushman), *Heterohelix globulosa* (Ehrenberg), *H. labelosa* Nederbragt, *Rugoglobigerina macrocephalla* Brönnimann, *R. rugosa* (Plummer), *Globotruncana arca* (Cushman). The next 3.5 m are characterised by the presence of *Muricohedbergella monmouthensis* (Olson), *M. holmdelensis* (Olson), *Guembelitria cretacea* Cushman, *Rugoglobigerina macrocephalla* Brönnimann, *Laeviheterohelix glabrans* (Cushman), *Heterohelix globulosa* (Ehrenberg), and *Globotruncana arca* (Cushman). The uppermost 2.5 m of the section reveal typical lowermost Paleocene assemblages, characterised by low taxonomical diversity – only *Eoglobigerina eobulloides* (Morozova) and *E. fringa* (Subbotina). The investigated boundary interval is marked by comparatively uniform benthic foraminiferal assemblages dominated by agglutinated taxa.

Keywords: foraminiferal assemblages, Cretaceous–Tertiary boundary, Emine Fm., Eastern Balkan

ФОРАМИНИФЕРНИ АСОЦИАЦИИ ОТ ГРАНИЧНИЯ ИНТЕРВАЛ КРЕДА-ТЕРЦИЕР В ЕМИНСКАТА ФЛИШКА СВИТА В РАЙОНА НА НОС КОЧАН (ИЗТОЧНА СТАРА ПЛАНИНА): ПРЕДВАРИТЕЛНИ РЕЗУЛТАТИ

Борис Вълчев

Минно-геоложки университет "Св. Иван Рилски", 1700 София

РЕЗЮМЕ. Изследван е 24-метров интервал в турбидитите на Еминската флишка свита (горен Кампан–горен Палеоцен), намираща се на 300 m северно от нос Кочан в Източна Стара планина, с цел установяване на промени във фораминиферните асоциации от граничния интервал Креда–Терциер. Пробите, взети от долните 18 m съдържат типични късномастрихтски видове като by *Pseudotextularia elegans* (Rhehak), *Laeviheterohelix glabrans* (Cushman), *Heterohelix globulosa* (Ehrenberg), *H. labelosa* Nederbragt, *Rugoglobigerina macrocephalla* Brönnimann, *R. rugosa* (Plummer), *Globotruncana arca* (Cushman). Следващите 3,5 m се характеризират с присъствието на *Muricohedbergella monmouthensis* (Olson), *M. holmdelensis* (Olson), *Guembelitria cretacea* Cushman, *Rugoglobigerina macrocephalla* Brönnimann, *Laeviheterohelix glabrans* (Cushman), *Heterohelix globulosa* (Ehrenberg) и *Globotruncana arca* (Cushman). Най-горните 2,5 m от разреза разкриват типични раннопалеоценски асоциации, характеризиращи се с ниско таксономично разнообразие – установени са само видовете *Eoglobigerina eobulloides* (Morozova) и *E. fringa* (Subbotina). Изследваният граничен интервал показва присъствието на сравнително еднообразни асоциации от бентосни фораминифери с преобладаване на аглутинираните форми.

Ключови думи: фораминиферни асоциации, граница Креда-Терциер, Еминска свита, Източна Стара планина

Introduction

The Emine Formation is widely distributed in the East Balkan Unit (*sensu* Dabovski, Zagorchev, 2009 – Figs 1, 2) and comprises a thick turbidite sequence (at least 1670 m – Sinnyovsky, 2004). The rocks were first described as a distinct lithological body by Gočev (1932) who named them as "Emine beds" of Lutetian age. Later on, Botev (1953) referred them to the "Upper Senonian – flysch type", Bonchev (1955) named the unit "Emine formation", and Atanasov and Kanchev (1965) used the term "Emine flysch formation". Bochev et al. (1967) published a detailed investigation concerning the coastal part of the East Balkan, and provided data on the lithology, genesis and age of the unit. They described its lower levels as "Campanian–Maastrichtian – south strip" and the upper levels referred to the "Danian–Paleocene". Karagjuleva and Kostadinov (1977) divided and described an "Emine formation" (corresponding to the "Campanian–Maastrichtian of Bochev et al., 1967) and a "clayey–terrigenous formation" ("Danian-Paleocene" of Bochev et al., 1967). Nachev (1977) gave additional data to the lithology of these bodies. Juranov and Pimpirev (1989) determined the rank of the unit, described the lectotype section and proved the Campanian–middle Paleocene age on the basis of planktonic foraminifera.

Sultanov et al. (1990) provided planktonic foraminiferal and calcareous nannoplankton data determining late Campanian–late Paleocene age. Sinnyovsky and Sultanov (1994) characterised the formation's boundaries and specified the nannofossil data confirming late Campanian – late Paleocene age. Nachev and Dimitrova (1995) also pointed out this chronostratigraphic range.

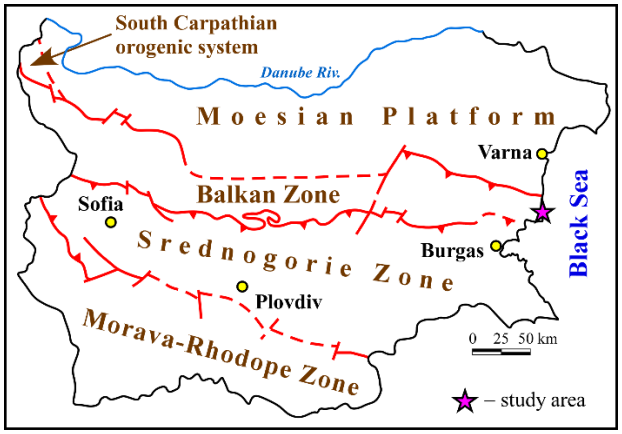

Fig. 1. Tectonic subdivision of the territory of the Republic of Bulgaria (after Dabovski, Zagorchev, 2009) with the location of the studied area

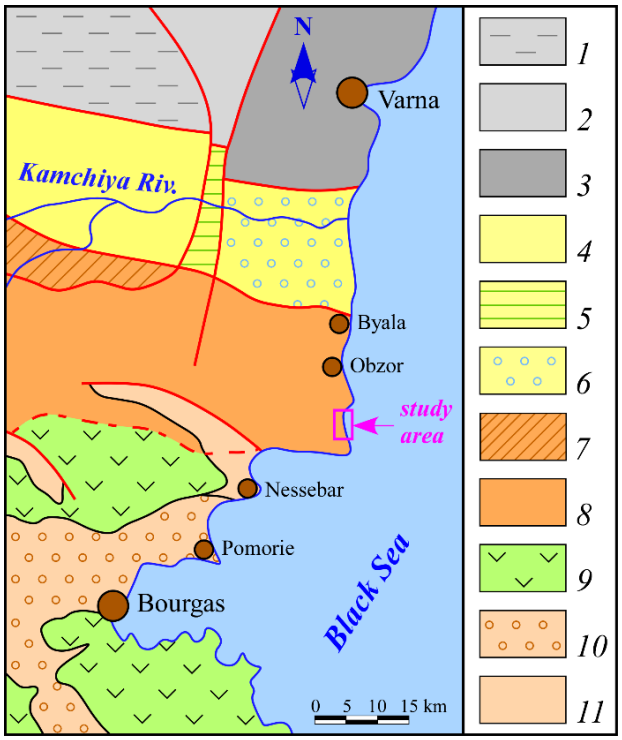

Fig. 2. Location of the studied area amongst the tectonic units in eastern Bulgaria (after Dabovski, Zagorchev, 2009; Bokov et al., 1987, with modifications)
1–2, North Bulgarian Dome (*1*, Hitrino-Kaspichan Block; *2*, Dobrich-Vetrino Block); *3*, East slope of the North Bulgarian Dome; *4*, Provatiya Syncline; *5*, Goren Chiflik Horst; *6*, Dolna Kamchiya Basin; *7*, Fore Balkan Unit; *8*, East Balkan Unit; *9*, East Srednogorie Unit; *10–11*, Intraorogenic basins (*10*, Paleogene–Neogene–Quaternary, *11*, Neogene–Quaternary)

The Cretaceous–Tertiary (K-T) boundary in the Emine Formation was first established by Sinnyovsky and Stoykova (1995) north of the village of Emona by means of calcareous nannofossils. Later on, Sinnyovsky (2003, 2004) proved it near the village of Kozichino and north of Kochan Cape, while Stoykova and Ivanov (2004) established this boundary near the Marash River. Valchev (2006) provided planktonic foraminiferal data from the transition near the village of Kozichino.

The present article aims to represent preliminary data on the taxonomical composition and stratigraphic range of the foraminiferal assemblages (both planktonic and benthic) obtained from the K-T sequence at Kochan Cape locality. Eleven samples from a 24 m thick interval were studied for this purpose.

Geological setting

The area of study is located in the coastal part of the East Balkan Unit (Fig. 2) in the northern limb of the Banya Syncline, which was first established by Radev (1927). Botev (1953) described it as "Banya syncline", and later on it was described by Atanasov and Kanchev (1965), Bochev et al. (1967), Kanchev (1971), Karagjuleva and Kostadinov (1977), Juranov et al. (1994). The fold is entirely formed by the Emine Formation's beds as the limbs are composed of these of late Campanian–Maastrichtian age (Fig. 3).

The K-T transition crops out 300 m north of Kochan. It comprises thin-bedded turbidites dipping 30 to 40° to SSW (Figs 3, 4).

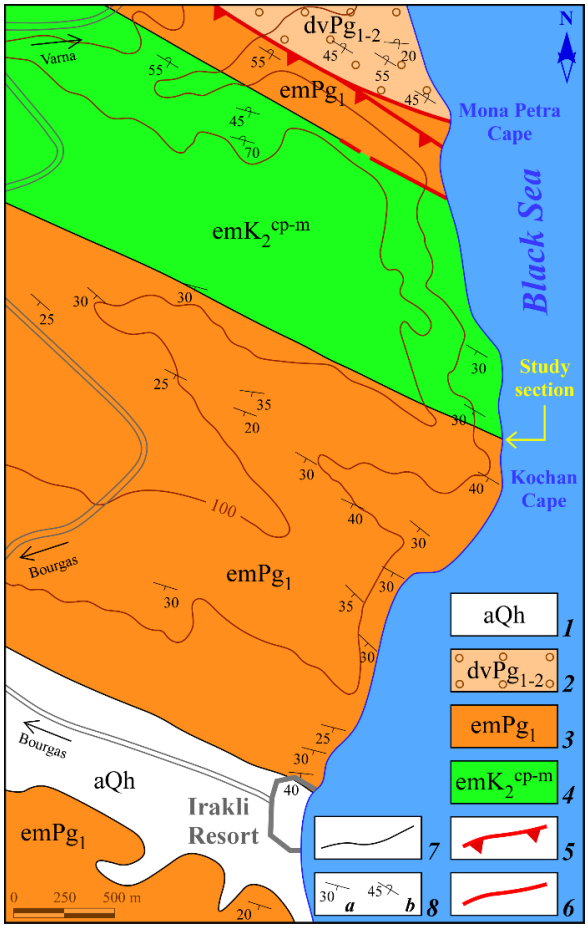

Fig. 3. Geological map of the coastal part of East Balkan (after Juranov et al., 1994, modified) with the location of the K/T transition
1, alluvium (Holocene); *2*, Dvoynitsa Fm. (Paleocene–middle Eocene); *3–4*, Emine Fm. (*3*, upper Campanian–Maastrichtian, *4*, Paleocene); *5*, reverse fault; *6*, normal fault; *7*, stratigraphic boundary; *8*, bedding (*a*, normal, *b*, overturned)

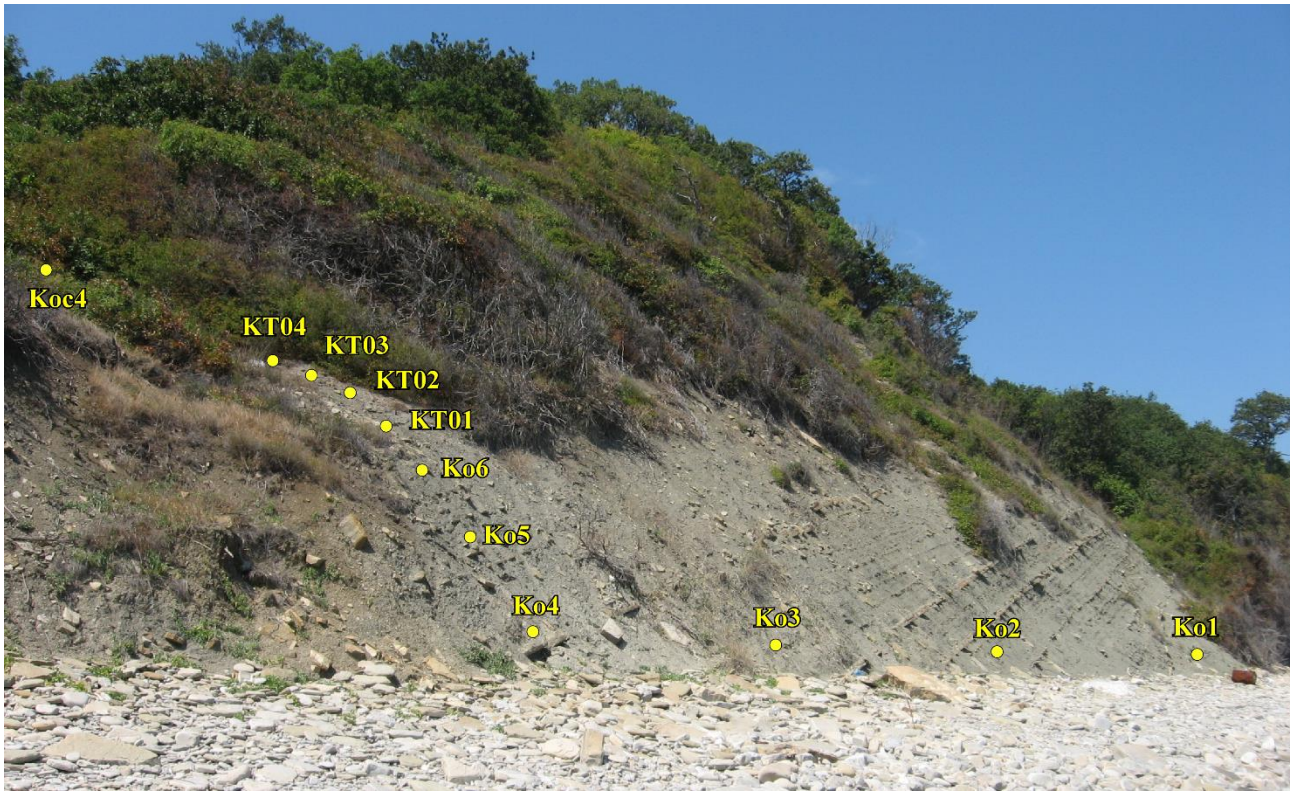

Fig. 4. The K-T transition in the turbidites of the Emine Formation 300 m north of Kochan Cape with the location of the studied samples

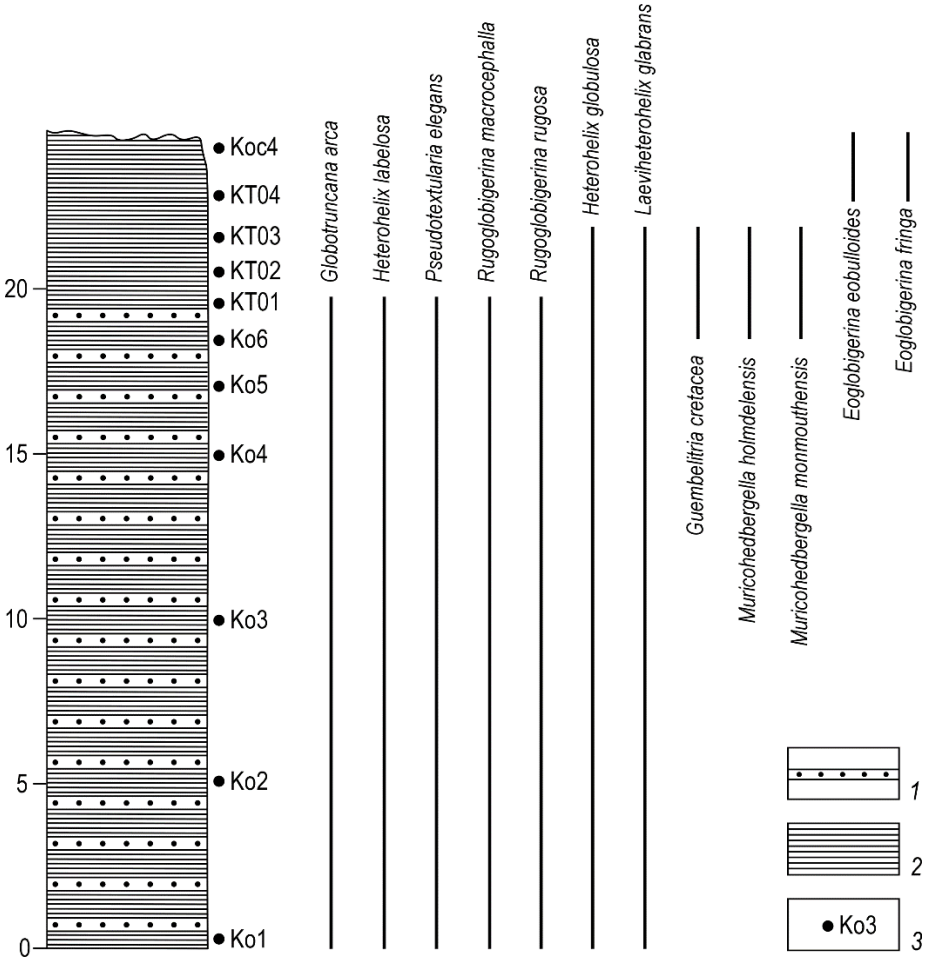

Fig. 5. Column section of the studied K-T transition with the stratigraphic distribution of the established planktonic foraminiferal taxa
1, thin-bedded sandstones; *2*, siltstones, argillites; *3*, sample

Results

Planktonic foraminifera

The lower 18 m of the studied interval (samples Ko1–Ko6 – Fig. 5) contain a poor, but typical lattermost Cretaceous assemblage, represented by rare or single specimens of *Pseudotextularia elegans* (Rhehak), *Laeviheterohelix glabrans* (Cushman), *Heterohelix globulosa* (Ehrenberg), *H. labelosa* Nederbragt, *Rugoglobigerina macrocephalla* Brönnimann, *R. rugosa* (Plummer), *Globotruncana arca* (Cushman). As a whole the recovered specimens are poorly preserved and they were derived predominantly from the 200, 112 and 63 μm residues.

The next 3.5 m (samples KT01–KT03) are characterised by the presence of *Muricohedbergella monmouthensis* (Olson), *M. holmdelensis* (Olson), *Guembelitria cretacea* Cushman, which are referred in the micropaleontological literature to the co-called survivors, as well as typical Late Cretaceous taxa like *Rugoglobigerina macrocephalla* Brönnimann, *Laeviheterohelix glabrans* (Cushman), *Heterohelix globulosa* (Ehrenberg), and *Globotruncana arca* (Cushman). All the species occur as single to rare. *L. glabrans* and *H. globulosa* were established in the lowermost Paleocene near the village of Kozichino (Valchev, 2006).

The uppermost 2.5 m (samples KT04 and Koc4) of the section reveal typical lowermost Paleocene assemblages, characterised by low taxonomical diversity – only *Eoglobigerina eobulloides* (Morozova) and *E. fringa* (Subbotina) were found in the samples. The assemblage, recovered from sample KT04 consists of single specimens, while the one from sample Koc4 reveals is more abundant.

Benthic foraminifera

The investigated boundary interval is characterised by comparatively uniform foraminiferal assemblages dominated by agglutinated taxa. Common species amongst them in all samples are *Dendrophrya excelsa* Grzybowski, *Ammodiscus cretaceous* (Reuss), *A. glabratus* Cushman and Jarvis, *Repmanina charoides* (Jones and Parker), *Paratrochamminoides irregularis* White which occur as rare specimens. Subsidiary elements to the assemblage structure are species like *Rhizammina indivisa* Brady, *Marssonella* spp., *Haplophragmoides* spp. which occur as single specimens.

As a whole the hyaline benthics occur as single specimens. The most common amongst them is *Quadrimorphina allomorphinoides* (Reuss). The other taxa were found at different levels of the section.

Discussion and conclusions

The well exposed turbidite sequence of the Emine Flysh Formation north of Kochan Cape, Bourgas District was investigated from planktic and benthic foraminiferal point of view. It is interesting that the Cretaceous assemblages are less abundant than the Paleocene ones (this fact was noted by Valchev, 2006, concerning the K-T transition near the village of Kozichino). As mentioned above, Cretaceous forms occur with rare or single specimens and this fact makes difficult the biostratigraphical characterisation of the interval. The index species *Abathomphalus mayaroensis* (Bolli) was not established.

The K-T boundary was marked easily in the upper part of the studied section because of the clear planktonic foraminiferal change. 5 species could be considered as survivors. All of them were derived from the 63 μm and 112 μm residue.

The Paleocene assemblages are more abundant, but with low taxonomical diversity. A further detailed sampling would provide a good opportunity for a precise biostratigraphical characterisation of the K-T boundary transition.

Benthic foraminifera show the typical features for the Upper Cretaceous-Paleogene flysch-type assemblages of the Tethys region – uniform taxonomical composition and structure without changes across the K-T boundary and strongly dominated by agglutinated taxa.

Appendix – List of planktonic and benthic foraminiferal species found in the present study

Cretaceous planktonic foraminifera
Globotruncana arca (Cushman)
Heterohelix labelosa Nederbragt
Pseudotextularia elegans (Rhehak)
Rugoglobigerina macrocephalla Brönnimann
R. rugosa (Plummer)

Survivors
Guembelitria cretacea Cushman
Heterohelix globulosa (Ehrenberg)
Laeviheterohelix glabrans (Cushman)
Muricohedbergella holmdelensis (Olson)
Muricohedbergella monmouthensis (Olson)

Paleocene planktonic foraminifera
Eoglobigerina eobulloides (Morozova)
E. fringa (Subbotina)

Cretaceous/Paleogene small benthic foraminifera
Ammodiscus cretaceous (Reuss)
A. glabratus Cushman and Jarvis
A. peruvianus Berry
Aragonia velascoensis (Cushman)
Bathysiphon sp.
Cyclammina sp.
Dendrophrya excelsa Grzybowski
Dentalinoides colei (Cushman and Dusenbery)
Glomospira diffundens (Cushman and Renz)
Gyroidinoides girardanus (Reuss)
Haplophragmoides sp.
Lenticulina sp.
Marssonella oxycona (Reuss)
Nodosaria limbata d'Orbigny
Nodosaria sp.
Osangularia florealis (White)
Paratrochamminoides irregularis (White)
Quadrymorphina allomorphinoides (Reuss)
Reophax duplex Grzybowski
Repmanina charoides (Jones and Parker)
Reussoolina emaciata Reuss
Rhizammina indivisa Brady
Saccammina placenta Grzybowski
Saccammina sp.
Spiroplectammina spectabilis (Grzybowski)
Trochamminoides dubius (Grzybowski)

References

Atanasov, A., I. Kanchev. 1965. Varna – Slanchev Bryag – Bourgas. – In: *Field Trip "A" Sofia-Varna. Guidebook. VII Congress CBGA*, 99–104 (in Russian).

Bokov, P., G. Georgiev, I. Monahov, A. Atanasov, S. Jelev, Ch. Dachev, D. Yordanova, M. Vavilova, M. Nikolova, R. Ognyanov. 1987. Tectonic zoning. – In: Bokov, P., Ch. Chemberski (Eds). *Geological Premise for the Oil-gas Bearing of the Northeast Bulgaria*. Tehnika, Sofia, 109–119 (in Bulgarian).

Bonchev, E. 1955. *Geology of Bulgaria. Volume 1*. Nauka i Izkustvo, Sofia, 264 p. (in Bulgarian).

Bochev, S., B. Strachimirov, S. Zafirov, R. Christov, M. Moev. 1967. Gèologie de la region litorale de Stara Planina d'Est . – *Ann. Ecol. Super. Min. et Gèol. Sofia*, *12*, Fasc. II, Geology, 7–62 (in Bulgarian with French abstract).

Botev, B. 1953. Sur la géologie de la partie la plus orientale de la Stara Planina de l'Est. – *Bull. Inst. Géol. Acad. Sci. Bulg.*, *2*, 3–26 (in Bulgarian with French abstract).

Dabovski, H., I. Zagorchev. 2009. Alpine tectonic subdivision of Bulgaria. – In: Zagorchev, I., H. Dabovski, T. Nikolov (Eds). *Geology of Bulgaria. Part II. Mesozoic Geology*. "Prof. Marin Drinov" Publishing House, Sofia, 30–37 (in Bulgarian with English abstract).

Gočev, P. 1932. Geologische Beobachtungen an der Küste des Schwarzen Meres zwischen der Mündung der Kamčija und Kap Emine.– *Rev. Bulg. Geol. Soc.*, *4*, 3, 200–213 (in Bulgarian with German abstract).

Juranov, S., H. Pimpirev. 1989. Lithostratigraphy of the Upper Cretaceous and the Paleogene in the coastal part of East Stara Planina. – *Rev. Bulg. Geol. Soc.*, *50*, 2, 1–18 (in Bulgarian with English abstract).

Juranov, S., D. Sinnyovsky, D. Vangelov, H. Pimpirev, M. Antonov, V. Jelev, G. Baltakov, I. Choleev. 1994. *Report on the Results of a Geological Task "Geological and Geomorphological Mapping at a Scale 1:25000 in a Part of East Balkan between Emine Cape and the Village of Staro Oryahovo"*. National Geological Fund, Report IV-411, 408 p. (in Bulgarian, unpublished)

Kanchev, I. 1971. East Balkan tectonic zone (Flysch Balkan). – In: Yovchev, Y. (Ed.). *Tectonic Structure of Bulgaria*. Tehnika, Sofia, 389–407 (in Bulgrian with English abstract).

Karagjuleva, J., V. Kostadinov. 1977. Geological structure of the eastern part of the Luda Kamčija Zone. – *Geotecton., Tectonophys., Geodynam.*, *7*, 42–75 (in Bulgarian with English abstract).

Nachev, I. 1977. Emine Flysch and the olistostromes in the Sliven Balkan. – *Palaeontol., Stratigr., Lithol.*, *7*, 45–58 (in Bulgarian with English abstract).

Nachev, I., E. Dimitrova. 1995. Upper Cretaceous stratigraphy of the Eastern Balkan Mountains. – *Geologica Balc.*, *25*, 5–6, 43–74.

Radev, J. 1927. East Stara Planina and the Kamchiya River valley. – *Ann. Univ. de Sofia*, *Fac. hist. et philosoph.*, *23* (in Bulgarian).

Sinnyovsky, D. 2003. Five protected outcrops of the Cretaceous/Tertiary boundary in Bulgaria. – *Ann. Univ. Min. and Geol.*, *46*, Part I, 141–147.

Sinnyovsky, D. 2004. Nannofossil subdivision and stratigraphic range of the Emine Flysch Formation in East Balkan, East Bulgaria. – *Ann. Univ. Min. and Geol.*, *47*, Part I, 131–137.

Sinnyovsky, D., A. Sultanov. 1994. Biostratigraphy and sedimentology of the Emine Flysch Formation in the nearshore part of the East Balkan. – *C. R. Acad. bulg. Sci.*, *47,* 1, 73–76.

Sinnyovsky, D., K. Stoykova. 1995. Cretaceous/Tertiary boundary in the Emine Flysch Formation, East Balkan (Bulgaria). – *C. R. Acad. bulg. Sci.*, *48*, 3, 45–48.

Stoykova, K., M. Ivanov. 2004. Calcareous nannofossils and stratigraphy of the Cretaceous/Tertiary transition in Bulgaria. – *J. Nannoplankton Res.*, *26*, 1, 47–61.

Sultanov, A., S. Juranov, D. Sinnyovsky, E. Chuparova. 1990. *Final report on contract 989: "Stratigrapgy and sedimentology of the Upper Cretaceous and Paleogene in NE Bulgaria, the coastal part of East Stara planina, and the Bourgas synclinorium"*. Scientific Fund of the University of Mining and Geology "St. Ivan Rilski", Sofia, 537 p. (in Bulgarian, unpublished)

Valchev, B. 2006. K/T boundary in the turbidite sequence of the Emine Formation near Kozichino Village, Bourgas District (Eastern Balkan): foraminiferal assemblages. – *Ann. Univ. Min. and Geol.*, *49*, Part I, 137–142.

MAIN FAULT ZONES CONTROLLING THE LATE ALPINE STRUCTURE IN THE AREA EAST OF SOFIA (SREDNOGORIE ZONE, WESTERN BULGARIA)

Ianko Gerdjikov[1], Dian Vangelov[1], Alexandre Kounov[2]

[1] *Sofia University "St. Kliment Ohridski", 1504 Sofia; janko@gea.uni-sofia.bg*
[2] *Department of Environmental Science, Basel University, CH-4056 Basel; a.kounov@unibas.ch*

ABSTRACT. The northwestern narrow tip of the Upper Cretaceous Panagyurishte sedimentary strip is cropping out along the eastern-north-eastern margin of the Neogene Sofia graben. In this area the sedimentary strip is split in two parts separated by an uplifted pre-Upper Cretaceous basement block. Both parts show syncline geometries with cores built of Upper Cretaceous rocks. The synclines are striking NW-SE and are extremely asymmetrical with vertical to overturned southwestern limbs. Within the overturned limbs meso-scale structural features such as imbrications, folds and small-displacement faults indicate strong flattening of the rock volume under generally top-to-the-N shear. These features were observed along the Kamenitsa-Rakovishki and Negushevo fault zones. Due to the relatively poor outcrop conditions the precise dips of these fault zones are still poorly known and there are no data about the fault cores. Thus, the general north-vergent character of the both fault zones is assumed on the basis of the semi-penetrative small-scale structures within their immediate footwalls and field relations. Our new data suggest that the northward translations along the Negushevo fault zone resulted in formation of approx. 30 long and 2 km wide basement uplift.

Keywords: Late Alpine tectonics, fault zones, Upper Cretaceous, Srednogorie

ГЛАВНИ РАЗЛОМНИ ЗОНИ КОНТРОЛИРАЩИ КЪСНОАЛПИЙСКАТА СТРУКТУРА В РАЙОНА НА ИЗТОК ОТ СОФИЯ (СРЕДНОГОРСКА ЗОНА, ЗАПАДНА БЪЛГАРИЯ)

Янко Герджиков[1], Диан Вангелов[1], Александър Кунов[2]

[1] *Софийски университет "Св. Климент Охридски",1504 София*
[2] *Департамент науки за природната среда, Университет Базел, CH-4056 Базел*

РЕЗЮМЕ. В източната и североизточна периферия на неогенския Софийски грабен се разкрива северозападният завършек на горнокредната Панагюрска ивица. На изток тя има монолитен характер, докато на запад (в изследвания район) е разделена на две части от издигнат блок на до-горнокредната подложка. И в двете части на ивицата пластовете на пост-херцинската подложка оформят синклинални гънки с ядра, изпълнени от горнокредни седименти. Синклиналите са с посока на осите NW-SE и са силно асиметрични с вертикални или преобърнати югозападни бедра. В тези гънкови бедра мезомащабни структури като имбрикации/дуплекси, гънки и малкоамплитудни разломи индикират силно изтискване на разреза и насочени към север срязвания. Регионално проявеното преобръщане или вертикализирането на разрезите, както и формирането на мезомащабните структури свързваме с транслациите по Каменишко-Раковишката и Негушевската разломни зона. Поради относително слабата разкритост, установяването на точния наклон на тези зони е невъзможно, а също така няма данни за строежа и особеностите на разломните ядра. Поради това северновергетният характер на тези две разломни зони се мотивира на базата на наличието на почти проникващите мезомащабни структури в обемите на техните непосредствени лежащи блокове, както и на някои теренни данни. Вероятно северно насочените транслации по Негушевската зона са довели до формирането на издигане на фундамента, приблизително 30 km дълго и 2 km широко, което е довело до разделянето на горнокредната ивица на две части.

Ключови думи: късноалпийска тектоника, разломни зони, Горна Креда, Средногорие

Introduction

Economically important Upper Cretaceous rocks, part of the large Apuseni-Banat-Timok-Sredna Gora volcano-sedimentary belt (Gallhofer et al., 2015), is traced from the area of the town of Panagyurishte to the NE margin of the Neogene Sofia graben in Western Bulgaria. Known as Panagyurishte strip (Bončev, 1940), this belt incorporates Upper Cretaceous sediments, volcanic and magmatic rocks as well as locally uplifted blocks of pre-Upper Cretaceous basement. All rocks are often strongly deformed and since the pioneering works of Poushkarov (1927) and Dimitrow (1936) the presence of upright regional-scale folds is well-documented. While in the area of Panagyurishte the Upper Cretaceous rocks form a coherent unit, to the NW, the Panagyurishte strip is split into two branches separated by the uplifted prominent basement block (Fig. 1). Two important tectonic zones are marking the southern margins of both branches. The aim of the current contribution is to re-evaluate their character and significance on the basis of new structural studies and tectonic analysis.

Geological setting

Key elements of the Alpine structures cropping out along the eastern margin of Neogene Sofia graben are NW-SE to E-W trending fault zones that juxtapose pre-Alpine basement to the rocks of the Cretaceous cover. The northern zone is Negushevo fault zone (Bontscheff, 1910) while the southern one is known as Kamenitsa-Rakovishki fault zone (Fig. 1; Poushkarov, 1927; Bončev, 1940; Iliev, Katskov, 1990;

Katskov, Iliev, 1993). Despite the fact that they have been known for about a century (Poushkarov, 1927; Ivanov, 1940; Bončev, 1940) and detailed geological mapping was done in the area (Tzankov, 1961), almost nothing is known about their exact geometry and kinematics. Since the earliest studies it has been suggested that these main fault zones are rather steep to almost vertical. Without providing new structural data Angelov et al. (1992; 1995) interpreted them as reverse faults and drew highly mobilistic picture of extremely imbricated thrust stack. Another model was suggested by Ivanov (1998, 2017) who reinterpreted Kamenishko-Rakovishka zone as a major strike-slip fault.

In the study area the pre-Alpine basement consists of several Variscan units, whereas the high-grade gneiss-dominated unit has the largest areal extent (Pirdop gneiss complex – Angelov et al., 2010c, d; Central Srednogorie High-grade Metamorphic Complex – CSHGMC – this work).

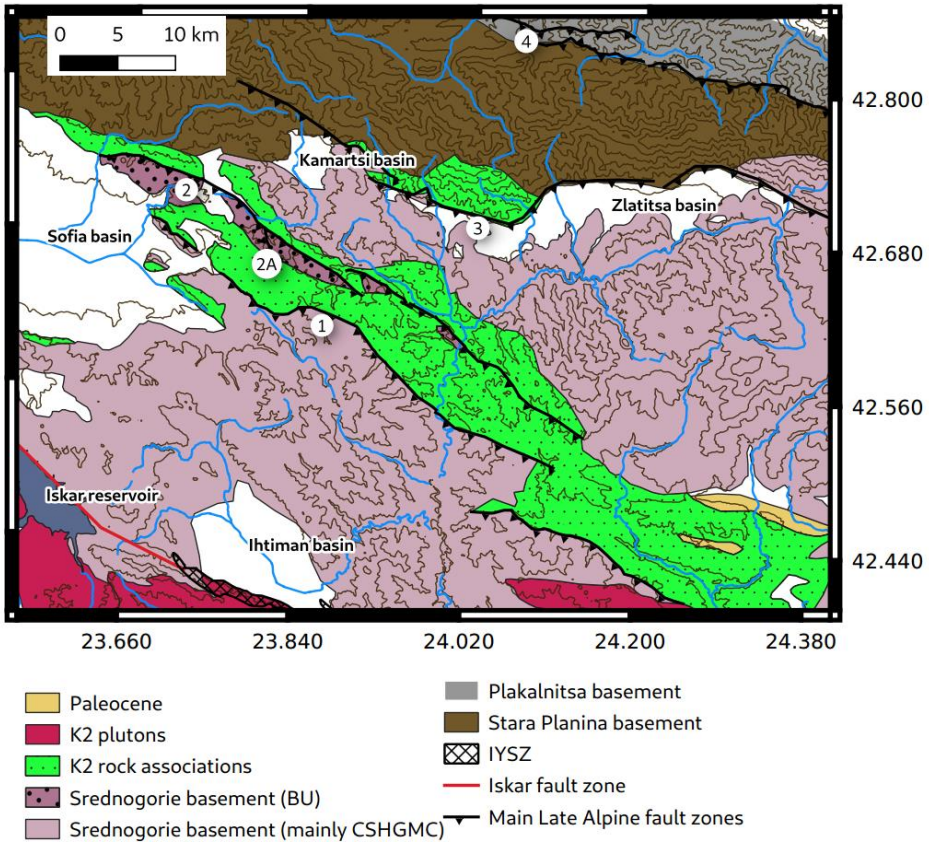

Fig.1. Tectonic sketch of a part of the Srednogorie Zone east of Sofia
Numbers: *1*, Kamenitsa-Rakovishki fault zone; *2*, Negushevo fault zone; *2A*, Upper imbricate of Negushevo zone, south of Makotsevo village; *3*, Mirkovo fault zone; *4*, Plakalnitsa fault zone. Abbreviations: *BU*, Basement Uplift; *CSHGMC*, Central Srednogorie High-Grade Metamorphic Complex; *IYSZ*, Iskar-Yavorishka Shear Zone

This unit is tectonically covered by a low-grade Frolosh unit which in the studied area consists mainly of "green rocks" – various in composition and fabric metabasic rocks. The uppermost position in the Variscan basement is built of weakly metamorphosed sediments – metapelites, metasiltstones and quartzites. Based on lithological similarities these rocks are considered as part of the Ordovician Grohoten Formation (Angelov et al., 2010c, d).

Triassic and Jurassic rocks are locally preserved. Details about Upper Cretaceous stratigraphy can be found in Angelov et al. (1992), Sinnyovsky (2005) and Angelov et al. (2010c, d).

Preliminary tectonic analysis and preparation for field work

Initial desktop GIS-based study was conducted as a first step of our research. We analysed all available map and cross-section data and they were incorporated into a GIS project. The geological data were cross checked against satellite and aerial imagery, thus allowing to delineate properly some geological boundaries. Since no precise descriptions about the dips of the main fault zones are available, geometric calculations were applied using three point problem method of the GeolMapDataExtractor software (Allmendinger, Judge, 2013).

The main results of this initial analysis are the following: 1) Remote sensing analysis clearly indicates that the existing geological maps (Angelov et al., 1992; Angelov et al., 2010a, b, c, d) do not show the real aerial extent of the Quaternary deposits. And this was confirmed via ground-truth collected data that also indicate that the aerial extent of the Miocene-Quaternary cover is much larger. The presented map (Fig. 2) is an attempt to show the real distribution of pre-Miocene basement. 2) Data analysis allow to propose synthesis of Late Alpine tectonics of the area (presented below) 3) Areas were delineated, where good outcrop can be expected to provide the necessary structural data.

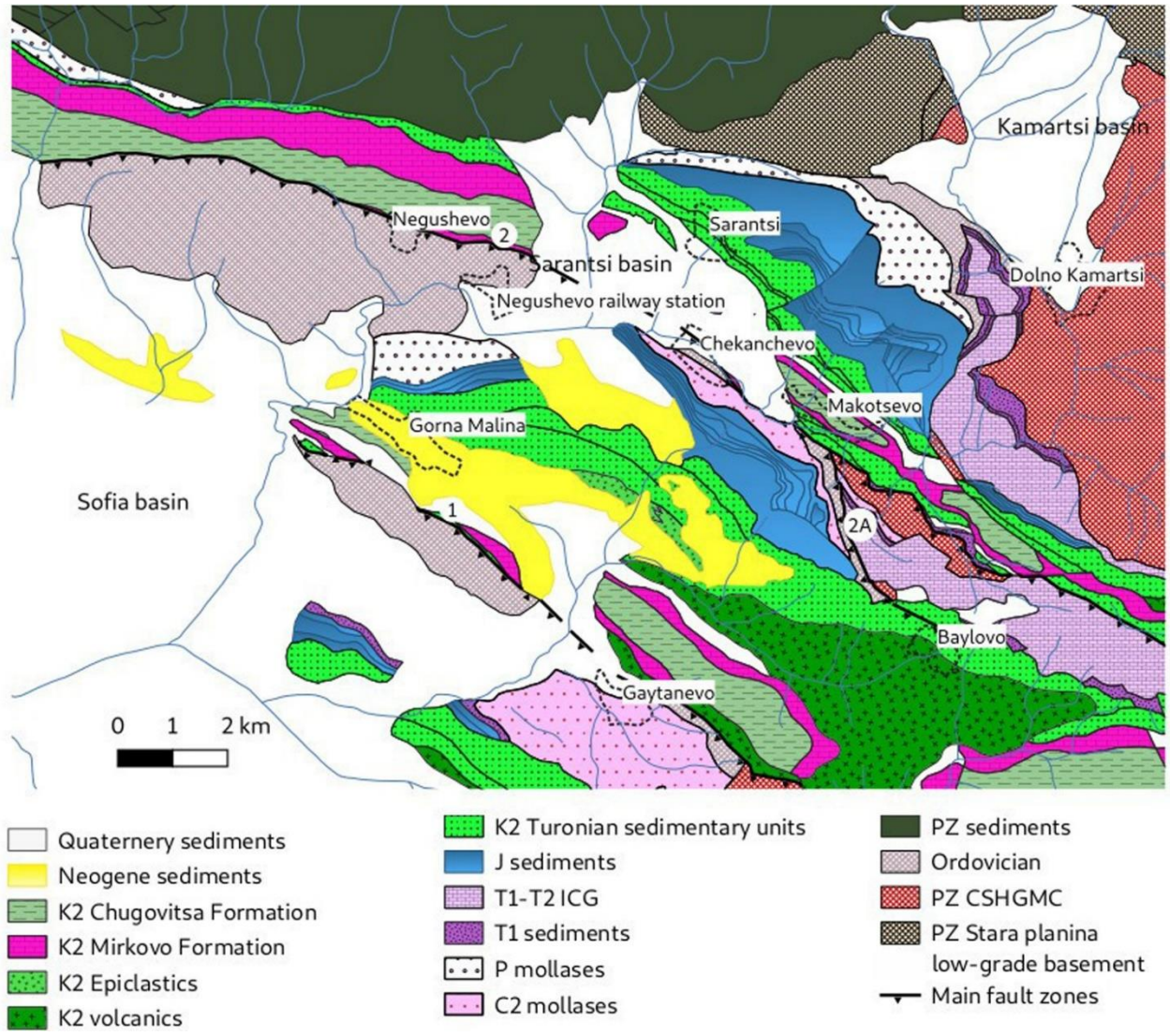

Fig. 2. Geological map with simplified stratigraphy and fault network
Numbers: *1*, Kamenitsa-Rakovishka fault zone; *2*, Negushevo fault zone; *2A*, Upper imbricate of Negushevo zone. Abbreviations: *CSHGMC*, Central Srednogorie High-Grade Metamorphic Complex

Field data

Situated at the margin of the Neogene Sofia graben, large part of the area is covered by Miocene and Quaternary sediments and their basement is cropping out sporadically, with the exception of the southern foot of Stara Planina Mountain. Field work was conducted along several profiles, oriented orthogonal to the strike of the main fault zones.

Kamenitsa-Rakovishki fault zone

In the studied area this zone is marked by the contact between the Ordovician basement and Upper Cretaceous rocks. Due to poor outcrop conditions it is impossible to observe the exact contact. The trace of the zone can be approximately mapped using sporadic outcrops and floating pebbles in the soil. Following its trace on the map and considering the steep dip of the Upper Cretaceous sediments it could be suggested that it is steeply dipping to the S. Only in one locality, SW of the village of Gorna Malina (E 23.68186, N 42.69218), the contact can be observed. Here, the Ordovician quartzites are juxtaposed to the Turronian sandstones along almost vertical contact. Unusually, strain localisation was not observed either on the very contact or within 2–3 metres of both sides of the contact.

Numerous structural data indicate that the Upper Cretaceous rocks from the footwall record strong shortening. On outcrop-scale this is marked by presence of cm-metre scale folds, often pronounced cleavage and presence of small-scale crosscutting bedding faults. Very informative outcrops were studied in the area SW of the village of Gorna Malina. Here Ordovician rocks are in contact with Turronian sandstones, siltstones and sandy limestones. Siltstones are penetratively cleaved and in some levels shallowly dipping to the S, SW, striated fault planes are rather common. They strongly resemble S1-C' fabric (Fig. 3).

Calcite fibres, as well as deflections of the cleavage toward the fault planes, indicate top-to-the N, NW sense of shear. In other cases (Fig. 4) striated fault planes are parallel to the penetrative cleavage. In rare cases, again in weaker siltstone lithologies, imbricated or duplex structures, indicating top-to-the N, NW shear are observed.

Fig. 3. Strongly cleaved (S1) sandstone with numerous shallow dipping to SW shear surfaces (white arrows) indicating top NW shear (E 23.68263675, N 42.69177306)

Fig. 4. Penetrative cleavage within siltstones and striated fault planes (arrows). Same locality

North of the village of Gajtanovo the immediate footwall of Kamenishko-Rakovishka zone is built by pinkish limestones belonging to the Mirkovo Formation. Bedding measurements indicate presence of decametre-scale tight upright folds with subhorizontal axes, trending parallel to the fault zone and axial planes being either vertical or steeply dipping to the S, SW. In an old excavation a mesoscale fold illustrates well this style of deformation (Fig. 5).

Fig. 5. Upright fold with axes 320/5. North of Gaytanevo village

Negushevo fault zone

In the area of Negushevo village the zone is traced along the contact between the Ordovician low-grade metasediments and the Upper Cretaceous sediments. North of Negushevo railway station the Ordovician succession is represented by greenish phyllites and grey, fine grained quartzites. Unfortunately, in the massive quartzites bedding and foliation have not been recognized. In the vicinity of the contact foliation the phyllites are dipping steeply (60–78°) to the S. Closer to the contact, the Upper Cretaceous sequence is represented by the red limestones of the Mirkovo Formation. The only place where close relations between the Ordovician and the Upper Cretaceous sediments can be observed is a section along the road to Negushevo village that continue along unpaved road (E 23.71998, N 42.72370). There the Ordovician phyllites are steeply dipping to the S. At the beginning of the unpaved road grey quarzites are cropping out. About 2 m northward (after an interval covered by soil and debris), below the Ordovician quartzite, strongly cleaved Upper Cretaceous red limestones are cropping out, whereas the contact between the two units was not observed. Cleavage is dipping steeply 70–80° to the south.

Eastwards, after being covered by the thin Quaternary cover of Sarantsi graben, the fault zone re-emerges in the SE outskirts of the village of Chekanchevo. Here, the Ordovician quartzites form spectacular outcrop just S of the centre of the village. On the easternmost margin of the village the Ordovician phyllites build the top of a small hill. Down-slope, to the north, after several metres covered interval there are outcrops of grey marly limestones, probably belonging to the Mirkovo Formation (E 23.77855, N 42.70023). The primary bedding is not recognizable as the main fabric is penetrative cleavage with steep (75°) dip to the S. These relations unambiguously indicate that the fault zone is steeply dipping to the S.

Further eastward the geometry of the fault zone is more complicated and it is represented by a splay of two or three stacked imbricates. Here, in the area south of Makotsevo village, field data, as well as calculation made by GeolMapDataExtractor software suggest that the Variscan basement (Ordovician rocks and CSHGMC) structurally overlie, along moderately dipping to the S (SW) contact, different units of the Upper Cretaceous succession. The upper thrust slab (labelled 2A in Fig. 1 and 2) is characterised by

normal stratigraphic succession: the lowermost part is built by thin (up to tens of metres) level of Ordovician phyllites and quartzites that are covered by coarse grained, red Upper Carboniferous molasse-type sediments. These rocks are covered by complete Jurassic succession. Internal deformation within this thrust slab was not observed. Strongly cleaved Turonian rocks or older Mezosoic units are building up the immediate footwall of the Upper imbricate.

The lower thrust imbricate emplaces Variscan gneisses (CSHGMC) and their Mezosoic cover onto various units of Upper Cretaceous sequence. According to Bončev (1940) and Angelov et al. (2010c, d) this is an independent fault zone called Frelin thrust that just by coincidence merges to the NW perfectly with Negushevo fault zone (cf. maps in the cited above publications). Our preferred interpretation is that the main fault zone is represented by the lower imbricate, thus we interpret Negushevo zone as NW-SE trending Late Alpine fault that probably merges further SE with Petrich fault (Bončev, 1940).

Synthesis of Late Alpine tectonics

Field data as well as calculations made using the GeolMapDataExtractor software indicate that both Kamenitsa-Rakovishki and Negushevo fault zones are steeply dipping to the south. The precise angle is difficult to estimate, and of course, for some of the segments of these zones, later reactivations which have changed the original dip cannot be excluded. Such reactivation seems the most plausible explanation also for the observed lack of intensive deformation at the supposed position of Kamenitsa-Rakovishki zone SW of the village of Gorna Malina. In most of the cases the dips of the fault zones are steep (>60°) and only in the area S of Makotsevo village the dip of Negushevo fault zone is moderate.

Fault cores of both zones are not cropping out, but on the basis of the character of small-scale structures in their footwalls (the case of Kamenishka-Rakovishka zone) and field relationships between the Variscan basement and the Upper Cretaceous sediments around villages of Makotsevo and Chakanchevo (the case of Negushevo zone) they can be regarded as N-NE-vergent compressional fault zones. The small-scale structures include decimetre-metre scale imbricate structures, stacks of lineated fault surfaces, north-vergent shear-related folds, etc. Our data indicates that in a number of cases these structures are often found in the immediate footwalls of the main fault zones. These findings are complemented by similar observations in the area of Topolnitsa River.

In a regional scale the Upper Cretaceous sequences form footwall synclines with subhorizontal axes trending parallel to the main fault zones. The synclines are strongly asymmetrical and have both overturned or vertical southern limbs and normal northern limbs. Greater complexity is typical for the inverted limbs while northern limbs, in most cases, preserve intact stratigraphy that can be used as a key to decipher the nature of the stratigraphic sequences within the different parts of the Upper Cretaceous basin. Features as inverted sequences, presence of strongly sheared domains, etc., all indicate that southern limbs are affected by secondary top-to-the-north faulting. Recently Butler et al. (2018) made a detailed review of the structural complexities and the possibilities for multiple structural scenarios in the similar thrust footwalls setting. Although not so well outcropped, the lack of significant late overprint of the immediate footwalls of both compressional fault zones in our studied area provides important insights into such complicated setting described by Butler et al. (2018). For example, our new data can further help constraining structural geometry and evolution in the footwall of Mirkovo fault zone (Fig. 1) – a zone severely overprinted by Miocene–Quaternery normal faulting.

The synclines (Makotsevo-Smolsko, Negushevo and Belopopsko-Kamenishka) have been known since pioneering researches in the area (Ivanov, 1940; Tzankov, 1961), but it must be noticed that they do not form classic syncline-anticline pairs as suggested previously (Tzankov, 1961; Angelov et al., 2010a, b, c, d), because the anticlines are simply not existing. What was described as anticlines (Babutitza-Voynyashka and Srednogorska) are actually south-dipping monoclines underlined by top-to-the-N fault zones (Negushevo and Mirkovo zones, Fig. 1). The origin of regional uplift at the place of the so called Babutitsa-Voynyashka anticline can be related to the uplift in the immediate hanging wall of the Negushevo fault zone. Such uplift is responsible for the division of the Panagyurishte sedimentary strip into two branches and the strong squeezing of the Upper Cretaceous sequences in the northern branch (especially pronounced north of Negushevo).

The relative timing between folding and movements along the main fault zones has long been commented. Recently, it was explicitly stated that the folding of Upper Cretaceous sequence and the movements along the main fault zones are temporarily distinct events (Angelov et al., 2010a, b) – the first one regarded as a result of the Laramian (latest Cretaceous) deformation, while the second one – as a product of the Iliryan (Eocene) compression. Despite being not conclusive, our data fit better with a model of simultaneous formation of these two types of structures. This is in line with the original ideas of Bončev (1940) and interpretations of Ivanov (1998; 2017).

The proposed tectonic synthesis is a product of ongoing research that must be further supplemented by balanced cross-sections and shortening estimates (work in progress, not presented here). As often in such models it will probably require further changes in the interpretations as a result of acquired new data.

Acknowledgments. The study was realized within the frame of the project funded by the Sofia University Scientific Foundation "Spatial and temporal distribution of the peri-Thethys CORB facies (Cretaceous Oceanic Red Beds) in parts of Central and Western Srednogorie tectonic zone", Grant 2570/2019.

References

Allmendinger, R. W., P. A Judge. 2013. Stratigraphic uncertainty and errors in shortening from balanced sections in the North American Cordillera. – *Geol. Soc. Am. Bull.*, *125*, 9–10, 1569–1579.

Angelov, V., K. Iliev, I. Haidutov, S. Yanev, R. Dimitrova, I. Sapunov, P. Chumachenko, Ts. Tsankov, D. Chunev, I. Rusanov. 1992. *Geological Map of Bulgaria on Scale 1:100000. Botevgrad Map Sheet*. Committee of Geology

and Mineral Resources, Enterprise of Geophysical Survey and Geological Mapping, Sofia.

Angelov, V., K. Iliev, I. Haidutov, I. Sapunov, P. Chumachenko, D. Chunev, Ts. Tsankov, R. Marinova, I. Rusanov, S. Yanev. 1995. *Explanatory Note to the Geological Map of Bulgaria on Scale 1:100000. Botevgrad Map Sheet*. Committee of Geology and Mineral Resources, Geology and Geophysics, Sofia, 117 p. (in Bulgarian with English abstract).

Angelov, V., M. Antonov, S. Gerdzhikov, P. Petrov, S. Tanatsiev, H. Kiselinov, R. Marinova, V. Valev. 2010a. *Geological Map of Bulgaria. Scale 1:50000. K-34-48-B (Elin Pelin) Map Sheet*. Ministry of Environment and Water, Bulgarian Geological Survey, Sofia.

Angelov, V., M. Antonov, S. Gerdzhikov, P. Petrov, H. Kiselinov, S. Tanatsiev, R. Marinova, V. Valev. 2010b. *Explanatory Notes to the Geological Map of Bulgaria. Scale 1:50000. K-34-48-B (Elin Pelin) Map Sheet*. Ministry of Environment and Water, Bulgarian Geological Survey, Sofia, 71 p.

Angelov, V., M. Antonov, P. Petrov, S. Gerdzhikov, S. Tanatsiev, H. Kiselinov, V. Vulev. 2010c. *Geological Map of Bulgaria. Scale 1:50000. K-34-48-Г (Etropole SW) Map Sheet.* Ministry of Environment and Water, Bulgarian Geological Survey, Sofia.

Angelov, V., M. Antonov, S. Gerdzhikov, P. Petrov, H. Kiselinov, S. Tanatsiev, V. Vulev. 2010d. *Explanatory Notes to the Geological Map of Bulgaria. Scale 1:50000. K-34-48-Г (Etropole SW) Map Sheet.* Ministry of Environment and Water, Bulgarian Geological Survey, Sofia, 72 p.

Bončev, E. 1940. Über die Geologie des Bajlovo Teiles der Panagjuriste-Zone der Srednogorie unter Berucksichtingung der Tektonik dieser Zone. – *Rev. Bulg. Geol. Soc.*, *11*, 205–238 (in Bulgarian with German abstract).

Bontscheff, S. 1910. Die Leitlinien der Geologischen Bau des Westlichen Balkans. – *Trav. Soc. Bulg. Sci. Nat.*, *4*, 1–59 (in Bulgarian, with German abstract).

Butler, R. W., C. E. Bond, M. A. Cooper, H. Watkins. 2018. Interpreting structural geometry in fold-thrust belts: Why style matters. – *J. Structural Geology*, *114*, 251–273.

Dimitrow, Z. 1936. Die westliche Verbindung zwischen Balkan und Sredna-Gora. – *Ann. Univ. de Sofia. Fac. Physico-mathematique*, *32*, Liv. 3, 175–208.

Gallhofer, D., A. von Quadt, I. Peytcheva, S. Schmid, A. C. Heinrich. 2015. Tectonic, magmatic and metallogenic evolution of the Late Cretaceous Arc in the Carpathian-Balkan orogen. – *Tectonics*, *34*, 1813–1836.

Ivanov, L. 1940. Beitrag zur Geologie des westlichen Teiles der Panagjurište-Zone der Srednogorie zwischen dem Dorfe Buhovo und dem becken von Saranci. – *Rev. Bulg. Geol. Soc.*, *11*, Festschrift, Prof. Dr Stefan Bončev zu Seinem 70-Geburtstag, 195–204 (in Bulgarian with German abstract).

Ivanov, Ž. 1998. *Tectonics of Bulgaria*. Professorship thesis, Sofia University “St. Kliment Ohridski”, Sofia, 579 p. (in Bulgarian)

Ivanov, Ž. 2017. *Tectonics of Bulgaria*. Sofia, University Publisher, Sofia, 271 p. (in Bulgarian)

Iliev, K., N. Katskov. 1990. *Geological Map of PR Bulgaria on Scale 1:100000. Ihtiman Map Sheet*. Sofia, Committee of Geology and Mineral Resources, Enterprise of Geophysical Survey and Geological Mapping.

Katskov, N., K. Iliev. 1993. *Explanatory Notes to the Geological Map of the Republic of Bulgaria on Scale 1:100000. Ihtiman map sheet*. Sofia, Committee of Geology and Mineral resources, Enterprise of Geophysical Survey and Geological Mapping, 63 p. (in Bulgarian with English abstract)

Poushkarov, N. 1927. Study of the geological structure of the western link between the Balkan and Sredna Gora Mountain. – *Contr. Bulg. Sci. Agricult. Inst.*, *14*, 1–44 (in Bulgarian).

Sinnyovsky, D. 2005. Campanian nannofossil zones in the Mediterranean Upper Cretaceous in Sofia Balkan between Buhovo, Jelyava and Eleshnitsa. – *Ann. Univ. Mining and Geol.*, *48*, Part I, 123–128.

Tzankov, Tz. 1961. Notizen über die Tektonik des Gebietes von Galabec und der angrenzenden Teile. – *Trav. Geologie de Bulgarie, Ser. stratigraphie et tectonique*, 2, 183–202 (in Bulgarian with German abstract).

GEODIVERSITY OF KHIBINY MOUNTAINS IN KOLA PENINSULA, NORTH-EASTERN FENNOSCANDIA AS A BASIS FOR GEOPARK DEVELOPMENT

Dimitar Sinnyovsky[1], Dimka Sinnyovska[1], Natalia Kalutskova[2], Nikolai Dronin[2], Natalia Telnova[3], Andrei Medvedev[3]

[1] University of Mining and Geology "St. Ivan Rilski", 1700 Sofia; sinsky@mgu.bg
[2] Moscow State University "M. V. Lomonosov", 119991 Moscow; nat_nnk@mail.ru
[3] Geographical Institute, Russian Academy of Sciences, 119017 Moscow; a.a.medvedeff@gmail.com

ABSTRACT. Geodiversity of the Khibini Mountains has two main aspects: petrographic/mineralogical and geomorphological. The first aspect makes this low mountain massif situated in the central part of the Kola Peninsula, in the northwestern part of the Russian Federation, world famous for its enormous mineral diversity and the richest apatite-nepheline ore deposits in the world. As a part of the Baltic shield, it is built mainly of Lower Palaeozoic crystalline rocks and represents an intrusive alkaline massif in the contact of granulite-gneiss complexes of the Archaen Kola Series (Central Kola megablock, including the oldest rocks in Europe) and Proterozoic Imandra-Varzuga volcanogenic-sedimentary belt. More than 1000 mineral species are found in Khibiny Mountains and 115 of them are described for the first time in the world. The second aspect, the geomorphological diversity of Khibiny Mountains with high aesthetic value, reflects their complex glaciation history including various glacial formations such as cirques, glacier valleys, different types of moraines, fluvioglacial deposits, relict and contemporary cryogenic formations. For a long time Khibiny Mountains have been a very popular place among geotourists. Several popular geotrails transecting Khibiny allow to visit also old abandoned mining sites of rare-elements. There are two geological museums in the local towns of Kirovsk and Apatity with great collections representing the unique Khibiny minerals and rocks.

Keywords: Kola Peninsula, Khibini Massif, geodiversity

ГЕОРАЗНООБРАЗИЕТО НА ХИБИНСКИТЕ ПЛАНИНИ В КОЛСКИЯ ПОЛУОСТРОВ, СЕВЕРОИЗТОЧНА ФЕНОСКАНДИЯ, КАТО ОСНОВА ЗА РАЗРАБОТВАНЕ НА ГЕОПАРК

Димитър Синьовски[1], Димка Синьовска[1], Наталия Калуцкова[2], Николай Дронин[2], Наталия Телнова[3], Андрей Медведев[3]

[1] Минно-геоложки университет "Св. Иван Рилски", 1700 София
[2] Московски държавен университет "М. В. Ломоносов", 119991 Москва
[3] Географски институт, Руска академия на науките, 119017 Москва

РЕЗЮМЕ. Георазнообразието на Хибинските планини има два главни аспекта: петрографско/минераложки и геоморфоложки. Първият аспект прави този нископланински масив, разположен в централната част на Колския полуостров в северозападната част на Руската федерация, световно известен с огромното си минерално разнообразие и най-богатите апатит-нефелинови руди в света. Като част от Балтийския щит, той е изграден главно от палеозойски нискометаморфни кристалинни скали и представлява интрузивен алкален масив на контакта на гранулито-гнайсовите комплекси от архайската Колска серия (Централен Колски мегаблок, включващ най-старите скали в Европа) и протерозойския вулканогенно-седиментния пояс Имандра-Варзуга. В Хибинските планини са открити над 1000 вида минерали, 115 от които са описани тук за пръв път в света. Вторият аспект, геоморфоложото разнообразие на Хибинските планини с висока естетическа стойност, отразява сложната им ледникова история, включваща ледникови релефни форми като циркуси, различни видове морени, флувиоглациални отложения, реликтови и съвременни криогенни образувания. От доста време Хибинските планини са много популярно място сред геотуристите. Няколко популярни геопътеки, пресичащи Хибините, позволяват да се посетят стари изоставени рудници за редки елементи. В местните градове Кировск и Апатити има два геоложки музея с богати колекции, представящи уникалните хибински минерали и скали.

Ключови думи: Колски полуостров, Хибински масив, георазнообразие

Introduction

The Khibiny Mountain massif (Fig. 1) is within the Polar circle in the central part of the Kola Peninsula between Imandra and Umbozero Lakes. The morphology of the massif is low mountainous with the highest peak Yudichvumchor (1200 m) which is rounded and flat, as most of the peaks in the mountain. Their slopes are steep with numerous firn fields, cirques and small glaciers. There are many remnants of the Quaternary glacial history in the area. During glaciation, the mountain valleys are widened, deepened and smoothed to form a U-shaped glacial troughs, as it is sometimes. At the end of the glacial valleys, where the glaciers left the mountain and flowed into the polar ice shield, triangular-shaped cliffs, called truncated spurs, were formed.

From geological point of view this massif is a part of the Baltic (Fennoscandian) Shield belonging to the East European Craton, representing a large part of Fennoscandia, northwestern Russia and the northern Baltic Sea. It is composed mostly of Archean and Proterozoic gneisses,

greenstones and other high-grade metamorphic rocks including the oldest rocks of the European continent.

The Baltic Shield yields important industrial minerals and ores, such as those of iron, nickel, copper and rare metals. The development of rich apatite deposits in the Khibiny Mountains begins after the geological study of the famous Russian mineralogist A. E. Fersman during the 20–30th years of the twentieth century. Fersman is the founder and chairman of the Khibiny research mountain station of the USSR Academy of Sciences "Tietta" (1930–1938), later transformed into the Kola branch of the USSR Academy of Sciences (now Kola Scientific Centre of the Russian Academy of Sciences). Fersman's expeditions discovered the Khibiny apatite deposits, the world's largest apatite deposits.

Fig. 1. The Khibiny Mountain is a low mountainous massif in the centre of the Kola Peninsula with rounded peaks, glacier valleys and cirques

Geological setting

The Kola Peninsula is the north-eastern suburb of the Baltic shield. It is built mainly of lower Paleozoic, Proterozoic and Archean crystalline rocks, among which are the oldest rocks in Europe. Structurally it is divided into 4 parts: the Murmansk Block (along the Barents Sea), built of Archean and lower Proterozoic rocks; Belomorian Block (southwestern and southern parts of the peninsula), built of Archean Belomirian rocks; Granulite belt (northwest) and Karelitic geosyncline folded zone (in the central part) formed through the early and middle Proterozoic.

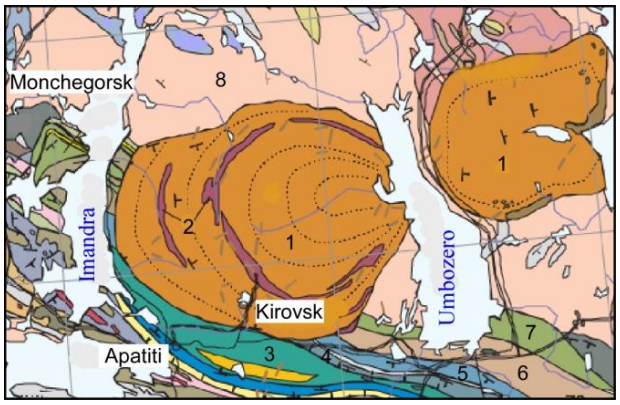

Fig. 2. Geological map of the Khibini Mountain (after Mitrofanov, 2001): *1*, nepheline syenite (Devonian); *2*, alkaline dykes, pikrit, kimberlite, carbonatite (Devonian); *3–7*, Lower Proterozoic (Kalevian-Sumian): *3*, basalt-porphyry, diabase (Kalevian); *4*, diabase, basalt-andesite-porphyry (Yatulian), *5*, pikrit-diabase porphyry (Sariolian), *6*, riolite-dacite, dacite, andesite-dacite (Sumian), *7*, basalt-porphyry, mandelsteine, diabase (Sumian); *8*, Upper Archean (Lopian) – granodiorites, tonalities, enderbites

The Khibini Mountains represent an intrusive massif composed of nepheline syenites, to which rich apatite-nepheline deposits, such as Kukisvumchor, Yukspor, Radvumchor, etc., are attached. It is an approximately 350 Ma-old multiphase intrusive with the total area of 1327 km^2 intruded in late Archean (Lopian) granodiorites, plagiogranites, harzburgites and gabbro as well as various early Proterozoic volcanic rocks – Kalevian-Yatulian basalt porphyry and diabase, Sariolian pikrit-diabase porphyry and Sumian riolite-dacite, dacite, andesite-dacite, basalt porphyry, mandelsteine and diabase (Fig. 2). This unique intrusive massif is formed of compositionally and structurally varied nepheline syenites crystallised from magmas intruded along conic faults (Voyteckhovsky, 2014). The magmatism ended with dykes of phonolites and tinguaites having intruded along faults.

Geodiversity

Geodiversity of the Khibini Mountains can be considered in two main aspects: petrographic/mineralogical and geomorphological. The first aspect is the basis of the idea for geopark development. Due to the multiphase magmatic activity during Paleozoic a huge variety of minerals have been formed that made the Khibini Mountain massif world famous mineralogical deposit, often called the Mecca of minerals. More than 1000 types of minerals are found here, 115 of which are described for the first time in the world. Another outstanding feature of the Khibiny minerals is that they occur in the form of big crystals and aggregates. Among the most frequently encountered giant forms are the crystals of eudialyte, aegirine, astrophillyte, apatite, titanite, nephelline, lamprophyllite, granate, as well rare minerals such as cancrinite, villiaumite, lomonosovite, mosandrite, fersmanite, murmanite, natrolite, narsarsukite, annite, etc. (Plate I, 1–19).

Along with the unique minerals, many unique petrographic varieties are encountered in Khibiny Mountains, such as khibinites, lujavrites, foyaites, tinguaites, urtites, etc. (Plate II, 1–16). Many of these rock varieties are of great decorative value and can be promoted as a raw material for the production of rare decorative stones. All this mineralogical treasure is stored in two professionally arranged museums: the Mineralogical museum of the Kola Science Centre of Russian Academy of Sciences in the town of Apatity (Fig. 3) and Mineralogical museum in the town of Kirovsk (Fig. 4).

Fig. 3. Mineralogical museum of the Kola Science Centre of Russian Academy of Sciences in the town of Apatity, Kola Peninsula

Fig. 4. Mineralogical Museum in the town of Kirovsk, Kola Peninsula

The second aspect, the geomorphological diversity of Khibiny Mountains with high aesthetic value, reflects their complex glaciation history including various glacial formations such as cirques, glacier valleys, different types of moraines, fluvioglacial deposits, relict and contemporary cryogenic formations. During the Quaternary glaciations the ice of several short mountain glaciers flowed into the great continental glacier (ice sheet), forming typical U-shaped glacier valleys of Belaya River, Malaya Belaya River, Golcovka, Kuniyok, Kaskasnewyok, Tuliyok, and Vuonemyok. Glacial lakes are very characteristic feature of this polar landscape. While the big lakes surrounding Khibini Massif – Imandra and Umbozero are of tectonic-glacial origin, the small lakes such as Bolshoy and Maliy Vudyavr near Kirovsk, Golcovoe, Verhniy and Nizhniy Newyavr, are of glacial origin. There are also several tarns formed in the deep cirques mainly in the western part of the mountains. The largest tarn is Ozero Academicheskoe, which is the source of Yuzhnoy Kaskasnewyok River. On the western slope of the Belaya glacier valley near Kirovsk glacially plucked bedrock of trachytoid khibinites can be observed (Fig. 5).

Fig. 5. Western slope of Belaya glacier valley SW of the town of Kirovsk is a glacially plucked bedrock of trachytoid khibinites

It was at the exit of the glacier valley where the small mountain glacier was flowing into the large sheet glacier. Tens of cirques in the feeding area of the mountain glaciers are carved during the Quaternary glaciations. Only in the vicinity of the town of Kirovsk more than 10 circuses can be counted, which give the alpine appearance of the otherwise low mountain.

One of the largest cirques Snezhniy (Fig. 6) is developed in the feeding area of Belaya glacier valley east of the famous Fersman's Rock that rises on the western slope of the valley (Fig. 7). Different kinds of moraines are developed here. Lateral and bottom moraines predominate in the glacier valleys (Fig. 8) while outside the mountain, ground moraines are developed, formed by the continental sheet glacier that covered the surrounding terrain where erratic boulders are frequently encountered in the lesotundra (Fig. 9).

Fig. 6. Snezhniy cirque in the feeding area of Belaya River Glacier

Fig. 7. Fersman's Rock in rischorites of the Polchvumchor Ridge

Fig. 8. Moraines with tundra vegetation represented by dwarf shrubs, grasses, mosses, and lichens

Fig. 9. Erratic boulders in lesotundra south of Knibini Massif

Geotourism

Most of the geological landmarks in the area are related to the activities of the Finnish geologist W. Ramsay and the Russian academician A. E. Fersman. Due to Fersman's expeditions in the 1920's and 1930's the mineral deposits in the area are systematically studied and industrially developed. A good basis for geotourism development in the Khibini Mountains are the routs described by Voytekhovsky (2014) in the form of a guidebook application to the geological map of the Khibini Mountain at a scale 1:50000, published by the Geological Survey of Finland and the Geological Institute of the Kola Science Centre of the Russian Academy of Sciences.

Within 16 routes the most famous geological and geographic sights associated with the history of geological/geographic studies of the Khibines are described. Among the most famous routes are the Fersman's Trail, along which A. E. Fersman passed for the first time in the Khibiny on August 25, 1920, the Molybdenite Mine and Geographers' Pass with mount Vudyavrchorr, Lake Maly Vudyavr with the first mountain station "Tietta", Ramsay Gorge with Malaya Belaya River valley, Western and Eastern Petrelius Passes, Aku-Aku Gorge, Eveslogchorr mount astrophyllites, and so on.

All these merits of the Khibini Mountains make this polar mountain very attractive in terms of geoconservation and geopark establishment. The recent development of its status in the context of its proclamation as a national park under the management of the Lapland Reserve, is a step in the right direction. However, the development of a Geopark is related to the activation of the local initiative and the provision of own funding. Despite the difficulties, the Khibini Mountain, representing an invaluable mineralogical treasure of global importance, deserves to take its place among the most attractive UNESCO geosparks.

Acknowledgements. This research has been supported by the National Science Fund under the contract DNTS/Russia 02/14 and contract 18-55-18013.

References

Mitrofanov, F. P. (Ed.) 2001. *Geological Map of Kola Region*. Ministry Natural Resources of Russia, Comm. Nat. Resources Murmansk District, Russian Academy of Sciences Geological Institute KSC RAS, Apatity.

Voytekhovsky, Y. L. 2014. *Khibiny Tundra. Geological Outdoor Map 1:50000 and Guidebook*. Grano Oy, Rovaniemi, Finland, 56 p.

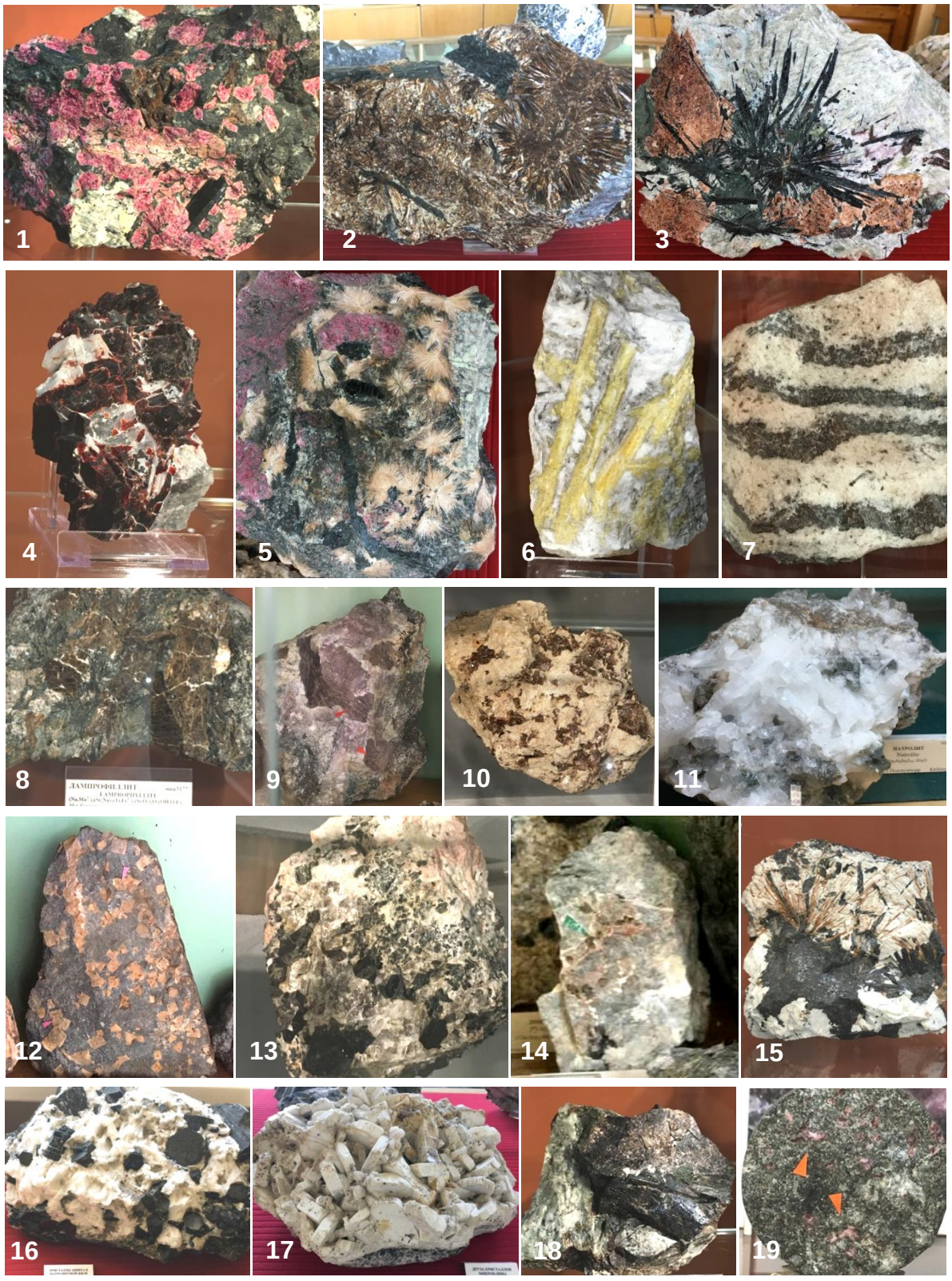

Plate I: ***1***, Eudialyte, Kukisvumchorr, Apatiti Museum; ***2***, Astrophillyte, Eveslogchorr, Apatiti Museum; ***3***, Radiate-fibrose aegirine with eudialyte, Lovozero, Apatiti Museum; ***4***, Villiaumite, Koashva, Kirovsk Museum; ***5***, Radiate-fibrose pink titanite, Kukisvumchorr, Apatiti Museum; ***6***, Cancrinite, Nyorkpakhk, Kirovsk Museum; ***7***, Widely-banded apatite-nepheline ore, Rasvumchorr, Kirovsk Museum; ***8***, Lamprophyllite, Kukisvumchorr, Kirovsk Museum; ***9***, Murmanite, Lovozero, Apatiti Museum; ***10***, Giant zircon crystals, Lovozero, Kirovsk Museum; ***11***, Natrolite, Poachvumchorr, Apatiti Museum; ***12***, Narsarsukite, Lovozero, Apatiti Museum, ***13***, Annite, Kejvy, Kirovsk Museum; ***14***, Fersmanite, Kukisvumchorr, Apatiti Museum; ***15***, Mosandrite, Kukisvumchorr, Kirovsk Museum; ***16***, Annite crystals in natrolite vein, Khibini, Apatiti Museum; ***17***, Microcline, Khibini, Apatiti Museum; ***18***, Lomonosovite, Jukspor, Kirovsk Museum; ***19***, Khibinskite, Hackman valley, Kirovsk Museum

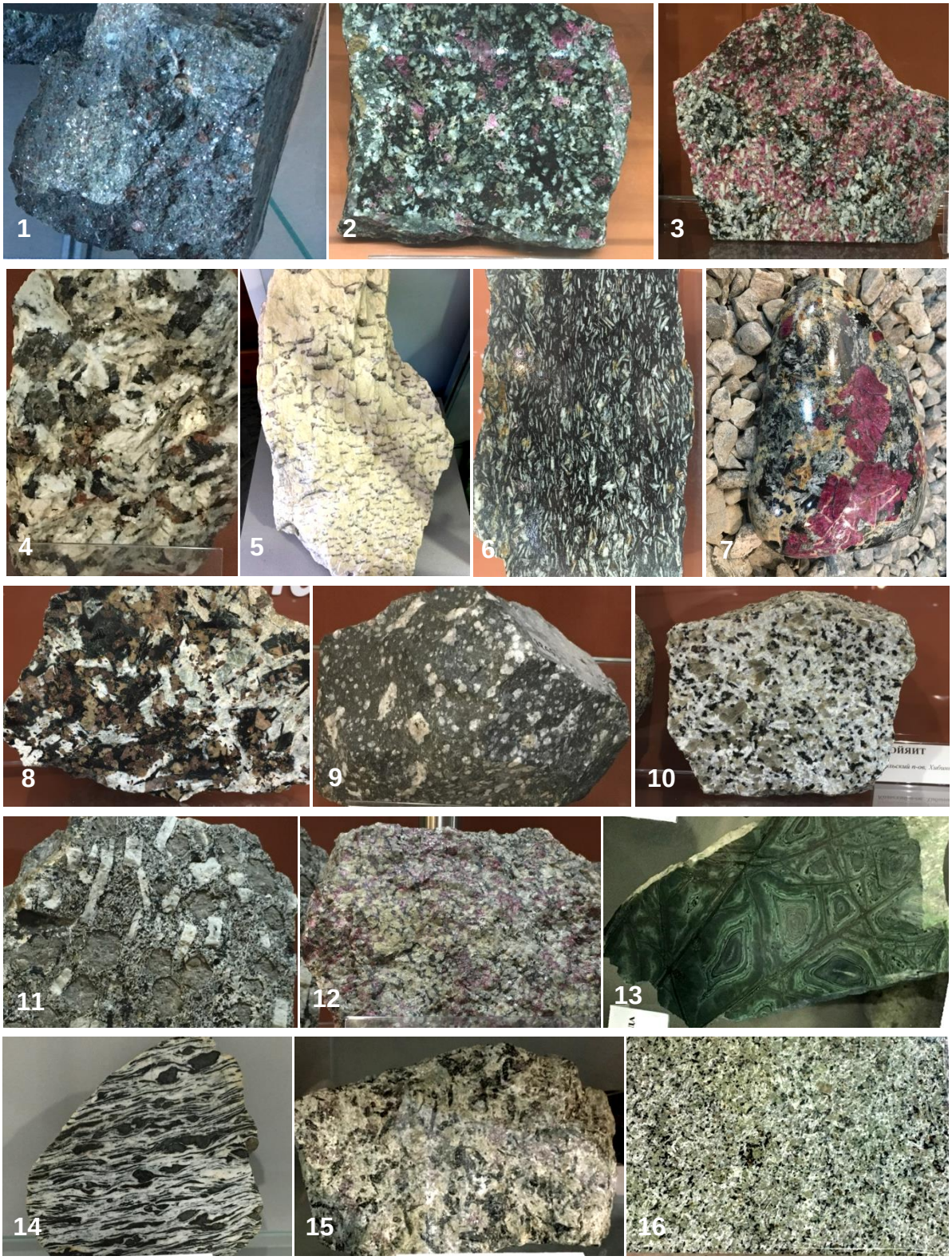

Plate II: *1*, Explosive kimberlite pype "Ermakovskaya", Apatiti Museum; *2*, Eudialite urtite, Khibini, Kirovsk Museum; *3*, Eudialyte luyavrite, Khibini, Kirovsk Museum; *4*, Foyaite, Eveslogchorr, Kirovsk Museum; *5*, Graphic pegmatite, Rikolatva, Kirovsk Museum; *6*, Luyavrite, Lovozero, Kirovsk Museum; *7*, Polished eudialyte pegmatite, Art Arctic creative centre, Apatiti; *8*, Khibinite, Khibini, Kirovsk Museum; *9*, Mandelstone, Khibini, Kirovsk Museum; *10*, Foyaite, Khibini, Kirovsk Museum; *11*, Nepheline syenite porphyry, Yudichvumchorr, Kirovsk Museum; *12*, Nepheline syenite with eudialite, Khibini, Kirovsk Museum; *13*, Dactyloscopic tinguaite, Partomchor, Apatiti museum; *14*, Milonitised gabbro, Monche tundra, Apatiti museum; *15*, Murmanite jolite-urtite, Lovozero, Kirovsk Museum; *16*, Khibinite as decorative stone, Khibini, Kirovsk Museum

MATHEMATICAL MODELS OF CONTAMINATION WITH HEAVY METALS FROM THE ABANDONED MINES IN THE MADJAROVO ORE FIELD, EASTERN RHODOPES

Nikolay Stoyanov, Svetlana Bratkova, Stefan Dimovski

University of Mining and Geology "St. Ivan Rilski", 1700 Sofia; nts@mgu.bg

ABSTRACT. Mathematical 3D models of the flow field and of the mass transport are developed for the groundwater contamination caused by the abandoned mines waters and for the possible drainage of the polluted groundwater flow into the Arda River. Behaviour of heavy metals Zn, Pb, Cd, and Ni in the water-saturated medium is studied and assessments of their possible distribution in the aquifers are made. The scheme of convection-diffusion transport is used in the mass transport models, taking into consideration the complementary processes of reversible elimination (sorption-desorption), mechanical dispersion, and mixing. On the basis of model solutions, the water budget elements are assessed and the current limits and degree of groundwater and surface water pollution are determined for the area of the abandoned mines in the Madjarovo ore field. A prognosis for the expansion of the negative processes in the period up to 2030 is also made. The 3D mathematical models are developed using the computer programmes Modflow and MT3D-MS.

Keywords: groundwater contamination, flow model, mass transport model, contamination with heavy metal, Madjarovo ore field

МАТЕМАТИЧЕСКИ МОДЕЛИ НА ЗАМЪРСЯВАНЕТО С ТЕЖКИ МЕТАЛИ ОТ ЗАКРИТИТЕ МИНИ В МАДЖАРОВСКОТО РУДНО ПОЛЕ, ИЗТОЧНИ РОДОПИ

Николай Стоянов, Светлана Браткова, Стефан Димовски

Минно-геоложки университет "Св. Иван Рилски", 1700 София

РЕЗЮМЕ. Разработени са математически филтрационни и миграционни 3D модели на замърсяване на подземните води с изтичащи от старите мини руднични води и възможното дрениране на замърсения подземен поток в р. Арда. Изследвано е поведението на тежките метали Zn, Pb, Cd и Ni във водонаситена среда и са направени оценки за тяхното възможно разпространение във водоносните хоризонти. В миграционните модели е използвана схемата на конвективно-дифузионен пренос на вещество с отчитане на съпътстващите процеси обратимо елиминиране (сорбция-десорбция), механична дисперсия и смесване. Въз основа на моделните решения за района на старите мини в Маджаровското рудно поле е направена оценка на елементите на водния баланс , определени са съвременните граници и степен на замърсяване на подземните и повърхностните води и е изготвена прогноза за развитието на негативните процеси в периода до 2030 г. Математическите 3D модели са съставени с компютърните програми Modflow и MT3D-MS.

Ключови думи: замърсяване на подземните води, филтрационен модел, миграционен модел, замърсяване с тежки метали, Маджаровското рудно поле

Introduction

The development of Madjarovo ore field started in 1958 and ended in 1997. The exploited ore bodies were grouped in several mining areas – Arda, Harman Kaya, Momina Skala, and Brousevtsi (Fig. 1). The parts of the rock massif that are affected by mining activities are characterised by a very high water permeability and play the role of complex drainage systems. Data from the system monitoring conducted by East Aegean River Basin Directorate (EARBD) along Arda River, as well as hydrochemical studies carried out in 2015 by our team, revealed increased contents of Fe, Mn, Zn, Pb, Cd, As, Ni, and other heavy metals in the mine and surface waters in the region of Arda mining area.

The abandoned mines are the main source of contamination. The established connections between the galleries create conditions for gravitational drainage of all mine waters to the cross gallery at horizon -30 m and their storage in the deep impermeable parts of the rock massif. The large hydraulic head of the waters coming from the higher horizons, combined with the reduced relief forms, the tectonic faults and the presence of near-surface hydraulically connected mine workings, is responsible for the formation of ascending flows and the resulting underground drainage of mine waters into the terrace of Arda River at the big meander after the town of Madjarovo (Fig. 1). Here, during rainy seasons, these waters outflow at the ground surface along the left slope of the gorge in the area nearby the Spomagatelna shaft. According to the determined concentrations of heavy metals in mine waters, the soluble forms of Zn, Pb, Cd, and Ni are identified as key contaminants.

Applying the Modflow and MT3D-MS computer programmes, several 3D numerical models are composed, regarding the conditions for the key pollutants distribution in the main hydrogeological structures of Arda mining area – the Paleogene poor water-bearing complex and the Quaternary aquifer. The main objective of the model studies is to make a quantitative assessment and a medium-term forecast of the groundwater pollution caused by the abandoned mine workings and of the possible drainage of the contaminated underground flow into the Arda River.

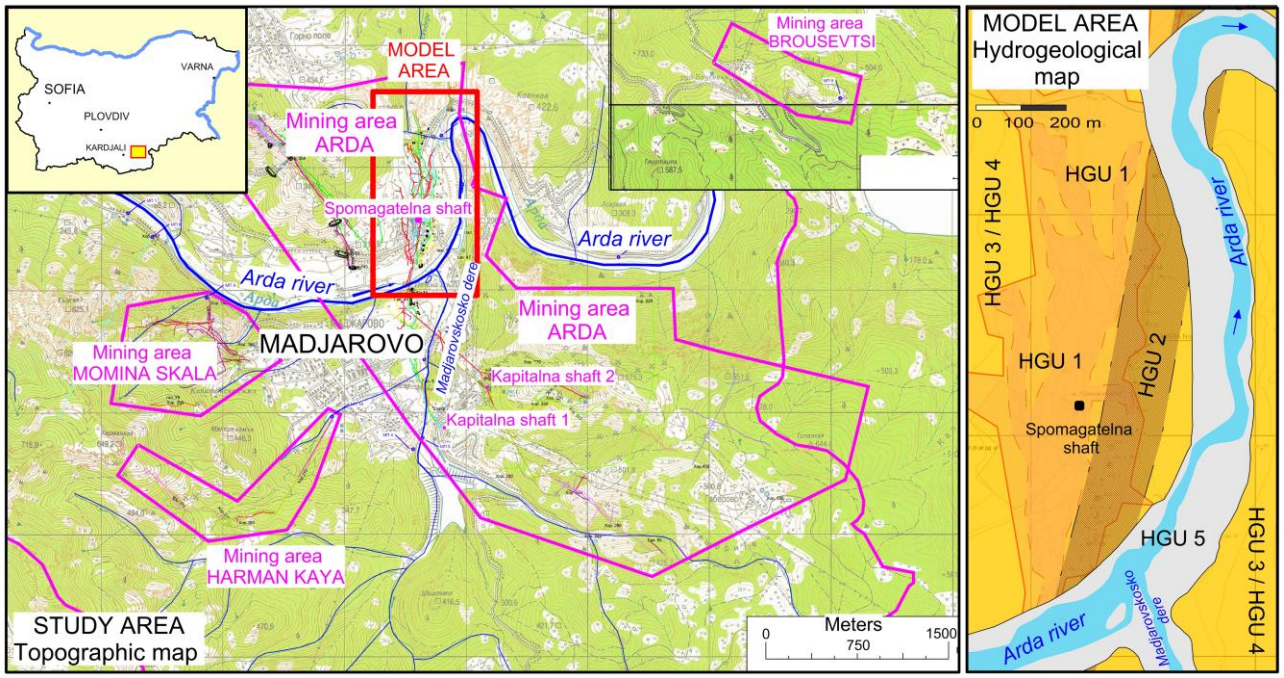

Fig. 1. Location of the study area and hydrogeological background

Conceptual model of the hydrogeological and mining technology conditions

The following general concept for the hydrogeological and mining technology conditions is accepted at the stage of development of the 3D numerical models:

- Two major hydrogeological units (HGU) – the Paleogene poor water-bearing complex (Pg-cmx) and the Quaternary aquifer (Q-cmx) are determined in the section down to horizon -30 m.
- The Paleogene poor water-bearing complex is composed of volcanic rocks (latites and pyroclastites), crossed by dikes, small intrusive bodies and faulted ore-bearing structures. Taking into account the specific geologic-tectonic conditions and the large-scale mining activities carried out in the past, four hydrogeological units of lower rank (HGU1, HGU2, HGU3, and HGU4) are differentiated into the Paleogene poor water-bearing complex.
- The Quaternary aquifer (HGU5) is formed in the alluvial deposits that fill the Arda river terrace. It is represented by cobblestones, gravels, and sands with a total thickness of about 5–6 m.
- The characteristics of the so-determined hydrogeological units of different rank and the model zones delimited in their boundaries are presented in Table 1 and Table 2.
- The hydrogeological complexes are unconfined to weakly confined. The hydraulic head is very high only in the deeper parts of HGU1 and HGU2. In the elevated part of the studied territory, the water table is at a depth of 40–50 m, and around the Arda River – at 1–5 m below the ground.
- The groundwater flow structure is generally controlled by the Arda River. Local distortions are observed in the region where mine workings are present and in the tectonic zone. The main direction of groundwater in the Paleogene complex is targeted towards the river terrace and the Arda River, and the hydraulic gradient ranges from 0.008 to 0.03. The groundwater flow in the Quaternary aquifer is orientated along the river course and the average gradient is 0.0014.
- The recharge of groundwater is accomplished by a variety of sources – precipitation, small rivers with unstable runoff, slope waters, groundwater flow along the ore field boundaries, and in high water periods, also by Arda River (Table 3). According to the water permeability of the near-surface layer, two zones characterised by different degree of recharge are separated (MZW-1.1 and MZW-1.2). Their range coincides with the outcrops of the Paleogene poor water-bearing complex and the Quaternary aquifer. The recharge rates for the two zones are determined as a function of the average annual precipitation (577 mm), the average annual air temperature (13°C), and the average hydraulic coefficient in the respective zone. The achieved values of 6E-5 m/d for MZW-1.1 and 3E-4 m/d for MZW-1.2 are refined during the calibration of the flow model.
- The main part of the naturally clean and technogenically contaminated waters in the Paleogene complex is drained underground in the Arda river terrace, while a small part streams on the surface and discharges into the river network. Part of the groundwater flow in the Quaternary aquifer (clean and polluted), especially in low water periods, is drained into the Arda River. The remaining part drains underground beyond the boundaries of the study area.
- Main sources of contamination are mine waters from the galleries above horizon 25 m, mine waters from the galleries in the southern part of the Arda area, and an ascending mine waters flow from horizon -30 m. The concentrations of key pollutants in the galleries above horizon 25 m are assumed according to data from chemical analyses of mine waters from surface run-offs. Therefore, in the simulated by the models conservative scenario, the following values are implemented as initial concentrations in this source: Cd – 0.04 mg/l; Pb – 0.38 mg/l; Ni – 0.065 mg/l; Zn – 62.0 mg/l. The concentrations in the ascending flow from horizon -30 m and in the mine waters coming from south are unknown values that are determined during the calibration of the mass-transport models, and the above-mentioned values are used as input data in the calibration procedure.

Table 1. *Hydrological units and model zones. Hydraulic coefficient k*

Hydrological unit (HGU)		General description (scope)	HGU №	Model zone №	Hydraulic coefficient k, m/d
I-st rank	II-nd rank				
Paleogene poor water-bearing complex	First high permeability zone	Parts of the rock complex affected by the mining activities – galleries, shafts, shattered zones, pillars	HGU1	MZK-1.1; MZK-2.1; MZK-3.1	3.0
	Second high permeability zone	Tectonic zones	HGU2	MZK-1.2; MZK-2.2; MZK-3.2	4.5
	Low permeability zone	Regionally fractured and secondary altered parts of the rock complex down to elevation 110 m	HGU3	MZK-1.3	0.35
	Very low permeability zone	Weakly affected by secondary changes parts of the rock complex (between elevations -30 and 110 m)	HGU4	MZK-2.5; MZK-3.5	0.02
Quaternary aquifer	-	River terrace - cobblestones, gravels, and sands	HGU5	MZK-1.4	100

Remark: The hydraulic coefficient values are assumed according to reference data for similar medium types. The values, presented in the table, are refined during the basic flow model calibration.

Table 2. *Physical and mass transport characteristics of the hydrogeological units*

HGU №	Volumetric mass density ρ_n, kg/m^3	Longitudinal dispersivity α_L, m	Coefficient of molecular diffusion D_M, m^2/d	Coefficients of distribution K_D, cm^3/g			
				Cd	Pb	Ni	Zn
HGU1	1850	3.0	5E-4	9.5	15.0	22.0	7.3
HGU2		4.5					
HGU3	2150	10.0	7E-4	10.5	16.0	24.5	10.0
HGU4							
HGU5	2100	5.5	3E-4	8.5	14.0	20.5	4.5

Remark: Main sources of the implemented averaged values of ρ_n, α_L, D_M, and K_D for Cd, Pb, Ni, and Zn: (1) Spitz, K., J. Moreno. 1996. A practical guide to groundwater and solute modelling. JW&S, Inc., NY, p. 460; (2) Enviro Base – software product of Waterloo Hydrogeologic Inc., Ontario Canada.

Table 3. *Boundary conditions*

Definition of the boundary condition	Type	Model layers	Index
Western – groundwater flow from the uncontaminated part of the Paleogene complex that is drained in the mine workings and the river terrace	GHB	ML-1, ML-2, ML-3	GHB-W ML 1-2-3
Eastern – groundwater flow from the uncontaminated part of the Paleogene complex that is drained in the river terrace	GHB	ML-1, ML-2, ML-3	GHB-E ML 1-2-3
Southern (near-surface part of the section) – groundwater flow from the uncontaminated part of the Quaternary aquifer	GHB	ML-1	GHB-S ML 1
Southern (in depth) – lateral flow (mine waters) from the galleries in the southern part of the Arda mining area that gravitationally that is drained in the cross gallery at horizon -30 m	GHB	ML-2, ML-3	GHB-S ML 2-3
Cross gallery and mine galleries at horizon -30 m – ascending flow (mine waters)	Specified Head	ML-3	SH – B ML 3
Rivers – Arda River and Madjarovsko dere	River	ML-1	Riv ML-1
Recharge from precipitation	Recharge	ML-1	MZW 1, MZW-2

- The baseline concentrations of Cd, Pb, Ni, and Zn in uncontaminated groundwater (Table 4) have been employed as starting conditions in the mass transport models.

Table 4. *Baseline concentration of Cd, Pb, Ni, and Zn*

Hydrogeological unit (HGU)	Baseline concentration C_{0i}, mg/l			
	Cd	Pb	Ni	Zn
HGU2, HGU3, HGU4	8.00E-5	9.50E-3	3.50E-4	1.24E-2
HGU5	3.00E-3	9.75E-3	2.25E-3	1.50E-2

- The hydrogeological conditions and the characteristics of the key pollutants suggest that the mass transport is performed through convection, accompanied by molecular diffusion processes, mechanical dispersion, reversible elimination (sorption-desorption), and mixing.

Methodology

A mathematical simulation of the conditions for pollutant mass transport is performed by means of five 3D numerical models, taking into account the past mining in the Arda area. The models are composed using computer programmes Modflow and MT3D-MS (McDonald, Harbaugh, 1988; Zheng, Wang, 1999; etc.). The applied approach is successfully tested for modelling the mass transport of pollutants in different hydrogeological conditions and for diverse in type and intensity technogenic sources of contamination on the territory of the Republic of Bulgaria – Kozloduy NPP; Panagyurishte mining and ore processing region; uranium ore deposit Momino; etc. (Stoyanov, 2012, 2019; etc.). One basic flow model and four mass transport models are developed.

The basic flow model is a 3D simulation of the groundwater flow structure in the model area. The model includes 3 layers (ML) and 10 zones characterised by a different degree of water permeability (MZK) and 2 infiltration zones (MZW) simulating the spatial limits of the hydrogeological units and the high heterogeneity of the medium (Fig. 2). The different boundary conditions – lateral and ascending flows, rivers and recharge (Table 3 and Fig. 2A), are defined with the help of the respective packages. The model is calibrated, taking into account the groundwater and surface water levels at four monitoring points, applying variation in the hydrodynamic coefficient and in the infiltration and runoff rates.

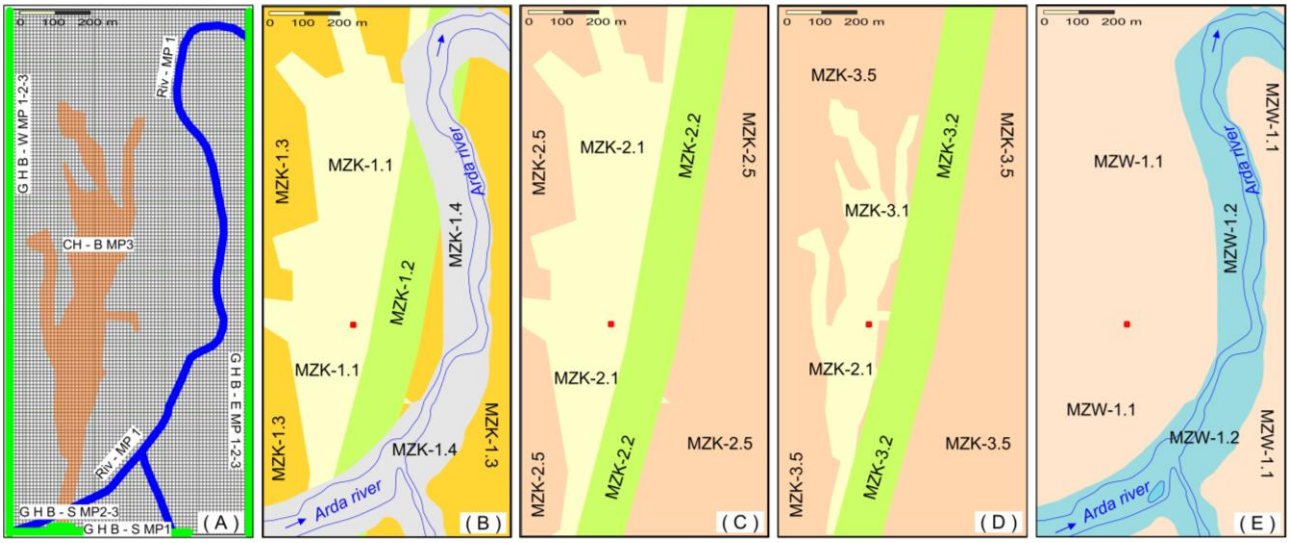

Fig. 2. Spatial gridding of the model area, boundary conditions, and model zones: *A*, modelling grid and boundary conditions; *B–D*, zoning according to the hydraulic coefficient in model layers ML-1, ML-2 и ML-3; *E*, zoning according to the recharge rate in model layer ML-1

The 3D mass transport models simulate the movement of the key pollutants Cd, Pb, Ni, and Zn. They are based on the developed flow model. The calculation scheme takes into account the processes of convection, reversible elimination, dispersion, diffusion, and mixing. The implemented averaged values for the parameters volumetric mass density ρ, longitudinal dispersivity α_L, coefficient of molecular diffusion D_M and coefficients of distribution K_D are presented in Table 2. The transverse horizontal and vertical dispersivities (a_{TH} and a_{TV}) are determined applying the ratio $a_L = 10\ a_{TH} = 100\ a_{TV}$. In the uncontaminated part of the model area, the specified baseline concentrations of Cd, Pb, Ni, and Zn (Table 4) are set. The same initial values are set in the rivers and in the groundwater flows from the unpolluted parts of the Paleogene and the Quaternary complexes located along the external borders of the model. In the zones with presence of galleries (MZK-1.1, MZK-2.1, MZK-3.1) the concentrations characteristic for mine waters and specified in the conceptual model are set. When the mass transport models are calibrated, these values are assumed to be initial in the ascending flow and in the mine waters along the southern border. The model simulation covers the period 1995–2030.

Results and discussion

The basic flow 3D model determines the spatial distribution of hydraulic heads, gradients and velocities. The model solution revealing the structure of the flow field is illustrated in Figure 3. The obtained good correspondence between real and model piezometric data guarantees the reliability of the hydrodynamic base for the mass transport models. The water budget for the Quaternary aquifer is presented in Table 5.

The Cd, Pb, Ni, and Zn concentration ranges defined by the 3D mass transport models are illustrated with maps of the contamination spread that represent the scale, magnitude and dynamics of the negative processes in the studied subsurface area (Figs 4–7). The selected zoning scale takes into account the natural background, the threshold values and the quality standards for drinking water. Only on the Pb maps, the external boundary is outlined by the acceptable standard value because the values recorded for this ingredient exceed the background and threshold values. The presented solutions provide a quantitative esteem for the contamination of groundwater with heavy metals by 2015 and a forecast for its development in the period up to 2030. Based on the model solutions, a summary map of the chemical impact on groundwater caused by the abandoned mines in the Madjarovo ore field (Fig. 8) is composed.

Table 5. *Water budget in the Quaternary aquifer*

Income elements, Q_i^{IN}, l/s		
Recharge along the western boundary of the model (from the outer parts of the Quaternary aquifer)		11.24
Recharge from Arda River		0.21
Recharge from the Paleogene poor water-bearing complex	Inflow along the fault zone	33.21
	Inflow from the zone of the galleries	4.58
	Inflow from the undisturbed rock massif	8.84
Recharge from precipitation		1.19
Total		59.27
Outcome elements, Q_i^{OUT}, l/s		
Drainage across the eastern boundary of the model (towards the outer parts of the Quaternary aquifer)		6.12
Drainage in Arda River		53.14
Drainage towards the Paleogene poor water-bearing complex in the scope of the fault zone		0.02
Total		59.28
Budget error 0.02% (difference)		

The presented results of the performed model studies give reason to make the following summaries and conclusions:

- The groundwater flow is directed from the old galleries to the river terrace. The difference in the hydraulic head between the levels of the river terrace and mine waters in the near-surface galleries is 2–3 m, and if compared to the mine water in the cross gallery at horizon -30 m it is 1–2 m higher. This creates conditions for ascending flows that uplift mine waters to the surface. The large gradients of the groundwater flow along the left slope of the gorge suggest intense drainage of mine waters into the river terrace.

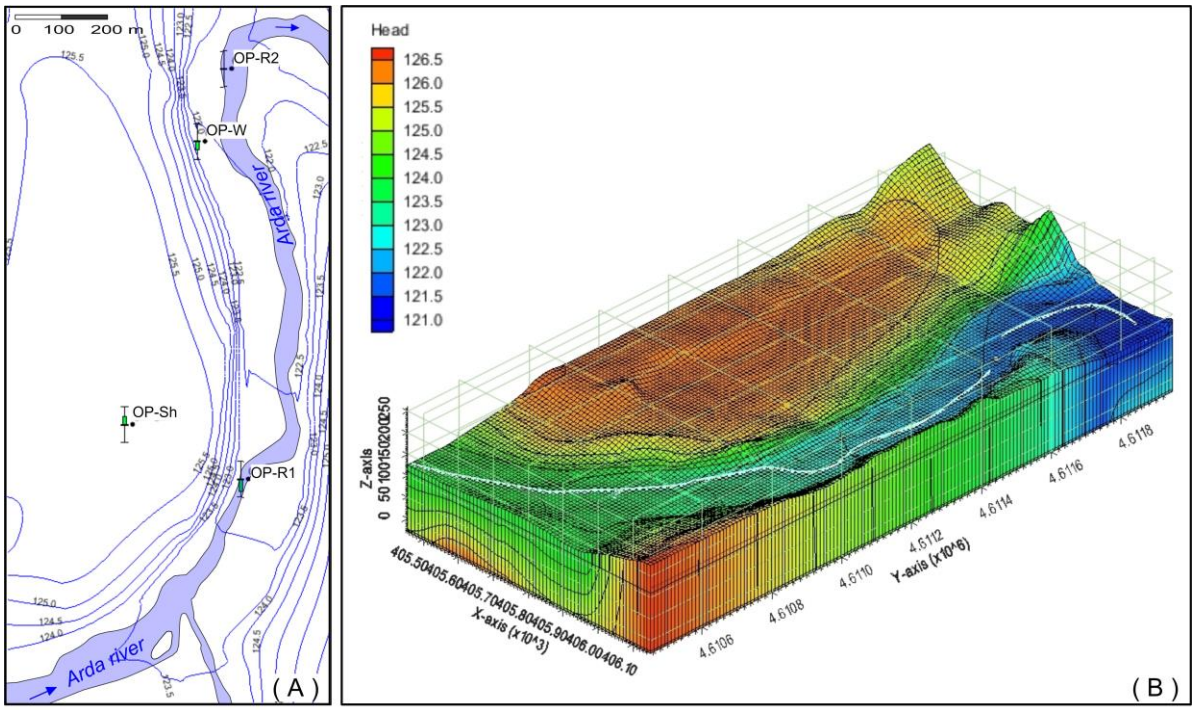

Fig. 3. Basic 3D flow model; hydraulic head distribution in the model area

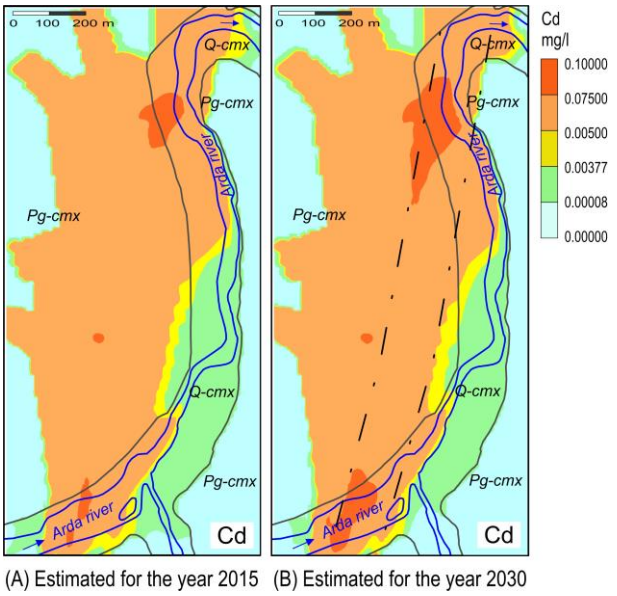

Fig. 4. Mass transport 3D model; maps of Cd contamination

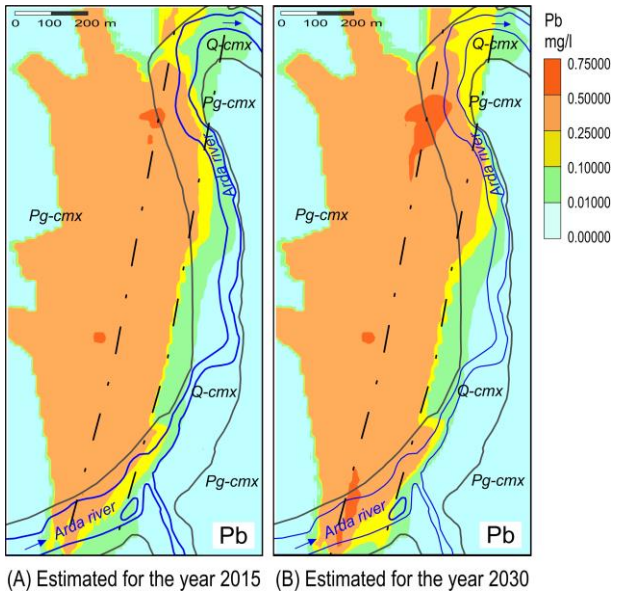

Fig. 5. Mass transport 3D model; maps of Pb contamination

- The total flow from the Paleogene complex towards the Quaternary aquifer is 46.63 l/s, and these are predominantly (over 80%) mine waters and contaminated groundwater. The mine waters are drained into the river terrace along the fault zone as ascending flows with a total outflow of about 30 l/s.
- Within the boundaries of the studied area, the mine and highly contaminated waters (about 38 l/s) form about 65% of the Quaternary aquifer resources. This implies an abrupt change in the chemical composition of groundwater in the river terrace, accompanied by a noticeable deterioration in their properties.
- Around 90% of the groundwater flow formed in the terrace is drained in the narrowing at the big meander of Arda River, which is the cause of heavy metals pollution, accompanied by a significant deterioration of the quality of river waters.
- Groundwater pollution is concentrated in the range of mine workings along the left slope of the gorge and in the river terrace in the area before the big meander of Arda River.
- The total area of these parts of the Paleogene poor water-bearing complex and of the Quaternary aquifer, where groundwater is contaminated by mining activities is about 0.85 km^2.
- The established boundaries and extent of the negative impact caused by the abandoned mine galleries on the groundwater and surface waters in the region remain relatively constant over time until 2030. The prognosis calculations show that a slight displacement of the impact zone can be expected in the direction of Arda River.

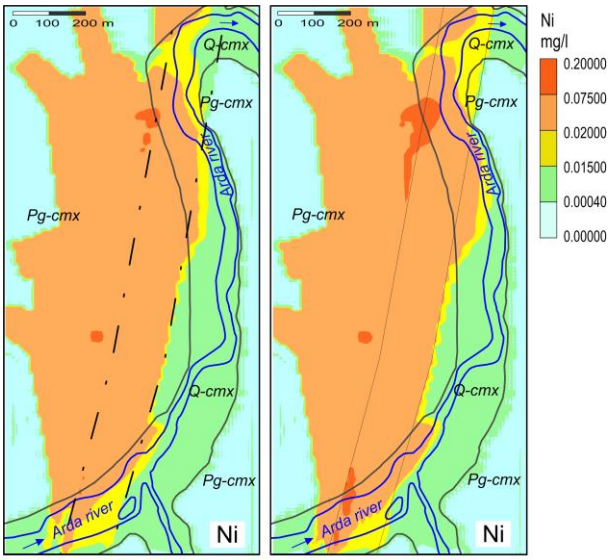

(A) Estimated for the year 2015 (B) Estimated for the year 2030

Fig. 6. Mass transport 3D model; maps of Ni contamination

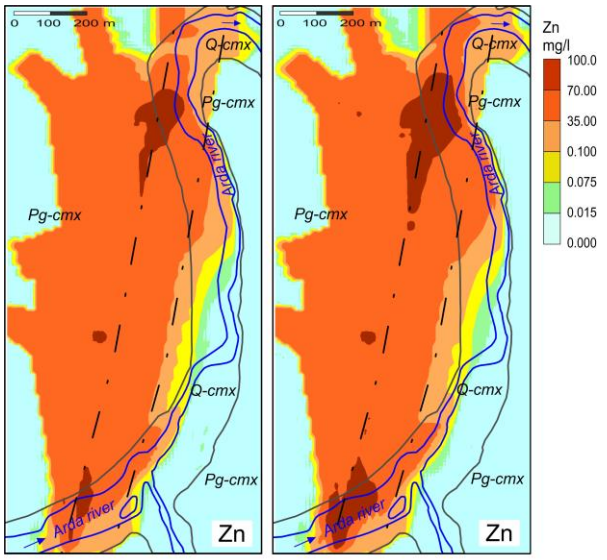

(A) Estimated for the year 2015 (B) Estimated for the year 2030

Fig. 7. Mass transport 3D model; maps of Zn contamination

Conclusions

The results of the performed model studies show that the abandoned mines in the Madjarovo ore field have a noticeable negative impact on the composition and qualities of groundwater and surface waters in the region between the town of Madjarovo and the big meander of Arda River. The underground inflow of mine waters contaminated with heavy metals is significant (about 40 l/s) and covers a section of the river terrace over 1 km in length. Partially affected by heavy metals pollution are the Paleogene poor water-bearing complex, in which the ore mining activities have developed, and the Arda River waters.

Acknowledgements. The implemented conceptual schemes are based on unpublished authors' work in the frames of the EARBDMINING – Contract D-34-15/07.04.2015 under the Programme BG02 "Integrated Marine and Inland Water Management, co-funded by the European Economic Area Financial Mechanism". This work has been carried out in the framework of the National Science Programme "Environmental Protection and Reduction of Risks of Adverse Events and Natural Disasters", approved by the Resolution of the Council of Ministers № 577/17.08.2018 and supported by the Ministry of Education and Science of Bulgaria (Agreement № DO-230/06-12-2018).

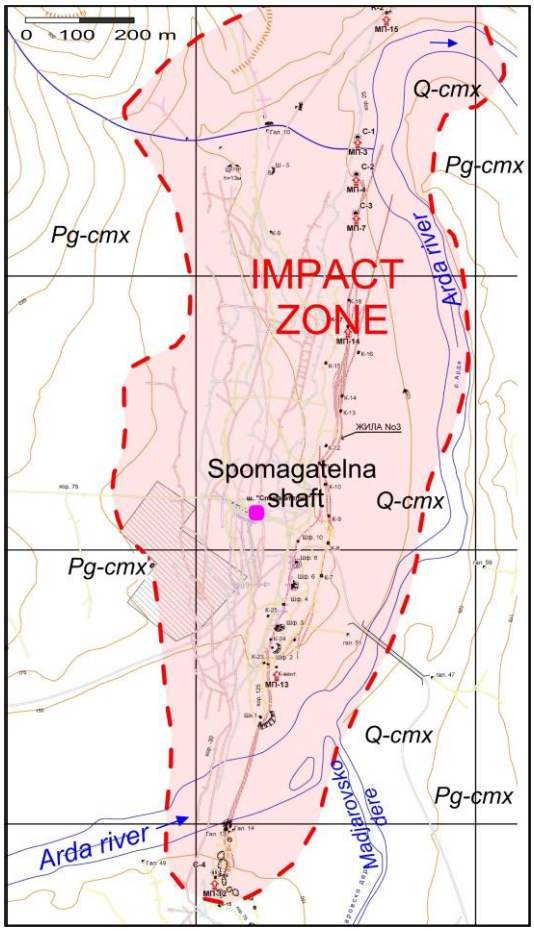

Fig. 8. Boundaries of the zone where impact on groundwater is observed, caused by the abandoned mines in the Madjarovo ore field

References

McDonald, J. M., A. W. Harbaugh. 1988. *A modular three-dimensional finite-difference flow model*. Techn. of Water Resources Investigations of the USGS, Book 6, 586 p.

Spitz, K., J. Moreno. 1996. *A practical guide to groundwater and solute modelling.* John Wiley & Sons, New York, 460 p.

Stoyanov, N. 2012. Model studies estimating the risk of a possible pollution in the geological basis and groundwater caused by the designed national disposal facility for storage of radioactive waste in the area of NPS "Kozlodui". – *Ann. Univ. Mining and Geol.*, *55*, Part I, 140–145 (in Bulgarian with English abstract).

Stoyanov, N. 2019. *Matematichesko modelirane v hidrogeologiata*. "Vanyo Nedkov" Publ. House, Sofia, 246 p. (in Bulgarian)

Zheng, C., P. P. Wang. 1999. *MT3DMS – A modular 3-D multispecies transport model for simulation of advection, dispersion and chemical reactions of contaminants in groundwater systems (Release DoD_3.50.A)*. University of Alabama, 239 p.

STUDY OF ADSORPTION/DESORPTION OF ARSENATE ON/FROM GOETHITE-COVERED QUARTZ SAND UNDER FLOW REGIME OF OPERATION

Ivelina Zheleva, Plamen Georgiev
University of Mining and Geology "St. Ivan Rilski", 1700 Sofia; ps_georgiev@mgu.bg

ABSTRACT: The main aim of this article was to assess adsorption/ desorption of arsenate under a continuous regime of operation of a filter filled with goethite-covered quartz sand. The results showed that at constant experimental conditions (temperature, arsenate concentration, and pH), the arsenate adsorption depends mainly on the filter`s height and the flow rate of the inlet solution injection into the filter. The following parameters: efficiency of arsenate adsorption, equilibrium uptake, adsorbent exhaust rate, as well as the rate constant of adsorption and bed sorption capacity were determined by breakthrough curves and the applied Adams-Bohart model. the pH of desorption solution played a paramount role in the arsenate desorption, as the process was very efficient at slightly alkaline conditions in comparison to the desorption`s efficiency at slightly acidic pH.

Keywords: arsenate, goethite, breakthrough curves, Adams-Bohart model

ИЗСЛЕДВАНЕ АДСОРБЦИЯ/ДЕСОРБЦИЯ НА АРСЕНАТНИ ЙОНИ ВЪРХУ/ОТ КВАРЦОВ ПЯСЪК, ПОКРИТ С ГЬОТИТ ПРИ ПРОТОЧЕН РЕЖИМ НА РАБОТА

Ивелина Желева, Пламен Георгиев
Минно-геоложки университет "Св. Иван Рилски", 1700 София

РЕЗЮМЕ: Основната цел на настоящата статия е оценка на сорбцията/десорбцията на арсен при проточен режим на работа на филтър, състоящ се от кварцов пясък, покрит с гьотит. Получените резултати показват, че при постоянни условия на средата (температура, концентрация на арсен, pH), сорбцията на арсен зависи основно от височината на филтъра и скоростта на постъпване на разтвора във филтъра. Показателите ефективност на сорбция, равновесно натоварване, скорост на изтощение, както и скоростната константа и сорбционен капацитет на филтъра, са определени посредством кривите на сорбция на арсен и приложения модел на Адамс-Бохарт. pH на десорбиращия разтвор, от своя страна, има ключова роля по отношение на десорбцията на арсенатните йони от филтъра, като процесът е значително по-ефективен при слабоалкални условия в сравнение с ефективността, установена при слабокисели условия.

Ключови думи: арсен, гьотит, криви на сорбция, модел на Адамс-Бохарт

Introduction

The natural weathering of arsenic-bearing minerals and discharge of arsenic-containing wastes from petroleum refining, melting of base metal sulphide ores are the main reasons for the elevated concentrations of pollutants in surface and subsurface waters.

Arsenic occurs in natural waters both in organic and inorganic forms, as the arsenite, As(III), and arsenate, As(V)), are the major inorganic arsenic species. Arsenite is the chemically dominant form in reducing environments, whereas, arsenate dominates at oxidising conditions. Arsenate is a chemical similar to phosphate which enhances its transport and accumulation of the pollutants in the organisms under exposure to the pollutant (Sharma, Sohn, 2009).

Numerous methods for arsenic removal from aquatic environments have been studied including ion exchange, precipitation, coagulation, membrane filtration, flocculation, ozone oxidation, biological treatment, electrochemical treatment, and adsorption (Choong et al., 2007). Adsorption is evolving as one of the most applicable method for the arsenic removal from water because of the wide range of commercial and low-cost adsorbents (activated carbon, oxides, hydrotalcite, metal-based methods, biosorbents, soils and constituents, industrial by-products/ wastes, etc.,) that could be used (Mohan, Pittman, 2007).

The previous studies have shown that goethite possesses higher adsorption capacity and it adsorbs arsenate more efficiently from slightly acidic to slightly alkaline waters in comparison to hematite (Zheleva et al., 2016). The higher efficiency of that process is based on the inner sphere complex formation between adsorbate and the mineral surface (Manning et al., 1998).

The main aim of this article is to test the capability of goethite-covered quartz sand to adsorb arsenate from slightly alkaline spring water under a continuous regime of operation of a filter column and to determine the value of some important parameters about that treatment.

Materials and methods

The experiments about the arsenic removal from studied spring water by means of adsorption were performed in the column type reactor. The experimental set-up consisted of a feed vessel (1), a peristaltic pump (2), a column (4), and a vessel collecting treated solutions (4) (Fig. 1). The columns' height for all experiments was 10 cm. In each column, two zones were distinguished – an adsorption and a supporting

zone. The adsorption zone occupied the central part of the column and it consisted of goethite-covered quartz sand (dominant particle size minus 0.315 mm – 81%). The supporting zones, situated in the inlet and outlet point of the column, consisted of glass wool.

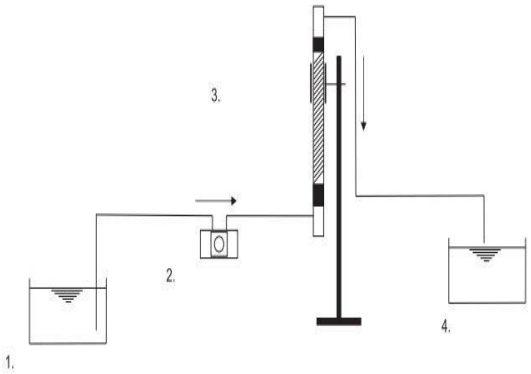

Fig. 1. Scheme of the experimental set up used in these experiments

The surface of quartz sand was preliminary cleaned and activated by means of treatment with 4N HCl at conditions of agitation at a temperature of 70°C. The residual acidic solution was separated and the quartz sand was washed three times with distilled water. The goethite was deposited on the quartz sand by means of its mixing with $FeSO_4.7H_2O$ and the serial alteration of chemical ferrous oxidation (by means of H_2O_2 addition) and the ferric iron precipitation (by means of NaOH addition). As a result of that treatment, the colour of quartz sand changed from snow white to yellow-brown. Each column was filled with the relevant amount of goethite-covered-quartz-sand. After their preparation, the adsorption zone in each column was washed with the amount of distilled water equal to three times the column`s operating bed volume.

The ration between the adsorption and supporting zone changed in some experiments which had an effect on the adsorption zone bed height. The working volume of the adsorption zone in each column (so-called bed volume) was determined before the start of each experiment by means of an upward injection of water until all pores filled up with water.

The columns operated in an upward continuous regime which provided for the optimal contact between the goethite-covered-quartz-sand and the treated solution. The spring water with slightly alkaline pH, spiked preliminary with arsenate (as K_2HAsO_4), was used as a model solution in this study (Table 1). The temperature during the experiment was in the range of 25–27°C.

Table 1. *Chemical content of water being treated*

Index	Value
Na, mg/L	50
K, mg/L	1.6
Ca, mg/L	3.2
F, mg/L	2.4
Cl, mg/L	5.3
SO_4, mg/L	20.5
CO_3, mg/L	24.0
HCO_3, mg/L	65.5
H_2SiO_3, mg/L	50.6
As, mg/L	0.025
pH	8.95

Two types of experiments regarding the arsenate adsorption on goethite-covered-quartz-sand were carried out. Firstly, the effect of adsorption's zone height in the column on the arsenate adsorption was studied. In that case, the flow rate applied to all columns was identical. In the second set of experiments, the arsenate adsorption was studied in dependence on the column`s flow rate. The adsorption zone height of columns was constant in that case. The kinetic parameters of arsenate adsorption on goethite-covered-quartz-sand at flow regime of operation were determined and assessed by means of Adams-Bohart model:

$$t = N_0 . Z/ Ci . V – (1/ K .Ci). \ln [(Ci/ Cb) - 1]$$

where:
C*i* is the initial arsenic concentration (μg/L), Cb is the breakthrough arsenic concentration (μg/L), t is the time of breakpoint (hour), N_0 is the sorption capacity of sorbent (μg/L), Z is the bed height of column (cm), V is the linear velocity (cm/min) and K is the rate constant (L/mg.min). From the slope and intercept of the respective iso-removal line, the adsorption capacity (N_0) and the rate constant of adsorption (K) were calculated.

The following parameters were measured during the experiments: pH and the arsenate concentration in effluents. The samples from effluent solutions were stored in a refrigerator until the arsenic determinations. pH was measured daily. Based on the collected data for each column, the relevant parameters were determined: a breakthrough point; total amount of solutions being injected into the column to the breakthrough point (Veff), point of the column exhaustion, total amount of arsenic entered the column until the moment of breakthrough point (m_{total}), the total amount of adsorbed arsenic (q_{total}), equilibrium amount of adsorbed arsenic (q_{eq}), the efficiency of arsenic removal (%), and adsorbent exhaustion rate.

The desorption experiments were also carried out in a continuous regime of operation with filter columns, characterised with an equal bed height of goethite-covered quartz sand and to which the same flow rate during the period of arsenate adsorption have been applied. The arsenate desorption was carried out with arsenic-free spring water as the main solution, which was spiked with 75 μg/ L HPO_4^{3-} (added as Na_2HPO_4). The effect of pH was studied by the addition of sulphuric acid (or sodium hydroxide) to the above-mentioned solution with an aim to study the desorption process at acidic (or alkaline pH). The flow rate of desorption solutions to the columns was 0.176 L/ 24h. The effluent solutions were collected in plastic vessels. pH was measured daily. The samples from effluent solutions were stored in a refrigerator until the arsenic determinations. The arsenic concentration was measured by means of a spectrophotometer MERCK SQ22 at 820 nm and 20 mm cuvette (Johnson, Pilson, 1971).

Results and discussion

The main advantages of the pollutant removal by means of sorption are: the process carried out without significant changes in the water chemistry and the high percent of the pollutant removal is combined with a lower residence time of waters being treated. For that reason, the methods based on

adsorption processes are preferred into practice for the treatment of waters polluted by one or two compounds presented in lower concentrations as a rule.

Effect of the bed height on the arsenate adsorption

The experiments were carried out with an upward injection of arsenate-containing spring water into the column as the measured pollutant's concentration in the effluents was related to the duration of the experiment. The arsenate adsorption on the goethite-covered quartz sand was a very efficient process at the very beginning of the experiment which resulted in its zero concentration in the column's effluent. As the volume of the solution being treated increased and the arsenic adsorption continued, the arsenic concentration in the effluents gradually rose. Finally, the adsorption zone reached the column's top and the arsenic concentration in effluents was almost equal to the concentration in the inlet solution. Several parameters about the arsenate adsorption on goethite-covered quartz sand were determined. Time for arsenic breakthrough concentration – the time when the arsenic concentration in effluents reached 10 µg/L (which is the arsenic permissible concentration for drinking water; it meant that the efficiency of the pollutant removal at this time of the column's operation was about 60%), a column exhaustion time referred to the moment when only about 10% of the inlet arsenic concentration (around 2–2.5 µg/L) sorbed on goethite during the column operation.

The bed height of goethite-covered quartz sand in the filter column had a strong effect on the arsenate adsorption, the appearance of the arsenic breakthrough concentration and the time of filter's exhaustion. For example, the time for arsenic breakthrough concentration for 1.8 cm bed height was at 13 days since the start of column operation and 30 days for 4.0 cm bed height, respectively (Table 2). These results were logical having in mind that shorter bed height of goethite-covered quartz sand directly determined the smaller number of binding sites on which the arsenate adsorption could take place. The effect of bed height of goethite-covered quartz sand on the arsenic breakthrough curves is depicted in Figure 2.

The rate of arsenate adsorption was strongly dependent on several factors like pH, ambient temperature and the arsenic concentration. With the main aim to make the comparison between variants easier, the temperature (in the range 25–27°C) and the arsenic concentration (25 µg/L, i.e. 2.5 times higher than the element`s permissible concentration for drinking water) during the experiments were constant. However, the pH of treated spring waters had a significant effect on the arsenate adsorption. That effect was determined by the Point of Zero Charge of goethite ($PZC_{goethite}$ = 5.35) and the slightly alkaline pH (8.95, Table 1) of the spring waters being treated. At these conditions, the goethite possessed slightly dominant negative surface charge which detained to some extent the arsenate adsorption because of the repulsive force acted between ions with identical charge. At such conditions, the arsenate adsorption on goethite-covered quartz sand took place by means of a ligand exchange mechanism which involved the exchange of aqueous ligand for a surface hydroxyl group:

$$=S\text{-}O^- + HAsO_4^{2-} + H_2O \rightarrow =S\text{-}OH\text{-}HAsO_4^- + OH^-$$

Table 2. *Characteristics of the experiment about the effect of height of goethite-covered quartz sand in the columns on the arsenic adsorption*

Index	Height of goethite-covered quartz sand in the column, cm		
	1.8	2.7	4.0
Arsenic in inlet solution, µg/ L	25.0		
Flow rate, L/ 24 h	0.33		
Applied bed volumes per 24 h	9.4	6.3	3.25
Time of arsenic breakthrough concentration, days	13	21	30
A column exhaustion time, days	16	25	34

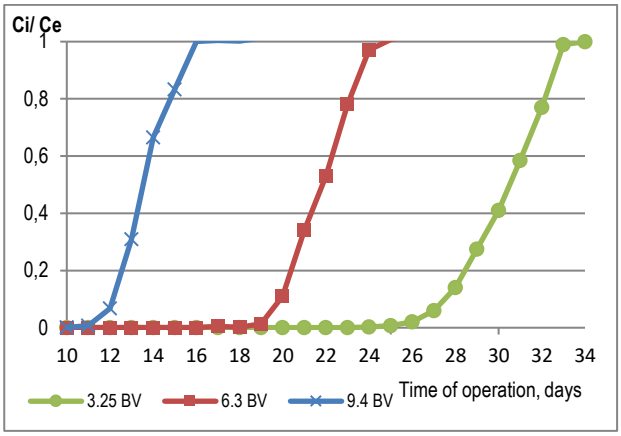

Fig. 2. Effect of the bed height of goethite-covered quartz sand in the column on the arsenate adsorption (flow rate 0.33 L/ 24 h, initial arsenic concentration 25 µg/ L, temperature 25–27°C)

That process led to the release of hydroxyl ion into the solution which maintained the slightly alkaline pH of the column effluents (8.32–8.40) for the largest bed height of goethite-covered quartz sand (4.0 cm).

The effluents from the goethite-covered quartz sand with the shortest bed height (1.8 cm) was with almost neutral (pH 7.62–7.86) especially when the duration of column operation was near its breakthrough time. It was evident that the decreasing of effluent's pH was due to the deprotonation of near-surface situated hydroxyl groups of goethite.

The arsenic adsorbed in the filter columns strongly depended on the bed height (Table 3) – the adsorbed amount steadily increased from 107.8 µg for 1.8 cm bed height to 258 µg for bed with 4.0 cm height, respectively. However, the equilibrium arsenic content (q_{eq}) in the whole column was in a narrow range. The efficiency of arsenic adsorption was the highest (94.7%) for a bed with 4 cm height. The higher bed height of goethite-covered quartz sand combined with a constant flow rate of inlet spring water determined a smaller value for bed volumes being treated per day. It meant, that the treated solution remained longer in the filter column which enhanced the contact and adsorption between the binding sites of goethite-covered quartz sand and arsenate ions. For that reason, the rate of adsorption zone movement in the

Table 3. *Parameters characterising the arsenic adsorption on goethite-covered quartz sand under a continuous regime of operation in dependence on the bed height*

Index	Height of goethite-covered quartz sand in the column, cm		
	1.8	2.7	4.0
Veff, L	4.95	7.59	10.9
q_{total}, μg	107.76	167.1	258
m_{total}, μg	123.75	189.75	272.3
q_{eq}, μg/ g	3.59	3.71	3.77
Efficiency of the arsenic adsorption, %	87.1	88.1	94.7
Adsorbent exhaustion rate, kg/ L	0.0061	0.0059	0.0062
Breakthrough capacity ($Q_{50\%}$), μg As/ g adsorbent	3.71	3.76	3.66
Rate of adsorption zone movement in the column Uz, cm/ 24 h	0.071	0.024	0.0045

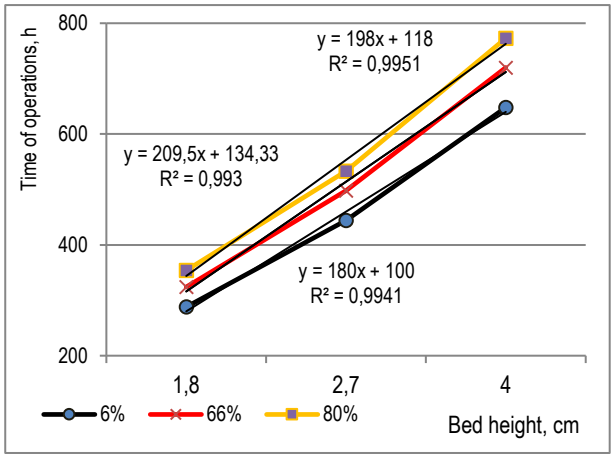

Fig. 3. Bohart-Adams model for 6, 66, and 80% breakthrough at different bed heights and constant inlet arsenic concentration (25 μg/ L) and flow rate (0.33 l/ 24 h)

column steadily decreased from 0.071 to 0.0045 cm/ 24 h when the bed height increased from 1.7 to 4.0 cm. However, the determined equilibrium arsenic content (q_{eq}) was quite lower in comparison to the values determined by other researchers (Kundu, Gupta, 2005). It is well-known that the slightly alkaline pH of waters being treated as well as the significantly higher concentrations of anions (sulphate, hydrocarbonate, silicate, (Table 1) hinders the arsenate adsorption (Genc-Fuhrman et al., 2005).

Data modelling about the arsenic adsorption from the operation of the laboratory filter column was carried out by Bohart-Adams mathematical model (Bohart, Adams, 1920) and bed depth service time approach proposed by Hutchins (1973). The data from each column operation was assessed by means of determination of three different points of arsenic isoremoval from the spring waters being treated, i.e. at 1.5, 10, and 20 μg/L breakthrough concentration in effluents (Table 4). So, for each arsenic isoremoval percent, the Bohart-Adams model was simplified to the equation

$t = a.x + b$ where a = slope's line = N_0/Ci. V and b = intercept = $1/ KC_i . \ln((Ci/ Ce) - 1)$.

The relationship between the bed depth versus time of the operation for the three isoremovals is depicted in Figure 3. It is evident that these lines were almost parallel to each other and the horizontal distance between them was 0.12 cm (so-called height of exchange zone). The results showed clearly that the rate of arsenic adsorption under continuous way of operation (K_{BA}) and the adsorption capacity of goethite-covered quartz sand (N_0) decreased significantly at longer columns' service operation (Table 4). That trend was logical having in mind that the higher number of binding sites of sorbent have been already occupied at such conditions which determined the higher breakthrough arsenic concentration in the effluents.

Table 4. *Bohart-Adams model constants for the arsenic adsorption on goethite-covered quartz sand*

Iso-removal, %	Breakthrough concentration μg/L	N_0, μg/ L	K, L/μg.h	R^2
6	23.5	373.1	-0.0011	0.9941
60	10.0	410.4	0.0001	0.9951
80	5.0	434.2	0.0004	0.9930

Table 5. *Comparison between the measured and predicted breakthrough times (in hours) at 60% arsenic removal using Bohart-Adams model constants*

Index	Height of the adsorption zone, cm		
	1.8	2.7	4.0
Flow rate: 0.33 L/24 h			
Measured	312	504	720
Predicted	474	650	910

The results included in Table 5 revealed that the values of measured breakthrough time at 60% arsenic concentration were 25% averagely lower than the values predicted by the Bohart-Adams model. The main reason was probably the insufficient bed height being used in those experiments. It is shown that the model could be used roughly for designing other column operation experiments over a range of flow rate or arsenic concentration. There are other models too, i.e. Thomas, Yoon-Nelson that could be used in modelling of the data about the arsenate adsorption in a continuous regime of operation.

Effect of the flow rate on the arsenate adsorption

The flow rate of a column operation has a crucial effect on factors as volumes of water being treated and a residual arsenic concentration lower than permissible concentration, are needed to be combined at a pilot or industrial scale. In that experiment, the arsenic inlet concentration and the bed height were constant to all columns and only the flow rate of spring waters being treated distinguished from one variant to other (Table 6). The breakthrough curves are shown in Figure 3. The applied flow rate varied between 0.131–0.33 L/24 h which related to 3.7 to 9.4 bed volumes of spring waters treated per day. That range of bed volumes meant that the residence time which water spent into the filter column varied 2.5 times. So, the arsenate ions and the binding sites of goethite-covered quartz sand had different contact times to react with each other.

Table 6. *Characteristics of the experiment about the effect of flow rate on the arsenic adsorption*

Index	Applied flow rate, L/24 h		
	0.33	0.221	0.131
Arsenic in inlet solution, µg/ L	25.0		
Height of the adsorption zone, cm	1.8		
Volume of solutions being treated, L	5.30		
Applied bed volumes per 24 h	9.4	6.3	3.7
Time of operation until 100 % arsenic breakthrough, days	16	24	40

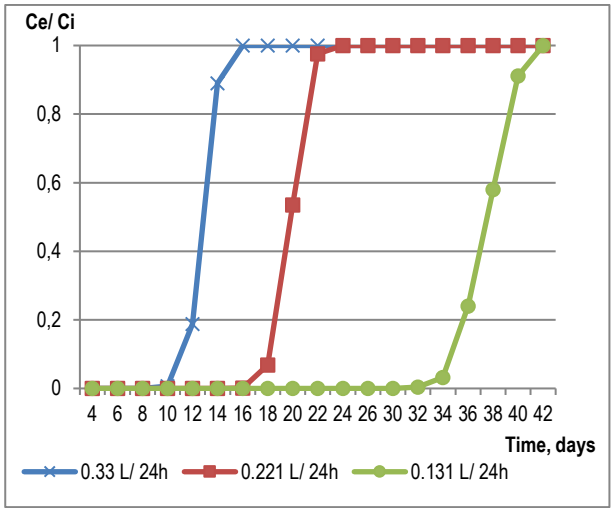

Fig. 3. Breakthrough curves of arsenic for varying flow rates (L/24 h) at a bed height of 1.8 cm and 25 µg/ L inlet concentration of arsenic

As a result, the lower the flow rate was, the higher the residence time of waters into the column was and arsenates removed more efficiently by adsorption of goethite-covered quartz sand. At higher flow rate, the arsenic left the column before the equilibrium between the adsorbate and adsorbent took place. For example, the time for arsenic breakthrough concentration steadily increased from 13.4 to 36.7 days due to the decreasing of the water`s flow rate (Table 7). The value of rate constant of arsenate adsorption (K) increased gradually at a higher flow rate of spring waters (Table 8). However, the value of sorption capacity of goethite-covered quartz (N_0) sand was higher at the lowest tested flow rate which was an indication that the process of arsenate adsorption was rate-dependent. For that reason, the equilibrium arsenic content (q_{eq}) and maximum adsorption capacity (q_0) of goethite-covered quartz sand were 3.97 µg/g and 4.04 µg/g for 0.131 L/24 h. At all tested flow rates, the value for the maximum adsorption capacity (q_0), predicted by Adams- Bohart model, was close to the experimentally determined values of the equilibrium arsenic content (q_{eq}). However, we must keep in mind that some review shows that the maximum adsorption capacity determined by Adams-Bohart Model usually underestimate the value in comparison to other models applied to continuously operated experiments (Podder, Mjumder, 2018).

Table 7. *Parameters characterising the arsenic adsorption on goethite-covered quartz sand under a continuous regime of operation in dependence on the applied flow rate*

Index	Applied flow rate, L/24 h		
	0.33	0.221	0.131
Veff, L	4.95	5.08	5.11
q_{total}, µg	108.61	111.72	119.03
m_{total}, µg	131.25		
q_{eq}, µg/ g	3.62	3.72	3.97
Efficiency of the arsenic adsorption, %	82.7	85.1	90.7
Adsorbent exhaustion rate, kg/L	0.0061	0.0059	0.00587
Breakthrough capacity ($Q_{50\%}$), µg As/ g adsorbent	3.56	3.65	3.90
Time for arsenic breakthrough concentration, days	13.4	20.6	36.7

Table 8. *Bohart-Adams model constants for the arsenic adsorption on goethite-covered quartz sand under a continuous regime of operation in dependence on the applied flow rate*

Flow rate, L/24h	N_0, µg/L	K, L/µg.h	q_{eq}, µg/g	q_0, µg/g	R^2
0.33	21.22	0.0936	3.62	3.69	0.9856
0.221	21.74	0.0589	3.72	3.78	0.9326
0.131	23.23	0.0369	3.97	4.04	0.981

Although the experiments were carried out until 100% arsenic breakthrough, the process of arsenic removal from the spring water was very efficient. For example, at the highest tested flow rate, 0.33 L/24h, the efficiency of arsenic removal was higher than 82%.

Arsenate desorption from goethite-covered quartz sand under a continuous regime of operation

The arsenate desorption from goethite-covered quartz sand was carried out with phosphate containing water whose concentration was three times higher than the arsenic concentration in the waters being treated. The results suggested that the arsenate adsorption on goethite-covered quartz sand led to the formation of a covalent bond. For example, the total amount of desorbed arsenic was 13.3 µg, when the desorption solution was with slightly alkaline pH, which related to 11.2% of efficiency (Fig. 4). When the pH of the above-mentioned desorption solution decreased to 5.00, almost the same amount of arsenic desorbed from the sorbent. If the pH decreased further to pH 3.00, additional 4.9 µg arsenic desorbed just in a few cycles and the final percent of desorption reached 13.0% (Fig. 5).

Arsenate desorbed most efficiently when the pH of the desorbing solution increased above 8.5. In that case, the percent of desorption reached 55.2% (Fig. 6). A ligand exchange process between adsorbed arsenate and hydroxyl anions was the mechanism and the decreasing pH of effluents to values in the range 7.6–7.8 evidenced it. Further alkalisation of desorption solution to 9.5–10.0 led to the release of 12.5 µg additionally and the total arsenate desorption reached 65.8%.

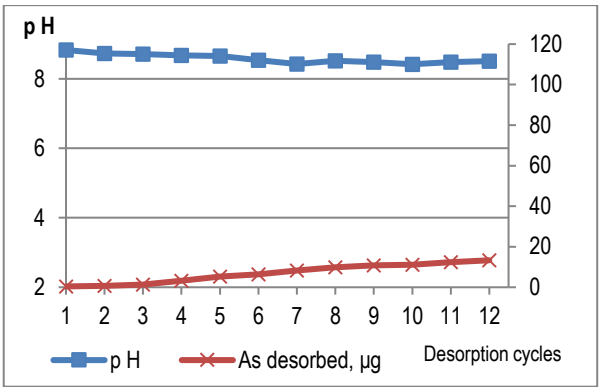

Fig. 4. Arsenic desorption from goethite-covered quartz sand by HPO_4^{2-} -spiked spring water in a continuous regime of operation

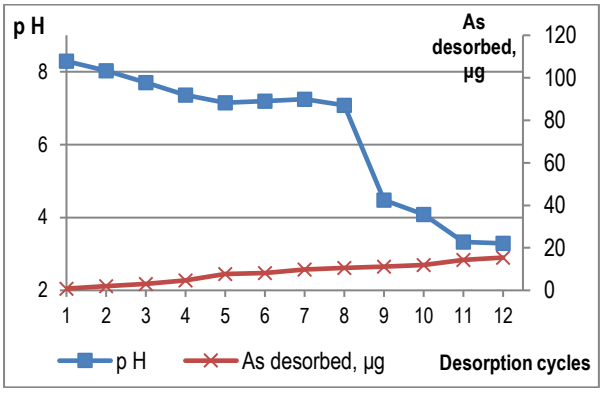

Fig. 5. Arsenic desorption from goethite-covered quartz sand by HPO_4^{2-} -spiked spring water at acidic pH in a continuous regime of operation

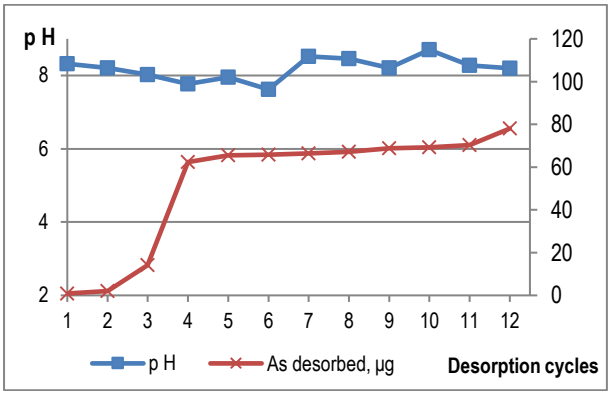

Fig. 6. Arsenic desorption from goethite-covered quartz sand by HPO_4^{2-}-spiked spring water at alkaline pH in a continuous regime of operation

Conclusions

1. The equilibrium content of adsorbed arsenates on goethite-covered quartz sand in a filter column, operated in flow regime, was in the range of 3.5–3.9 µg/g. The bed height of the adsorption zone and the applied flow rate had a crucial effect on the efficiency of the pollutant removal.

2. There is a need to test other widely applied column adsorption kinetic models such as Thomas, Yoon-Nelson, etc., to the experimental data to predict the arsenic breakthrough curves and for estimating the column kinetic parameters.

3. The arsenate desorbed more efficiently under a continuous regime of operation at alkaline in comparison to acidic pH. It revealed that the ligand exchange mechanism played the main role in sorption/ desorption process of arsenate on/ from goethite-covered quartz sand.

References

Bohart, G., E. Adams. 1920. Some aspects of the behavior of charcoal with respect to chlorine. – *J. American Chemical Soc.*, *42,* 523–544.

Choong, T., T. Chuah, Y. Robiah, F. Gregory Koay, I. Azni. 2007. Arsenic toxicity, health hazards, and removal techniques from water: an overview. – *Desalination Water Treatment, 217*, 139–166.

Genc-Fuhrman, H., B. Henrik, D. McConchic. 2005. Arsenate removal from water using sand-red mud columns. – *Water Research*, *39,* 2944–2954.

Hutchins, R. A. 1973. New method simplifies design of activated carbon systems. – *Chemical Engineering*, *80,* 133–138.

Jonhson, D. L., M. E .Q. Pilson. 1971. Spectrophotometric determination of arsenite, arsenate, and phosphate in natural waters. – *Analytica Chimica Acta*, *58,* 289–299.

Kundu, S., A. K. Gupta. 2005. Analysis and modelling of fixed bed column operation on As (V) removal by adsorption onto iron oxide-coated cement. – *J. Colloid and Interface Sci.*, *290,* 52–60.

Manning, B. A., S. E. Fendorf, S. Goldberg. 1998. Surface structures and stability of arsenic(III) on goethite: spectroscopic evidence for inner-sphere complexes. – *Environmental Science & Technology*, *32*, 2383–2388.

Mohan, D., C. U. Pittman. 2007. Arsenic removal from water/ wastewater using adsorbents. A critical review. – *J. Hazardous Materials*, *142*, 1–53.

Podder, M. S., C. B. Majumder. 2018. Biological detoxification of As(III) and As(V) using immobilized bacterial cells in fixed bed bio-column reactor: Prediction of kinetic parameters. – *Groundwater for Sustainable Development*, 6, 14–42.

Sharma, V., M. Sohn. 2009. Aquatic arsenic: toxicity, speciation, transformation, and remediation. – *Environment International*, *35*, 743–759.

Zheleva, I., P. Georgiev, S. Groudev. 2016. Adsorption/desorption of arsenate on/from goethite and hematite. – *Ann. Univ. Mining and Geol.*, *59*, Part II, 137–141.

A MODEL OF THE CONDITIONS FOR SPONTANEOUS RELEASE OF BIOGAS FROM A SANITARY LANDFILL IN SOUTHERN BULGARIA

Stefan Dimovski, Nikolay Stoyanov, Svetlana Bratkova

University of Mining and Geology "St. Ivan Rilski", 1700 Sofia; dimovski@mgu.bg

ABSTRACT. The conditions that lead to a spontaneous release of biogas are studied, as well as the reasons for the following self-ignition of the sanitary landfill situated near the town of Haskovo, Southern Bulgaria. A geophysical survey was performed according to the method of electrical resistivity tomography (ERT) and a two-dimensional geoelectrical model of the sanitary landfill was constructed in the area of the studied site. The geoelectrical model has been transformed into an anthropogenic section of the work areas affected by the fire. The constructed section is in accordance with the applied technology for deposition of waste materials and the geodetic measurements of their volume. A model for the conditions for accumulation, circulation, critical mass formation and biogas explosion has been developed, presenting in detail the possible scenario for the occurrence and the progress of such incidents. Measures and principle schemes are proposed for limiting the dangerous accumulation of biogas in the sanitary landfill.

Keywords: sanitary landfill, electrical resistivity tomography, biogas, self-ignition, ecology

МОДЕЛ НА УСЛОВИЯТА ЗА СПОНТАННО ИЗТИЧАНЕ НА БИОГАЗ ОТ ДЕПО ЗА НЕОПАСНИ (БИТОВИ) ОТПАДЪЦИ В ЮЖНА БЪЛГАРИЯ

Стефан Димовски, Николай Стоянов, Светлана Браткова

Минно-геоложки университет "Св. Иван Рилски", 1700 София

РЕЗЮМЕ. Проучени са условията за спонтанно изтичане на биогаз и причините за последвалото самозапалване на регионалното депо за неопасни (битови) отпадъци край град Хасково, Южна България. Проведено е геофизично изследване по метод ERT (Electrical Resistivity Tomography) и е съставен двумерен геоелектричен модел на сметищното тяло в района на проучвания обект. Геоелектричният модел е трансформиран в антропогенен разрез на засегнатите от пожара работни участъци, който е валидиран с прилаганата технология за депониране на отпадъци и геодезичните измервания на техния обем. Разработен е модел на условията за натрупване, циркулация, формиране на критични количества и взривяване на биогаза, представящ в детайли възможния сценарий за възникване и протичане на подобни инциденти. Предложени са мерки и принципни схеми за ограничаване на взривоопасното натрупване на биогаз в сметищното тяло.

Ключови думи: депа за битови отпадъци, електротомография, биогаз, самозапалване, екология

Introduction

The subject of the presented study is the north-western part of the Regional Sanitary Landfill of the municipalities of Haskovo, Dimitrovgrad and Mineralni Bani, located near the village of Garvanovo, where an incident related to spontaneous leakage and self-ignition of biogas occurred (see Fig. 1).

The studied region is about 10000 m^2. The terrain is flat with a slight slope to the south-southeast. The geological base is made up of volcanic rocks, which in their upper parts are cracked and weathered to a different degree and in separate places are decomposed to clay. The rock massif is partially overlaid by diluvial clays with small thickness (less than 1 m). According to the accepted technology, a shielding layer of compacted clay with a thickness of 0.5 m is applied to the bottom of the landfill. The waste depositions are spread over certain work areas. The studied region includes two work areas – northern (a new one) and southern (an old one). The waste is defragmented and compressed in 20–30 cm thick seams that are accumulated in layers with a working height of about 1.8–2.0 m. These layers are covered (sealed) with separating coats of clay. In the upper part of the landfill body the waste depositions are slightly water-saturated. Zones completely saturated by landfill waters (leachate) are present at the landfill bottom. Part of the leachate may penetrate through the clay screen and infiltrate into the geological base.

Geoelectrical model

Electrical resistivity methods have wide application in the detailed mapping of the near-surface section. Their efficiency is connected to the differentiation according to electrical resistivity and is tied to the existing preconditions for presence of ionic conductivity (Keller, Frischknecht, 1981; Grigorova, Koprev, 2019). Electrical resistivity tomography was selected for the performed surveys as it can be effectively applied for obtaining a detailed picture of the geoelectrical differentiation in the near-surface section of landfill sites (Gyurov, Stoyanov, 2004; Dimovski, Stoyanov, 2011). This method is based on the use of modern equipment, optimal measuring techniques, and computer processing of acquired data (Griffiths, Barker, 1993; Dimovski et al. 2007; Grigorova, Koprev, 2018).

The objectives of the performed ERT survey are development of a geoelectrical model of the near-surface section, determination of the thickness and degree of water-

saturation of the landfilled waste, achievement of a qualitative assessment regarding the conditions for the accumulation and circulation of biogas in the work areas where the incident occurred. The field measurements were accomplished a few days after the incident.

The geoelectrical model is based on the determined by the computer programme RES2DINV (Loke, 1999; 2001) electrical resistivity distribution, as well as on the available information for the geological section, the waste disposal technology and the results of the performed systematic monitoring. The composed scheme of the geoelectrical section in the studied area is illustrated in Figure 2.

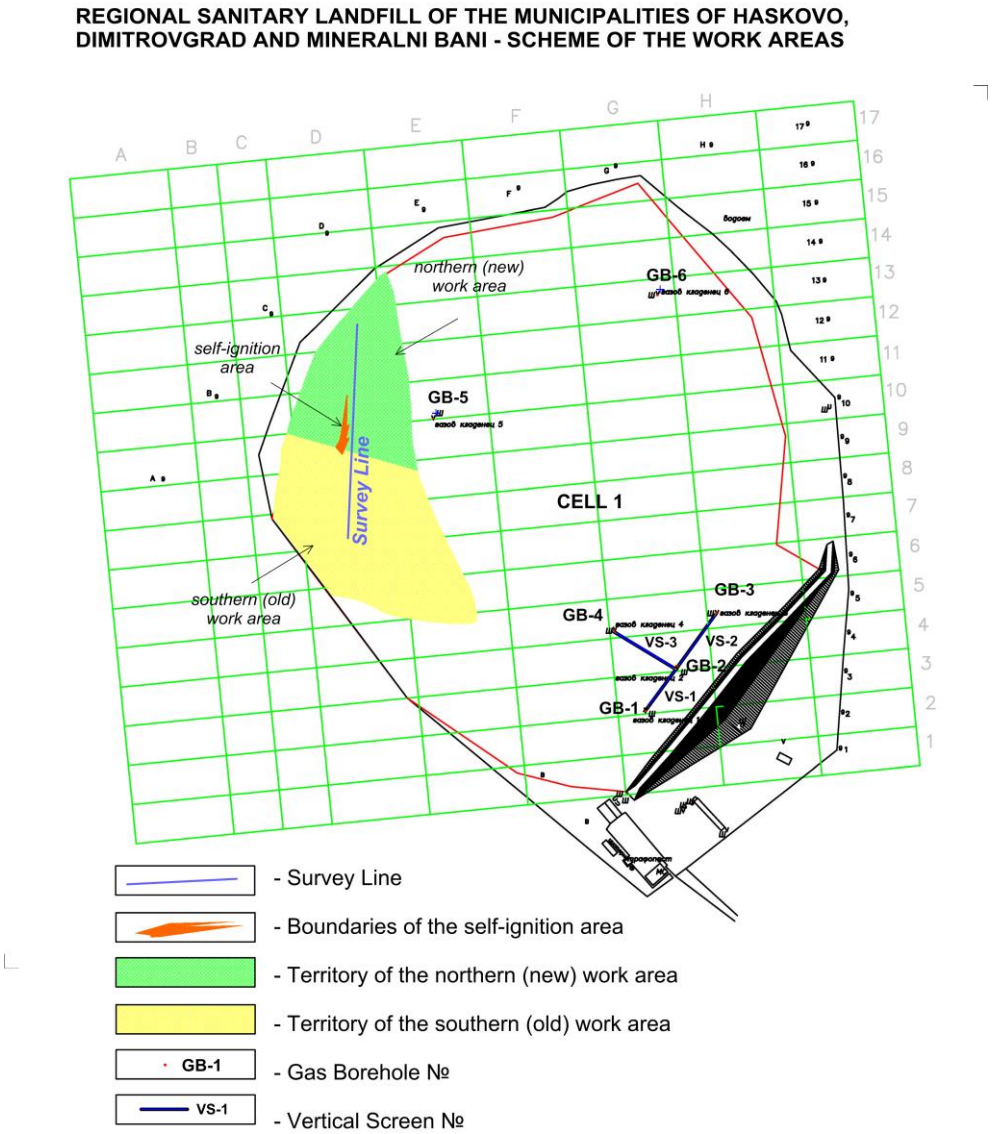

Fig. 1. Scheme of the studied region, illustrating the location of the survey line and the scope of the self-ignition incident

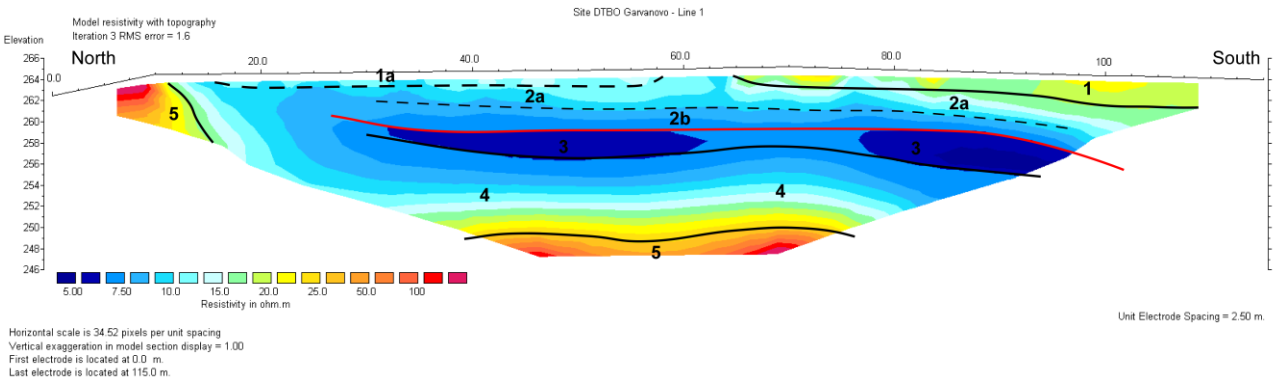

Fig. 2. Electrical resistivity distribution along the survey line

Taking into account the specifics of the ionic conductivity (Daniels, Alberty, 1966), the cross-section is differentiated in seven electrical resistivity media, marking layers of different origin and characteristics:

- The first electrical resistivity medium (Layer 1) is characterised by relatively high values of the resistivity of the studied section – in the range from 17.5 Ωm to 22.5 Ωm. It covers the near-surface part of the section in the southern half of the studied area. The thickness of this medium is about 1–3 m, with high values referring to the most southern end of the profile. It most probably maps the upper sealing layer of sandy clays and the very poorly water-saturated to dry part of the underlying last (topmost) layer of deposited waste.
- The second electrical resistivity medium (Layer 1a) has lower values of the electrical resistivity than the first one – from 12.5 Ωm to 17.5 Ωm. It covers the near-surface part of the section in the northern half of the studied area. Its thickness does not exceed 0.8–0.9 m. The second electrical resistivity medium is likely to represent the top sealing layer of clay over the last layer of deposited waste in the northern part of the sanitary landfill.
- The third electrical resistivity medium (Layer 2a) is typified by average resistivity values of 10 Ωm to 15 Ωm and has a thickness of about 2.0 m. It is likely to map the last (topmost) layer of deposited waste, the underlying clay layer and the uppermost parts of the waste deposited underneath. These parts of the section are poorly saturated and with relatively low density.
- The fourth electrical resistivity medium (Layer 2b) has lower resistivity values – in the range of 7.5 Ωm to 10 Ωm. It is spread ubiquitously underneath the third electrical resistivity medium and has a thickness of 1.7 m to 2.2 m. It is most likely to outline the boundaries of the first layer of waste deposited at the base of the sanitary landfill. This part of the section is saturated with landfill waters (leachate) typified by excessive total mineralisation and high electrical conductivity.
- The fifth electrical resistivity medium (Layer 3) is characterised by the lowest resistivity values for the studied section – from 5 Ωm to 7.5 Ωm. It denotes a layer-like body with a thickness of about 1.5–2.0 m and more. Layer 3 maps the clay barrier layer placed in the bottom of the landfill and the upper part of the underlying geological section, represented by highly weathered volcanic rocks, decomposed to clay. This part of the studied section is water saturated with the landfill leachate.
- The sixth electrical resistivity medium (Layer 4) locates parts of the subsurface section with a wide range of electrical resistivity – from 7.5 Ωm to 25 Ωm and has a thickness of about 7–8 m. It outlines the upper part of the geological base of the landfill, represented by marginally cracked and weathered to a different degree volcanoes. The established differentiation in the values of the electrical resistivity implies that Layer 4 is partially contaminated by leachate emissions penetrating beneath landfill bottom and infiltrating in depth.
- The seventh electrical resistivity medium (Layer 5) is characterised by the highest resistivity values – from 25 Ωm to over 150 Ωm. It most likely maps the relatively solid and unaltered by secondary changes segments of the rock massif. In the central part of the research area Layer 5 is almost horizontal (with a barely visible slope to the south) and is situated at a depth of about 15–16 m. At the start of the survey line, on the northern border of the landfill and beyond it to the north, it is located in the surface part of the section, where there are also visible surface outcrops.

Model of the anthropogenic section

The model of the anthropogenic section is composed along a line passing through the work areas affected by the fire. It is based on the results of the geophysical survey and is illustrated in Figure 3. Basically, it follows the geoelectrical section and is validated with the applied waste disposal technology and the performed regular geodetic measurements.

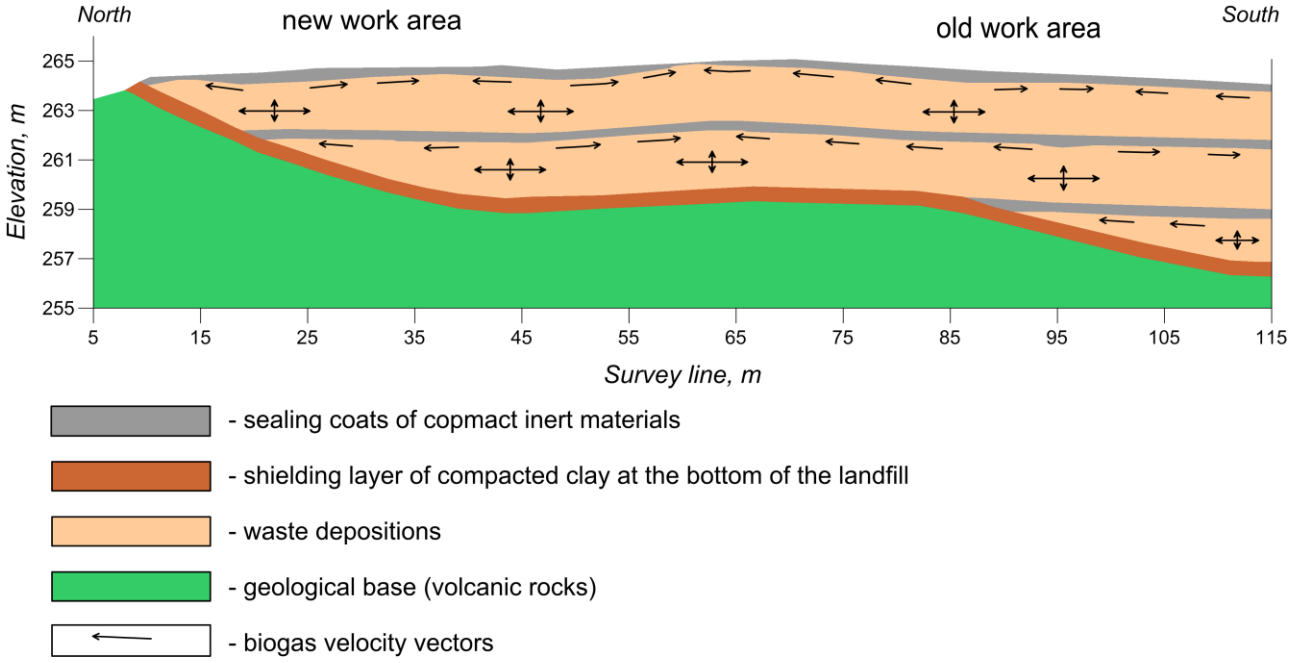

Fig. 3. Anthropogenic section of the sanitary landfill site along the survey line

The composed model gives an idea of the environment in which the critical accumulation of biogas has occurred, clarifies the conditions for the emergence and development of gas-transport processes and reveals the reasons of spontaneous explosions and fires. It illustrates the spatial boundaries and geometric characteristics of the differentiated layers and coats in the northwestern part of the sanitary landfill in the so-denoted northern (new) and southern (old) work areas.

Based on the presented in Figure 3 anthropogenic section, the following summaries and conclusions can be made:

- The geological base is covered by a compacted clay layer about 50–60 cm thick.
- The average thickness of the landfill body along the studied line is about 5–6 m.
- In the new work area the section includes two layers of waste with a total thickness of 4–5 m. Only in its most northern part, where the geological base is elevated, only one layer of waste is present with a thickness of 1–2 m.
- The old work area in its northern half is composed of two layers of waste and in the southern one - of three layers. The total thickness of the landfill body increases from north to south from 4–5 m up to more than 6–7 m.
- In both areas the waste layers are covered by a compact coat of inert materials 20–30 cm thick. In some places, the last sealing layer is unconsolidated, thinner (5–10 cm) or missing. This feature is quite distinct at the boundary between the old and the new work area as well as along the northern periphery of the landfill.
- The waste layers are practically encapsulated between the coats of compacted inert materials. This presupposes that the gas-transport in the landfill is predominantly in horizontal direction and the vertical one is of subordinate importance. In Figure 3 this aspect is illustrated schematically with the velocity vectors of the landfill biogas migration.
- Large amounts of biogas accumulate under high pressure in the encapsulated wastes. This process is accelerating in periods characterised by more rainfalls and higher temperatures when the degradation processes are more intense and the quantity of biogas formed is bigger.
- Interlayer gas exchange and/or spontaneous leakage of gas emissions into the atmosphere occur in areas with unconsolidated, very thin or disintegrated coating layer (the so-called "windows"). Through these "windows" it is possible that atmospheric O_2 can enter into the landfill, which in turn leads to the formation of an explosive mixture with the landfill biogas.

Conditions for biogas accumulation, circulation, spontaneous leakage, formation of critical quantities and self-ignition

Biogas gas is produced by the degradation of organic waste (manure, sewage sludge, municipal solid waste) under anaerobic conditions in a landfill. The various groups of anaerobic microorganisms are involved in the whole biogas-production process. The main steps are three: hydrolysis, acetogenesis and methanogenesis (Wellinger et al., 2013).

The hydrolysis is a process of breakdown of organic polymers (cellulose, hemicellulose, starch, proteins) into smaller compounds through the activity of bacterial produced extracellular enzymes.

In the second step (acidogenesis), the resulting intermediates with a low molecular weight (sugars, amino acids) initially ferment to organic acids and alcohols. After secondary fermentation the key products acetic acid (CH_3COOH), hydrogen (H_2) and carbon dioxide (CO_2), sources of carbon and energy for methanogenic bacteria, are produced.

In the methanogenesis (the third step) methanogenic bacteria convert the resulting products from the second phase to biogas (methane and CO_2). Methanogenic bacteria and acid-producing bacteria act in a symbiotical way.

The scheme of accumulation, circulation, formation of critical quantities and self-ignition of the biogas according to which the incident occurred is illustrated in Figure 4. Following the general scheme presented, the processes passed under the subsequent scenario:

1. The landfill biogas gradually accumulated in larger amounts in the upper part of the landfill body in the areas encapsulated by well-persistent layers of compacted inert materials (Fig. 4-A).
2. In the old work area, the amount of biogas and the space it occupies are much larger than these in the new work area. The reasons for this are the bigger volume of disposed waste, the better "encapsulation" and the possibility for inflow of additional quantities of biogas from the southern parts of the landfill.
3. At the same time, small amounts of biogas continuously flow into the atmosphere through the so-called "windows" in the near-surface "sealing" layer (Fig. 4-A). This process does not pose a serious risk of self-ignition or explosion if there is no accumulation of a critical amount of explosive mixture of CH_4, H_2 and O_2.
4. The degradation processes that have been going on for many years cause the accumulation of larger and larger quantities of landfill biogas in the encapsulated spaces, which is accompanied by a significant increase in pressure (Fig. 4-B).
5. An important fact is that, at the time of the incident, the weather conditions were favorable for the formation of much larger quantities of biogas. The amount of rainfall is one of the highest in the last 5 years (50% higher than the average for this period). The temperature is also among the maximum recorded in the same period. The bigger amounts of biogas and the high temperature released under these conditions are responsible for a more rapid increase in the concentration of flammable components (CH_4 and H_2) and for raised pressure in the landfill.
6. The increased pressure forms more intense flows to the surface and respectively amplifies the rate of gas emissions. As a consequence, in the spontaneously leaking areas the permeability increases, channels and larger gaps are formed in depth. The opportunities for entry of atmospheric O_2 into the landfill body also greatly escalate.
7. The intermixing of biogas, characterised by high CH_4 and H_2 content, and atmospheric O_2 resulted in the accumulation of a critical quantity of explosive mixture in the surface area of the sanitary landfill at the boundary between the old and the new work area (Fig. 4-C). Most likely, when the process reached its critical point self-ignition occurred.

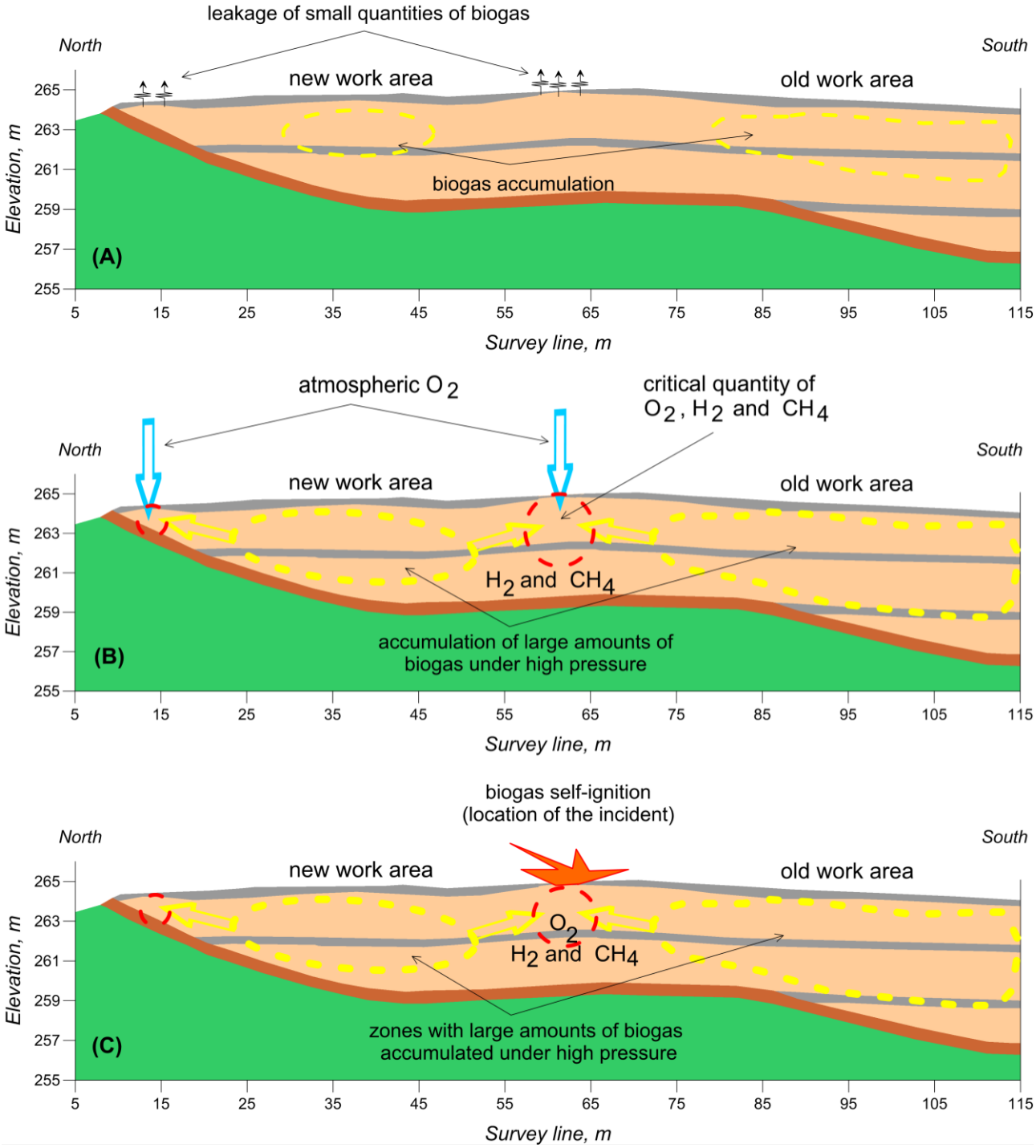

Fig. 4. Scheme of accumulation, circulation, formation of critical quantities and self-ignition of the biogas

Conclusions

The performed retrospective analysis of the conditions and the reasons for the incident occurrence shows that the main problem is connected to the accumulation of large quantities of high-pressure biogas in the new part of the landfill.

The problem can be solved by building a sufficiently well-developed system of facilities (gas boreholes and vertical screens) for collecting and removing biogas outside the landfill body. For illustration, in Figure 5 a schematic solution for the affected by the accident northwestern part of the sanitary landfill is presented.

The solution includes the construction of two new gas boreholes that have to be located in the central parts of the work areas at a distance of 50–60 m apart. The newly built boreholes will drain the biogas formed in the two work areas, thus eliminating the possibility of its accumulation under high pressure, the formation of critical quantities and subsequent self-ignition. Vertical screens (four-beam pattern) can be constructed around the boreholes in order to increase the efficiency of the system.

The proposed approach toward resolving the problem is a more moderate option, which makes a reasonable compromise between the effectiveness of the measures and the financial costs incurred for their completion.

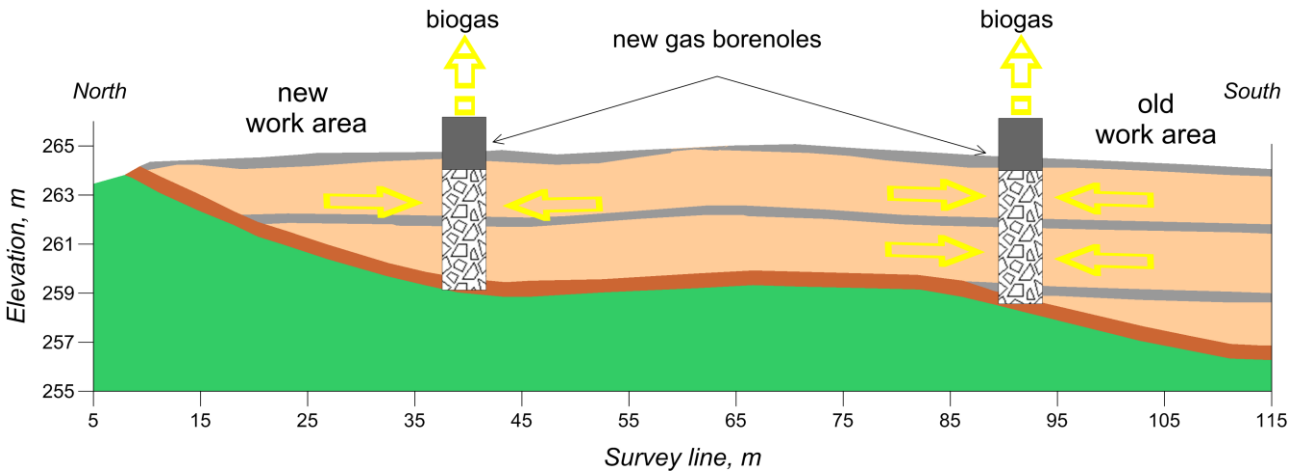

Fig. 5. Scheme of the proposed solution for the affected by the accident northwestern part of the sanitary landfill. Location of the new boreholes

References

Daniels, F., R. Alberty. 1966. *Physical Chemistry.* John Wiley & Sons, New York, 674 p.

Dimovski, S., N. Stoyanov. 2011. A geoelectrical approach for studying the hydrogeological conditions in the region of Asenovgrad sanitary landfill. – *Ann. Univ. Mining and Geol.*, *54*, Part I, 125–130 (in Bulgarian with English abstract).

Dimovski, S., N. Stoyanov, Ch. Gyurov. 2007. Efektivnost na elektrotomografiyata za detailno geoelektrichno kartirane na pripovarhnostnia geolozhki razrez. – *BULAKVA*, *4*, 47–55 (in Bulgarian).

Griffiths, D. H., R. D. Barker. 1993. Two-dimensional resistivity imaging and modelling in areas of complex geology. – *Journal of Applied Geophysics*, *29*, 211–226.

Grigorova, M., I. Koprev. 2018. Application of electrical resistivity tomography for sands underwater extraction. – *Proceedings of the 4th International Scientific Conference Geobalcanica*, *15–16 May 2018*, Ohrid, 15–20.

Grigorova, M., I. Koprev. 2019. Geophysical investigations in "Starite Kolibi" marble deposit in Central Southern Bulgaria. – *Proceedings of the 5th Jubilee International Scientific Conference Geobalcanica*, *13–14 June 2019*, Sofia, 6 p. (in press)

Gyurov, C., N. Stoyanov. 2004. Possibilities of 2D resistivity method for locating the extension of old landfills. – *Proceedings of the 4th National Geophysical Conference with International Participation "Geophysics in Economic Activity, Environment and Cultural Heritage Investigations"*, *4–5 October 2004*, Sofia, 128–131.

Keller, G., F. Frischknecht. 1981. *Electrical Methods in Geophysical Prospecting.* Pergamon Press, Oxford, 535 p.

Loke, M. H. 1999. *Electrical Imaging Surveys for Environmental and Engineering Studies. A Practical Guide to 2-D Surveys.* Geotomo Software, Penang, Malaysia, 57 p.

Loke, M. H. 2001. *A Practical Guide to RES2DINV v. 3.4; Rapid 2-D Resistivity & IP Inversion using the Least-squares Method.* Geotomo Software, Penang, Malaysia, 96 p.

Totev, I. 1998. *Tretirane na tvardite bitovi otpadatsi*. UASG, Sofia, 268 p. (in Bulgarian)

Wellinger, J., J. Murphy, D. Baxter. 2013. *Biogas Handbook: Science, Production and Application*. Woodhead Publishing, Cambrige, UK, 512 p.

SEISMIC SOURCE COMPARISON FOR HIGH RESOLUTION DATA PROCESSING

Bozhurka Georgieva

University of Mining and Geology "St. Ivan Rilski", 1700 Sofia; bojurkageorgieva97@abv.bg

ABSTRACT. Nowadays, high resolution seismic processing is a key issue for achieving reasonable and reliable information for subsurface geology structure. The importance of the seismic methods lies above all in the fact that the data produced by seismic work, if properly handled, yields an almost unique and unambiguous interpretation. Seismic work is comprehensive and delicate process which depends on many factors and circumstances. On the first place, this is the type of source used to produce seismic waves. A widely used method in the past is to explode dynamite charge in a hole. In the last 10 years, however, there has been a tendency toward replacing explosive sources with some other environmentally less harmful seismic sources. The following work presents a comparison between two type of source signal – Vibroseis and Dinoseis and shows potential advantages and drawbacks in both cases on real seismic data.

Keywords: seismic method, seismic data, sources of seismic signal

СРАВНЕНИЕ НА СЕИЗМИЧНИ ДАННИ ПОЛУЧЕНИ ОТ РАЗЛИЧНИ ИЗТОЧНИЦИ НА СИГНАЛА

Божурка Георгиева

Минно-геоложки университет "Св. Иван Рилски", 1700 София

РЕЗЮМЕ. Понастоящем високоразрешаващата обработка на сеизмични данни е основа за получаването на информация за дълбочинният строеж на Земята. При извършване на качествена сеизмична обработка, получените сеизмични разрези носят уникална информация за структурният строеж на земната кора. За осъществеване на така поставените цели обработката на данните изисква да се вземат под внимание редица фактори. Основен фактор се явява изборът на система за създаване на сеизмичния сигнал. За разлика от широко използваният в миналото динамит поставен в сондажи, на съвременен етап голямо разпространение имат неинвазивните източници. Настоящата работа разглежда и сравнява предимствата и недостатъците на два от най-популярните неинвазивни източници на сеизмичен сигнал – Вибросеиз и Диносеиз.

Ключови думи: сеизмичен метод, сеизмични данни, източници на сеизмичен сигнал

Introduction

The main purpose in seismic work is the correct illustration of geology in the study area. Seismic processing is a delicate process so even small variations can have a significant impact, hiding the real signature of the signal or introducing artifacts. Nowadays, technology has gone a long way and the processing of seismic data obtained even in the middle of the last century is not difficult. In the era of state-of-the-art technology, it is possible to achieve high resolution seismic models which in turn leads to an increase in the potential of the subsequent interpretation of the processed data. In recent decades there has been a rapid development in the technical industry and sources for generating seismic waves.

The present work aims to examine and compare the advantages and drawbacks of two of the most popular land sources of seismic signal – Dinoseis and Vibroseis. Recent advance in source technology is further improving the data quality by putting more seismic energy into the earth at wider range of frequencies. The ideal source for seismic exploration is an impulsive source that concentrates its energy at a point in space and releases it instantaneously. In practice, however, sources have finite spatial size and emit signals over a finite period, producing broadened wavelets that add complexity to the processing. The choice which source to be used depends on several factors, including geophysical objectives, cost and environment constraints.

Land seismic survey

Seismic data acquisition requires an energy source, a receiver, and a recording system. In seismic exploration surveys, source–receiver distance is small compared to the target depth. This means that a small part of the down-going energy is reflected on geological layer boundaries. The main fraction of the energy is transmitted and travels deeper where reflections occur at the next layer boundary and so on. This method results in a good vertical and horizontal structural resolution of the subsurface (Hubscher, Gohlb, 2014).

According to Jeffryes (2006) seismic surveying is when a source of seismic energy is caused to produce seismic energy that propagates downward through the Earth. The downwardly-propagating seismic energy is reflected by one or more geological structures within the earth that act as partial reflectors of seismic energy (Fig. 1). The reflected seismic energy is detected by one or more receivers. It is possible to obtain information about the geological structure of the earth from seismic energy that undergoes reflection within the earth and is subsequently acquired at the receivers.

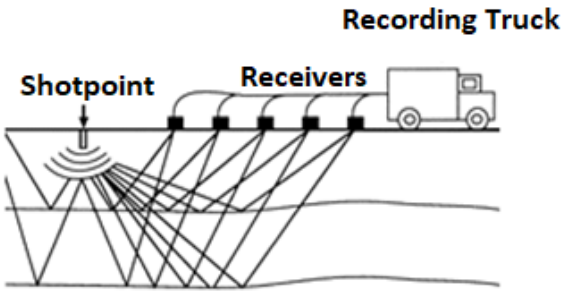

Fig. 1. Seismic land acquisition

In practice, a seismic surveying arrangement comprises of an array of sources of seismic energy. This is essential because it has to generate sufficient energy to illuminate structures deep within the earth and a single seismic source generally cannot do this.

Characteristics of seismic signal received from Dinoseis land seismic source

Since the beginning of seismic exploration the most popular impulse source for land acquisitions is dynamite, because it produces great quantities of energy. Other impulse source, which uses air and gas guns to produce energy is Dinoseis (Fig. 2). This energy source, largely used in the past, produces sufficient results in good seismic conditions, but is questionable in areas of poor response. The energy here is created by exploding a mixture of oxygen and propane gases, mostly, contained in a confined chamber, the bottom of which is a moveable plate resting on the ground surface. This way the designed chamber is attached to the bottom of a heavy vehicle to increase coupling its plate with ground surface.

Fig. 2. Dinoseis truck

When detonating the gas mixture, a sudden pressure impact occurs, which is transmitted through the base-plate to the ground surface (Alsadi, 2017).

Dinoseis generates relatively weak seismic energy, developing strong surface waves, and producing low-frequency seismic pulses. The method is rarely applied these days, but there are seismic sections acquired by Dinoseis and reprocessed nowadays. This makes it necessary to compare this energy source with the modern Vibroseis source. Defining the similarities and the differences between the shapes of the signal can help geoscience engineers to tie the lines received with both seismic sources when reading previously collected data or reprocessed one.

Characteristics of seismic signal received from Vibroseis land seismic source

Seismic sources are mainly divided into two groups - impulse and non-impulse sources of energy. However, the current dominant non-impulse energy source for land seismic exploration is a seismic vibrator. The use of such a vibrator is generally identified by the trademark Vibroseis. In Vibroseis survey, specially designed vehicles lift their weight onto a large plate, in contact with the ground, which is then vibrated over a period of time, with sweep of frequencies (Fig. 3). Seismic vibrators are the predominant source used in land acquisition (Grigorova, 2016).

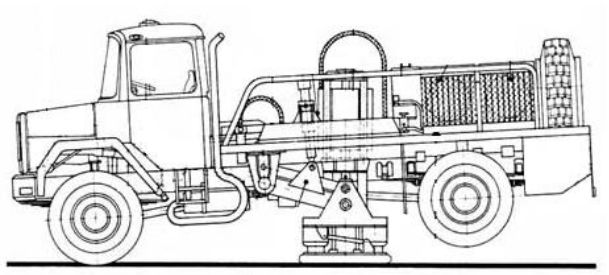

Fig. 3. Vibroseis truck

The vibrator is a surface source that emits seismic waves by forcing vibrations of the vibrator baseplate which is kept in tight contact with the earth through a pulldown weight. The driving force applied to the plate is supplied either by a hydraulic system, which is the most common system in use, or an electrodynamic system. Nowadays driving force can be managed also by magnetic levitation which is a new development in the field of seismic vibrator technology. The plate can vibrate in different directions: P-wave vibrators (where the motion of the plate is in the vertical direction) as well as S wave vibrators (vibrating in the horizontal direction).

There are many advantages using vibrators for seismic acquisition:

- The frequencies can be controlled easily;
- Real time monitoring and adjustment of the vibrations to the ground;
- This technique can be used both in urban areas and in environmentally sensitive areas, such as sand dunes or arctic snowpack;

Of course, this technique has also several drawbacks:

- It still has areas of limited access like swamps, mountains and coastal areas;
- The input signal is not impulsive, so additional processing and filtration is required to extract interpretable data;
- A recorded trace is correlated with a reference trace to extract the reflected signal.

One of the most important characteristic of the Vibroseis method is the limitation of the bandwidth of the source. Thus, the Vibroseis technique allows us to generate only those frequencies we actually need, whereas with an impulsive source like dynamite, some of the frequencies generated by the blast are ignored during the seismic acquisition (Levi, 2015).

Real data comparison between Vibroseis and Dinoseis

According to Grigorova (2016) in reflection seismology seismic data are usually contaminated with noise, which refers to any unwanted features in the data. One of the most important criteria for data quality is visibility of primary reflections, often quantified as signal-to-noise ratio. In seismic processing we usually manipulate our measured data, so that we can obtain an accurate image of the subsurface. One of the key components of seismic processing is determining which part of the recorded energy is noise and removing it from the data.

Results after pre-processing of Dinoseis and Vibroseis seismic data are presented in this paper. On shot records filtration techniques are demonstrated and different kind of signal behaviour is observed.

In Figure 4 is shown Dinoseis shot record before filtration procedures and its corresponding spectrum. In the case of the surface impact sources such as Dinoseis, the pulse is predominantly low frequency, due mainly to the coupling effect between the impact pad and the surface.

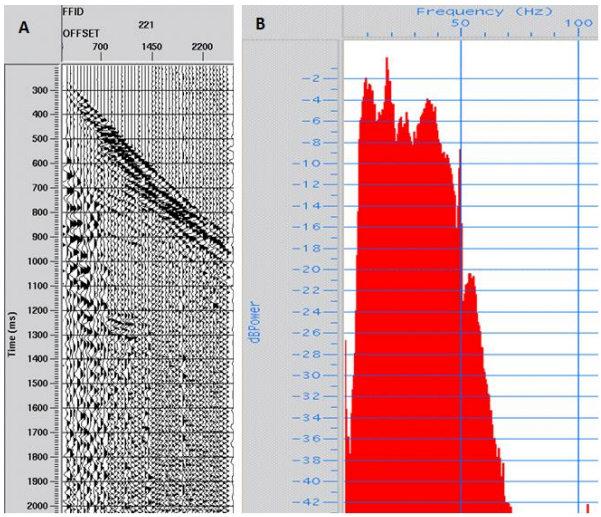

Fig. 4. Seismic shot (A) and its corresponding frequency spectre (B), received by Dinoseis seismic source

On the record low frequency noise can be noticed, which makes it difficult to analyse the real reflection data. Removal of the noise is a key component in preparing the data for velocity analysis and next imaging techniques. Effective noise removal, which preserves the original amplitude and phase characteristics of the data, provides the opportunity for advanced attribute work and inversion for better understanding of the reservoir (Dingus, 2011).

Looking at the spectra of these data, i.e., by transforming the time axis to a frequency axis using the Fourier transformation, different arrivals will give different peaks in the Fourier spectra. What we achieve is that we can analyse and interpret different frequencies in terms of different events. Moreover, we can start thinking about using the Fourier-transformed data for filtering purposes, i.e. removing certain frequency bands with the aim to remove undesired signal, like, e.g. cultural noise (Drijkoningen, 2019). It produces a characteristic 50 or 60 HZ sinusoidal noise on traces that can be measured. Its amplitude is relatively constant with recorded time, whereas the seismic data amplitudes decay with time. Notch filters are used to attenuate this type of noise and were often applied in the recording of the data. The notch filter is applied here and it attenuates all recorded data at a given frequency.

The same Dinoseis seismic shot is presented filtered in Figure 5. According to Dingus (2011) properly addressing the noise and then its removal provides the opportunity to track amplitude anomalies and stratigraphic objectives with confidence.

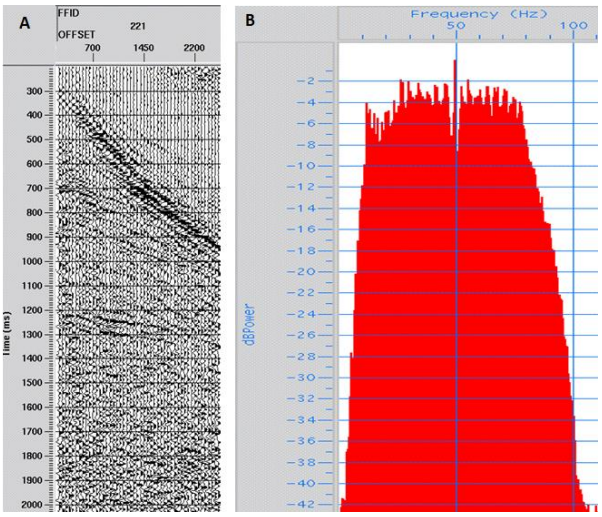

Fig. 5. Seismic shot (A) and its corresponding frequency spectre (B), received by Dinoseis seismic source after noise attenuation

Significantly better real reflection data in comparison with the same shot before filtration in the time range of 700-1400ms can be noticed after filtration procedures (Fig.6).

Another seismic shot but recorded using Vibroseis as a source signal is presented on Figure 6. Although it is received with generally modern technology row data still consist of relatively much ambient noise. Surface waves and ground rolls waves have strong energy and reflection data can hardly be observed in the upper time of the section.

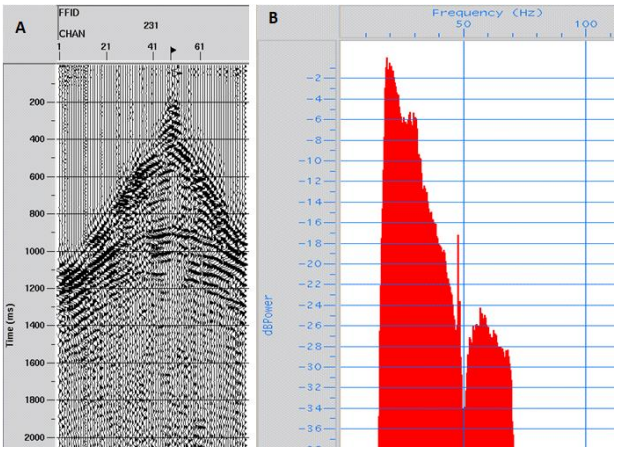

Fig. 6. Seismic shot (A) and its corresponding frequency spectre (B), received by Vibroseis seismic source before noise attenuation

In frequency domain notch filter is applied during the field works, but the spectrum is presented of predominantly low frequencies. According to Wardell (1970) frequency spectrum from surface sources, which influences the reflection quality, may not have sufficient high frequency energy where very high resolution is required.

After application of several filtration procedures and whitening of the spectrum, the frequency domain becomes broadband and respectively the shot data become more readable. Applying spectral whitening improves the resolution and appearance of seismic data and it is crucial to correct the frequency attenuation.

In Figure 7 it is obvious that better signal-to-noise ratio is achieved, which leads to more confident determination of real reflection data.

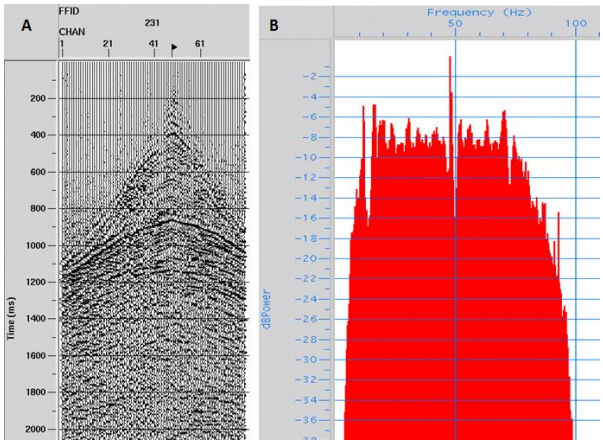

Fig. 7. Seismic shot (A) and its corresponding frequency spectre (B), received by Vibroseis seismic source after noise attenuation

Conclusions

In conclusion, both sources are capable of giving satisfactory seismic data in conditions suited to their use. The real goal for pre-processing of seismic data is to minimise all artefacts that are not part of the seismic signal, such as noise, multiple and acquisition irregularities. There are many areas which are now being re-evaluated. Many of these areas are being recorded using Dinoseis as seismic source, so they require special consideration in processing. In these areas, proper noise attenuation that maintains the amplitude and phase characteristics of the primary signal is a key issue. Proper seismic pre-processing gives the opportunity to extract the maximum benefit of seismic data. In such a way pre-processed data meets the exploration and development targets by providing quality information for pre-stack imaging techniques, and appropriate data for such reservoir characterisation techniques as rock properties, attribute analysis and inversion.

References

Alsadi, H. 2017. *Seismic Hydrocarbon Exploration: 2D and 3D Techniques*. Springer, 115 p.

Dingus, C. 2017. Seismic processing – noise attenuation techniques for relative amplitude processing. – *Petroleum Africa*, *11–12*, 47–49.

Drijkoningen, G. 2019. Interpretation of Raw Seismic Records. – https://ocw.tudelft.nl/course-readings/chapter-4-interpretation-raw-seismic-records/ (accessed 09.07.19). Grigorova, M. 2016. *Rakovodstvo za practicheski zanyatiya po seizmichni metodi v geofizikata*. Izdatelska kashta "Sv. Ivan Rilski", Sofia, 104 p. (in Bulgarian)

Grigorova, M. 2016. High resolution velocity analysis in seismic data processing – *Ann. Univ. Mining and Geol. "St. Ivan Rilski"*, *59*, Part I, 135–139 (in Bulgarian with English abstract).

Hubscher, Ch., K. Gohlb. 2014. *Reflection/Refraction Seismology* – In: *Encyclopedia of Marine Geosciences*. Springer, Dordrecht, 1–15.

Jeffryes, B. 2006. *Method of Seismic Surveying*, Patent No. US7050356B2.

Levi, A. 2015. Land seismic sources – vibrators vs explosives. – https://www.slideshare.net/Seiseng01/land-seismic-sources-explosives-vs-vibroseis

Wardell, J. 1970. A comparison of land seismic sources. – *Geoexploration*, *8*, 205–229.

FILTRATION TECHNIQUES FOR WATER BOTTOM MULTIPLES

Maya Grigorova

University of Mining and Geology "St. Ivan Rilski", 1700 Sofia; maya.grigorova86@gmaill.com

ABSTRACT. In seismic processing multiples are events commonly seen in marine surveys, but they are also present in land seismic works. Multiples can be assumed as energy that has been reflected more than once. It is common knowledge in seismic processing that the whole energy that has to be recorded has a single upward reflection beneath the surface. In fact, the acoustic energy could experience two or more upward reflections before being recorded. The presence of multiple reflections in the section can lead to incorrect forward processing of the data and hence interpretation of the subsurface geology structure. For this reason, when detected this kind of seismic energy has to be removed from the processed data. Attenuation is often made by set of procedures specifically aimed at multiples suppression. In the following work the mechanism of multiples detection and some popular techniques for multiples suppression are described.

Keywords: seismic method, seismic multiples, multiple suppression.

ПОПУЛЯРНИ ТЕХНИКИ ЗА ФИЛТРАЦИЯ НА КРАТНИ ВЪЛНИ

Мая Григорова

Минно-геоложки университет "Св. Иван Рилски", 1700 София

РЕЗЮМЕ. В сеизмичните проучвания, главно в моретата и океаните, едни от най-често срещаните негативни ефекти върху записите се дължат на наличието на кратни вълни в тях. В сеизмичните изследвания се счита, че цялата енергия, която се получава като сигнал има само едно отражение от под-повърхностен слой. На практика обаче акустичните вълни могат да се отразят няколко пъти под повърхността, променяйки посоката си на движение, което води до появата на така наречените кратни вълни. Кратните вълни се считат за шум и по тази причина трябва да бъдат премахнати от сеизмичните данни, за да се избегнат по-нататъшни грешки в обработката и интерпретацията на данните. Това се извършва чрез специални процедури, които са насочени специално към потискането и премахването на кратни отражения.

Ключови думи: сеизмични методи, кратни вълни, филтрация на кратни вълни.

Introduction

Multiple reflections in reflection seismograms are assumed as unwanted noise that often seriously harms correct imaging of the subsurface geology. To achieve accurate interpretation of subsurface seismic images, it is necessary this images to be of good quality and also to correspond to the energy from the primary reflections. Multiple reflections, energy that has been reflected at more than one interface, are particularly a problem for seismic interpretation since they can be easily mistaken as primary reflections. For this reason, multiple suppression techniques remain an integral part of almost every marine processing flow.

Described by Alvarez (2003) primary reflections in a common midpoint gather can be presented like a hyperbolic moveout as a function of offset. The equation of the hyperbolic move-out is:

$$t_x = \sqrt{t_0^2 + \frac{x^2}{V_s^2}} \quad (1)$$

where t_x corresponds to the arrival time of the reflection at offset x, t_0 corresponds to the arrival time at zero offset and V_s is the NMO-stacking velocity. Stacking velocity is the one that best fits the move-out of the hyperbola and if correctly chosen, this velocity allows the moveout corrected primary reflections to become horizontal. In this way stacking velocities correct for the moveout of the primary reflections and not for the multiples. So, the difference in moveout makes it possible to flatten the primary reflections while leaving the multiples under-corrected with a moveout approximately parabolic (Hampson, 1986).

According to Basak et al. (2012) conventional processing methods have limited approaches to achieve a separation of signal and noise in t-x domain. By transforming the data from the t-x domain to other domains such as the frequency-wavenumber (f-k) domain or the time-slowness (τ-p) domain, those noises can be separated more effectively from the meaningful signal to produce the best subsurface precise images minimising artefacts.

Commonly used multiple suppression techniques

Removing multiples and reverberations from reflection seismograms has been a longstanding problem of exploration geophysics. Multiple reflections often destructively interfere with the primary ones making interpretation almost impossible.

The methods generally used to suppress multiples can be placed in three basic categories (Xiao et al., 2003):

- Methods based on a difference in spatial behaviour of multiple and primary reflections;
- Methods based on periodicity and predictability of the multiples.
- Wave field predication and subtraction methods that use recorded data or models to predict multiples and then subtract them from the original data.

Methods in the first category exploit the fact that multiples have travelled along a different path in the subsurface, so primaries and multiples show different moveout behaviour (Grigorova, 2013). These filtering techniques can be applied in the pre-stack domain, e.g. by differentiation on the moveout (NMO) in the mid-point offset domain, or in the post-stack domain, by the difference in dips between primaries and multiples.

One of the most useful and effective way to suppress multiples is stacking normal move-out (NMO) corrected seismic gathers (Foster, Mosher, 1992). A weak point of moveout algorithms is that they are less effective in the situation of complex wavefields e.g., non-hyperbolic wavefronts. Moreover, these algorithms start to fail when the moveouts of primaries and multiples approach each other e.g., with reflections from deep targets. According to Berkhout and Verschuur (2006) successful moveout-based methods use the Radon transform.

The second group of methods include deconvolution. Deconvolution methods use periodicity to suppress multiples. The periodicity of the multiples is exploited to design a filter that removes the predictable part of the wavelet (multiples), leaving only its non-predictable part (signal). Deconvolution methods overall include predictive deconvolution, adaptive deconvolution and multichannel deconvolution. So, predictive deconvolution can be used to remove multiple energy from the seismic data by predicting and suppressing the multiple reflection series. A successful predictive deconvolution can remove the complete multiple energy from the seismic data. Generally speaking, periodic assumption is valid only at zero offset in the t-x domain and when the interfaces generating multiples are horizontal or have minor lateral variations. Even though, deconvolution methods still can be used when insignificant deformations of the interface or layer generating multiples are observed.

The third group of methods, wavefield prediction and subtraction, are based on the wave equation. These methods use recorded data to predict multiples by wave extrapolation and inversion procedures. The aim is to obtain multiple–free data by subtracting the predicted multiples, e.g. creating subsurface model. In this way all multiples generated by any system of reflectors can be suppressed theoretically, no matter how complicated it is. These methods assume that the medium between primaries and multiples is almost homogeneous. That group of methods are powerful because of their ability to suppress multiples that interfere with primaries without coincidentally attenuating the primaries. Wavefield prediction and subtraction methods have proved themselves as original and are among the most promising methods for multiple suppression, but they are limited by data acquisition and processing more than other methods (Verschuur et al., 1992).

In the following research real seismic data has been tested, using Radon filtration, deconvolution in τ-p domain and surface-relative wave equation multiple rejection methods (SRWEMR).

Radon transform for multiple attenuation

Radon filtering is able to separate the primary and multiple energy in τ-p domain because of their different moveout velocities. A velocity function is estimated and used to flatten the primaries on common midpoint gathers (Fig. 1). The moveout–corrected gathers are then transformed to the Radon domain. After the transformation the flattened hyperbolic primaries in time-offset domain (t-x) are presented as points in τ-p domain where the multiples are separated from the primaries. In practice this process differs from the theory. Because the transforms produce distortions, the multiples are estimated in Radon domain, transformed back to the t-x domain, and then subtracted from the original data, leaving only the primary data (Berndt, Moore, 1999).

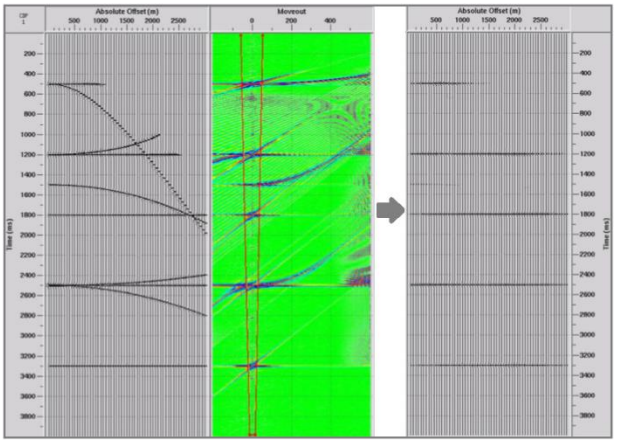

Fig. 1. Radon transform on synthetic data

The primaries are computed by subtracting the multiples from the original data in this domain. This method was first introduced with the name “inverse velocity stacking” (Hampson, 1986).

In Figure 2 Radon filter is effectively applied for attenuating the multiple reflections on real dataset.

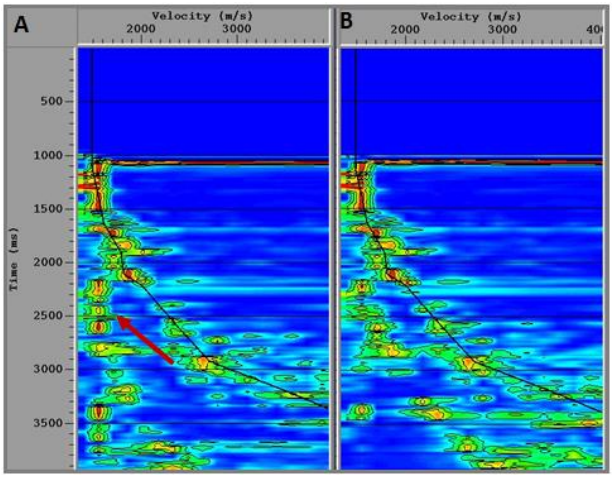

Fig. 2. Velocity analysis before (A) and after (B) applying Radon filter

On the figure is shown velocity gather before (A) and after (B) applying Radon filtration. It can be observed that velocity events in the range 2000–2500 ms are caused by first water

bottom multiple. After applying filtration, the first water bottom multiple is being effected and more confident velocity picking can be applied.

A comparison of stack data obtained before (A) and after (B) Radon filter is shown in Figure 3. The image obtained after the application of Radon filter is helpful in carrying out correct imaging of the data and for achieving more accurate geological interpretation.

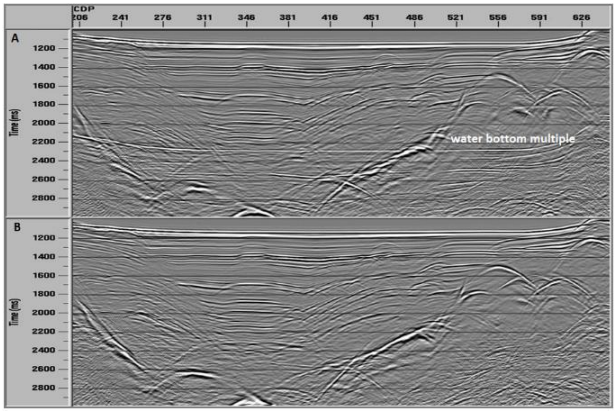

Fig. 3. Part of stack data before (A) and after (B) Radon filter

Radon filter provides a high degree of multiple attenuation, especially on long period multiples found in deep water. It works similarly well in all areas, but experiences difficulties when the moveout differential decreases under 30ms from near trace to far trace, such as with peg-leg multiples.

Deconvolution techniques in the tau-p domain

Deconvolution in the τ-p domain can be classified as multiple attenuation techniques that rely on the periodicity of the multiple wavefield. Multiples are periodic in the τ-p domain, and predictive deconvolution applied in the τ-p domain can be successfully used to suppress them. According to Brooymans et al. (2013) perfect periodicity in the time-space domain occurs only for plane wave propagation, so the best alternative is to compute the τ-p transform of common shot point or common midpoint gathers, which simulates plane waves. By transforming data into the τ-p domain, multiples can be forced to behave like periodic events for all values of p and effectively attenuated with predictive deconvolution. This technique is particularly effective in shallow water areas where muting in the τ-p domain can be accompanied with linear noise attenuation.

This τ-p processing can be applied to remove unwanted noise from meaningful reflection signals and for more truthfully determining the stacking velocity function. In Figure 4 velocity semblance after applying τ-p deconvolution allows more adequate and reliable conclusions about stacking velocity to be made. It is clearly obvious how first water bottom multiple is affected of applying the procedure.

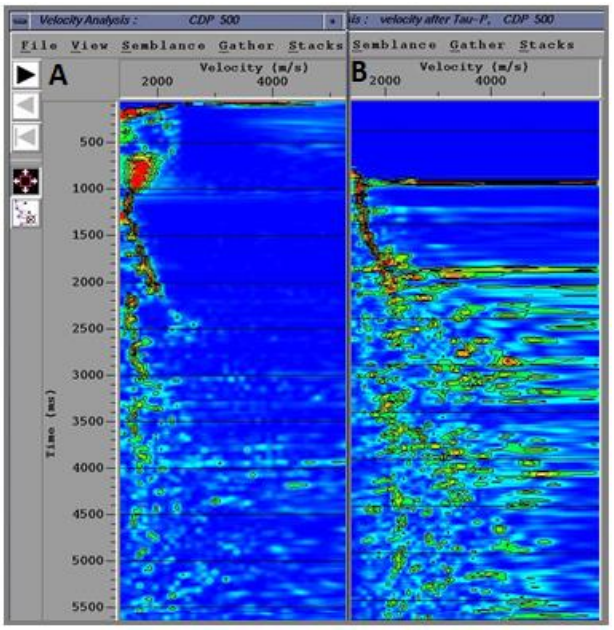

Fig. 4. Velocity analysis before (A) and after (B) applying τ-p deconvolution

According to Xiao et al. (2003) in shallow water, where the water bottom is very flat and peg–leg multiples are the main problem, τ-p deconvolution can be very effective. On the other hand, deconvolution methods are less effective in deep water where the period of the multiples is longer, relative to the length of the record. One possible reason can be the lack of enough multiples in the record length to satisfy the periodic requirements. Another problem is that long–period multiples require long operators. Since primaries can be periodic over long time windows, long operators have the potential to suppress primaries as well as multiples.

In principle, periodic assumption is valid only at zero offset in the time–space domain, so pre-stack deconvolution has limited use as a multiple suppression technique.

In Figure 5 is demonstrated stack data with clearly defined water bottom multiple. This seismic section confirms the rule for effectiveness of τ-p deconvolution in shallow waters.

Very often multiple attenuation techniques modify the whole dataset and produced artefacts on the section. As Stewart et al. (2007) mentioned as a drawback of τ-p deconvolution, is that the entire ensemble passes through the transform. As a consequence, transform artefacts may be embedded in the data. Many multiple attenuation techniques model the multiple reflections and subtract them from the original data. This helps minimise process-induced artefact. It becomes clear that there is no single multiple attenuation technique suitable for all datasets.

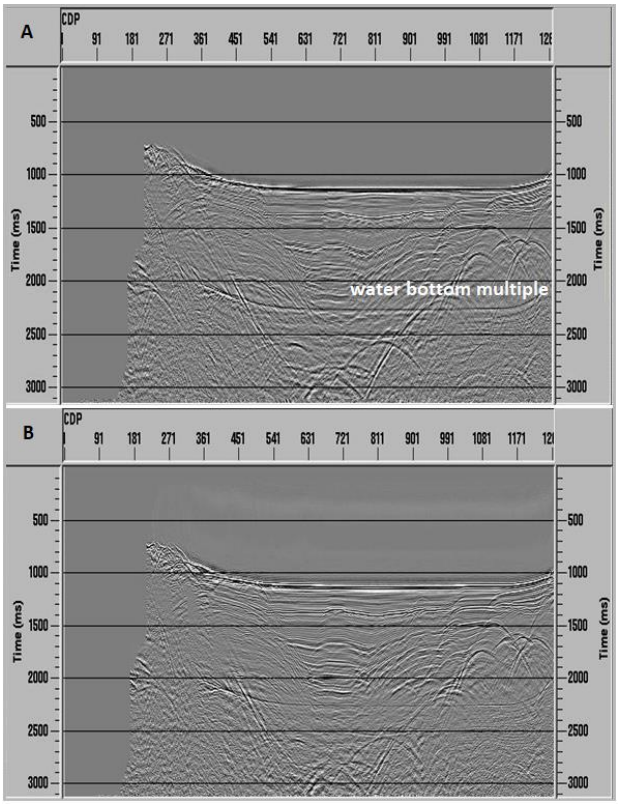

Fig. 5. Part of stack data before (A) and after (B) applying τ-p deconvolution

Wavefield prediction and subtraction technique - surface-relative wave equation multiple rejection (SRWEMR)

Wavefield prediction and subtraction methods are among the most promising methods of multiple suppression. These methods use wave equation and recorded data to predict multiples in the section. As Xiao et al. (2003) pointed out wave extrapolation and inversion procedures are designed to subtract the predicted multiples from the original data and to produce multiple – free data. The biggest advantage of these methods over other multiple attenuation methods is their ability to suppress all multiples, especially the multiples that have stacking velocities close to the primary reflections without attenuating the primaries.

Prediction and subtraction techniques for multiple attenuation have also another advantage over the other multiple subtraction methods – these methods are suitable for prestack analysis and particularly for amplitude– versus–offset analysis, because they do not transform the input signal.

In Figure 6 is presented the result of application of surface-relative wave equation multiple rejection method (SRWEMR) before (A) and after (B) filtration. The technique proved itself as the most promising amongst the tested methods in this research. Multiple reflections generated by the water bottom are predicted by a combination of wave extrapolation through the water layer and estimation of the water bottom reflectivity, then the predicted wave field is subtracted from the original data.

This method can be used successfully to attenuate the long period multiple reflection, because the attenuation is based on wave equation inversion. As stated by Wiggins (1988) multiple reflections that are generated by the water bottom in marine seismic data can be predicted by a combination of numerical wave extrapolation through the water layer and estimation of the water bottom reflectivity. Therefore, inversion of wave equation and seismic wave amplitude observed are used to get the water bottom reflectivity which is then used to design the prediction filter to eliminate the multiple reflections.

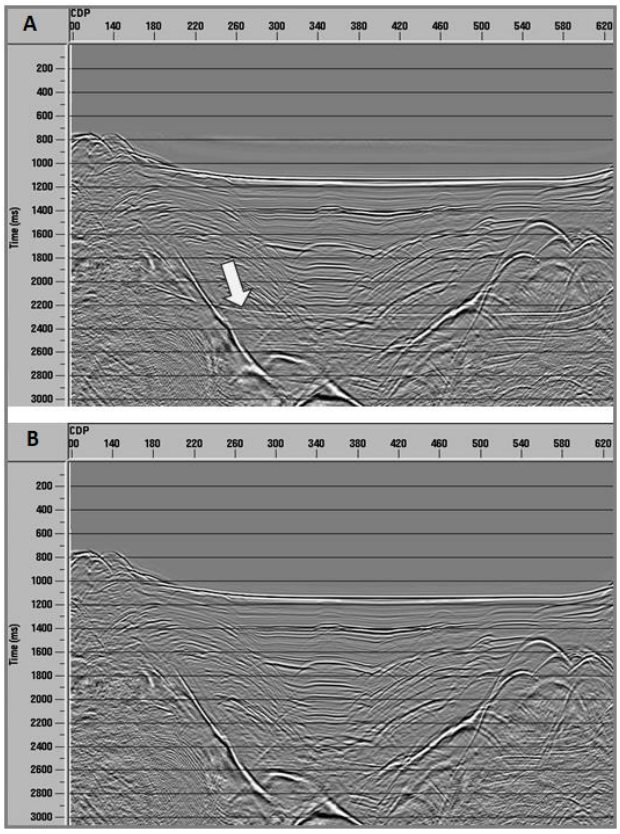

Fig. 6. Part of stack data before (A) and after (B) surface-relative wave equation multiple rejection

According to Erlangga (2015) the SRWEMR method does not depend on the moveout difference to attenuate the long period multiple reflection. So, the SRWEMR method can be applied to the seismic data which has even small moveout difference.

Conclusion

Over the years, many multiple attenuation techniques have been tested. Most of them proved to be effective in certain physical-geological conditions. It is essential a proper multiple suppression approach to be chosen depending on the type of multiples, data acquisition and processing flow.

Multiple attenuation not only makes interpretation easier by highlighting the primaries, but also improves the resolution of the primaries by allowing a better selection of the primary stacking velocities. A careful examination of stacking velocity leads to more confident and adequate seismic section, which is the main goal in the process of seismic investigations. These are just few key issues multiple suppression methods to be recognized as an integral part of almost every marine processing flow.

References

Alvarez, G. 2003. Multiple suppression with land data: A case study. – *Stanford Exploration Project, Report 108*, 1–14.

Angelov, V. 2009. *Methods for enhancing signal-to-noise ratio on 2D seismic data*. Master Thesis, Sofia, 130 p. (in Bulgarian)

Basak, R. L., K. S. Rana, A. K. Rao, A. Gangaiah, C. R. Chandrasekaran. 2012. Removal of noises using Tau-P transformation - an indigenous tool for noise attenuation in shallow seismic data. – *9th Biennial International Conference & Explosition on Petrolelum Geophysics, P-273*, 1–6.

Berkhout, A. J., D. J. Verschuur. 2006. Imaging of multiple reflections. – *Geophysics*, *71*, 4, 209–220.

Berndt, C., G. F. Moore. 1999. Dependence of multiple–attenuation techniques on the geologic setting: A case study from offshore Taiwan. – *The Leading Edge*, *18*, 74–80.

Brooymans, R., T. Mojesky, L. Pham. 2013. A Review of Current Marine Demultiple Techniques with Examples from the East Coast of Canada. – *CSEG Conference*, 465S0204, 1–7.

Erlangga, M. P. 2015. Multiple attenuation to reflection seismic data using Radon filter and Wave Equation Multiple Rejection (WEMR) method. – *AIP Conference Proceedings 1656*, 1, 070005.

Foster, D. J. C. C. Mosher. 1992. Suppression of multiple reflections using the Radon transform. – *Geophysics*, *57*, 9, 386–395.

Grigorova, M. 2013. Characteristics of multiples in reflection seismic and main approaches for their suppression. – *Proceedings of XV Balkan Mineral Processing Congress*, *2*, 1251–1254.

Hampson, D. 1986. Inverse velocity stacking for multiple elimination. – *J. Canadian Soc. Exploration Geophysicists*, *22*, 44–55.

Stewart, P., I. Jones, P. Hardy. 2007. Solutions for Deep Water Imaging. – *SPG GeoHorizons*, 8–22.

Verschuur, D. J., A. J. Berkhout, C. P. A. Wapennar. 1992. Adaptive Surface related multiple eleimination. – *Geophysics*, *57*, 9, 1166–1177.

Wiggins, J. W. 1988. Attenuation of complex water-bottom multiples by wave-equation-based prediction and subtraction. – *Geophysics*, *53*, 12, 1527–1539. 1442434.

Xiao, C., J. R. Bancroft, R. James Brown, Z. Cao. 2003. Multiple suppression: A literature review. – *CREWES Research Report*, *15*, 1–17.

IMPLEMENTATION OF AN ENERGY SEPARATION DEVICE BASED ON THE HARTMANN-SPRENGER EFFECT IN A PRESSURE REDUCTION UNIT OF A GAS DISTRIBUTION STATION

Alyona S. Dmitrieva, Artyom E. Belousov, Andrey M. Shipachev

Saint Petersburg Mining University, 199106 Saint Petersburg; alena_dmitrieva57@rambler.ru

ABSTRACT. Energy efficient management of main pipeline transportation and distribution of natural gas is one of the priorities of sustainable development and cost optimisation in the gas industry. The study is devoted to solving the problems of energy and resource saving by introducing an energy-separation device based on the Hartmann-Sprenger resonance effect into the gas distribution station (GDS) pressure reduction unit. When the gas pressure is reduced at the GDS, due to the Joule-Thomson effect and the work done by the gas, a significant drop in its temperature occurs. To prevent a drop in temperature and the possible formation of hydrates, special measures are applied. All of them require significant investments and resource costs (gas for combustion, electricity, and methanol). Introduction of energy-separating devices to the reduction unit is a rational solution that will allow to carry out the general or partial gas heating by utilising the energy of its pressure. There are many types of energy-separating devices based on different effects. Among them are: Ranque-Hilsch vortex tubes, ejection with a negative ejection coefficient, an energy separation device with a phase transition, pulsation tubes, energy separation in gas flows in the flow around various obstacles and in a free flowing stream of gas. Using the analysis of existing methods of energy separation and numerical simulation, justification of the effectiveness of the energy separation device of the resonant type is given. Hartmann-Sprenger effect is based on the principle of aerodynamic resonance and thermal energy separation in the case of non-linear gas oscillations in a pipe plugged from one end. An energy-separation device has been developed with a non-fire gas preheating to provide a predetermined temperature at the outlet of the gas distribution station and a warning of possible hydrate formation at the station pipelines. The proposed technology will make it possible to partially or completely exclude the generation of thermal energy at the gas distribution station by gas combustion.

Keywords: Natural gas, gas pipeline, energy saving, energy separation, Hartmann-Sprenger effect, pressure reduction, gas distribution station

ВЪВЕЖДАНЕ НА УСТРОЙСТВО ЗА ОТДЕЛЯНЕ НА ЕНЕРГИЯТА, ОСНОВАНО НА ЕФЕКТА НА HARTMAN-SPRENGER, В РЕДУКТОРА НА ГАЗОРАЗПРЕДЕЛИТЕЛНА СТАНЦИЯ

Алена С. Дмитриева, Артьом Е. Белоусов, Андрей М. Шипачев

Санктпетербургски минен университет, 199106 Санкт Петербург

РЕЗЮМЕ. Енергийно ефективното управление на магистрални тръбопроводи и разпределението на природен газ е един от приоритетите за устойчиво развитие и оптимизиране на разходите в газовата промишленост. Докладът е посветен на решаване на проблемите за спестяване на енергия и ресурси чрез въвеждане на устройство за отделяне на енергията, основано на резонансния ефект на Hartmann-Sprenger, в редуктора на газоразпределителната станция. Когато налягането на газа се понижи в газоразпределителната станция поради ефекта на Джоул-Томсън и работата, извършена от газа, настъпва значителен спад в температурата му. Използват се специални мерки за предотвратяване на спада на температурата. Всички те изискват значителни инвестиции и разход на ресурси (газ за горене, електричество, метанол). Инсталирането на устройства за отделяне на енергията в редуктора е рационално решение, което ще позволи общо или частично загряване на газа чрез използване на енергията от налягането му. Съществуват много видове устройства за отделяне на енергия, основани на различни ефекти. Сред тях са: вихрови тръби Ranque-Hilsch, изхвърляне с отрицателен коефициент на изтласкване, устройство за отделяне на енергията с фазов преход, пулсационни тръби, енергийно разделяне на газовите потоци при преминаване покрай различни препятствия и в свободно течащ газов поток. На базата на анализа на съществуващите методи за отделяне на енергията и числената симулация е дадена обосновка за ефективността на работата на устройство от резонансен тип за отделяне на енергията. Принципът на отделяне на аеродинамичния резонанс и топлинната енергия при нелинейни колебания на газ в тръба, включена в единия край, е в основата на ефекта на Hartmann-Sprenger. Разработен е термоакустичен газов подгревател за поддържане на зададената температура на изхода на газоразпределителната станция и предотвратяване на възможно образуване на хидрат в тръбопроводите на станцията. Предложената технология ще позволи частично или напълно да се изключи генерирането на топлинна енергия от газоразпределителната станция чрез изгаряне на газ.

Ключови думи: природен газ, газопровод, енергоспестяване, отделяне на енергия, ефект на Hartmann-Sprenger, редукция, газоразпределителна станция

Introduction

Energy efficient management of main pipeline transportation and distribution of natural gas is one of the priorities of sustainable development and cost optimisation in the gas industry. At present, Gazprom's gas transmission companies pay serious attention to the problems of rational use of natural gas for their own technological needs, observing the conditions for ensuring industrial safety and optimal control of the gas transmission system, and improving the energy efficiency of production processes (*Gazprom PJSC*, 2011; 2016).

One of the most important problems in the operation of gas pipelines is the formation of gas hydrates. In the process of reducing the gas pressure on the GDS, due to the Joule-Thompson effect, a significant drop in the gas temperature occurs. This leads to the formation of condensate in the form of gas hydrates, a solid snow-like mass that can accumulate inside the gas pipelines, reducing their flow cross-section, and affect the efficiency of the valves (Kitaev, 2011). Most often, the blockage of the pipeline can occur in the winter period due

to the significant cooling of the gas flow moving in the pipeline. As a result, an emergency stop of the pipeline operation may occur. The costs of oil and gas companies to prevent and eliminate gas hydrate plugs constitute a significant part of the cost of transport and distribution of gas.

The paper presents the topical problem of resource and energy saving in the system of transport and distribution of natural gas and a method is proposed for its solution based on the introduction of an energy separation device (ESD) at the reduction unit of gas distribution station.

The traditional methods for reducing hydrate formation in the GDS include: general or partial heating of the gas, local heating of the regulator housing, and the introduction of methanol into the gas pipeline. All of them require either significant investment or resource costs: gas for combustion, electricity for local heating, methanol.

In order to minimise the transportation costs of gas, the urgent task is to develop new ways to carry out gas heating during the reduction, taking into account energy saving requirements.

One of the solutions is the introduction of alternative sources that use the energy of wind, water, sun, etc. However, the effectiveness of these methods strongly depends on the climatic conditions.

To prevent frosting of gas equipment and gas preheating, the introduction of a machine-free power separation unit is proposed. The term “energy separation” or “machine-free energy separation” means the redistribution of total enthalpy (stagnation temperature) in a gas stream without external work and without heat exchange with the environment.

The reasons for the energy flow separation may be different. In some cases, these are vortex flows, in others – pressure pulsations and shock waves. These effects form the basis of devices for the energy separation of gases.

Analysis of existing methods of energy separation

Energy separation is the process of the emergence of “hot” and “cold” regions in a gas flow without the supply/removal of energy from outside. The implementation of this process is possible in special devices without a machine power separation. Due to its geometry, these devices allow the redistribution of thermal energy of the gas flow, utilising its pressure (Gurin, 2008).

There are many types of energy-separating devices (ESD) based on different effects. Among them are: Ranque-Hilsch vortex tubes, ejection with a negative ejection coefficient, an energy separation device with a phase transition, pulsation tubes, energy separation in gas flows in the flow around various obstacles and in a free flowing stream of gas.

ESD are multifunctional: with different designs it is possible to obtain both ultra-low and ultra-high temperatures. A distinctive feature of these devices is their simplicity, the absence of moving parts, low inertia, low weight and reliability of structures (Parfenov, 2018).

With regard to the working conditions of the GDS, the following methods of energy separation can be distinguished: temperature stratification in supersonic flow; the vortex effect of the Ranque-Hilsch; Hartmann-Sprenger effect (H-S).

Based on the first method, the author (Popovich, 2016) developed an energy separation device in the main pipeline for organising a supersonic flow in an internal or external channel (Fig. 1). Its principle of operation is the following: high-pressure gas is divided into two parts, one of the streams accelerates in a Laval nozzle to supersonic speeds, and the other – subsonic high-pressure flow – is directed through the inner pipe. For a supersonic flow, the stagnation temperature diagram is redistributed. For a subsonic flow, the wall temperature is almost equal to the stagnation temperature. As a result of interaction through the heat-conducting wall in the energy-separation device, the supersonic flow is heated, and the subsonic is cooled using a gas with a Prandtl number less than one. If the Prandtl number of the working substance is greater than unity, the effect is reversed — the supersonic flow is cooled and the subsonic flow is heated up.

Fig. 1. The energy-separation device in the pipeline during the organisation of a supersonic flow in the internal channel

The disadvantages of this technology are: the need to maintain a supersonic gas flow rate; cooled subsonic flow is sent back to the gas pipeline.

The main principle of the vortex effect is the separation of gas when twisting in a cylindrical or conical chamber into two fractions. At the periphery of the chamber, a swirling flow is formed with a higher temperature, and in the centre – a swirling cooled flow, and rotation in the centre occurs in a different direction than at the periphery.

On the basis of the vortex effect, a device is known, the gas pressure regulator RDU-T with a heat generator, produced by PJSC “Plant Staroruspribor”. Energy separation occurs due to the presence of the Ranque-Hilsch vortex tube (VT). The cold component is removed and discharged into the rear flange of the regulator, which helps to heat the heat generator to a temperature of +40–50°C for 6–8 minutes. The heating temperature of the heat generator is sufficient to prevent frosting of the valve.

It was experimentally established that the preheating of the inlet gas due to the hot wall of the VT allows the gas temperature to rise before entering the vortex tube by 3–5°C (Gurin, 2008.). The tests of the developed device showed that in the design mode with absolute inlet pressure P=0.4 MPa and pressure decrease of natural gas to absolute pressure of 1.003 MPa, the heated air at the outlet of the HT (when mixing cold and hot streams) at the maximum flow rate is 5.5°C, with a minimum flow rate of 2.7°C (about 10% of the maximum value). The tests of the developed device showed that in the design mode with absolute inlet pressure P=0.4 MPa and pressure decrease of natural gas to absolute pressure of 1.003 MPa, the temperature of heating the air at the outlet of the HT (when mixing cold and hot streams) at maximum flow rate is

5.5°C. The amount of heating of natural gas in the design mode is equal to 2.0°C and 1.0°C for maximum and minimum flow. Despite such an advantage as the possibility of carrying out several processes at the same time (cooling, heating, phase separation), this device has low energy efficiency.

The principle of aerodynamic resonance and thermal energy separation in nonlinear oscillations of a gas in a dead-end pipe is the basis of the Hartmann-Sprenger energy separation effect (Fig. 2).

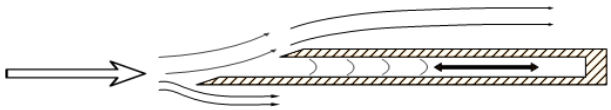

Fig. 2. The flow of gas inside the dead-end cavity

The Hartmann-Sprenger (H-S) effect is the following: breaks in the jet of high-speed gas flow at the entrance to the dead-end cavity cause pressure pulsations, the waves of which propagate in the direction of a dead end, reflect and move in the opposite direction, entering with subsequent waves in resonance with a sharp temperature rise. Inside the dead-end tube it is possible to create temperatures up to several hundred degrees. At the same time, the gas flow loses energy and comes cooled to the exit of the installation.

The H-S effect was not previously considered as a way to preheat the gas at the GDS. The following applications are known: in aircraft industry, as a heating element of the anti-icing system in the air intake of the aircraft; gasdynamic igniter for sparkless burning of combustible gases; a device for pulsating impact on the bottom hole formation zone; rotary wave cryogenerator for low-tonnage production of liquefied natural gas.

The following advantages of the effect H-S can be identified: a simple theoretical description of the physical meaning of the effect; shared hot and cold streams do not come in direct contact and are separated by a wall; ease of obtaining high temperatures: in certain situations, the actual overheating temperature can reach values of ~ 500–1500 K.

In the gas transportation system, the H-S effect was considered only as negative. In (Parfenov, 2018), cases of heating of individual elements of the block valve station during the filling of the sections of the gas pipeline with melting of outer insulation, emitting acrid smoke and loss of tightness of the shut-off and control valves were considered.

Thus, the analysis of the devices proves the limited effectiveness and application of the effect of temperature stratification in supersonic flow and the vortex effect of Ranka-Hilsch for heating the gas in the GDS.

Justification of the efficiency of energy separation on the Hartmann-Sprenger effect by numerical simulation in ANSYS FLUENT

The simulation of the effect of resonant energy separation is a complex mathematical problem that requires large computing resources and time. In this paper, a simplified 2D model is proposed to provide a qualitative representation of energy separation processes in a dead-end cavity.

The description of the gas movement under arbitrary conditions is made using the Navier-Stokes equations. For the solution, numerical methods implemented in various software products are used. In this paper, the ANSYS FLUENT package is used to solve this problem. It is applicable for solving various problems of gas dynamics.

The turbulent flow is characterised by the presence of vortex structures. Special models of turbulence are used to solve practical problems in order to reduce the calculation time. RANS models (Reynolds Averaged Navier–Stokes) are most prevalent today. In these models, the following approach is used: for all desired parameters (velocity, pressure, temperature, etc.), the value is represented as two terms — the averaged and the pulsation value (Savchenkov, 2013; Voronin, 2014).

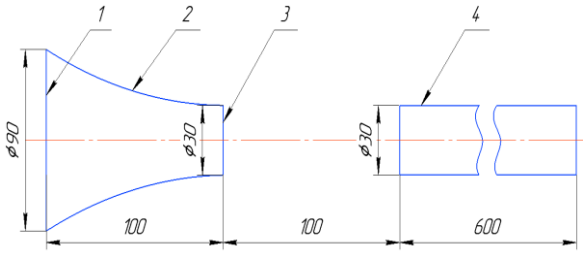

Fig. 3. The scheme of the resonant tube: *1*, gas inlet; *2*, nozzle; *3*, exit from the high-speed flow nozzle; *4*, resonant tube

Modelling is carried out in the software package ANSYS FLUENT. Air is accepted as a gas mixture and is described by the Redlich-Kwong real gas law. At the entrance to the nozzle, the speed is set at 15 m/s and the temperature is 300 K. The outlet pressure is set to 0 Pa. To determine the initial conditions, the problem is solved in a stationary formulation. For this purpose, the Menter turbulence model is chosen — shear stress transfer SST. The calculation is based on the DES-model of turbulence with a time step of 1·10-5 s. The pulsation effects are stabilised in 0.2 s. Visualisation of the simulation results is presented in Figure 4.

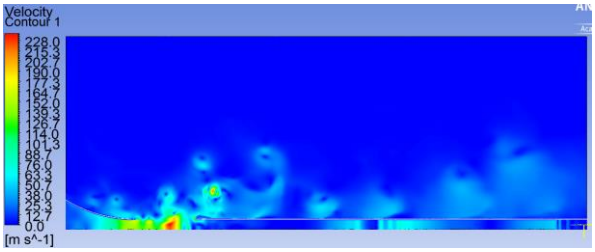

Fig. 4. Speed contours in the case of a steady-state oscillatory process

In the case of oscillation due to flow interruptions at the entrance to the dead-end cavity without using artificial pulsators (for example, pistons), the frequency of pressure oscillations will depend only on the cavity length (l_T) and the speed of sound in the medium (c) and will be $f = c/2l_T$. The frequency in the process of resonance is half as much, because the wave changes sign when reflected from the open end, and the rarefaction wave passes through the pipe instead of the reflected shock wave. Therefore, the theoretical frequency of oscillations in resonance is equal to:

$$f = c/4l_T .$$

The resonant frequency of pressure oscillations is within the range f_{calc}≈150÷160 Hz. According to the formula (1), the theoretical frequency of pulsations in resonance is (the speed of sound in the air is 340 m/s):

$$f_{theor} = \frac{340}{4 \cdot 0,6} = 142\ Hz$$

The deviation of the received frequency from the theoretical frequency is 5.9–12.9%, which is within the normal range. The range of amplitudes of pressure pulsations at the bottom of the cavity is 30–70 kPa.

As a result of the simulation, we obtain the graphs of the pressure and temperature pulsations in the dead-end cavity (Figs 5, 6). In the first approximation, we assume that the temperature growth rate at the bottom of the dead-end cavity is described by a linear function (Fig. 7).

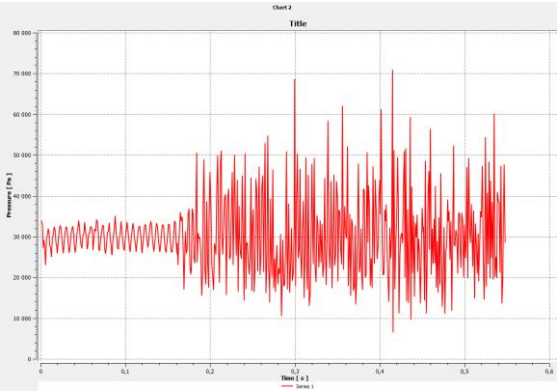

Fig. 5. Pulsations of pressure in the dead-end cavity for the time interval t= 0÷0.55 s

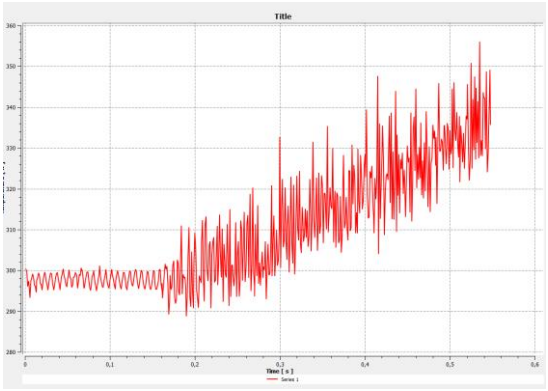

Fig. 6. Pulsations of temperature in the dead-end cavity for the time interval t= 0÷0.55 s

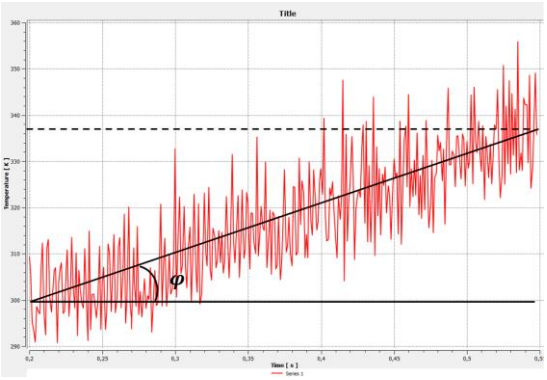

Fig. 7. The scheme for calculating the temperature growth rate at the bottom of the dead-end cavity

The temperature growth rate at the bottom of the dead-end cavity is:

$$\tan(\varphi) = \frac{337\text{-}300}{0,55\text{-}0,2} = 105,7\ \text{K/s}.$$

The temperature growth rate at the bottom of the dead-end cavity is 105.7 K/s. The calculation is made without taking into account the thermophysical properties of the wall material (without heat loss through the wall), therefore, the value of the final heating temperature is not considered.

Conclusion

A search study of existing devices without a machine power separation has been made. A wide range of their varieties is presented. The description of physical processes in ESD is given.

A numerical model has been developed that describes the processes of energy separation in a resonant tube.

Further research is aimed at applying the developed numerical model for more complex structures taking into account spatial phenomena (3D model) and physical properties of the resonator walls, comparing the results of numerical calculations with laboratory tests.

References

Gazprom PJSC. 2011. *Gazprom concept of power saving and improvement of energy effi ciency in 2011–2020*. Moscow, 122 p. (in Russian)

Gazprom PJSC. 2016. *Program on installation of turbine expanders at gas-distributing stations for production of liquefied natural gas and generation of electric power. Adopted by the directive No. 03-42 on March 22*. Moscow, 72 p. (in Russian)

Gurin, S. V. 2008. *Development of technology for quasi-isothermal pressure reduction for objects of the system of transportation and distribution of natural gas*. PhD thesis, Ufa, 111 p. (in Russian)

Kataev, K. A. 2011. Hydrate formation in natural gas pipelines. – *All-Russian J. Sci. Publications*, *1*, 2, 22-23 (in Russian).

Parfenov, D. V. 2018. *Prevention of heating elements of crane units when filling gas sections of gas pipelines*. PhD thesis, Ukhta, 37–46 (in Russian).

Popovich, S. S. 2016. *Effect of shock waves on the effect of machine-free energy separation*. PhD thesis, Moscow, 172 p. (in Russian)

Savchenkov, S. V., R. V. Aghiney, D. G. Repin, D. V. Parfenov. 2013. Numerical modeling in ANSYS CFX of the heating phenomenon of dead-end branches of crane nodes. – *Gas Industry*, *10*, 13–16 (in Russian).

Voronin, A. A., G. N. Lukyanov, E. V. Frolov. 2014. Detached eddy simulation of turbulent air flow. – *Scientific and Technical Journal of Information Technologies, Mechanics and Optics*, 1 (89), 187–192 (in Russian).

METHODICAL APPROACH FOR DETERMINING PETROPHYSICAL PARAMETERS USING THE VINCI 3.28 HELIUM POROSIMETER

Nikolay Hristov, Efrosima Zaneva-Dobranova

University of Mining and Geology "St. Ivan Rilski", 1700 Sofia; nk.hristov@gmail.com; edobranova@abv.bg

ABSTRACT. The present study aims to review current methodological approaches for the laboratory determination of reservoir parameters of reservoir rocks using the helium porosimeter (HeP-E) of the French company Vinci Technologies. The variations in the technological solutions of the measurement methods are considered, as well as the qualitative and quantitative representation of the results. A methodology is offered for determining petrophysical parameters (porosity and permeability) using the Vinci 3.28 helium porosimeter which the Laboratory in the Physics of the Stratum at the University of Mining and Geology "St. Ivan Rilski" is equipped with. In the final part of the study, the advantages of the helium porosimeter are substantiated both in terms of the expediency and versatility of the research process and with respect to the presentation and reliability of the results obtained.

Keywords: porosity, permeability, laboratory assessment

МЕТОДИЧЕН ПОДХОД ЗА ОПРЕДЕЛЯНЕ НА ПЕТРОФИЗИЧНИ ПАРАМЕТРИ С ПОМОЩТА НА ХЕЛИЕВ ПОРОЗИМЕТЪР ТИП VINCI 3.28

Николай Христов, Ефросима Занева-Добранова

Минно-геоложки университет "Св. Иван Рилски", 1700 София

РЕЗЮМЕ. Настоящата разработка има за цел преглед на съвременните методични подходи за лабораторното определяне на резервоарните параметри на скали-колектори чрез използване на хелиев порозиметър (HeP-E) на френската фирма Vinci Technologies. Разгледани са вариациите в технологичните решения на методите на измерване, както и качественото и количественото представяне на резултатите. Предложена е методика за определяне на петрофизични параметри (порестост и проницаемост) чрез използване на хелиев порозиметър тип Vinci 3.28, с който е оборудвана лабораторията по Физика на пласта към МГУ „Св. Иван Рилски". В заключителната част на разработката са обосновани предимствата на хелиевия порозиметър както по отношение експедитивността и универсалността на изследователския процес, така и по отношение на начина на представяне и достоверността на получените резултати.

Ключови думи: порестост, проницаемост, лабораторна оценка

Introduction

A number of important issues in the geology of oil and gas, in the prospecting, exploration, and development of hydrocarbon fields, in the assessment of the resources/deposits of hydrocarbons in various categories, as well as in determining the output technological indicators for their development, are related to the study of the petrophysical properties of reservoir rocks. The purpose of this study is to review the current methodological approaches for the laboratory determination of reservoir parameters of reservoir rocks using a helium porosimeter (HeP-E) of the French company Vinci Technologies, type Vinci 3.28 (Fig. 1), with which the Laboratory of the Physics of the Stratum at the University of Mining and Geology "St. Ivan Rilski" is equipped. The equipment was partially funded by a project from the Research Fund.

As a leading laboratory at the University of Mining and Geology "St. Ivan Rilski", it provides fluid and rock analysis services for the purposes of petroleum engineering. The methodological basis for the training of students in various courses of study has also been developed. Researchers ensure the functioning of the laboratory and strive for modernising the laboratory equipment and introducing contemporary analytical systems to determine important quantitative parameters of reservoir and fluid systems (Zaneva-Dobranova, 2017; Zaneva-Dobranova et. al., 2017; 2019).

Theoretical framework and equipment

Theoretical framework

The most important physical properties that characterise the ability of rocks to contain fluids and to release them under certain conditions are their capacity and permeability. Various groups of methods exist: geophysical, hydrodynamic, petrographic, etc. Laboratory methods are also important. In carrying out the experiment, the following ones were essential for obtaining the correct results: the technological solutions to the measurement methods; the qualitative and quantitative presentation of the results; the preliminary preparation of the sample studied; the genesis of the capacity and filter spaces; the laboratory equipment; the role of deformation effects; the skill of the laboratory assistant, etc.

Fig. 1. General view of the Vinci 3.28 helium porosimeter

The classical laboratory methods applied in practice were developed in the middle of the 20th century and are associated with the works of Kobranova and Leparskaya (1957), Kalinko (1963), Hanin (1969), Balinov and Troshanov (1968), Goroyan (1971), Balinov et al. (1972), Archer and Wall (1986), Dake (1994), etc. Recently, due to the need to apply specific methods and approaches, research activities have been focused on the study of rocks with unconventional reservoir properties (Zaneva-Dobranova, Georgiev, 2016). Along with that, traditional laboratory methods have been refined and laboratory equipment is being upgraded. A number of leading laboratories throughout the world are examples in this respect: the American Core Laboratories, Inc., the Russian GC Agrosi Ltd., CORETEST SERVICE Ltd. in Tyumen, etc., acting as service providers for the analysis of rock and fluid material for the needs of the petroleum industry.

The helium porosimeter allows to determine the size of the grains and pores in the test specimen due to the isothermal expansion of helium, and then the density and effective capacity are determined. The results of the tests, using a helium porosimeter, are characterised by correctness of measurement, high accuracy (precision), and negligible random error of the results obtained in repeating conditions (Ahmed, Mehan, 2016; Twardowski et al., 2004).

In its essence, the methodology of this type of porosimeter does not differ significantly from the classical ones that study the reservoir properties of rocks. It is based on fundamental achievements and the laws of the physics of the oil stratum, the hydro- and thermodynamics, etc. At the heart of the principle of operation of the Vinci 3.28 helium porosimeter is the Boyle-Mariotte law. It can be used to calculate the volume of the grains and pores based on two consecutive pressure measurements and on the helium mass data. The analytical expression includes the initial and the measured (final) pressure, volume and temperature.

$$\frac{P_{ref} * V_{ref}}{T_{ref}} = \frac{P_{exp} * V_{exp}}{T_{exp}}$$

where:
P_{ref} is the reference (initial) pressure;
V_{ref} is the reference (initial) volume;
T_{ref} is the reference (initial) temperature;
P_{exp} is the measured (final) pressure;
V_{exp} is the measured (final) volume;
T_{exp} is the measured (final) temperature.

During the series of tests, it is assumed that the temperature is kept constant, therefore:

$$T_{exp} = T_{ref}$$
$$P_{ref} * V_{ref} = P_{exp} * V_{exp}$$

The Vinci 3.28 helium porosimeter equipment and the test sequence

What is different in the design, in comparison with the mercury porosimeter, is the ability to comprehensively study various characteristics, to automate the process, and to shorten the duration of the experimental work. The helium porosimeter used is significantly safer and the results obtained are commensurate with those of the mercury porosimeter. The storage conditions of the reagent used (helium) do not require special equipment of the laboratory and thus the risk of performing measurements is reduced.

The porosimeter has the following structure which is schematically shown in Figure 2.

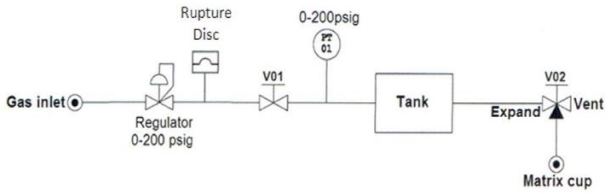

Fig. 2. Structure of the Vinci 3.28 helium porosimeter

Description (*from left to right*):

- Gas inlet – saturating agent – helium gas (a bottle with a pressure regulator and a shut-off mechanism);
- Discharge line;
- Regulator – primary pressure regulator (200 bar);
- Rupture disk – gas temperature control and regulation system;
- V01 – functional valve;
- PT01 – main electronic block with a computer output and a digital pressure gauge on the front panel;
- Tank – helium tank;
- V02 – distributing cock with positions for sample saturation and specimen ventilation;
- Discharge line;
- Matrix cup – saturation group - a system of an encapsulated core holder and a core holder attachment mechanism.

The developed methodology of the research process includes several important elements (Fig. 3).

The primary material is received in the laboratory and some procedures are performed that are related to its photographing and the attachment of a unique identifier. The primary material produces test specimens which are cleaned, dried to a constant weight and the corresponding sequential research identifier is attached. The next step in the process is

to carry out quality control of the specimen, monitoring its integrity as required. The specimen prepared is photographed.

The following are important elements of the research process:

- the size of the samples tested;
- the calibration of the instrument.

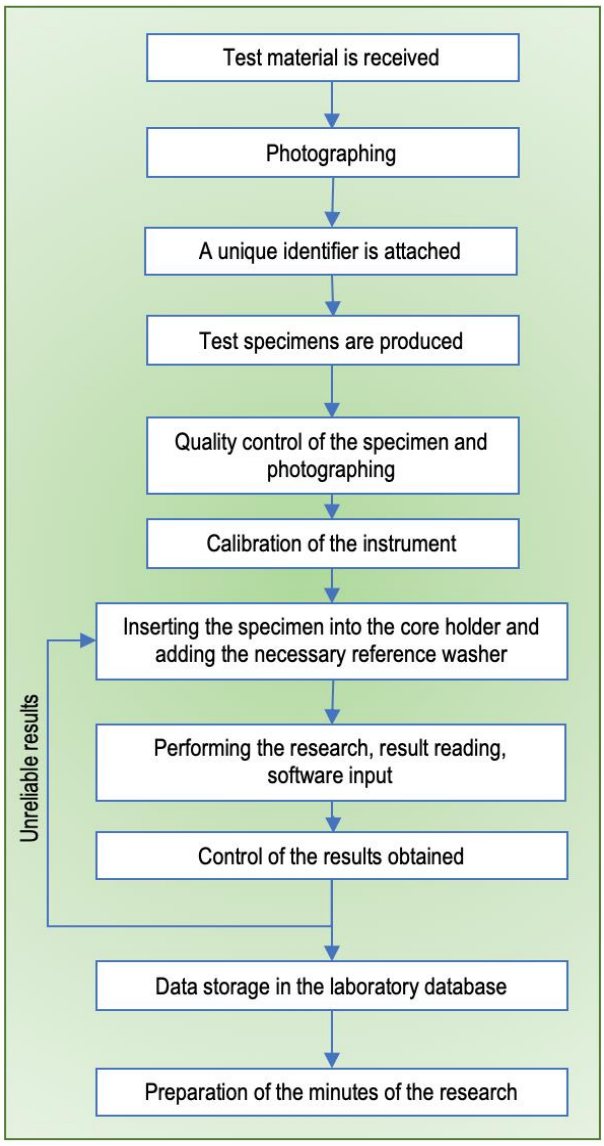

Fig. 3. Schematic presentation of the research sequence

To ensure greater reliability of the test, the sample size rule (the ratio of specimen height to specimen diameter) should be observed. The above should be 2:1. The core holder has a fixed diameter of 38.5 mm (1.5 inches); therefore, the optimum specimen height should be 76.2 mm (3 inches). If specimens of this height cannot be prepared from the test material, the height may be reduced to 38.5 mm (1.5 inches), i.e. to the ratio of 1:1, without significantly affecting the measurement results. The height of the specimen in the core holder (up to 76.2 mm) is supplemented by a set of 6 washers supplied with the apparatus. These are reference metal washers (Fig. 4), calibrated by the manufacturer, with a definite thickness and volume, depending on the need to adjust the height of the test specimen. When inserting any of the washers into the core holder, its factory number is input in the software product with the helium porosimeter. This is done in order to automatically read and correct the imperfection of the test core and, accordingly, the measurement result.

Fig. 4. Reference washers for the Vinci 3.28 helium porosimeter

The calibration of the instrument is based on the Boyle-Mariotte law on the volume constancy in an isothermal process (Fig. 5).

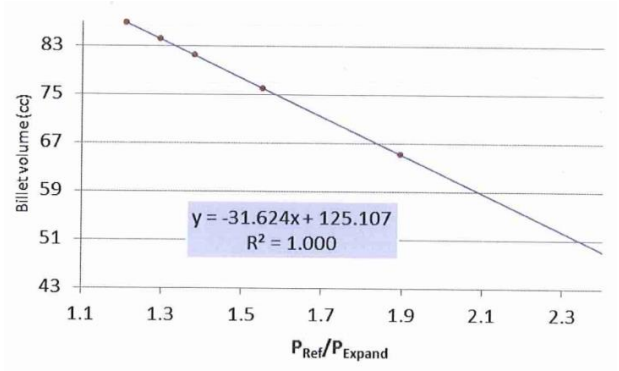

Fig. 5. Calibration curve of the helium porosimeter

It is a *sine qua non* that before each series of measurements, the apparatus must be properly calibrated. Technologically, this procedure in the helium porosimeter has been considerably simplified to avoid technological errors on the part of the operator. The six available washers are sequentially inserted into the core holder and volume and pressure measurements are carried out.

Once the volume has been established, an indication is made in the apparatus software of the particular washer being used at the time of measurement, and the computer automatically determines the Pref/Pexp ratio. The variation range should be between 1.3 and 5 depending on the installed calibration washer.

Another essential part of the preliminary preparation is checking for leaks from the apparatus. In case the pressure constantly changes, the system automatically signals for helium leakage. This requires a thorough check of the

connections in the system and the elimination of the problem before resuming the measurements.

Through these two preliminary procedures, the manufacturer guarantees the relevance and reliability of the results obtained during the measurement. The instrument calibration procedure is carried out on a daily basis, prior to commencing laboratory work and measurements, and lasts for about 30–40 minutes.

Following the instrument calibration procedure, the steps outlined in the schematic diagram of the research sequence are performed: inserting the sample, adding the necessary reference washer, and starting the test. The gas initially fills the reference tank and then saturates the sample. Usually, the time to stabilise the saturation pressure is in the range of 3–10 min. This stage is controlled by the operator. Depending on the lithological composition of the rock studied, with denser rocks, the stabilisation interval can be lengthened up to 20 min. If stabilisation is not achieved, the study should be repeated by adjusting the gas temperature or checking for helium leaks.

After the saturation is completed, the measurement results are input into the instrument software. The results obtained are controlled. In case they deviate significantly and/or the pressure ratios are not observed, the measurement procedure is repeated. If the results are satisfactory, they are stored in a database. An individual measurement report is prepared in accordance with a report form of the laboratory.

The main results include: porosity, permeability, volume and mineral density of the rock.

Conclusion

The methodical approach considered is versatile and offers expeditiousness of the research process and reliability of the obtained results. Thus, it can be applied both in research work and in the training of students and Ph.D. students in the petroleum field. The methodology and equipment have been implemented in the laboratory of “Physics of the Oil and Gas Stratum” at the University of Mining and Geology “St. Ivan Rilski”.

References

Ahmed, U., N. Mehan. 2016. *Unconventional Oil and Gas Resources: Exploitation and Development*. CRC Press, New York, 894 p.

Archer, J. S., C. Wall. 1986. *Petroleum Engineering: Principles and Practise*. Graham & Trotman, London, 362 p.

Balinov, V., V. Troshanov. 1968. The methodology for determining the water permeability of rocks. – *Annuaire de l'Ecole Supérieure des Mines et de Géologie*, *14*, 81–85 (in Bulgarian).

Balinov, V., E. Deshev, V. Troshanov, I. Dobrilov. 1972. Method for estimation of residual water saturation and capacity of fractured-cavernous rocks. – *Annuaire de l'Ecole Supérieure des Mines et de Géologie*, *18*, 122–129 (in Bulgarian).

Dake, L. P. 1994. *The Practise of Reservoir Engineering. Vol. 36*. Elsevier, 546 p.

Goroyan, W. I. 1971. Some results of measuring the solid volume of a phase of rock samples using an integrated volume meter. – *Trudi VNIGRI*, *90*, 1–86 (in Russian).

Hanin, A. A. 1969. *Oil and gas reservoirs rocks and their study*. Nedra, Moscow, 368 p. (in Russian)

Kalinko, M. K. 1963. *Methodology for the study of the reservoir properties of cores*. Gostoptehizdat, Moscow, 225 p. (in Russian)

Korbanova, V. N., I. D. Leparskaya. 1957. *Determination of physical properties of rocks*. Gostoptehizdat, Moscow, 160 p. (in Russian)

Twardoowski, K., J. Traple, S. Rychlicki. 2004. Evaluation of rock porosity measurement accuracy with a helium porosimeter. – *Acta Montanistica Slovaca*, *9*, 3, 316–318.

Zaneva-Dobranova, E. 2017. The research potential of petroleum engineering – a guarantee for modern education at the University of Mining and Geology “St. Ivan Rilski”. – *Vth International Scientific and Technical Conference Geology and Hydrocarbon Potential of the Balkan-Black Sea Region*. *18–22 September*, *Varna,* 295–301.

Zaneva-Dobranova, E., L. Georgiev. 2016. Review of the modern approaches for laboratory assessment of the reservoir properties of solid rocks-collectors. – *Ann. Univ. Mining and Geol.*, *59*, Part I, 202–205.

Zaneva-Dobranova, E., N. Hristov, D. Merachev, N. Sechkariov, 2017. Field methodology for hydrocarbons areol survey. – In: *Vth International Scientific and Technical Conference Geology and Hydrocarbon Potential of the Balkan-Black Sea Region*. *18–22 September*, *Varna,* 226–233.

Zaneva-Dobranova, E., N. Hristov, S. Bratkova, N. Sechkariov. 2019. Methodology for Assessing Surface Hydrocarbon Dissipation. – *19th International Multidisciplinary Scientific Geoconference SGEM 2019.* Proceedings, 192–197.

OPERATIONAL CONTROL AND MANAGEMENT OF DRILLING PARAMETERS AS THE KEY TO EFFICIENT DIRECTIONAL AND EXTENDED REACH DRILLING

Vyacheslav Kadochnikov

Saint Petersburg Mining University, 199106 Saint Petersburg; kadochnikov93@gmail.com

ABSTRACT. Every year the volumes of drilling wells with complex trajectories increase, and vertical wells are successfully occupied by directional wells with large waste from the vertical ones (extended reach drilling). Several sections with changes in the zenith and azimuth angles have difficult trajectories. The drill string in the well is in a complex stress-deformed state, as a result, tool landing and tightening occur, as well as the risk of loss of its elements' strength. It should be noted that a change in the geometry of the drill string in the presence of critical trajectory angles determines the slurry (formation of a slurry pad) and the change in the equivalent circulating density (ECD). The paper substantiates the necessity of operational control and management of drilling parameters in order to prevent emergencies in the well, especially while drilling in a narrow range of absorption and fracturing pressures. The results of a multifactor computational experiment are presented: the dependence of the hydrodynamic pressure in the well on the consumption of the cleaning agent and on the rate of penetration. The principle of determining the actual axial load on the bit and the algorithm for the operational control and management of the drilling parameters are presented: axial load on the bit, rotational speed of the drilling tool, cleaning agent flow, rate of penetration.

Keywords: drilling parameters, operational control, equivalent circulation density (ECD), well flushing, axial load on bit, extended reach drilling (ERD)

ОПЕРАТИВЕН КОНТРОЛ И УПРАВЛЕНИЕ НА ПАРАМЕТРИТЕ НА СОНДИРАНЕ КАТО СРЕДСТВО ЗА ЕФЕКТИВНО НАСОЧЕНО И РАЗШИРЕНО ВЕРТИКАЛНО СОНДИРАНЕ

Вячеслав Кадочников

Санктпетербургски минен университет, 199106 Санкт Петербург

РЕЗЮМЕ. Всяка година обемите на сондажи със сложни траектории се увеличават, а вертикалните сондажи успешно се заменят от насочени сондажи с големи отпадъци от вертикалните сондажи (сондиране с разширен обхват). Трудните траектории съдържат няколко секции с промени в ъглите на зенита и азимута. Сондажният комплект е в сложно, деформирано от напрежението, състояние, в резултат на което инструментът се приземява и затяга, както и има риск от загубване на здравината на елементите му. Трябва да се отбележи, че промяна в геометрията на сондажния комплект, при наличието на критични ъгли на траекторията, определя сондажния разтвор (образуване на шламова подложка) и промяната в еквивалентната циркулираща плътност (ЕЦП). Докладът обосновава необходимостта от оперативен контрол и управление на параметрите на сондажа с цел предотвратяване на аварийни ситуации в него, особено при сондиране в малък диапазон на абсорбционно и разрушително налягане. Представени са резултатите от многофакторния изчислителен експеримент: зависимостта на хидродинамичното налягане в кладенеца от консумацията на промивката и от скоростта на проникване. Представени са принципът за определяне на действителното осово натоварване върху короната и алгоритъмът за оперативен контрол и управление на параметрите на сондиране: осово натоварване върху короната, скорост на въртене на сондажния инструмент, дебит на промивката, скорост на проникване.

Ключови думи: параметри на сондирането, оперативен контрол, еквивалентна циркулационна плътност (ЕЦП), промиване на сондажите, осево натоварване върху короната, разширено вертикално сондиране (РВС)

Introduction

The reliability and the highest productivity of the equipment in the well is achieved by monitoring and managing the basic drilling parameters, including the axial load on the bit, the tool's speed rotation and the mud flow rate. Analysis of directional wells drilling data showed that the drilling of complex trajectories (wells with a deviation from the vertical of more than 3000 m) is accompanied by a 25 to 30% likelihood of tool puffs and landings. These complications are caused by the uncontrollable nature of the drill string's stress-deformed state when an axial load is applied to the rock-breaking tool. This, taking into account the hydrodynamics of flushing of wells, leads to the twists-off and breaks of the drill string elements, differential sticking and kick.

Significance of equivalent circulation density's control

Today, in drilling complex intervals in directional drilling, rotary-steerable systems (RSS) are widespread. These systems allow to post the well profile closest to the design (smoother, with minimal waviness and helicity), and also significantly reduce the likelihood of tool sticking due to the high penetration rate with a constant rotation of the drill string (Dvoynikov et al., 2017). However, it is impossible to completely solve the problem of differential sticking using only the RSS. The main cause of this type of complications is the uncontrollability of the pressure in the annulus, which is determined by the equivalent circulating density (ECD) of the mud. Downhole pressure is determined by the hydrostatic and hydrodynamic pressure during circulation in the annulus,

and/or the impulse pressures created by the movement of pipes in the well. The ECD consists of the equivalent static density (ESD) and the equivalent dynamic density (EDD) of the mud (1–4):

$$\rho_{ECD} = \rho_{ESD} + \rho_{EDD} \quad (1)$$

$$\rho_{ECD} = \frac{P_{bot}}{g \cdot H} + \frac{\Delta P_{bot}}{g \cdot H} \quad (2)$$

$$\Delta P_{bot} = \lambda \frac{\upsilon^2 \cdot \rho_{mud}}{D - d} L \quad (3)$$

$$Re = \frac{\upsilon \cdot D \cdot \rho_{mud}}{\mu} \quad (4)$$

where ρ_{ESD} and ρ_{EDD} – equivalent static and dynamic densities, respectively, kg/m^3; P_{bot} – bottom-hole pressure, MPa; ΔP_{bot} – pressure loss in the annular space, MPa; g – acceleration of gravity, m/s^2; H – vertical depth, m; λ – hydraulic resistance coefficient; υ – mud flow rate m/s; ρ_{mud} – mud density, kg/m^3; D – borehole diameter, m; d – bottom-hole assembly diameter, m; L – well length, m; Re - Reynolds criterion; μ - plastic viscosity, Pa·s (Makovey, 1986).

In fact, EDD, which depends on the hydraulic friction, is the mud density in the annular space and increases as the number of particles of drilled-cuttings in the annulus increases. This leads to a change in the density of the drilling fluid, and as a result, its rheological properties.

The problems of pressure regulation in the well are directly connected to the ECD, which is significantly higher in wells with large zenith angles and extended reach wells. The change in the ECD depending on the change in the wellbore length is considered (Fig. 1, Table 1).

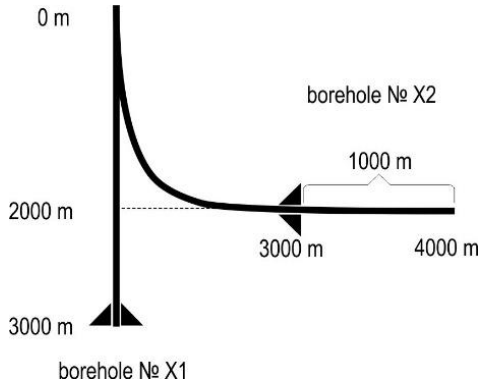

Fig. 1. ECD comparison in wells X1 and X2

Table 1. *Input data*

Parameter	Unit	Value
Mud density	kg/m^3	1200
Diameter of a bit	mm	220
Diameter of BHA	mm	120
Hydraulic resistance coefficient	-	0.02
Flow rate	m/s	1.2
Length of well X1	m	3000
Vertical depth of well X1	m	3000
Length of well X2	m	4000
Vertical depth of well X2	m	2000

The results showed that the ECD in well No. X1 is 1218 kg/m^3, and in well No. X2, 1235 kg/m^3. The ECD difference was 17 kg/m^3. It can be said that, the increasing of the well length along the trunk by 1000 m, while decreasing the vertical component by the same amount, leads to an increase in the ECD by 50% due to changes in the hydrodynamic environment. However, Figure 1 does not show changes in ECD associated with the complexity of interpreting processes at the bottom of a well like accumulation of drilled-cuttings, changes in pressure as a result of pipe movement (swab /surge).

To measure ECD and solve the difficulties associated with determining the pressure in the bottom-hole zone, an APWD (annular pressure while drilling) sensor is installed in the bottom-hole assembly (BHA), which provides the driller with real-time pressure information. However, it does not show reliable ECD values, as it is installed in the MWD measurement module (measurement while drilling), above the stabilizer located at least 10–20 m from the bit (Fig. 2). Its distance from the bit may underestimate the value of the ECD, while at the bottom of the hole the actual value may be significantly higher than that measured by the sensor.

The disadvantages of this measuring device include:

• The APDW sensor is not a reliable indicator of well cleaning during ERD;

• The APDW sensor detects ECD with a small amount of suspended drilled-cuttings;

• The APDW sensor does not detect a layer of drilled-cuttings deposited on the bottom wall of the well.

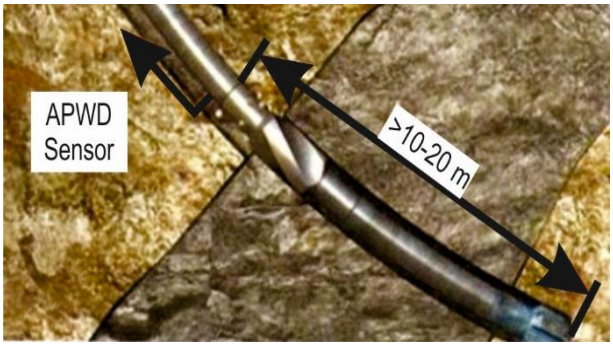

Fig. 2. APWD Sensor position in BHA

It is especially important for the driller to know the reliable value of the ECD and quickly regulate it at the bottom-hole not only during the drilling process, but also during tripping. The traditional method of drilling involves stopping the circulation, and the prolonged absence of circulation at the bottom-hole entails sticking of particles of drilled-cuttings onto the BHA elements and leads to sticking. Abrupt changes in ECD with a narrow range of mud density's acceptable values can lead to mud absorption or, conversely, to the manifestation of formation fluid, which would result in hydraulic fracturing or kick, respectively (Dolgopol'skiy, 2014; Cunningham et al., 2014).

It should be noted that the rate of penetration (ROP) is one of the main factors in determining and controlling ECD. This is because, the faster the rock destruction process, the bigger the amount of drilled-cuttings formed per unit time. Since the mechanical drilling speed is a function of tool rotational speed and axial load on the bit (5), determining the optimal drilling

parameters is the primary task for an efficient and trouble-free well construction process.

$$ROP = f(G; n) \quad (5)$$

where ROP – rate of penetration, m/h; G – axial load on the bit, t; n – tool frequency, rpm.

Control of equivalent circulation density

To determine the reliable value of EDS, a mathematical simulation of the flow of drilling in an inclined well was performed. To conduct a multifactor computational experiment, the drilling process of a J-shaped profile was modelled. The input data and the scheme are presented in Table 2 and in Figure 3.

Table 2. *Input data*

Parameter	Unit	Value
construction		
Measured depth (MD)	m	3000
Length of vertical section	m	1500
Radius of curvature	m	300
Length of slope part	m	1200
Angle of slope part	degree	45
tool		
Length of drill pipes	m	2920
Length of BHA	m	80
Diameter of drill pipes	mm	127
Diameter of BHA	mm	152
Diameter of bit	mm	216
mud		
Density	kg/m^3	1050
Plastic Viscosity	mPa·s	30
other		
Rock density	kg/m^3	2100
Diameter of particles	mm	3
ROP	m/h	50
Fracturing pressure (over static)	MPa	2

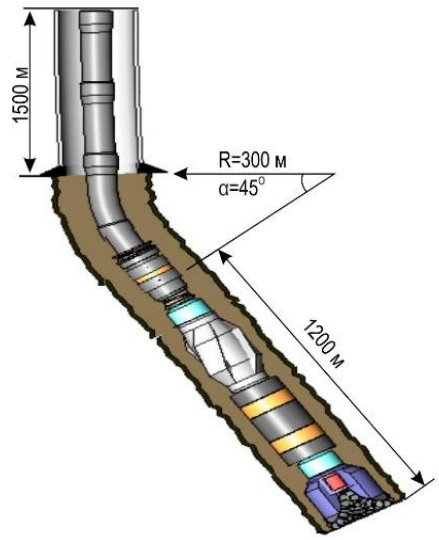

Fig. 3. Well profile and scheme of BHA

As a result of a multifactor computational experiment in the mathematical environment MathCad (Kudryavcev, 2005) the dependence (Fig. 4) of the change in the hydrodynamic pressure in the well on the mud flow was obtained at constant ROP – 50 m/h.

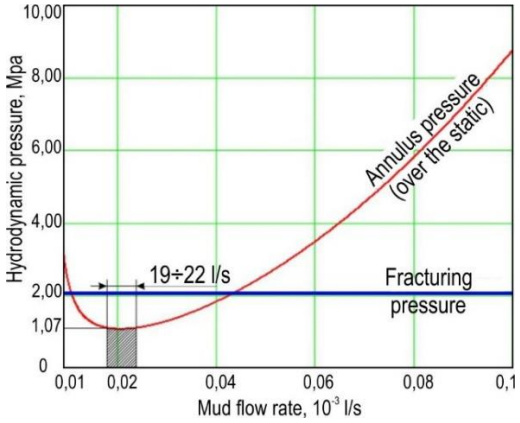

Fig. 4. The dependence of the hydrodynamic pressure (over the static) on the mud flow rate

This model takes into account the trajectory of the well, the sedimentation rate of the particles of the cuttings, the rheological properties of the cleaning agent, the ROP and the pressure due to hydraulic friction.

This dependence reflects the change in pressure with increasing flow rate of the cleaning agent from 9 l/s to 100 l/s and with the available upper limit of the hydraulic fracturing pressure at 2 MPa (over hydrostatics). The optimum flow rate at which the pressure drop is minimal, which is very important with a narrow window of absorption and fracturing pressures, ranges between 19–22 l/s.

When calculating the well pressure, pressure loss due to hydraulic friction and additional pressure caused by an increase in mud density due to drilled-cuttings accumulation were taken into account. To calculate the density of drilling mud with particles of drilled-cuttings at different intervals of the projected profile, the Moore correlation was adapted (Fig. 5). Preston Moore proposed a technique for calculating the sliding velocity of particles, taking into account the non-Newtonian behaviour of the drilling fluid, using the equation of the drag coefficient and the Reynolds number equation for spherical bodies during the deposition of particles through a non-Newtonian fluid (Sample, Bourgoyne, 1977).

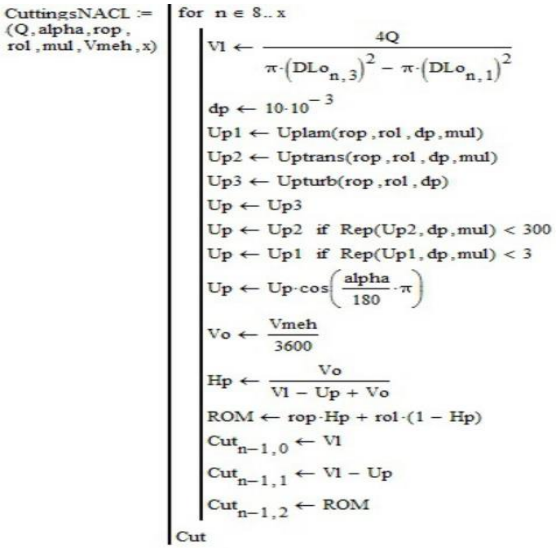

Fig. 5. Part of the software algorithm (Mathcad) for calculating the sedimentation rate of sludge particles

If we reconstruct the resulting graph of pressure change versus flow rate and obtain the dependence of the EDS change on the flow rate, then at a constant mechanical speed and a selected flow range of 19–22 l/s (when the pressure drop is minimal), the increase to the ECD value is 47 kg/m^3. The obtained dependence is similar to the graph of the drilled-cuttings transportation model (Fig. 6) presented in the article "Using downhole annular pressure measurements to improve drilling performance" (Aldred, 1998).

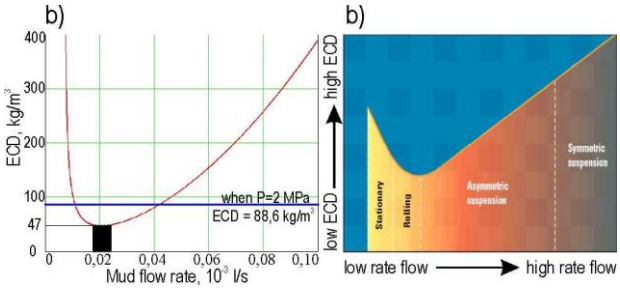

Fig. 6. The dependence of the ECD from the mud flow rate: a) received model; b) Schlumberger model

In Figure 6, it can be noticed that at low flow rates, drilled-cuttings can be deposited from the suspended state on the bottom wall of the wellbore, forming a slurry bed. The reduction of the annular space entails an increase in the ECD. With increasing mud flow, the particles of the drilled-cuttings begin to roll along the wellbore, destroying the cutting bed. Due to the partial destruction of the precipitated drilled-cuttings, the annular gap increases and the ECD begins to decrease. As the flow rate increases, most of the drilled-cuttings are transported along the bottom wall of the wellbore, with some particles being weighed in the fluid flow over the cutting bed (asymmetric suspension), which leads to an increase in ECD. At higher mud flow rates, pressure losses are significant due to viscous friction forces, and the drilled-cuttings are completely transferred to the fast-moving fluid (symmetrical suspension) (Walt, 1998).

Considering the drilling experience of Schlumberger, the similarity of the drilled-cuttings transportation model graphics and the dependence of pressure change with increasing cleaning agent consumption justifies the reliability of the model.

Figure 7 shows the graphs of pressure as a function of drilling fluid flow at various ROP. In accordance with the developed model, at a drilling rate of 15 m/h, the optimal mud flow rate (at which the pressure drop is minimal) is in the range of 13–18 l/s, at 30 m/h – 16–19 l/s and at 50 m/h – 19–22 l/s.

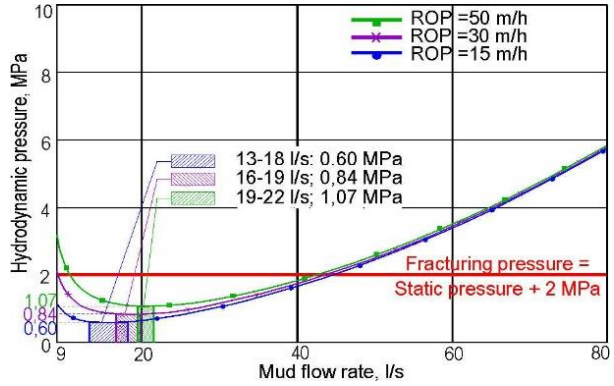

Fig. 7. Optimal mud flow rate (pressure drop is minimal) at various ROP

In the course of the simulation, the dependence of pressure on the ROP, with a constant value of the mud flow rate (Fig. 8), was determined. It can be seen from the graphs that only at low flow rates – 10 l/s, tg α ≈ 1 (α ≈ 45˚), which corresponds to a high intensity of pressure, increases with increasing the ROP.

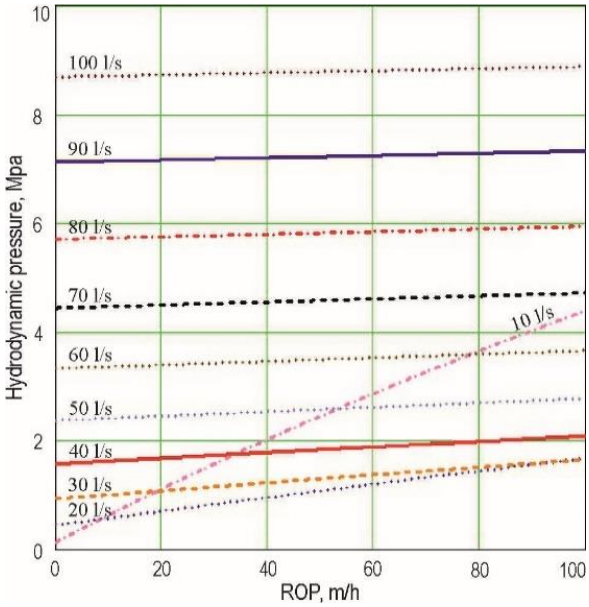

Fig. 8. The dependence of hydrodynamic pressure on ROP constant mud flow rate

An increase in the drilling mud consumption results in a decrease in *tan α* and the graph will take a flatter form. Hence, we can conclude that with increasing flow rate, the ROP has a far lesser effect on the pressure drop in the well. Further, the ROP completely loses its meaning, due to incompatibility with the drilling conditions, and the function takes the form (6):

$$P = f(ROP) \rightarrow const \qquad (6)$$

The resulting hydraulic model allows you to control the ECD in the bottom-hole zone by determining the optimal flow rate of the drilling fluid. However, for trouble-free well construction, in addition to effective flushing, it is also necessary to regulate the axial load on the bit and the rotational speed of the drill string.

Control of axial load on the bit

Analysis of practical data from drilling wells with a complex profile showed that the actual axial load on the bit differs significantly from the load measured at the geotechnical well testing (GWT) station. As a result, when drilling wells, the rate of penetration decreases, and the wellbore is formed with large cavities and grooves that impede the advancement of the BHA. Also, the intensity of the curvature and the radius of the build-up/drop off sections does not correspond to the permissible strength characteristics of the drill pipe. It is practically impossible to drill such areas using, for example, a hydraulic downhole drilling motor (DDM). This is primarily due to the large friction between the drill string and rocks. As a technological method of improving the efficiency of drilling with

DDM, while drilling oblique-rectilinear sections of the well, the drillers use the simultaneous periodic or constant rotation of the drill string with a rotor or with a top drive. Drillers call this method combined. Its use allows drilling wells of various depths with different types of profiles, a wide range of changes in the type and properties of drilling fluids, drilling mode parameters, as well as using different designs and sizes of rock-cutting tools (Dvoynikov et al., 2018).

The most effective technical solution of the problem aimed at improving the quality of the implementation of the project well trajectories and controlling the actual load on the bit is the use of displacement of the drill string relative to the axis of the well, the moment of resistance to friction of the drill string against the borehole wall, taking into account the loss of stability, as well as the tool rigidity when changing its stress-deformed state in the calculations of parameters.

The axial load on the GWT station is determined only by the change (loss) of the weight on the rig hook in terms of hydraulic weight indicator (7):

$$G_{GWT} = G_{hook} - G_{bit} \quad (7)$$

where G_{hook} – drill string weight on hook, N; G_{bit} – load on the bit, N.

Moreover, the actual axial load on the bit, taking into account the stress-strain state of the drill string, is determined by the formula (8) (Dvoynikov et al., 2018):

$$G_{fact} = G_{GWT} - \left[\frac{(M_{rw} - M_{ri}) \cdot ROP}{\omega \cdot \pi \cdot D \cdot a}\right] \quad (8)$$

where M_{rw} – moment on rotor in DDM operating mode, N·m; M_{ri} – moment on rotor in DDM idle mode, N·m; D – borehole diameter, m; ROP – rate of penetration (mechanical drilling speed), m/s; ω – the frequency of drill string rotation relative to the borehole wall, rad/s; a - displacement indicator (movement of drill string along the well axis), m.

$$a = \frac{\pi^4 \cdot f^2}{t} \quad (9)$$

Where f – the gap between drill string and wall of the well, m; t – pipe helix pitch with respect to the well axis in 2π, m.

$$t = \sqrt{\frac{4\pi \cdot EI}{G_{GWT}}} \quad (10)$$

where E – Young's modulus, Pa; I – drill string's polar moment of inertia, m.

The implementation was carried out using the example of drilling a section for stabilising the zenith angle using drill pipes with a diameter of 127 mm and a bit with a diameter of 215 mm. The ROP varied in the range from 20 to 28 m/h. Immediately before drilling, the following parameters were calculated: the rotational speed of the drill string; moments on the rotor in idle and operating modes of the DDM; displacement rate and the helix pitch of the drill string with respect to the well axis over 2π (Dvoynikov, 2018).

The difference of the moments on the rotor when the DDM operates in the idle mode and the operating mode is 5 kN·m, with measured Mrb= 5 kN·m, Mrw = 10 kN·m. The drill string's rotational speed relative to the borehole wall varies from 5.3 to 14.1 rad/s (with rotation from 30 to 80 rpm). The displacement of drill string with respect to the borehole axis *a* is $3.48 \cdot 10^{-3}$ m. The helix pitch of the drill string with respect to the well axis is 54.2 m. The axial load on the bit according to the GWT station is 10 kN.

Analysis of the results showed that the value of the actual load on the bit does not coincide with the value of the load on the bit at the GWT station (Fig. 9).

With a drill string's rotational speed of 5.1 rad/s (30 rpm) the load on the bit does not reach amounts to 7.8 kN. With increasing RPM to 14.1 rad/s (80 rpm) the load on the bit increases and is 9.2 kN (Dvoynikov et al., 2018).

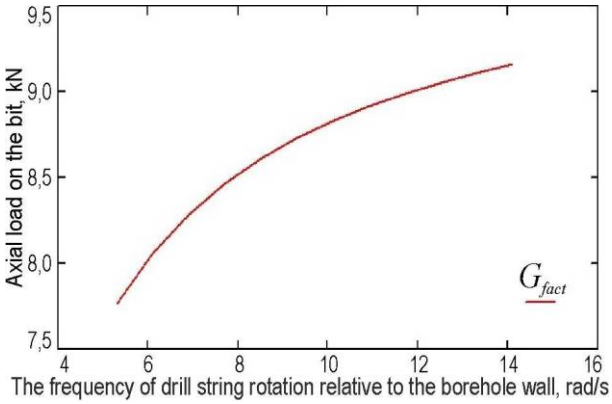

Fig. 9. Determination of the actual axial load on the bit

Algorithm of drilling parameters operational control

Knowing the axial load on the bit and the mechanical drilling rate, according to the data of the GWT station, the actual axial load reaching the bottom (with the available rotational speed of the drill string) is calculated using the formula (8).

The value of the mechanical speed, taking into account a certain actual load on the bit, is used when calculating the hydraulic programme, which allows controlling the ECD, maintaining the optimal mud flow rate. The algorithm of the programme is presented in Figure10.

In case of incompatibility of the drilling conditions, when there is likelihood of a hydraulic fracturing or kick, it is necessary to reduce (increase) the mechanical drilling speed, and the axial load reaching the bottomhole is achieved by adjusting the rotational speed of the drill string.

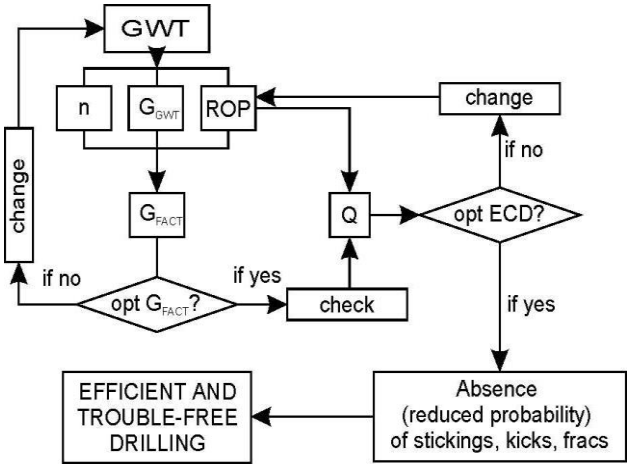

Fig. 10. Algorithm of operational control and management of drilling parameters

Conclusion

The resulting EDS control model takes into account well trajectory, sedimentation rate of particles of drilled-cuttings, mud rheological properties, ROP, pressure loss due to hydraulic friction and additional pressure caused by an increase in mud density due to cuttings accumulation. The similarity of the hydraulic model with the Schlumberger drilled-cuttings transport model justifies the correctness of the model.

However, for trouble-free drilling, it's necessary to regulate the axial load on the bit and the rotation frequency of drill string, in addition to effective flushing. This is achieved through the implementation of the method of controlling the axial load on the bit. The distinctive feature of the method involves the use of parameters like displacement indicator, moment of friction resistance and tool rigidity in the calculations.

The algorithm presented in the paper is a scheme for operational selection of optimal drilling parameters. This scheme is simplified and requires input of more factors.

The implementation of operational control and monitoring of the actual load on the bit, taking into account the rotational speed of the drill string, with insufficient speed and quality of signal transmission through the hydraulic communication channel from the telemetry system, allows us to predict ROP, to regulate the ECD, and also it preserves the reservoir properties and prevents problems in the well.

Acknowledgements. The author gratefully acknowledges the mentoring of the scientific supervisor Mikhail Dvoynikov, the recommendations of Dmitry Vodorezov in computer modelling, and the support of Daniel Edem Tsikplornu.

References

Aldred, W. 1998. Using downhole annular pressure measurements to improving drilling performance. – *Oilfield Review,* 40–55.

Cunningham, J., R. K. Bansal, G. George, E. De Leos. 2014. A New Continuous Flow System (CFS) for Managed Pressure Drilling. – *IADC/SPE Drilling conference and exhibition*, 7 p.

Dolgopol'skiy, A. L. 2014. Sistema neprerivnoy cirkulyacii dlya bureniya s kontrolem davleniya. – *Inzhenernaya Praktika*, *9*, 32–34 (in Russian).

Dvoynikov, M. V., P. A. Blinov, V. G. Kadochnikov. 2018. Sposob kontrolya osevoy nagruzki na doloto pri burenii naklonno napravlennih skvazhin vintovim zaboynim dvigatelem. – *The patent of Russia № 2646651 RU, E 21B 44/02, Byul. 7* (in Russian with English abstract).

Dvoynikov, M. V., V. G. Kadochnikov, A. A. Kunshin. 2017. Programmno-informitsionnoe soprovozhdenie stroitel'stva skvazhin arkticheskogo shelfa. – *Inzhener-neftyanik*, *1*, 23–28 (in Russian with English abstract).

Kudryavcev, E. M. 2005. MathCad 11. *Polnoe rukovodstvo po russkoy versii*. DMK Press, Moscow, 592 p. (in Russian)

Makovey, N. 1986. *Gidravlika bureniya*. Nedra, Moscow, 536 p. (translation from Romanian to Russian)

Sample, K. J., A. T. Bourgoyne. 1977. An experimental evaluation of correlations used for predicting cutting slip velocity. – *SPE Annual fall technical conference and exhibition*, 15 p.

FEATURES OF SEASON RESTRICTED ROADS' DESIGNING IN AREAS OF MINING FACTORIES UNDER CONSTRUCTION

Marina Romanenko

Saint Petersburg Mining University, 199106 Saint Petersburg; m.romanenko@geo-sz.ru

ABSTRACT. The article focuses on the question of season restricted roads' studying. In difficult geological, hydrological and climatic conditions of northern countries, such as Russia, Finland, Sweden, Norway, Canada, USA (Alaska), the basis of transport infrastructure is season restricted roads. The problem of season restricted roads' designing is still unresolved, which makes it difficult to maintain and operate such sites. The aim of research is advanced technology of season restricted roads' designing for their further title registration. This technology gives opportunity of first-ever defining possible changes of roads' boundaries by results of field measurements of physical and mechanical soil properties. The technology is developed with the application of similar stationary sites' rules, and also takes into account features of season restricted roads' existence in space and time. The main research objectives are: economic importance definition of season restricted roads; uncovering geographical and climatic conditions, providing possibility of road's functioning; reviewing the methodological approach of their accounting and systematisation. The research is carried out on the basis of information about the location of season restricted road's baselines, and also using the results of monitoring studies of highway service's department. To identify the possible location of roads a buffer zone's model is presented.

Keywords: mining regions, transport infrastructure, season restricted roads

ХАРАКТЕРИСТИКИ НА ПРОЕКТИРАНЕ НА СЕЗОННИ ПЪТИЩА В РАЙОНИ, КЪДЕТО СЕ ИЗГРАЖДАТ МИННИ ПРЕДПРИЯТИЯ

Марина Романенко

Санктпетербургски минен университет, 199106 Санкт Петербург

РЕЗЮМЕ. Статията се фокусира върху изучаването на сезонни пътища. В сложни геоложки, хидроложки и климатични условия в северните страни, като Русия, Финландия, Швеция, Норвегия, Канада, САЩ (Аляска), основата на транспортната инфраструктура са сезонните пътища. Проблемът с проектирането на сезонни пътища все още не е решен, което затруднява поддържането и експлоатацията на такива обекти. Целта на изследванията е усъвършенствана технология за сезонно ограничени пътища, предназначени за по-нататъшната им регистрация. Тази технология дава възможност за първоначално определяне на възможните промени на границите на пътищата чрез резултати от полеви измервания на физични и механични свойства на почвата. Технологията е разработена с прилагането на правила на подобни неподвижни обекти и също така отчита особеностите на съществуването на сезонни пътища в пространството и времето. Основните цели на научните изследвания са: определяне на икономическо значение на сезонните пътища; разкриване на географски и климатични условия, осигуряващи възможност за функциониране на пътя; преглед на методологичния подход на тяхната отчетност и систематизация. Изследването се извършва въз основа на информация за изходното местоположение на сезонните пътища, както и резултатите от мониторинговите проучвания на отдела за обслужване на магистрали. За идентифициране на възможното местоположение на пътищата е представен моделът на буферната зона.

Ключови думи: минно-добивни райони, транспортна инфраструктура, сезонни пътища

Introduction

Transport infrastructure is one of the most important elements on which development of the economic conditions of mining regions directly depends. Therefore, the most important problem of such areas is to provide all conditions for successful roads designing, their construction and operation.

Environmental features (climate, relief, soil properties) define roads` classification depending on the functioning mode: constant and season restricted. Season restricted roads with the base of snow, ice and frozen soil function only from October to March. They are common for many countries which have difficulties in the access to their northern regions: Canada, Finland, Estonia, Iceland, Norway, Russia, Sweden and USA (Nassiri et al., 2015).

Both kinds of roads (constant and season restricted) are complex engineering constructions in the form of linear objects. On the one hand, season restricted roads represent the way of certain direction which location changes every season. On the other hand, they have features of real estate items as they are inseparably linked to the ground surface, and their movement without disproportionate damage to appointment is impossible. In both cases season restricted roads require immediate strategic decisions concerning their construction and operation (Navratil, Frank, 2008).

Today the question of territory planning while designing such sites in difficult geological and climatic conditions is one of the most difficult in the field of civil engineering, geodesy and land management.

Main exposition

Easement areas of any road consist of land plots that determine location of the site's structural elements and road constructions. In other words, easement area represents the

borders of transport road. Formation of land plots under roads' construction includes not only land management works, but also actions, the result of which is creation of the site with new legal status (Kostyrchenko et al., 2016). The main difficulty is allocation of land plots for season restricted roads, because of their changing location during the seasons of the year.

The aim of research

The isolated regions of Northern countries are hard-to-reach areas with poorly developed infrastructure. In difficult geological, hydrological and climatic conditions of northern regions the basis of transport infrastructure are season restricted roads (Yukari et al., 2017). The extent of seasonal roads of such territories is comparable to federal highways as development, arrangement and operation of mineral deposits demand delivery of large-size loads and the equipment.

The aim of research involves advanced technology of designing work's development for seasonal roads' registration. This technology gives opportunity of first-ever defining possible changes of seasonal roads' boundaries by results of field measurements of physical and mechanical soil properties. Basic research tasks: to define specifics of season restricted roads as real estate items; to expose the need of registration of research sites taking into account distribution of their structure in time; to rank the factors defining physical and mechanical soil properties according to the extent of their influence on season restricted roads' location; to develop regression model of easement area's width depending on the extent of influence of indicated factors; to develop the technology of spatial basis' construction allowing to solve problem of season restricted roads' registration in view of their changing location.

Main thesis of the research

The research is carried out on the basis of information about the location of the season restricted roads' baselines, and also using the results of the monitoring studies of highway service's department. From the point of view of legal systems, the formation of land plots for such highways as typical linear sites is wrong. The algorithm for designing works of the object of seasonal operation has to consider distribution in space and time of a number of indicators which define location of such sites (Fig. 1).

As a result it is possible to note a divergence of lines that is connected with the site's specifics of seasonal existence. It can be explained with the changing location of a site depending on climatic conditions, topographic features, hydrogeological characteristics of the territory (Pavlov, 2010).

The creation of the image of the average line was carried out by the method of perpendiculars on points whose location is determined by extreme seasonal lines. It is necessary to obtain the first indicator – deviation of each line, from the drawn average line.

Knowledge of position of the average line in the presence of communication of indicators of certain physical characteristics with coordinates of each point can be used for forecasting the position of border lines in the set buffer zone. Each point corresponds to certain results of the studied indicators.

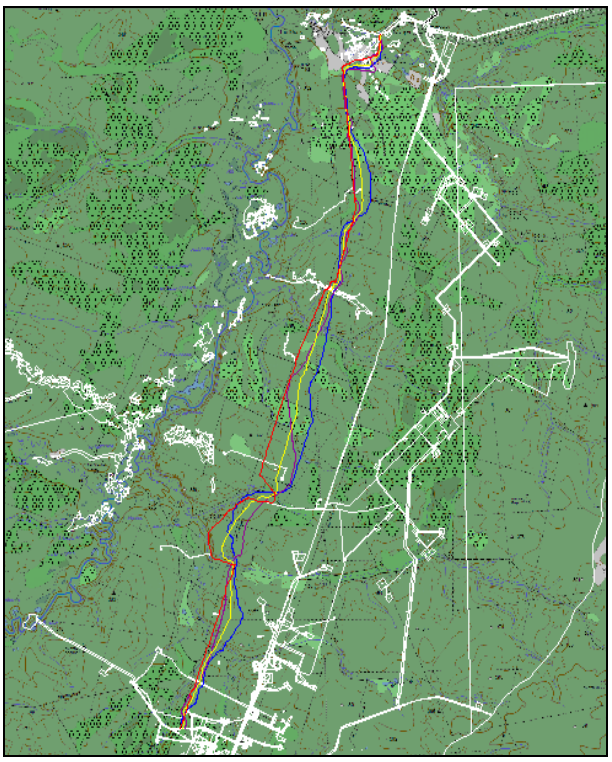

Fig. 1. The winter highways' lines with reference to the cartographic image of metric scale 1:200 000 and to the cadastral plan of the territory: the red colour indicates the line of 2016–2017 years, purple – 2011–2012, blue – 2007–2008, yellow – middle line

Field research on values of the indicators have been received by a testing laboratory of the State Highway Service in November 2007, 2011 and 2016. We need to determine them by carrying out an analytical research of each lines' groups with a binding to the values of their deviation. So far, the distribution of indicators of zones is only an assumption, its scientific justification is possible by a clustering method. Each point of three seasonal lines is characterised by the following signs:

- frozen ground depth, cm;
- snow density, g/cm³;
- time of soil freezing at the average air temperature: -10ºC, hours.

These observations need to be broken into "k" number clusters. Parameters should be considered with average line and should be spread out in clusters (groups). The main aim of statistical research is to find out dependence between deviations on points of lines of different seasons and physical parameters. For future clustering it is offered to establish the following zones:

- zone of maximum divergence;
- zone of average divergence;
- zone of minimum divergence.

The term "divergence" offers to designate distance between points of extreme axes regardless of a season (Skvortsov et al., 2005). The result of research for lines of the highway for the season 2011–2012 is set as an example. It is obvious that such research has been conducted for each of the seasonal lines (Fig. 2).

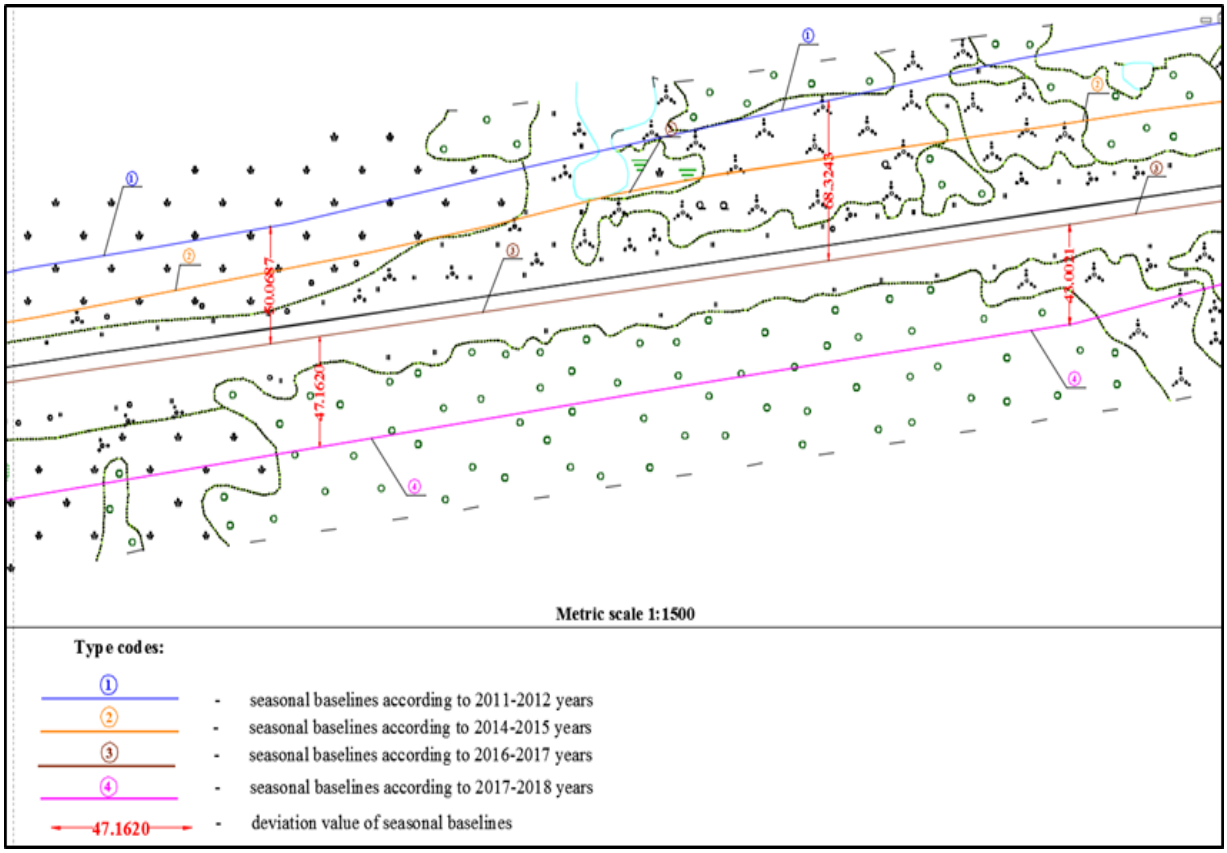

Fig. 2. Result of carrying out of analysis for the roads' seasonal baselines according to 2011–2017 years

The distribution of indicators' values is uneven. Certain groups and classes are obviously allocated. The following conclusions can be made: with the increase of the frozen ground depth, the divergence of lines also increases. As the snow density decreases, the divergence of lines increases. The maximum divergence of lines is in the zones, which have minimum time of soil freezing. Thus, the revealed dependence is logical and can be used for subsequent clustering of the indicators.

The result of cluster analysis is clear division of zones of divergence into three groups. Having information about the coordinates of points for each zone, it is possible to indicate them on the territory (Fig. 3).

The initial stage of the work is the construction of an exact image of the winter highway's baseline by seasons using geodetic survey data. As a result, we can note the divergence of the axes, which is related to the specificity of the site of seasonal function.

Then the middle line, built up by offset method due to the points of seasonal baselines, is determined. It is necessary to obtain the first indicator – the deflection of each baseline from the central one. Using the value of such deflection (with reference to other investigated indicators), it will be possible to explain and predict the location of the site in the future season.

Achieved major results

Knowledge of the position of the central baseline in accordance to these physical indicators can be used to predict the position of the winter highway for the next season. Therefore, an analytical study was carried out for each of the seasonal axes (on the slide as an example for one of them), as a result of which groups were identified. The result of the cluster analysis was a clear division of the zones of divergence into three groups. Having information about the coordinates of points for each zone, they can be indicated on the territory.

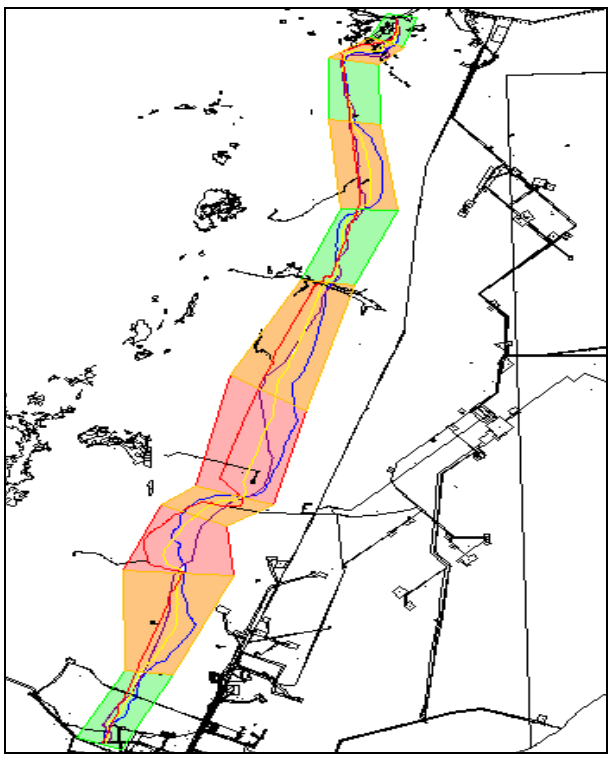

Fig. 3. The territory zones of lines' divergence
1, zone of the maximum divergence (marked with pink color); *2*, zone of the average divergence (marked with orange color); *3*, zone of the minimum divergence (marked with green color)

In addition, the location of the seasonal function site is affected not only by climatic and hydrological, but also by geological factors. That's why we need to take into account the natural features of the territory for cadastral work. All the stages of research are the framework for the algorithm of work for winter highway's cadastral registration. The algorithm is sustainable and requires knowledge of the distribution of a number of indicators in space and time.

Conclusion

The practical importance of research consists in the advanced algorithm of designing and land planning works of constant and seasonal highways. All presented milestones for the study are framework for such algorithm implementation, which requires knowledge of distribution in space and time of a number of indicators which define existence of such sites. It confirms the need of natural indicators' accounting. They can be designed only with the use of knowledge of laws of statement of similar stationary sites and taking into account features of existence in space and time.

Besides, another result of research is the creation of the buffer zone that defines borders of possible site's location for future seasons. The established zone will allow to keep account of such sites, and, secondly, will allow to avoid overlapping (most often, with forested land, royalty-based lands, and sometimes territories of Arctic Indigenous Peoples), the legal disagreements and other local questions caused by features of use and development of the territory.

References

Kostyrchenko, V. A., T. M. Madjarov, Sh. M. Merdanov. 2016. Osnovnyye aspekty razvitiya transportnoy infrastruktury Kraynego Severa (Basic aspects of the transport infrastructure's development of the Far North). – *Fundamental Research. Akademiya Yestestvoznaniya*, *Penza, 3-1*, 31–36 (in Russian).

Nassiri, S., A. Bayat, S. Salimi. 2015. Survey of Practice and Literature Review on Municipal Road Winter Maintenance in Canada. – *J. Cold Regions Engineering*, *29*, 3, p. 31.

Navratil, G., A. U. Frank. 2008. Expropriation in the Simple Cadastre. – *Nordic J. Surveying and Real Estate Research, Special Series. Vienna, Austria*, *3*, 27–29.

Pavlov, Ph. A. 2010. *Stroitelstvo i ekspluatatsiya zimnikh avtomobil'nykh dorog v severnykh shirotakh. Uchebnoye posobiye (Construction and operation of the winter roads in the northern latitudes. Tutorial)*. Northern Federal Univercity M. V. Lomonosov Publ., Arkhangelsk, 201 p. (in Russian)

Skvortsov, A. V., P. I. Pospelov, A. A. Kotov. 2005. *Geoinformatika v dorozhnoy otrasli: Uchebnoye posobiye dlya vuzov po spetsial'nosti "Avtomobil'nyye dorogi i aerodromy" (Geoinformatics in the road industry: A textbook for the specialty "Highways and Airfields")*. MADI University Publ., Moscow, 249 p. (in Russian)

Yukari, H., W. A., Gough, K. Butler, L. J. S. Tsuji. 2017. Trends in the seasonal length and opening dates of a winter road in the western James Bay region, Ontario, Canada. – *Theoretical and Applied Climatology*, *129*, 3–4, 1309–1320.

DEVELOPMENT OF CEMENT STONE WITH ENHANCED STRENGTH PROPERTIES

Daria Zimina, Michail Dvoinikov

Saint Petersburg Mining University, 199106 Saint Petersburg; ziminadar@yandex.ru

ABSTRACT. It is shown that cementing in conditions of permafrost is a complicated technical problem requiring the use of special technical means and technological methods. Well cementing experience in difficult conditions demonstrates that the use of traditional Portland cement clinker-based materials does not provide high quality well casing. The analysis of the main complications arising during well cementing at low temperature is presented. Quick-hardening and non-shrinking cements that form a strong stone and have high adhesion to casing pipes are necessary for high-quality cementing in difficult geological condition. The aim of the research was to study the additives that increase the strength of the cement stone. One such additive is silica fume, which is formed by cleaning the ore-thermal furnaces at metallurgical plants. The microsilica's properties improve concrete characteristics such as strength, wear hardness and frost resistance. The use of waste metallurgical production also makes the composition more environmentally friendly and reduces its cost.

Keywords: permafrost, microsilica, well cementing, strength properties

РАЗРАБОТВАНЕ НА ЦИМЕНТЕН КАМЪК С УВЕЛИЧЕНИ ЯКОСТНИ СВОЙСТВА

Дария Зимина, Михаил Двойников

Санктпетербургски минен университет, 199106 Санкт Петербург

РЕЗЮМЕ. Показано е, че циментирането в условията на вечно замръзнали почви е сложен технически проблем, който изисква използването на специални технически средства и технологични методи. Опитът при циментиране на сондажи при тежки условия показва, че използването на традиционен Портланд цимент на базата на клинкер не осигурява висококачествен циментов пояс на сондажа. Представен е анализ на основните усложнения, възникващи при циментирането на сондажа при ниска температура. За висококачествено циментиране в трудни геоложки условия са необходими бързо втвърдяващи се и не-свиващи се цименти, които образуват здрав камък и имат висока адхезия към обсадните тръби. Целта на работата е да се изследват добавки, които увеличават якостта на циментовия камък. Една от тези добавки е силициевият дим, който се образува чрез почистване на рудно-термичните пещи на металургичните предприятия. Свойствата на микросиликата подобряват характеристиките на бетона като якост, износване и устойчивост на замръзване. Използването на отпадъчна металургична продукция също прави състава му по-екологично чист и намалява цената му.

Ключови думи: вечно замръзване, микросилика, добре циментиращи, якостни свойства

Introduction

All cementing methods have one goal – to displace the cement slurry from the well annulus and raise it to a predetermined height. As a result, the possibility of movement of any liquid or gas from one layer to another through the annular space is prevented and the unstable, prone to collapses and scree rocks, are strengthened;

The importance of high-quality cementing is due to the fact that this is the final stage of well construction. Therefore, failures in its implementation can minimise the expected effect, cause an incorrect assessment of the prospect of explored areas, etc. The process of cementing wells (which is an irreversible operation), their repair and restoration are associated with significant costs and time.

Permafrost rocks are widespread throughout the world, occurring on all continents with the exception of Australia. In the northern hemisphere, the northern parts of Eurasia and North America are covered with permafrost. In Europe, permafrost is found in certain mountainous regions of the Caucasus, the Alps, Norway, the Kola Peninsula, and the Polar Urals.

Permafrost is currently about 25% of the total land area of the world, including 75% of Alaska's territory, 63% of Canada's territory and 47% of Russia's territory. The discoveries of large gas and gas condensate fields: Medvezhye, Urengoyskoye, Yamburgskoye, Kharasaveyskoye, Bovanenkovskoe and others in the north of the West Siberian Lowland attracted great attention to the study of the permafrost conditions in the region.

The presence of permafrost in the geological section and the poor quality of well casing can cause serious problems leading to such complications as inter-column flows, thawing of frozen rocks, low cement top, collapse of casing during reverse freezing, etc. In the permafrost interval a cement stone in the annulus of the well is formed with simultaneous exposure to a negative temperature — from the side of the borehole wall and positive — from the side of the casing string. A small amount of setting of cement stone, in addition to the presence of frozen rocks, is also due to the deformation of shrinkage during cement hardening. Sufficient operational reliability of well cementing in such conditions predetermines the use of special cement mixtures (Kozlov, Shepherds, 2014; Samsonenko et al., 2014).

In the studies devoted to this topic little attention was paid to the joint development of a non-shrinking cement mixture and the analysis of the dependence of porosity and permeability on the difference of thermal fields in the well, taking into account

the additives introduced into the composition of the solution. In general, the problem of insufficient tightness of wells in the permafrost zone remains relevant, in accordance with which there is a need to develop effective compositions of sedimentation-resistant cement slurries that ensure trouble-free flow of frost-resistant processes in frozen rocks (Kozhevnikov et al., 2014).

The main task of the development of cement compositions for cementing wells in the interval of permafrost is to ensure their setting in a short time before freezing at a rapid rate of cement strength.

Hypothesis of the study

Analysis of theoretical studies in the field of hydration processes of hardening of mineral binders of chemical and morphological composition of minerals allowed recommending microsilica as the main additive to cement, as a component that increases the strength of cement stone (Ovchinnikov et al., 2013).

Currently, the great scientific and practical interest of researchers is associated with the possibility of using microsilica in various industries, since most metallurgical enterprises store the microsilica obtained on special dumps. In this regard, there are significant economic losses associated, firstly, with the cost of storing and storing waste, and, secondly, with lost profit from their industrial use. The utilisation and use of dust waste from silicon production (microsilica) should be considered as an important direction in saving material resources and improving the environmental safety of adjacent territories.

At present, it is known that microsilica is widely used mainly in the production of concrete for the manufacture of very strong mixtures for the production of durable cement stone. Practical use has shown that 1 kg of silica fume provides the same strength as 5 kg of ordinary Portland cement. The high properties of silica fume improve such characteristics of the stone as compressive and flexural strength, adhesion, wear resistance, frost and chemical resistance and significantly reduce the permeability and porosity of the cement stone. "The data are published by Munkhtuvshin, Balabanov and Putsenko (2017), as well as by Butakova et al. (2017)".

In the process of production of metallic silicon, as a rule, two types of products are obtained:

– metallic silicon (with a purity of at least 98%, used in aluminum, chemical and other industries);

– silicon dust (ultrafine material obtained in the gas cleaning process of ore-thermal furnaces).

According to European and American standards for the use of microsilica (EK 13263 and ASTM C 1240), the silica content (SiO_2) in microsilica should be at least 85%. From the table (Table 1) it can be seen that the largest mass fraction is SiO_2 (at least 98%).

Microsilica is a highly active pozzolan additive to cement with fine grain size distribution, and when it interacts with cement mortar, conditions are created for the conversion of fragile calcium hydroxide (formed by mixing cement mixture with water and hydrating clinker material) into crystalline calcium silicate hydrate, which creates conditions for increasing the strength of cement stone, and microspheres fill the space that is released by water. Accordingly, the density of the composition increases, which in turn also increases its strength, and hence, its durability.

Table 1. *The chemical composition of the nanostructure concentrate based on silicon dioxide*

Substance identification	Mass fraction, %
SiO_2	no less than 98.0
CaO	no more than 0.3
MgO	no more than 0.3
Fe_2O_3	no more than 0.1
Na_2O	no more than 0.1
Al_2O_3	no more than 0.3
K_2O	no more than 0.3

Microsilicates are conglomerates of solid particles, ranging in size from submicron to several tens of microns with complex chemical and phase composition. A photograph giving an idea of the diversity of the grain size distribution of silicon dust is presented in Figure 1.

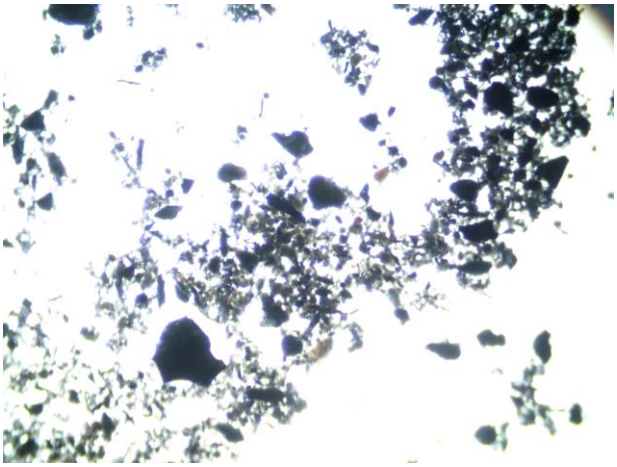

Fig. 1. Silicon dioxide nanostructures under the microscope

It should be noted that at present there are quite a few wells in which the permafrost interval is fixed by conventional pipes cemented by traditional cementing Portland cements. Therefore, for these conditions, it is important to estimate the probability of thawing of the near-wellbore zone during the operation of a well. This will solve the problem of reducing the intensity of thermal interaction in the "well-soil" system and substantiate the requirements for cement materials for securing wells in these conditions.

There is a vertical well passing through the permafrost. As a result of heat exchange between the fluid moving in the well and the frozen ground, it thaws.

We make the following assumptions: the rocks are uniform and isotropic; the density of the frozen rock is equal to the melted density; heat is transferred only by heat conduction; during the movement of the phase transition front in the permafrost, there is no mass transfer of liquid fluids.

The use of plugging materials with low thermal conductivity still leads to thawing of the near-wellbore zone of permafrost. The only question is the timing of the soil thawing around the

well and the time when it loses stability. Therefore, the development of cement materials with low thermal conductivity or the use of other thermal insulation materials and technologies continue to be relevant.

In this case, another important factor affecting the strength of a cement stone is its porosity. With an increase in the total porosity of cement stone from 10 to 60%, its strength is very significantly reduced. Of all the types of pores, capillary and also pores containing trapped air have the greatest effect on porosity. With an increase in the number of such pores, the strength of the cement stone decreases. Finally, with the same degree of hydration and porosity, the strength of the cement stone depends on the nature of crystallisation of the hydrates as a filling (calcification) of large pores.

The studies were carried out with the help of computer microtomography - this is a reconstruction of three-dimensional models of x-ray images.

Methods

In accordance with the goal and objectives, the work included theoretical and experimental research. Cement samples were prepared in accordance with test standards. First, the dry components of the composition were mixed (Portland cement grouting PCT I-50, silica fume). The remaining components (amendment agent, stabiliser, plasticiser, and calcium oxide) were included in the mixing fluid. Then they were mixed in a paddle mixer with a rotation speed of 1500±100 rpm within 3 min. The water-cement ratio (W/C) for all samples was 0.5.

Low and negative temperatures slow down the setting of the cement stone, which increases the time of setting in the winter period of well construction. In this case, it is advisable to use additives that accelerate the setting. Under standard well conditions, at normal temperatures, the $CaCl_2$ electrolyte serves as a set accelerator. Calcium chloride is also often used in drilling at low temperatures; however, if the accelerator is used excessively in negative temperatures, thawing of frozen rocks during its exothermic reaction may be caused. When using 4% $CaCl_2$ solution, the solution has a high heat release rate at the beginning of the mixing (during hydration) with a minimum amount of heat generated in general.

In further studies, a 4% calcium chloride solution was used as a mixing fluid.

In addition to measuring the main properties of cement mortar, such as water-cement ratio, water separation, spreading, density, thickening time, setting time, expansion ability, adhesive strength of cement with metal, rheological properties, sedimentation stability, and permeability, significant attention was paid to measuring the strength characteristics

The temporary resistance to bending, compression and less tearing are characterised by the strength of the cement stone. Cement stone strength is variable. Usually at the beginning of hardening, it quickly increases, and then gradually stabilises, and after a while it begins to decrease. Strength is determined by the destruction of samples on a hydraulic press.

Compressive strength is determined by the destruction of samples on a hydraulic press. The prism size is 4x4x4 cm. Flexural strength is determined by the destruction of prism specimens on a tensile machine. The dimensions of the prisms are 4×4×16 cm.

To determine the compressive strength, samples are first made (cement mortar is poured into moulds of appropriate sizes, which are made of steel or plastic). At least 3 samples are made (from one batch), they are kept under the same conditions and the same amount of time. After 24±2 hours, the samples are freed from the moulds and subjected to testing on a hydraulic press. The strength is taken as the average of three dimensions. The loading rate should be no more than 2 MPa per 1 s when tested in compression.

To determine the bending strength, samples (Fig. 2) are also made (the preparation procedure is the same as for compression images). It was established that the final strength characteristics of the cement stone are acquired after 28 days of hardening. But after 2 days the strength of the cement stone is able to reach 90% or more of the maximum. Therefore, operational strength assessment is given after 2 days of hardening.

Fig. 2. Samples of cement stone under the influence of different temperatures

In this work, the samples were made and placed for a period of strength set-up (1 day) in a refrigeration chamber at temperatures of -5°C and -15°C. Further, to study the difference in the formation of cement stone with the same and different effects of thermal fields, the samples were placed in the refrigeration chamber simultaneously with the installation of the heating element (with a temperature of about 50–60°C) on the upper surface of the sample and were also left at rest for 1 day. The installation was filled with foam for thermal insulation of samples (Fig. 3).

Since the phase transformations of the components of the cement stone should be accompanied by its destruction, it is logical to assume that these changes will directly affect the structure of the pore space of the samples. In this regard, in accordance with the methodology described by Dvoynikov (2017), studies were carried out to assess changes in the structure of the pore space of samples obtained from cement slurry, which were stored at temperatures of -15, 5, 20°C at 2 and 28 days.

Studies were conducted at temperatures of 20, -5 and -15 °C with simultaneous exposure of the thermal field to the sample (heating element consisting of metal plates) and cold field (the sample was placed at negative temperatures). The time to build strength in specified modelled conditions is 2 day. Then the samples were tested for flexural strength and compression. The broken parts of the samples were checked

on a microtomograph. Open, closed and total porosity, and the results of the study were divided into two "parts" – the upper side of the heat and the lower side of the cold.

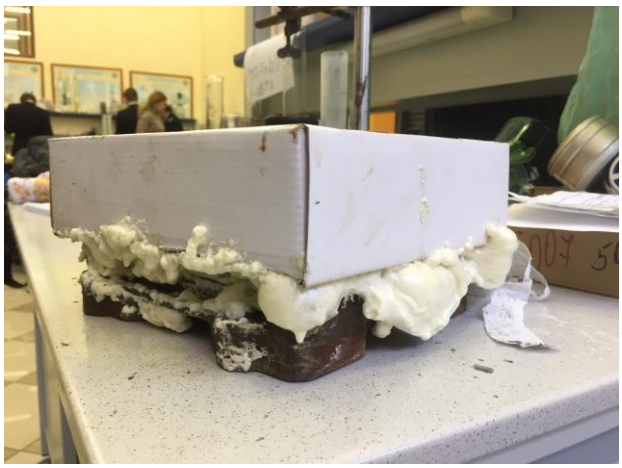

Fig. 3. Samples of cement paste in the form

Results

The table below (Table 2) presents the results of the measurement of the flexural and compressive strengths based on the average maximum value of the three samples in each experiment.

The table compares the samples prepared without the addition of microsilica and with a 10% addition to the dry mix. Samples were tested both at normal and at negative temperatures

Table 2. *The results of the study of strength characteristics of cement stone*

Temperature Max amount of strength	Standard composition (normal/negative)	Using microsilica (normal/negative)
Compressive (2 days)	10.2/8.0	19.1/14.3
Bending (7 days)	22.8/15.3	30.2/21.2
Compressive (2 days)	3.8/1.1	4.7/3.5
Bending (7 days)	9.4/3.5	12.6/5.5

According to the obtained results, it can be concluded that the addition of silicon production wastes to the cement slurry, together with the use of calcium chloride, was theoretically supposed to positively affect the properties of the cement stone and improve such indicators as strength, frost resistance, and permeability, provided that the cement content is low.

On the basis of the results in the table, we can build a graph of dependence of the amount of microsilica injected and the indicators of the strength of cement stone. The optimal percentage of microsilica is 10% of the dry mixture of the composition (Fig. 4).

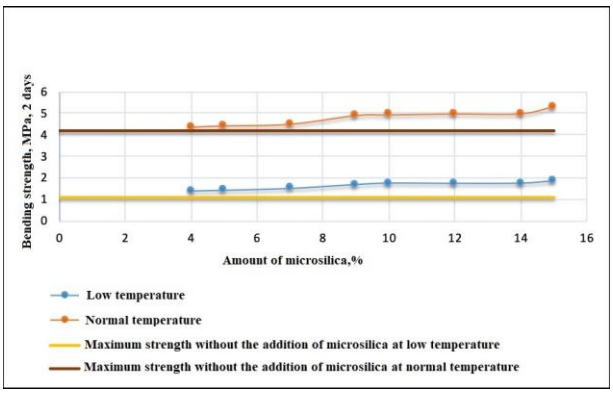

Fig. 4. Dependence of the influence of the amount of microsilica on the strength characteristics of cement stone

The analysis of the samples' porosity shows that the total porosity has solidified for 2 days at normal temperatures and practically remains constant. For samples formed at lower temperatures, the total porosity is slightly lower. This is explained by the phase composition of the hardening products. Indeed, the cement stone obtained at these temperatures is mainly represented by hydroaluminates and calcium hydrocarboaluminates, the surface of which is blocked by the gel-like mass of partially reacted calcium hydrosilicates. Therefore, the fusion of these aggregates leads to the formation of a structure with a small pore volume and smaller size.

The confirmation is the data on the change in the integral porosity. It is noted that with increasing temperature there is an increase in pore sizes, and an increase in subcapillary pores (usually the cause of destruction processes) is not observed.

For samples hardened for 28 days, an increase in total porosity with increasing ambient temperature was observed.

However, for samples obtained and stored at the same temperature, the change in total porosity does not occur. Only redistribution of pores occurs, together with an increase in the volume of smaller pores. The result obtained is explained by the formation of the structure of the cement stone, mainly calcium hydrosilicates, which have a large specific surface, naturally a greater number of accretion contacts, and therefore a lower porosity. The redistribution of pores is caused by ongoing hydration processes. And since there is a reduction in size and there is no change in the total porosity, the results serve as another confirmation of heat resistance in the considered temperature range of stone formed from cement slurry using microspheres.

The results obtained by changing the pore structure at a temperature of -5°C for two days are quite interesting. Apparently, in this case, there are broken bonds between hydrosilicate compounds of high basicity. Since at these temperatures the solubility of the silica component is sufficiently small, the resulting low-base hydrosilicates do not have time to compensate for the negative effects of the phase transformations of the highly basic calcium silicate silicates.

For a stone made of cement-based Portland cement, without silica additives, in the study of its physical and mechanical properties a sharp drop in strength was found at temperatures of -5 and -15°C of the environment. The sample is marked by cracks. Therefore, they have not been subjected to research on changes in the pore structure.

Below (Fig. 5) a histogram is presented based on the generalised porosity data of cement stone samples.

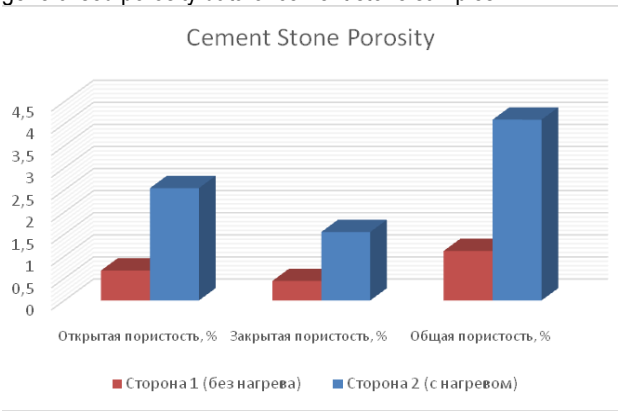

Fig. 5. Cement stone porosity

The heat side is red, the cold one is blue, respectively. As can be seen from the histogram, both open and closed (as well as total) porosity is more observed in the cold region of the sample, that is, from the frozen rocks in the well. In this regard, we can conclude that additional insulation material or technology is necessary to be added.

Conclusions

Based on the data obtained, we can draw the following conclusions: the material cracks when more than 15% of microsilica is added to the composition, so the further studies are not expedient. Adding 10% of microsilica to the solution increases the strength of the cement stone. By using it as a tempering fluid, the strength of 4% $CaCl_2$ solution is increased at negative and low temperatures. On the basis of the researches performed, it is possible to recommend the addition of calcium chloride to the composition of the cement mortar together with microsilica in order to increase the strength characteristics.

By analysing the data on the results of porosity studies, we can also conclude that at low and negative temperatures the number of pores increases, that is, an additional heating element is needed in the well.

References

Butakova, M., A. Mikhailov, S. Saribekyan. 2017. Influence of silicon-containing additives on the property of the watertightness of concrete samples. – *Bull. South Ural State Univ., Ser. Construction Engineering and Architecture, 17*, 2, 34–41 (in Russian).

Dvoynikov, M. 2017. Studies of technical and technological parameters of drilling of inclined wells. – *Zapiski Gornogo Instituta, 223*, 86–92 (in Russian).

Kozhevnikov, Ye., N. Nikolayev, O. Ozhgibesov, R. Dvoretskas. 2014. Investigation of the effect of sedimentation of cement slurry on the properties of the resulting cement stone. – *Neftyanoye Khozyaystvo, 6*, 23–25 (in Russian with English abstract).

Kozlov, A., A. Shepherds. 2014. Cement material for casing cementing in permafrost intervals. – *Perm Nat. Res. Polytechnic Univ. Bull., Geology, Oil, Gas and Mining, 13,* 10, 42–48 (in Russian with English abstract).

Munkhtuvshin, D., V. Balabanov, K. Putsenko. 2017. Experience of use of adds of micro- and nanosilica from the wastes of silicone production in concrete technologies. – *Putsenko Proceedings of Universities. In-vestments. Construction. Real estate*, *7*, 3, 107–115 (in Russian with English abstract).

Ovchinnikov, V., S. Roder, I. Beley. 2013. The results of studies of volumetric changes during hardening of cement slurries with expanding additives under conditions of moderate temperatures. – *Burenie i Neft'*, *3*, 25–28 (in Russian with English abstract).

Samsonenko, A., S. Simonyants, N. Samsonenko. 2014. Novye materialy i innovatsionnaya tekhnologiya krepleniya skvazhin v usloviyakh Kraynego Severa. – *Stroitel'stvo Neftyanykh i Gazovykh Skvazhin na Sushe i na More, 11*, 40–47 (in Russian with English abstract).